N° d'ordre 206-2005
LYCEN – T 2005-43

Thèse

présentée devant

l'Université Claude Bernard Lyon-I
et l'Université Leopold Franzens d'Innsbruck

pour l'obtention du

DIPLOME de DOCTORAT
Spécialité PHYSIQUE NUCLEAIRE

(arrêté du 25 avril 2002)

par

Bruno COUPIER

Studies towards the understanding of the effects of ionizing radiations at the molecular scale (20-150 keV H^+/H + He collisions ; dissociative Electron attachment to water)

Soutenue le 17 novembre 2005
devant la Commission d'Examen

Jury :	Mme	S.	Schindler	Présidente du Jury
	Mme	N.	Moncoffre	
	M.	M.	Farizon	Directeur de thèse
	M.	T.D.	Märk	Directeur de thèse

N° d'ordre 206 Year 2005

THESIS

presented

at

UNIVERSITE CLAUDE BERNARD - LYON 1

and

LEOPOLD FRANZENS UNIVERSITÄT - INNSBRUCK

To obtain the titles

DIPLOME DE DOCTORAT

DOKTORAT DER NATURWISSENSCHAFT

(arrêté du 25 avril 2002)

Defended on the 17th of november

By

Bruno COUPIER

Studies towards the understanding of the effects of ionizing radiations at the molecular scale

(20 -150 keV H+/H + He Collisions ; Dissociative Electron Attachment to Water)

Supervisors :

Univ. Prof. T.D. Märk (Institut für Ionenphysik von Innsbruck),

Univ. Prof. M. Farizon (Institut de Physique Nucléaire de Lyon)

JURY : Univ. Prof. Sabine Schindler, Président

Univ. Prof. Tilmann Märk

Univ. Prof. Michel Farizon

Dr. Nathalie Moncoffre

Abstract

This work comes within the scope of recent studies towards a better understanding of the effect of ionizing radiation at the molecular scales on biological systems, initiated by the group IPM of the IPNL in collaboration with the Institute für Ionenphysik of the University of Innsbruck. It is composed of two parts. One presents a new set of coincidence measurements of cross sections for the impact of protons or hydrogen atoms on helium in the energy range 20-150 keV of interest for the radiation biology. It is an archetypal system of interest for the theoreticians and there exists only a few studies on the impact of hydrogen atoms on helium. This study with helium was also motivated for the sake of performing a general test of functioning of the apparatus before investigating more complicated systems. Similar studies were then performed by replacing helium with water and biological molecules of relevance (Uracil, Thymine …) as target. This constitutes a study of direct effects of fast ionizing radiations on molecules of biological interest. The second part of the thesis deals with another type of ionizing radiations which can be seen as indirect effects of the first fast ionizing radiations studied in the first part. Low energy electrons emission in the energy range 1 to 16 eV follows the bombardment of the matter by swift protons/hydrogen atoms; these electrons have in turn an ionizing influence on the environment. A review of the dissociative electron attachment to water was undertaken in the University of Innsbruck motivated by the existing discrepancies between old studies on the same subject. A special attention was given to the problem of high energy kinetic ion discrimination in the trochoïdal monochromator used for this work.

TABLES OF CONTENTS

Introduction

The studies presented in this thesis come within the scope of recent studies towards a better understanding of the effects of ionizing radiations on biological systems at the molecular scale, initiated by the group IPM of the IPNL in collaboration with the Institut für Ionenphysik of Innsbruck. Proton and neutral hydrogen impact experiments with an atomic helium target were carried out at IPNL, representing a model system for the study of direct interactions of ionizing radiation in more complex systems. The experimental program at Innsbruck focused upon the interactions of electrons with water molecules, recognized as a key process in the damage to biological molecules initiated by ionizing radiation.

New therapies by heavy ions impact are in development. The use of heavy ion radiation is advantageous to deliver highly localized energy deposition upon a tumor, while minimizing the exposure of healthy tissue. H^+/H interactions with matter are central to proton therapy and provide a model example of this type of radiation.

When they penetrate the matter the protons are progressively decelerated by numerous interactions with the electrons of the traversed medium, producing multiple ionizations and excitations by different mechanisms. A proton looses a small amount of its kinetic energy in each collision. It can also get dressed by one or several electrons from the medium and continue its course as a neutral hydrogen atom or, more rarely, a negative hydrogen ion (H^-). Its ionizing power is then reduced until it looses its electron(s) again, and returns to its initial charge state (H^+). This phenomenon of electron capture is however very improbable until the protons has lost enough energy mostly by ionizations. The cross sections of ionizations by proton impact on various simple atoms and molecules targets ($H^+ + T \rightarrow H^+ + T^{n+} + ne^-$) reaches a maximum for an impact energy of roughly 1MeV (Rudd, [11]). When the energy of the protons is further decreased down to 100keV and below, the processes of electron capture ($H^+ + (e^- + T^+) \rightarrow H^0 + T^+$) and electron loss ($H^0 \rightarrow H^+ + e^-$) become dominant with respect to ionization processes (Toburen, [1]). The interaction of the protons with the matter is very effective in the domain of energy between 20 and 150keV, for which the cross section of pure ionization is still high, the hydrogen atom electron loss cross section is at its maximum (~100keV) and the electron capture by proton increases to its maximum near 25keV. Hence, in this energy range, protons and hydrogen atoms have a very effective conjugated ionizing action on the matter.

The curve of deposition of energy as a function of the depth of penetration in matter is peaked at the end of the course of the projectile and is called the Bragg peak. The domain of the Bragg peak spreads from 20keV to 150keV. Typically, initial kinetic energies as high as 200 MeV are required for a proton to reach organs of a patient situated 25 cm beneath the skin, but most of the energy is deposited in the last cm. The differential survival of tumor and tissue determines the healing or wounding effects of such a therapy. Therefore the promising improvement of the use of heavy ions radiation for cancer therapy with respect to the more traditional X-Ray radiation is worth the price of very expensive installation needed for producing and controlling beam of heavy ions.

Only the effects of primary radiation have been discussed so far, but subsequent energy loss events by the ejected electrons and the chemical reactions initiated by the residual ions and/or excited states are also very important. The secondary interactions are responsible for the track structure and radiation damage in the medium. The effects of secondary electrons were long underestimated but actually for protons of 800keV around half of all ionizations are produced by the fast projectile itself and the rest by its secondary electrons (Paretzke, [2]).

Track structure simulations [2] are very useful for estimating the effect of ionizing radiations on a given medium. Estimates of cross sections for condensed media are usually extrapolated from gas phase data (water vapor, hydrogen, hydrocarbons and rare gases).

Naturally the gas phase represents a dramatically different environment to the *in vivo* situation (liquid / gel) and cross sections for specific processes are expected to change according to the phase. However liquid phase experiments are not practical for the isolation of single interactions whereas the irradiation of gas phase molecules provides the ideal conditions to observe single interactions and thus the clearest framework to study fundamental processes. Gas phase cross sections are essential for the analysis and modeling required to understand more complex systems (track structure models). Indeed the IPM group of the institute de physique nucléaire of Lyon and the Institut für Ionenphysik of Innsbruck are in collaboration to proton and electron collisions with clusters, which constitute an intermediate system between the gas and condensed phases.

The central point of the current project of the IPM group is to study the effect of swift protons and hydrogen atoms on a cluster of a DNA molecule surrounded by molecule of water as a closer approach to the *in vivo* conditions in the organisms. However we are at the beginning of this enterprise and we must firstly get acquainted with simple systems and know if the apparatus can be trusted for the realization of our ambitious program. The collisions of protons or hydrogen atoms upon helium constitute an archetypal system to understand the

elementary charge changes phenomena. Many features of the charge changing phenomena in this simple atomic sytem are applicable for more complex systems.

Part I : Charge changes phenomena in protons/hydrogen atoms collision on helium in the gas phase (Lyon)

Introduction

The purpose of our experiments is to develop an understanding of the swift protons and /or hydrogens impact effects on biological system at the molecular scale. Before going to such complex systems as the irradiation of DNA surrounded by water molecules in order to reproduce more faithfully the conditions in living organisms, the general method of investigation is to cut off the study of the complex system into studies of elementary processes which might occur during the irradiation of the complex system. Thus, before studying the irradiation of clustered-DNA or RNA, the separate study of radiation effects on its basis (Uracil [3], Adenine, Guanine, Cytosine …) has been undertaken for the sake of clearing the ground. Still, the studies of such systems remain complex, and the study of more elementary systems was of interest to get acquainted with the fundamental inelastic processes and for the sake of performing a general test of functioning of the apparatus before investigating more complicated systems. Hence, the successive studies of the irradiation of water molecules and of helium atoms constituted first steps before the further investigations of irradiation of more complex systems of biological interest.

The interaction of simple ion-atom systems like H^+ + He and H + He, provides a unique opportunity for experimental tests of the foundations of quantum scattering theory. In the collisions of these simple ion-atom systems, comparison of the experimental and theoretical results tests the quantum mechanical model of the process in situations where the fundamental interaction forces are known [4]. For this reason such simple collision systems have been extensively studied (Park [4], Tawara and Russek [41], Rudd et al [11]), however only a few studies are available about the hydrogen-impact on He [5,6,7,8,9]. Besides, H^+ + He is the most simple system which involves the electron-electron interaction of great interest for the theoreticians since it is a non-central, time-dependent component in the effective potential and much more difficult to describe than the nucleus-electron interaction. Double electron capture from helium and double ionization of helium measured in our studies are of particular interest to progress theoretically towards the better understanding of the electron-electron interaction in helium target [10]. Systems like H + He and H^+ / H + H_2O are of increasing complexity and start only to be handled by the theoretists in the intermediate energy range (<100keV).

Moreover, the complementary studies of the impact by swift hydrogen and/or the impact of swift protons are important because of the conjugated actions of H^+ and H in the matter: the interactive action of the one in a given medium goes necessarily with the action of the other since a swift proton having captured an electron becomes a swift hydrogen atom with almost unchanged velocity and interacts in turn with the target-medium.

In this thesis, we will present the study of inelastic collisions leading to the formation of helium ions by impact of hydrogen atoms or proton. We observed reactions of charge exchanges for which one or more electrons have been captured by the incident projectiles ($H^+ + He \rightarrow H + He^+$ or $H^+ + He \rightarrow H^- + He^{2+}$), as well as ionization reactions for which electrons have been released from He atoms ($H^+ + He \rightarrow H^+ + He^+ + e^-$ or $H^+ + He \rightarrow H^+ + He^{2+} + 2e^-$), and also reactions for which combinations of electronic capture and ionization processes occurred ($H^+ + He \rightarrow H + He^{2+} + e^-$). In our experiment, target ion signals can be detected in coincidence with the charge-analysed projectile to determine if one of the above-cited reactions occurred (Part I : Chapter 2.E.V)). On the basis of an event by event analysis, we determine branching ratios of the different reactions channels which can then be normalized to the well-known total cross section of the same collision process. These studies provide basics data for the radiation biology: the range of energy chosen goes from 20 to 150 keV, corresponding to the energy range where the Bragg Peak is positioned: the Bragg curve represents the number of ionisations caused by an ion as a function of the depth of its travel in the matter until it stops, it is peaked at the end of the course of the ion when the ion energy becomes of the order of Bohr's velocity v_e (Ee~25keV for the protons).

Chapter 1. Theoretical Approach

This chapter gives some overview on the theoretical description of atomic collisions. Two theoretical approaches are described known as the Born approximation and the coupled channel impact parameter whose domain of applicability corresponds respectively to the high- and low- energy range of collisions. More qualitative considerations about the comparison between the electron, proton or hydrogen atoms impact bring more physical intuition on the process of collisions which can be extended to more complex systems.

A. Description of charge changes phenomena

As atoms or ions pass through the matter, charge changes between the incident projectiles and the atoms/molecules of the target may occur. The inelastic collision which takes place can be expressed as follows:

$$A^p + B \rightarrow A^m + B^n + (m+n-p)e^- \ , \qquad 1\text{-}1$$

where the incident fast projectile A with initial charge p collides with the target neutral atom/molecule B and undergoes the loss or capture of electrons into the charge state m, while the target atom/molecule acquires charge state n. The conservation of charge necessitates the release of $(m+n-p)$ electrons.

The cross section of the process 1-1 is denoted by ${}_{p0}\sigma_{mn}$ or also in a simplified manner σ_{pm}^{n} because the target is usually initially neutral and it is enough to specify that the charge of projectiles changed from p to m and that the target was let in charge-state n.

The variation of the charge composition of a fast beam passing through an elementary layer of matter of thickness $d\pi$ is described by the following equations:

$$\frac{F_m}{d\pi} = \sum_{j=-1}^{Z} (F_j \sigma_{jm} - F_m \sigma_{mj}), \qquad m = -1, 0, 1, 2 \ldots Z \tag{1-2}$$

$$\sum_{j=-1}^{Z} F_j = 1 \tag{1-3}$$

Where $d\pi = ndl$ is the number of target gas atoms/molecules in a volume of matter of cross sectional area 1cm^2 encountered by the projectiles travelling over an elementary distance dl, F_j represents the fraction of projectiles of charge j in the beam and $\sigma_{pm} = \sum_j \sigma_{pm}^j$.

The target thickness is determined by the following relation:

$$\pi = \frac{273 L \nu P l}{760(273 + T)} \tag{1-4}$$

Where L is the Loschmit number of gas giving the number of gas molecules in 1cm^3, ν is the number of atoms in a molecule, P is the pressure of the gas target in Torr, l is the effective length of the target and T is the temperature in °C. Numerically, at 20°C for a monoatomic gas, it gives $\pi = 3.29 \times 10^{-16} Pl$.

For our case of interest, an incident beam of protons or of hydrogen atoms is mostly constituted by H^+ and H^0 projectiles, the part of H^- being negligible. Equation 1-2 relates the fractions F^0 and F^1 of projectiles in charge states 0 and 1 after traversing a target thickness $\pi = nl$. The increase of F^0 in traversing a thickness $d\pi = ndl$ is equal to:

$$dF_0 = F_1 \sigma_{10} d\pi - F_0 \sigma_{01} d\pi$$

Setting the initial conditions of composition $F_0 = F_{00}$ and $F_1 = F_{10}$ and using the conditions 1-3, we obtain:

$$\int_{F_{00}}^{F_0} \frac{dF_0}{\sigma_{10} - F_0(\sigma_{01} + \sigma_{10})} = \int_0^{\pi} d\pi .$$

The fraction F_0 of hydrogen atoms in a beam after traversing the thickness π is then given by

$$F_0 = \left(\frac{\sigma_{01}}{\sigma_{01} + \sigma_{10}} - F_{10} \right) e^{-\pi(\sigma_{01} + \sigma_{10})} + \frac{\sigma_{10}}{\sigma_{01} + \sigma_{10}} . \tag{1-5}$$

And similarly the fraction F_1 of protons in the beam is

$$F_1 = \left(\frac{\sigma_{10}}{\sigma_{01}+\sigma_{10}} - F_{00} \right) e^{-\pi(\sigma_{01}+\sigma_{10})} + \frac{\sigma_{01}}{\sigma_{01}+\sigma_{10}}. \qquad 1\text{-}6$$

Furthermore, it is interesting to consider the following approximations:

- If $\pi(\sigma_{01}+\sigma_{10}) \gg 1$, the thickness is great enough, the exponential term in equations 1-5 and 1-6 drops out and we are left with:

  $$F_0 = F_{0\infty} \simeq \frac{\sigma_{10}}{\sigma_{01}+\sigma_{10}} \text{ and } F_1 = F_{1\infty} \simeq \frac{\sigma_{01}}{\sigma_{01}+\sigma_{10}}.$$

  At equilibrium, the composition of the beam only depends on the cross sections involved.

- If the incident beam is composed mostly of projectiles of a given charge state, the equation 1-5 and 1-6 can be further simplified since $F_{00} \simeq 1$ and $F_{10} \simeq 0$. For a beam of hydrogen atoms, we obtain:

  $$F_0 \simeq \frac{\sigma_{01} e^{-\pi(\sigma_{01}+\sigma_{10})} + \sigma_{10}}{\sigma_{01}+\sigma_{10}} \text{ and } F_1 \simeq \frac{\sigma_{01}\left(1 - e^{-\pi(\sigma_{01}+\sigma_{10})}\right)}{\sigma_{01}+\sigma_{10}}.$$

- If $\pi(\sigma_{01}+\sigma_{10}) \ll 1$, the target is considered "thin" for the processes involved. The expansion of the exponential term to second order yields the following composition for a beam of hydrogen atoms:

  $$F_1 \simeq \pi\sigma_{01} - \frac{\pi^2}{2}\sigma_{01}(\sigma_{01}+\sigma_{10}) \text{ and } F_0 = 1 - F_1. \qquad 1\text{-}7$$

- Single collision conditions are obtained in a situation where the quadratic term can be neglected $\frac{\pi^2}{2}\sigma_{10}(\sigma_{01}+\sigma_{10}) \ll 1$; we are then left with the familiar linear growth: $F_1 \simeq \pi\sigma_{01}$.

B. Coincidence techniques

Among other techniques described in [4,11,13,41], the techniques of coincidence are especially appropriated for the investigation of charge changes phenomena. These coincidence techniques were used for the first time by Afrosimov and coworkers (1963) and Everhart and Kessel (1965). The apparatus detects both the charge-analysed outgoing projectiles and the recoil ions or/and electrons in coincidence. These techniques allow an event by event analysis of the charge changes phenomena during the experiments. Our apparatus is equipped sith such a coincidence system giving the possibility to measure simultaneously cross sections for the different channels. Two other examples of apparatus using these coincidence techniques are the apparatus of Shah et al [40] and Dubois et al [6], which are more described in Part I : Chapter 4.

C. Calculations of cross sections

What about the theoretical determination of the involved cross sections? “Even for the simplest case of protons collisions, there is no theoretical framework within which such cross sections can be reliably calculated for all impact energies and target “ [11].

The range of energy under study goes from 20 to 150keV, corresponding to velocities for the projectiles v_0 from 2×10^8cm.s^{-1} to $5{,}5\times10^8$cm.s^{-1} (vitesse de Bohr of e^-, $v_e=2.18\times10^8$cm.s^{-1}). In this energy range, it is known that the interactions change character [4,12]. It is usual to distinguish between low-, intermediate- and high-energy regions according to whether $v_0<<v_e$, $v_0\sim v_e$, or $v_0>>v_e$, respectively: in the low-energy region ($v_0<<v_{e)}$, the relative motion of the colliding projectiles is very slow compared with the electronic motion and the system can be viewed as a quasi-molecule which is changing its state adiabatically, the relative motion of the nuclei being treated as a perturbation. At high, but non-relativistic energies ($v_0>>v_{e)}$, the cross section for charge exchange is small and the interaction between the atoms can be considered as a small perturbation. In the intermediate region ($v_0\sim v_{e)}$, the cross section for charge exchange is often large and the theoretical simplifications implied by either an adiabatic or a perturbative treatment do not hold.

Quantum mechanical approaches essentially involve the scattering solution of the Schrödinger equation. This solution involves the wave function that describes the initial system, the

interaction potential between the projectile and the target, and the wave function that describes the final system after the collision has taken place. The Schrödinger equation is not solvable for more than two bodies, approximations have to be made. Various models have been developed in order to handle the problem under different conditions of approximation. A short review on the existing models and their domains of application can be found in [4,13,14], and the models are described in details in [12].

On the example of the simplest case of single ionization, the following paragraphs are intended to give an idea about the way charge changes phenomena are handled theoretically.

I) Plane Wave Born approximation (PWBA)

For simplicity let suppose we are considering the collision between an incident electron and a hydrogen atom. It is the simplest example, but it can be generalized easily to the impact of a fast ion by replacing the mass m_e of the electrons by the reduced mass Mr of the projectile-target system (Mr~m_e in the case of the electron impact) and e^2 is replaced by $Z'e^2$ where Z'e is the charge on the projectile. The nucleus of the hydrogen atom is supposed to stay at rest during the collision since the nucleus is much heavier than the electrons (in the center of mass frame the collision can be considered as that of a particle of mass Mr about a fixed scattering center). The electron of the target is located at coordinates $\vec{r}_a$, and the incident projectile electron is located at coordinates $\vec{r}_b$ and the distance between electrons is designated by r_{ba}, the time dependent Schrödinger equation of the system is:

$$i\hbar\frac{\partial\Psi(\vec{r}_b,\vec{r}_a,t)}{\partial t}=\left[-\frac{\hbar^2}{2m_e}\nabla_{rb}^2-\frac{\hbar^2}{2m_e}\nabla_{ra}^2+V(\vec{r}_b,\vec{r}_a)\right]\Psi(\vec{r}_b,\vec{r}_a,t) \qquad 1\text{-}8$$

V is the interaction potential energy between the three particles given by:

$$V(\vec{r}_b,\vec{r}_a)=-\frac{e^2}{r_b}-\frac{e^2}{r_a}+\frac{e^2}{r_{ba}} \qquad 1\text{-}9$$

After separation of the time and space dependence of the wave function, we are left with:

$$\left[-\frac{\hbar^2}{2m_e}\nabla_{rb}^2-\frac{\hbar^2}{2m_e}\nabla_{ra}^2+V(\vec{r}_b,\vec{r}_a)\right]\Psi(\vec{r}_b,\vec{r}_a)=E\Psi(\vec{r}_b,\vec{r}_a) \qquad 1\text{-}10$$

Where E is the total constant energy of the system of three particles.

If we expand the wave function $\Psi(\vec{r}_b,\vec{r}_a)$ in terms of the complete set of eigenfunctions of the unperturbed hydrogen atom $u_n(\vec{r}_a)$ and functions $F_n(\vec{r}_b)$ representing the projectile:

$$\Psi(\vec{r}_b,\vec{r}_a)=\left(\sum_n \ +\int\ \right)u_n(\vec{r}_a)F_n(\vec{r}_b)\equiv\sum\nolimits_n{}' u_n(\vec{r}_a)F_n(\vec{r}_b) \qquad 1\text{-}11$$

$$-\frac{\hbar^2}{2m_e}\nabla^2_{ra}u_n(\vec{r}_a)-\frac{e^2}{r_a}u_n(\vec{r}_a)=E_n u_n(\vec{r}_a) \qquad 1\text{-}12$$

E_n is the energy of the hydrogen atom in its unperturbed nth state. The prime in $\sum_n{}' u_n(\vec{r}_a)F_n(\vec{r}_b)$ indicates that the summation is over the discrete and continuous spectrum of states of hydrogen atoms.

The equation 1-10 can be rewritten using equation 1-11 and 1-12**:**

$$\sum\nolimits_n{}' u_n(\vec{r}_a)\left[\frac{\hbar^2}{2m_e}\nabla^2_{r_b}+(E-E_n)\right]F_n(\vec{r}_b)=\left(\frac{e^2}{r_{ba}}-\frac{e^2}{r_b}\right)\Psi(\vec{r}_b,\vec{r}_a) \qquad 1\text{-}13$$

By multiplying each side of equation by $u_n^*(\vec{r}_a)$ and integrating over $\vec{r}_a$, we obtain:

$$\left[\frac{\hbar^2}{2m_e}\nabla^2_{r_b}+(E-E_n)\right]F_n(\vec{r}_b)=\int\left(\frac{e^2}{r_{ba}}-\frac{e^2}{r_b}\right)\Psi(\vec{r}_b,\vec{r}_a)u_n^*(\vec{r}_a)dr_a \qquad 1\text{-}14$$

$\left[\frac{\hbar^2}{2m_e}\nabla^2_{r_b}+(E-E_n)\right]F_n(\vec{r}_b)=0$ holds for large $\vec{r}_b$, so that the functions $F_n(\vec{r}_b)$ are the waves function of a free electron of energy (E-E_n) at large $\vec{r}_b$. The wavelength $\kappa_n^2=\frac{2m_e(E-E_n)}{\hbar^2}$ associated is real only if $E>E_n$, that is if the electron has enough energy to excite the nth state of the target atom. Because the hydrogen atom is supposed to be in its ground state initially, F_0 is the sum of an incoming plane wave representing the incident electron and an elastically scattered spherical wave:

$$F_0\sim e^{i\kappa_0 z}+\frac{1}{r_b}e^{i\kappa_0 r_b}f_0(\theta) \qquad 1\text{-}15$$

z is the Cartesian coordinate preferred to locate the propagating incident electron along the Z

axis. The target atom is located at the origin. Spherical polar coordinates (r_b,θ) are better suited for the scattered spherical wave.

F_n represents the inelastically scattered electron (projectile) which has cause the excitation of the hydrogen atom to the nth states.

$$F_n \sim \frac{1}{r_b} e^{i\kappa_n r_b} f_n(\theta) \qquad 1\text{-}16$$

Finally, by introducing the matrix $[V_{mn}]_{m,n}$ which describes the interaction between the incident electron with the nucleus and the orbital electron of the target atom, whose elements are determined as follows:

$$V_{mn} = \int u_n^*(\vec{r}_a)\left(\frac{e^2}{r_{ba}} - \frac{e^2}{r_b}\right) u_m(\vec{r}_a) dr_a \qquad 1\text{-}17$$

We can rewrite equation 1-14 as:

$$\left(\nabla_{r_b}^2 + \kappa_n^2 - \frac{2m_e}{\hbar^2} V_{nn}\right) F_n(\vec{r}_b) = \frac{2m_e}{\hbar^2} \sum\nolimits'_{n \neq m} V_{mn} F_m(\vec{r}_b) \qquad 1\text{-}18$$

We have an infinite set of coupled equations to solve in order to obtain an asymptotic form of the wave functions $F_n(\vec{r}_b)$. Clearly approximations must be used consisting in selecting only the most important matrix elements and putting the others to zero.

The Born approximation is of great importance in the study of atomic collision. It comes from the observation that at high enough incident energy there is little interaction between the projectile and the target. The basic assumption is that the deflection of the projectiles results only from interaction with the target electron involved in the collision. Consequently, the outgoing wave describing the projectile is distorted only slightly during the collision, and the deflection of the projectile is very small. It does not acknowledge the Coulomb interaction and correlation between the scattered projectile and the ejected electron.

The plane wave born approximation (PWBA) supposes that the projectile in its initial state is well described by a plane wave function ($F_0(\vec{r}_b) = \mathrm{e}^{i\kappa_0 \vec{n}_0 \cdot \vec{r}_b}$). In addition, the assumption is made that the transition to the final state n results from a direct transition from the initial state (in $V_{mn} = 0$ for $m \neq 0$ where 0 designates the initial state). Furthermore, the interaction between the projectile and the atom in its final state is considered as small, so that distortion

of the scattered wave can be neglected (i.e. $V_{nn} = 0$).

Under these assumptions of the Born approximation:

$$\Psi(\vec{r}_b, \vec{r}_a) = \mathrm{e}^{i\kappa_0 \vec{n}_0 \bullet \vec{r}_b}\, u_0(\vec{r}_a) \qquad 1\text{-}19$$

And the infinite set of equations reduces to a single equation for excitation into state n:

$$\left(\nabla_{r_b}^2 + \kappa_n^2\right) F_n(\vec{r}_b) = \frac{2m_e}{\hbar^2} V_{0n}\, \mathrm{e}^{i\kappa_0 \vec{n}_0 \bullet \vec{r}_b} \qquad 1\text{-}20$$

As shown by Mott and Massey [15], the asymptotic form of the solution is:

$$F_n(\vec{r}) = \frac{m_e}{2\pi\hbar^2}\frac{1}{r} e^{i\kappa_n r} \int \mathrm{e}^{i(\kappa_0 \vec{n}_0 - \kappa_n \vec{n}) \bullet \vec{r}_b}\, V_{0n} d\vec{r}_b = \frac{1}{r} e^{i\kappa_n r} f_n(\theta) \qquad 1\text{-}21$$

The number of electrons (projectiles) per unit volume at distance r from the target atom that have excited the atom to its nth state is $\left|F_n(\vec{r})\right|^2$. The differential cross section for excitation of the atom into its nth state is:

$$I_{0n} d\Omega = \frac{\kappa_n}{\kappa_0}\left|f_n(\theta)\right|^2 d\Omega \qquad 1\text{-}22$$

$$I_{0n} d\Omega = \frac{\kappa_n}{\kappa_0}\frac{m_e^2}{4\pi^2\hbar^4}\left|\int \mathrm{e}^{i(\kappa_0 \vec{n}_0 - \kappa_n \vec{n}) \bullet \vec{r}_b}\, V_{0n} d\vec{r}_b\right|^2 d\Omega \qquad 1\text{-}23$$

By setting $\vec{K} = \kappa_n \vec{n} - \kappa_0 \vec{n}_0$, $\hbar K$ is the magnitude of the electron projectile's momentum change associated with the scaterring angle θ. The differential cross section can be rewritten as a function of K:

$$I_{0n}(K) dK = \frac{8\pi m_e^2 e^4}{\kappa_0^2 \hbar^4}\frac{dK}{K^3}\left|\varepsilon_{0n}(K)\right|^2 \qquad 1\text{-}24$$

Where $\varepsilon_{0n}(K) = \int e^{iKz} u_n^*(\vec{r}_a) u_0(\vec{r}_a) d\vec{r}_a$.

The total cross section of excitation of the atom into its nth state by the electron impact is obtained by integration over K:

$$\sigma_{0n} = \int_{K_{\min}}^{K_{\max}} I_{0n}(K)dK \qquad 1\text{-}25$$

$K_{\max} = \kappa_0 + \kappa_n \approx 2\kappa_0$ (for θ=180) and $K_{\min} = \kappa_0 - \kappa_n \approx \frac{m_e}{\hbar^2}\frac{E_n - E_0}{\kappa_0}$ (for θ=0) under the conditions of little energy transfers and high kinetic energy (Born approximation).

The generalization to the impact of a heavy ion onto an atomic target with N electrons and nuclear charge +Ne is straightforward by replacing V_{0n} by:

$$V_{0n} = \int \sum_{i=1}^{N} u_n^*(\vec{r}_1,...,\vec{r}_N)\left(\frac{e^2}{r_{bi}} - \frac{Ne^2}{r_b}\right)u_0(\vec{r}_1,...,\vec{r}_N)dr_1...dr_N \qquad 1\text{-}26$$

$$\text{with } \varepsilon_{0n}(K) = \sum_{i=1}^{N}\int e^{iKz_i}u_n^*(\vec{r}_1,...,\vec{r}_N)u_0(\vec{r}_1,...,\vec{r}_N)d\vec{r}_1...d\vec{r}_N \qquad 1\text{-}27$$

By integrating over final states in the continuum, the cross section for ionization can be determined in the first Born approximation using hydrogenic wave functions [15]. However the resulting equations are complicated and can only be determined by numerical calculation. Furthermore, this presentation of the Born approximation did not treat the indistinguishability of identical particles which gives an additional exchange term amplitude in the cross section for the case of the electron impact (see [14]), which must be taken into account in the case of ionization.

PWBA looks simplistic but gives good results because the large majority of collisions contributing to the total cross section are distant ones for which the assumptions are good approximation. In the Born approximation, the cross section for excitation and ionization depends only on the charge and velocity of the projectile. Therefore the results are expected to be the same for the protons or electrons impact.

The use of hartree fock wave functions in place of the hydrogenic ones is giving improved agreement in the backward direction (θ=180°) for the doubly differential cross section (DDCS in ejection angle and energy of the ejected electron), requiring more detailed description of the system than the integrated cross section (see [13]). The discrepancies of the results in the forward direction come from the neglect of the electron-projectile interaction, which requires an improvement of the Born approximation leading to the Distorted Wave Born approximation (DWBA).

II) Distorted Wave Born approximation (DWBA)

Indeed, especially when the impact velocity decreases, the approximation can be improved by taking into account the distortion of the incident and scattered waves by the static field of the target.

The terms V_{nn} and V_{00} are retained in the set of equations which reduces to the pair of equations 1-28 and 1-29:

$$\left(\nabla_{r_b}^2 + \kappa_n^2 - \frac{2m_e}{\hbar^2}V_{00}\right)F_0(\vec{r}_b) = \frac{2m_e}{\hbar^2}V_{0n}F_n(\vec{r}_b) \qquad 1\text{-}28$$

$$\left(\nabla_{r_b}^2 + \kappa_n^2 - \frac{2m_e}{\hbar^2}V_{nn}\right)F_n(\vec{r}_b) = \frac{2m_e}{\hbar^2}V_{0n}F_0(\vec{r}_b) \qquad 1\text{-}29$$

It is called the distorted wave Born approximation (DWBA).

When the projectile is fast enough, due to the slow moving ejected electron the fast moving projectile will see an effectively neutral system during the time it is in the scattering region. So that the Born approximation is justified in cases where the incident energy is high and the energy transfer is small. However the Born approximation also neglects the interaction between the ejected electron and the nucleus, which is much more questionable. As a consequence, an improvement of the model is to treat the ejected electron as a distorted wave by the Coulombic effective potential of the atomic ion at rest. In the review of Rudd [11], the DWBA model using plane wave for the initial and final states of the fast incident projectile, and distorted waves for the ejected electron, gives good agreement with the experimental results over a wide range of energy and a variety of atomic targets. The final state of the ion at rest was considered to be the same as the initial state (no time for evolution, approximation known as the sudden approximation). The hartree-fock orbitals calculated for the neutral atoms were used for the final state. The active electron orbital was removed without modification of the other orbitals. A spherically averaged, local radial potential of the ion is then formed from the charge distribution of the ion represented by the remaining hartree fock orbitals. As sketched in the PWBA treatment of the excitation of a hydrogen atom by a fast electron, the orthogonality of the orbitals is essential to simplify the calculations. In [11] the hartree fock orbitals were orthogonalized by using an orthogonalization procedure of the Schmidt type, for ensuring orthogonality between the distorted waves describing the ejected electron and the orbitals of the ion at rest.

The Figure 1-1 shows their result for the impact of H^+ onto He atom under the conditions of approximation sketched previously, compared to the experimental results determined at that time (1985). DWBA is in very good agreement above incident energies of 100keV and the discrepancies increase at lower energies.

Details can be found in the books of Mc Daniel [13,14], where the theoretical treatment of the Born approximation and other approximations are exposed in a comprehensive manner. Also the review of Rudd et al [11] is complementary on the subject of DWBA.

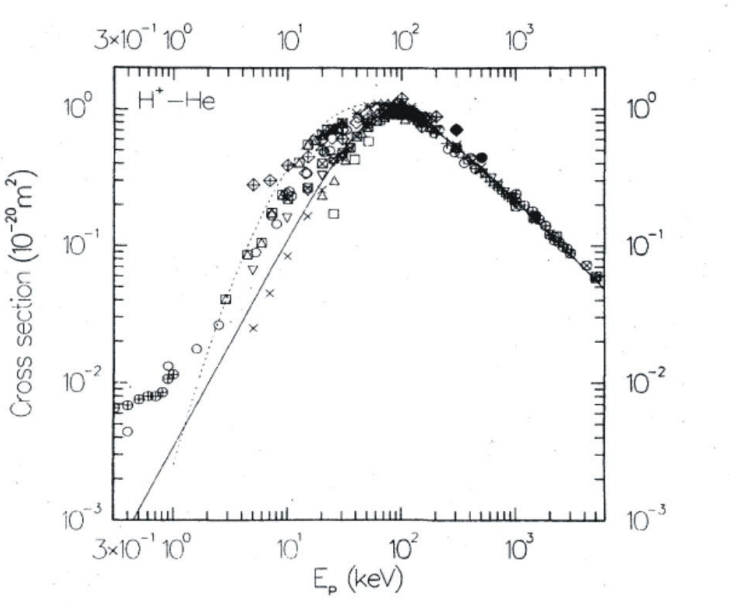

Figure 1-1: Comparison between DWBA theory and various experimental results on the cross section for electron ejection collected by Rudd et al in 1985 [11]. Reproduced from [11].

Electron ejection in proton impact upon helium shown in Figure 1-1 corresponds to the sum of cross sections of single and double ionization of helium by the protons ($11\sigma11+11\sigma12$ in the notation defined in Part I : Chapter 1.A). Electron ejection is important for our concerns of investigating the effect of radiations on matter and is further discussed later in this paragraph.

Under the conditions of the plane wave Born approximation the cross section for excitation or ionization depends only on the charge and velocity of the projectile. So at high impact velocities when the born approximation is valid, the cross section for ionization of a given target by electron impact is the same as the cross section by impact of protons.

However, the description of the collision by protons impact with incident energies lower than 100keV can not be done by using the Born approximation because the speed of the ions is not high enough for the approximation to be valid and because the electronic capture

of a target electron by the projectile becomes more probable. Discrepancies between experiments and DWBA theory start to appear under this limit energy of about 100keV in Figure 1-1. Since most of the energy range explored by our present experimental study lies under 100keV, it is important to present also a theory able to describe inelastic collisions in this range of energy.

III) Coupled channel impact parameter

Slim and Bransden [16,17,18] used a semiclassical model to describe the situation in the energy range under 100keV. The model is called Coupled Channel Impact Parameter Model. It is described in details in the book of Bransden and Mc Dowell [12]. It can both describe ionization and electron capture in proton-helium collisions. This method is known to be valid in the keV energy range, straight line trajectories are sufficiently accurate approximation for the projectiles incidence (impact parameter model).

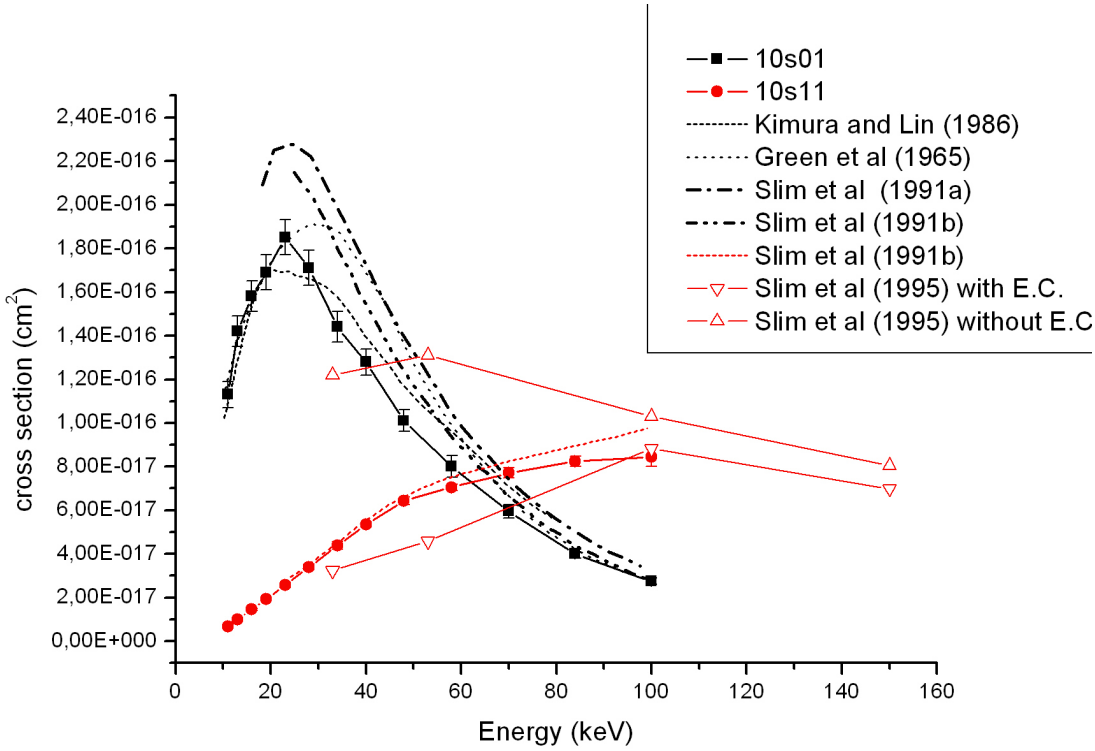

Figure 1-2: Comparison of theoretical and experimental results for electronic capture and single ionization by impact of protons onto helium targets. Slim et al (1991a) [16], Slim et al (1991b) [17], Slim et al (1995) [18], Kimura and Lin (1986) [19], Green et al (1965) [20].

The model used by Slim and Bransden for determining the electron capture cross section shown in Figure 1-2 is sketched as follows in [16]:

The two electrons are moving into the coulombic field of the nuclei H^+ (Z_P=1) and He^{2+}(Z_T=2). The electrons are located at coordinate $\vec{r}_1$ and $\vec{r}_2$, and their distance to the nucleus of the helium nucleus and proton are respectively $(r_{iT})_{i=1,2}$ and $(r_{iP})_{i=1,2}$. The time-dependant Schrödinger equation may be reduced to a set of coupled differential equations for the transition amplitudes, $a_i(b,t)$, and integrated with respect to the time, t, for a given value of the impact parameter, b :

$$i\frac{\partial}{\partial t}\Phi(\vec{r}_1,\vec{r}_2;t) = H(\vec{r}_1,\vec{r}_2;t)\Phi(\vec{r}_1,\vec{r}_2;t) \qquad 1\text{-}30$$

where

$$H(\vec{r}_1,\vec{r}_2;t) = \sum_{i=1}^{2}\left(Ti - \frac{Z_T}{r_{iT}} - \frac{Z_P}{r_{iP}}\right) + \frac{1}{|\vec{r}_1 - \vec{r}_2|} \qquad 1\text{-}31$$

and

$$\Phi(\vec{r}_1,\vec{r}_2;t) = \sum_{i=1}^{N_T} a_i(t)\phi_i^{He}(\vec{r}_{1T},\vec{r}_{2T})w^T(\vec{r}_1,t)w^T(\vec{r}_2,t)e^{-i\varepsilon_i^{He}t} \qquad 1\text{-}32$$
$$+\sum_{i=N_T+1}^{N_T+N_P} a_i(t)\frac{1}{\sqrt{2}}\left[\phi_{i1}^{He^+}(\vec{r}_{1T})\phi_{i2}^{H}(\vec{r}_{2P})w^T(\vec{r}_1,t)w^P(\vec{r}_2,t) + \phi_{i1}^{He^+}(\vec{r}_{2T})\phi_{i2}^{H}(\vec{r}_{1P})w^T(\vec{r}_2,t)w^P(\vec{r}_1,t)\right]\times e^{-i(\varepsilon_{i1}^{He^+}+\varepsilon_{i2}^{H})t}$$

Plane waves translational factor w^T are used for ensuring Galilean invariance of the model (see explanations in [12]). A basis set of N_T=11 states were chosen on the He atom (target T) nucleus which comprised He(n=1,n=2) together with $2s^2$,2s2p and $2p^2$ autoionizing states. A basis set of N_P=29 states was chosen on the proton (projectile P), including the states H(n≤4) together with 8 pseudostates.

Green et al [20] obtained however better agreement with the experimental results by using a two states atomic orbital basis containing He($1s^2$) in the incident channel (ϕ_i^{He} in 1-32) and a symmetrical product of H(1s) and He^+(1s) wave functions in the rearranged channel ($\phi_{i1}^{He^+}\phi_{i2}^{H}$ in 1-32). Hence the contribution of the additional states taken into account in the calculation of Slim et al [16] do not seem to improve the description. Other description like the one of Kimura and Lin [19], which include all capture channels of the form H(n=2) + He^+(1s) and the excitation channels H^+ + He(n=2) as well, agree closely with the experimental data of Shah et al [40]. It shows the importance of the choice of basis in such coupled channel

description : Kimura and Lin used a molecular and atomic (MO/AO) basis which is more adapted at low energy than the basis set formed by placing orbital atomic (AO) on each heavy particle centre as in the model of Slim et al [16] (see book of Bransden and McDowell [12] for more details). Slim et al improved the agreement with the experimental results by including some pseudo-continuum states on the helium centre yielding the theoretical cross section named Slim et al (1991b) in Figure 1-2. This model gave a good description of the single ionization channel as well.

In Figure 1-2 the results of Slim et al [16,17], as well as the results of Green et al [20] and other theoretical works of Slim et al [18] on the ionization channel are compared to the experimental results of reference for the protons impact from Shah et al [40] (see Part I : Chapter 4.B.I)).

The theoretical description of the double electron capture by proton impact from helium is envisaged in the last chapter.

IV) Collisions by hydrogen atoms impact

The coincidence techniques employed by Dubois et al [6], similar to those of our experiment, allowed a separation of the processes involving target ionization or projectile ionization and gives the possibility to test the predictive power of the theory in the separate cases. The Figure 1-3 shows a comparison between their experimental results on the impact of hydrogen atoms onto helium and some theoretical investigations by Bell et al [21] using the first Born approximation (described in Part I : Chapter 1.C.I)). In [21], the cross section was obtained as the sum of the ionizations cross sections for a proton and an electron. Due to the screening at large impact parameters, only small impact parameters, where binding forces can be neglected, were considered.

As shown in Figure 1-3, if taken into account, the concomitant excitation of the projectile H(1s) or target He($1s^2$) when considering the single target ionization or the single projectile ionization respectively, gives better agreement with the experimental results. It indicates that pure single ionization of either target or projectile results in the excitation of the collision partner.

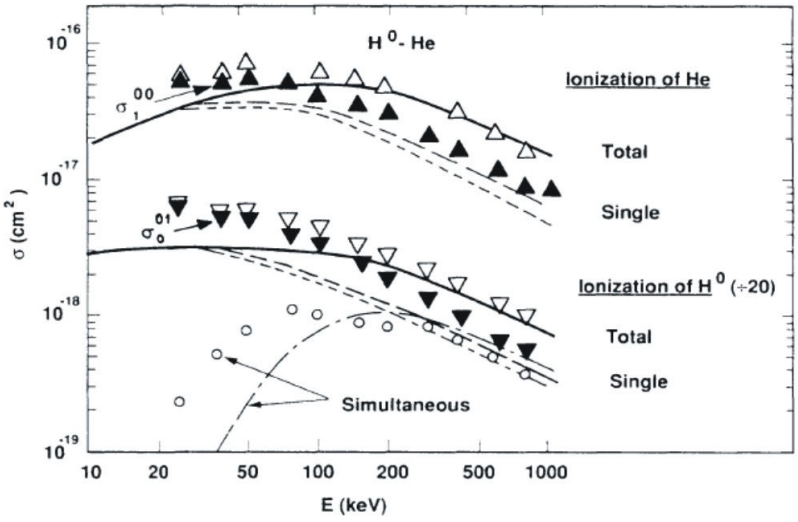

Experiment: present work; △, total single-target-ionization cross section $\sigma_1^{00}+\sigma_1^{01}$; ▲, pure single-target ionization σ_1^{00}; ▽, total single-projectile ionization $\sigma_0^{01}+\sigma_1^{01}$; ▽, pure single-projectile ionization σ_0^{01}; ○, simultaneous target and projectile ionization σ_1^{01}. Theory: ——, total cross sections for target or projectile ionization; · · · ·, single-ionization cross sections for target or projectile ionization, collision partner remaining in ground state; — — —, single-ionization cross sections for target or projectile ionization, collision partner excited to discrete state; —·—·—·, cross section for simultaneous ionization of both collision partners.

Figure 1-3: Comparison of experimental results from Dubois et al (=present work in the caption) [6] and calculations from Bell et al [21] using the first Born approximation. The projectiles ionization curves have been divided by 20 in order to separate them from the target ionization curves.

The experimental data for target ionization have incertainty of about 20%. The pure loss cross section without ionization of the target was determined with a greater incertainty since it was calculated from substracting the total amount of projectile ionizations measured by the scaler at the end of course of the projectiles from the electron loss cross sections resulting in target ionization determined by coincidences (see Part I : Chapter 4.C.II): $\sigma_0^{01} = \sigma^{01} - \sum_j \sigma_j^{01}$. Hence, the agreement with the Born approximation is excellent above 200keV as it was the case for the prediction of the DWBA approximation concerning the total electrons ejection in protons helium collisions [11] (see Figure 1-1). Generally the Born approximation is valid for higher energy than 200keV. Heil, Dubois et al [22] performed further experiments and theoretical investigations of doubly differential electron emission for the impact of hydrogen atoms on helium for impact energies above 500 keV. They found that PWBA could adequately describe single ionization of the projectile and of the target.

In the range of energy of interest for our present study, 20-150keV, no theoretical investigations were found in the literature.

V) Comparison between protons/hydrogen and electrons impact

In [3], we have been investigating the ionization of uracil molecules by protons impact in the range of energy 20 to 150keV compared to experiments of uracil ionization by 200eV-electrons impact performed in Innsbruck. The comparison of the data showed that at least for large enough excitation energy uracil decays in a similar fashion into the same fragment ions independent of the ionization projectile (e^- or H^+). It is a well known result that at high impact velocities the ionization cross sections of a given target by electron impact is the same as the ionization cross section by protons travelling with the same velocity: the relationship between proton and electron impact ionization data is discussed in the review of Rudd et al [11] or in the book of Mc Daniel [14]. The Bethe-Born theory predicts well the cross section for ionization by fast ions (fully stripped) [14, p 432].

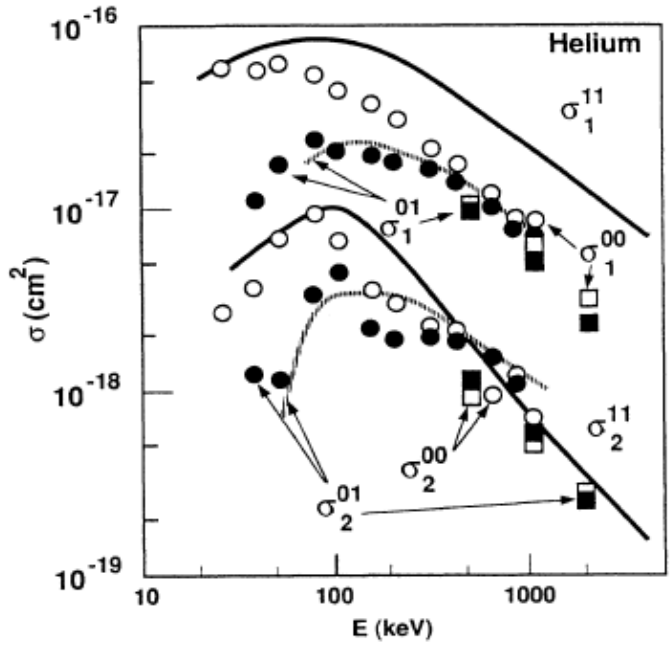

Figure 1-4: Comparisons of the magnitudes of the processes by protons impact and hydrogen atoms impact from Dubois compared to previous works. The exact references of the works shown in the figure can be found in the paper of Dubois and Kövèr [6]. The processes are indentified in the figure by the notation introduced in Part I : Chapter 1.A . Double target ionization processes have been multiplied by 10 for the comparison.

A comparison of the magnitudes of the processes by impact of protons with those by impact of hydrogen atoms in Figure 1-4 reveals that single ionization channels cross sections for the hydrogen atoms impact lie in amplitude lower than the corresponding channel by protons impact. On the other hand processes leading to double ionization of the helium target

have nearly identical magnitudes for both impact of protons or hydrogen atoms. The smaller cross section for hydrogen atoms impact is attributed to the absence of long range coulombic interaction in H + He collisions. On the other hand, double ionization processes require smaller impact parameter collisions in order that a greater energy transfert takes place, protons and hydrogen atoms interacts similarly with the target at short distance.

The comparison between the projectiles can be further developed.

It is interesting for this to consider a famous result often cited from an important paper concerning electron ejection (Rudd et al [23]). Double differential cross sections in energy and angular ejection (DDCS) are of particular interest for the radiation track simulations since the ionizing effects of electron emissions from primary radiations (like the impact of H^+ or H) have to be taken into account (see Conclusive Remarks and Introducing part II) and the DDCS provides all necessary informations on the further propagation of the electrons.

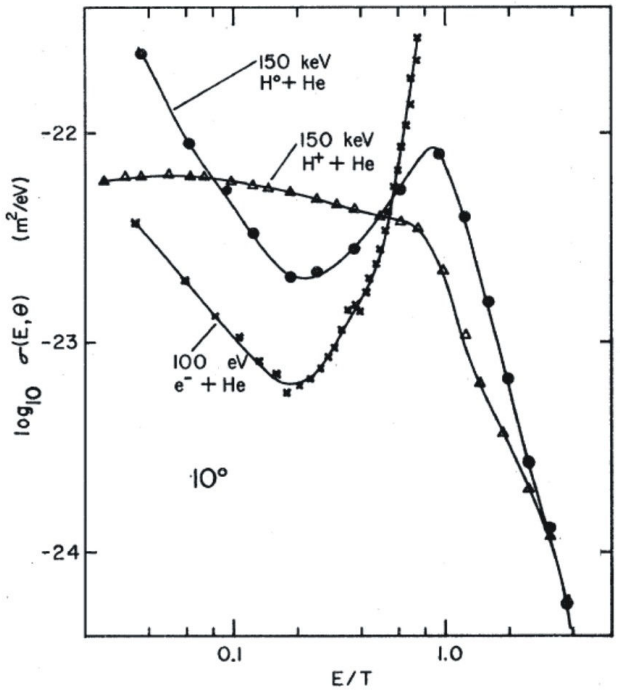

Figure 1-5: Comparison from energy spectrum of electrons ejected at 10° with energy E from 150 keV hydrogen atoms and proton impact and from 100 eV electrons impact on helium. T is the energy of the electron with the same velocity as the incident particle.

Rudd et al studied the doubly differential cross sections for electron ejection in hydrogen atoms impact on helium [23]. They observed that a rise in the energy spectra of the electron occur when the energy of the ejected electron is approximately equal to the energy of the incident hydrogen atoms. In Figure 1-5, a comparison is made of the electron yields at corresponding angle of 10° by impact of neutral-hydrogen, protons and electrons at

corresponding velocities. The exact corresponding velocity for the electron impact should be about 82eV, the closest available data at 100eV energy impact from [24] are used for the comparison. The spectra of ejected electron are plotted versus E/T, where E is the ejection energy and T is the equivalent electron energy of the projectile energy. The lower energy part of the electron impact spectrum results from the ejection of true secondary electrons from the target, while the rise at higher energies is from the corresponding scattered primary electrons, which have lost a small amount of their energies in the interaction. Up to E/T~1 the shape of the electron spectrum ejected by hydrogen atoms resembles the shape of spectrum obtained by electron impact. Electrons of lower energies are ejected from the target by collisions for which the impact parameter is largest, the nucleus is screened by the electron and the hydrogen atom tends to behave like an electron. Whereas collisions at small impact parameter give rise to faster electrons, and the doubly differential cross section by impact of hydrogen atoms look similar to the one corresponding to the protons impact because the nucleus of the hydrogen atom becomes less screened by the electron. The peak at E/T=1 in the cross section by hydrogen atom corresponds to the "electron loss to the continuum" i.e. to the hydrogen atom is ionized in the collision and its electron is scattered giving rise to this characteristic peak at an ejection energy for the electron corresponding to the incidence energy of the hydrogen atom projectiles. The electron loss is the same as ionization when viewed from the projectile frame of reference. Above E/T=1 the secondary electrons spectrum by hydrogen atoms resemble more the one resulting by protons impact: again, the secondary electrons of highest energy result from close collision for which the nucleus of the incident particle is not screened by the orbital electron.

Bolorizadeh and Rudd obtained similar results in a study of the impact of hydrogen atoms on water vapor [25], generalizing the results ontained in Figure 1-5. It has to be noted also that the electron loss peak revealed to represents one third to one half of the total electron emission in the collisions of H with water. The amount of ejected electrons is for this reason much more important by hydrogen atoms impact than by protons impact and the further ionizing action of the electrons in secondary reactions might compensate for the smaller ionizing cross section of the hygrogen atoms with respect to the protons impact due to the absence of long range coulombic interaction between the hydrogen atoms and the target.

Chapter 2. Description of the Experimental Set-up

This chapter gives details about the different part of the experimental setup and acquisition system employed for this study. The source, where the charged projectiles are formed, is first described in section A. After an acceleration stage, the beam undergoes successive transformations which give rise to a very diluted beam of the selected projectiles (H^+, or H) with a given time-structure (a series of bunches of 80 pulses), described in section B. The conditions of interaction with an effusive beam of gaseous helium inside the collision chamber are further described in section C. The product ions analysed by a Time of Flight mass spectrometer (described in section D) are measured in coincidence with the charge-state-analysed outgoing projectiles. The multi-coincident detection and acquisition system is finally described in section E.

A. The Source and Acceleration stage

I) The source

A continuous flow of Hydrogen H_2 enters a quartz bulb (10^{-2}mmHg), the creation and maintenance of the plasma are obtained by dissipation of the high frequency electromagnetic energy furnished by a 100MHz oscillator, coupled via a ring to the source bulb (see Figure 2-1). The free electrons oscillate with the high frequency electromagnetic field and ionize the gas contained in the bulb by collisions, giving birth to pink plasma. There is the possibility also to increase the course of the electrons in the plasma and enhance the ionization by applying a longitudinal magnetic field thanks to the concentration coil, this possibility was not used during the experiments. Different species of ions are produced, mostly monoatomic ions H^+ (80%), but also H_2^+, H_3^+ … Thanks to an extraction electrode placed upstream, the ions are repelled towards the exit of the bulb and the stabilization of the plasma by discharge is also possible. The extracted ions are then focused by a lens which forms a beam of a few tens of μA. The source is placed inside a big metallic box, put at high

voltage, to shield the rest of the apparatus from the radiofrequency radiations.

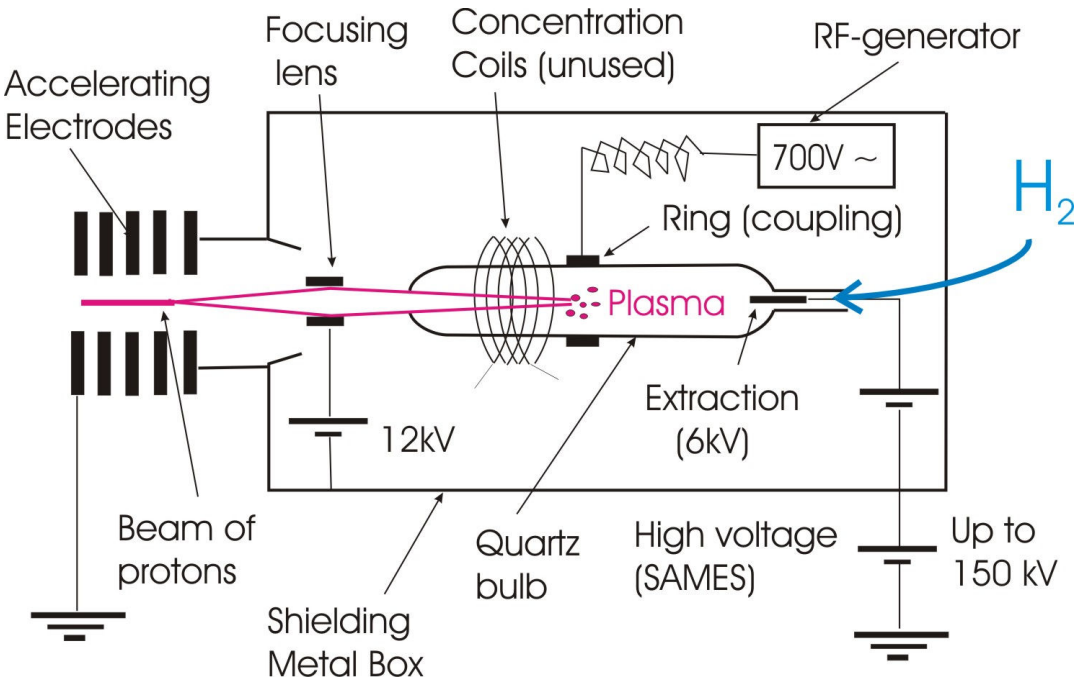

Figure 2-1: Schematic drawing of the source.

II) Acceleration of the positive ions out of the source:

A SAMES generator provides the energy needed for accelerating the ions up to 150 keV after the source. It is working according to the principle of the machine of Felici, and the resolution of energy is estimated to be of about 1%, the stability of the tension during the experiment being fixed at 10^{-4} of the current value. Hence, out of the source, the positive ions are uniformly accelerated by a series of 10 electrodes up to an energy of 150keV ($\Delta E/E=0.01$). At this stage, the beam is mostly made of protons (80%); its intensity is of a few tens of μA as measurable by an Amperemeter (see next paragraph).

B. Formation of the beam of interaction

A schematic drawing of the complete set up is shown in Figure 2-2.

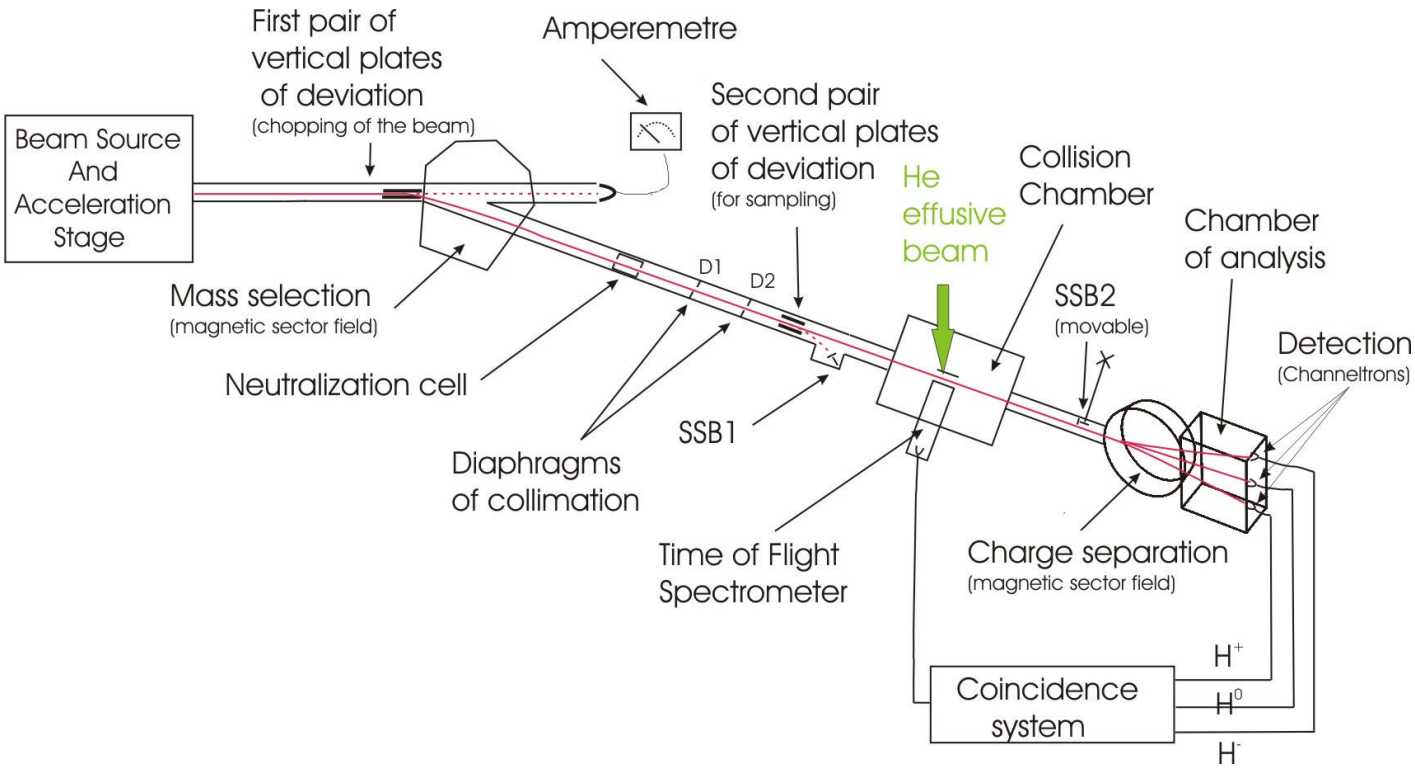

Figure 2-2: Schematic view of the experimental Set-up.

I) Chopping of the beam

When no tension is applied on the first vertical plates, the protons are deflected by the magnetic sector field into the "main beam line section" which leads to the collision chamber. The first pair of vertical plates gives the possibility to deflect the beam into a "straightforward beam line section", at the end of which a detector connected to an Amperemetre indicates the intensity of the beam coming out of the source. During the experiments, the beam is constantly chopped alternately between these two beam line sections. Indeed, for the sake of re-using the old program of hardware control and acquisition system from previous experiments on the fragmentation of hydrogen clusters ([26]), the beam going to the chamber was given a particular time-structure: a bunch of 80 pulses was sent into the "main section" during a lap of time called a "buse". The first pair of vertical plates are driven by fast commutators which gives the possibility to switch on and off the voltages of the vertical plates in a few hundreds of ns, thus we were able to switch very fast between the two sections. This fast switching capacity of the first pair of vertical plates is used to remove the beam from the "main section" during the short switching time of the second pair of vertical plates placed before the chamber. It avoids that the deflection of the beam between the surface barrier detector SSB1 and the chamber (see Part I : Chapter 2.B.V)) sprinkles around with

charged particles chargeable parts of the machine during the switching time of the second pair of vertical plates. After a “buse” has elapsed, the beam is deflected out of the “main beam line” by the same plates which ensure the chopping, for avoiding a permanent exposure of the detectors during the transfer of the memory.

II) Selection of the ionic species

At the beginning of the “main beam line section”, a magnetic sector field is used to select the mass of the projectiles, i.e. it separates the protons from the other ionic species present in the beam. After the magnet, the beam is usually constituted by more than 99.5% of H^+, depending on the intensity of the beam, since a small but constant amount of neutral hydrogen atoms and H^- is present in the beam due to neutralization occurring most probably inside the magnetic sector field (see Part I : Chapter 3.A.IV)). If the intensity of the incoming beam is increased, the proportion of H^+ in the beam tends towards 100%.

III) Nature of the projectiles of interaction:

A cell of neutralization (2 apertures of 0,8mm distant of about 60mm) is placed after the magnet on the course of the beam; it can be filled with a rare gas. The charge transfer occurring gives the possibility to neutralize a part of the incoming beam and form a beam of swift hydrogen atoms (see Part I : Chapter 3.A.III).

IV) Definition of the beam

Two collimators D1 and D2 of diameters 0.5mm distant of 95cm are placed after the cell of neutralization; they define the axis of the beam within an angular divergence of 5 mrad. Thanks to them, the incoming beam of protons of several μA (~10^{12} counts/sec.) is reduced to a diluted beam of an intensity of some thousands counts per second.

V) Determination of the beam’s composition

A permanent voltage is applied on the second pair of vertical plates before the chamber (~700V). And thus, protons would be constantly deflected onto the SSB detector (SSB1) as shown in the Figure 2-2 if another voltage would not be periodically applied in order to neutralize the vertical plates and allows the beam of charged particles to continue its course towards the chamber. During one out of two pulses the charged particles are deflected onto SSB1, and fly otherwise straight to the collision chamber. A second movable SSB detector (SSB2) can be introduced on the course of the beam after the collision chamber. Comparing the intensities of beam determined by both SSB detectors gives the possibility to verify that the incoming beam is reaching in integrity the second SSB detector after travelling through the collision chamber. It is a way to verify that the incident beam is not lost inside the chamber. As well, when SSB2 is removed, a comparison between the intensity measured by SSB1 and the sum of the intensities determined by the channeltrons detecting the charge-analysed projectiles (H^+, H and H^-) in the chamber of analysis can be used for the same purpose. And additional informations regarding the composition of the beam before and after the chamber can also be deduced (see Part I : Chapter 3.A).

Moreover, the deflection by the second pair of vertical plates is used when we want to form a beam of hydrogen atoms only. In this case, the AC voltage ensuring the periodic deviation of the protons between SSB1 and the collision is switched off. As a result, the vertical plates deflect constantly the charged particles (H^+, H^-) whereas the neutral particles (H^0) continue their course into the chamber. In this case, the second pair of vertical plates of deviation before the chamber play also the role of “quenching plates” to induce the decay of metastable hydrogen atoms into the ground state (see Part I : Chapter 3.A.III).

C. The chamber of collision

I) Conditions of collision

The apparatus is equipped with a differential pumping system allowing the maintenance of a high vacuum along the different sections by a series of turbo molecular pumps at a pressure of a few 10^{-6} Torr and one big diffusion pumps of 2000 l/s ensuring a vacuum pressure under 10^{-7} Torr in the chamber of collision. There is roughly a factor 10 and 15 between the pressure in the chamber and pressures in the adjoining beam line section upstream and downstream respectively.

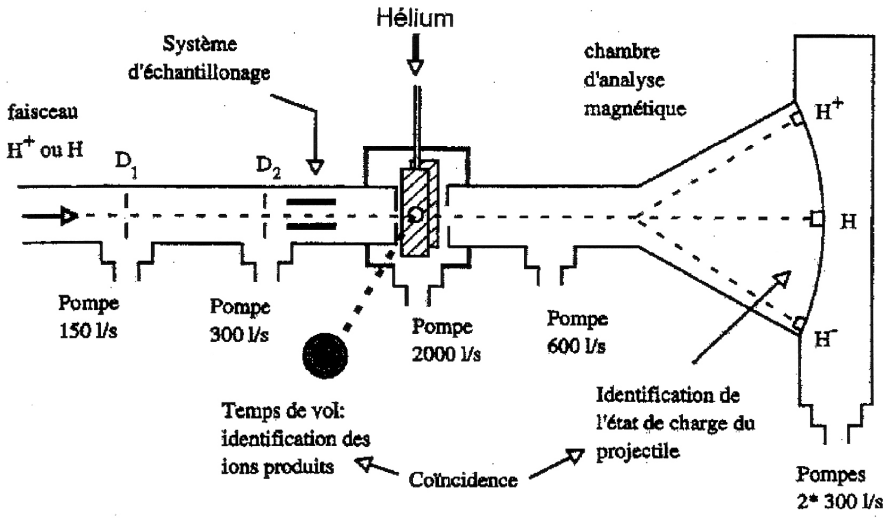

Figure 2-3 : Differential pumping sytem along the main beam line.

II) The target

An effusive beam of helium is produced by a capillary in inox (40mm long, diameter of 0.5mm), perpendicular to the direction of the beam and whose extremity is positioned 2mm above the beam. The capillary is connected to a reservoir where the pressure of Helium is kept constant. The relation between the pressure in the reservoir and the actual width of the target was studied previously [27], but in this work we restricted ourselves to the determination of relative cross sections of charge exchange phenomena. Enough is to know that the conditions of thin target $\pi\sigma<<1$ is respected (see Part I : Chapter 1), as well as the effusive beam is crossing the beam of projectiles right in front of the extraction window towards the TOF MS. The capillary used for our experiments is thiner and longer than the one used in [27].

D. Time of Flight Spectrometer

Ions produced by collisions in the crossed beam region are extracted towards a time of flight mass spectrometer represented in Figure 2-4. The book of R.J. Cotter is useful to abord the field of time of flight mass spectrometry oriented towards the research on biological systems [28].

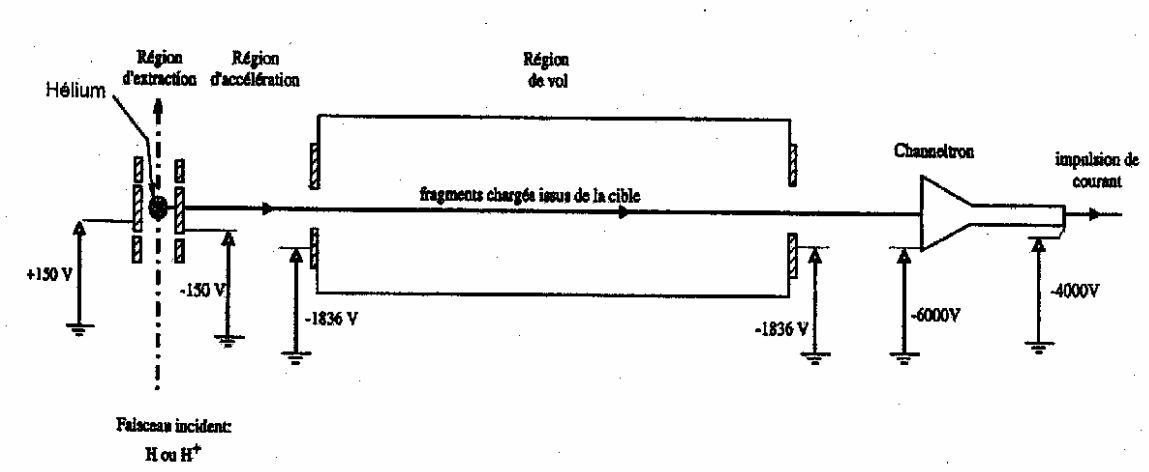

Figure 2-4: Schematic view of the TOF mass spectrometer. The dimensions of the extraction region, of the region of acceleration, of the drift tube and of the region between the end of the drift tube and the entrance of the channeltron are respectively 11mm, 47mm, 147mm and 40mm.

The principle of a TOF MS is to use the variation of times of flight of ions with different masses in order to disentangle them and form a mass spectrum. The time of flight *t* is a linear function of the square root of the mass to charge ratio of the ions:

$$t = a\sqrt{\frac{m}{2e}} + b. \qquad 2\text{-}1$$

Where *a* is a constant parameter only depending on the dimensions of the TOF MS and voltages applied on the different electrodes, and *b* is an offset which depends on the origin of time taken for the formation of the ions. In our case, *b* corresponds to the time of flight of the outgoing projectile on the way to the detectors after the collision (see Part I : Chapter 2.E.V)).

The resolution of such an apparatus depends on the length of the drift tube as $m/\Delta m = t/2\Delta t$. For a given initial dispersion Δt at the formation, if the length of the drift tube increases the resolution is improved because the overall time of flight *t* becomes longer. Our TOF MS is home made, its dimension were chosen for limiting the flight times to reduce the size of the coincidence time-window (see Part I : Chapter 2.E.V)) and however obtain a reasonably good resolution for low masses. From the fragmentation spectra of uracil, we determined a peak width of 41ns i.e. 0.3amu for the 1amu-mass-peak (H^+) and a peak width of 56ns i.e. 2.4amu for the peak at 112amu of the parent ion of Uracil ($C_4H_4N_2O_2^+$). It takes about 695ns for a He^+ (2amu) ion and 5200ns for the parent ion of Uracil (112amu) to travel through the TOF MS from the collision region until the channeltron of Figure 2-4. The dimensions of the different region of the TOF MS are indicated in the caption of Figure 2-4.

In order to improve the resolution we have to cope with the initial dispersion in time, space and kinetic energy of formation of the ions. Since we are detecting the ions produced in coincidence with the outgoing projectiles, the dispersion in time is negligible because of the high velocity of the ionizing projectile: the slowest projectiles pass in front of the window of extraction (10mm) of the TOF in 5ns (see also Part I : Chapter 3.B) and the resolution in energy is better than $\Delta E / E = 10^{-4}$ so that the incertitude on the duration of the outgoing projectile's travel until the detection is better than 20ns.

However the cross beam overlapping region has a definite spatial extension so that it is interesting to define a way to reduce the initial spatial extension. The existence of a space focal plane in the TOF MS where ions of identical masses are converging can be understood as follows: a first ion which appeared at a slightly farther position in the region of extraction at the same time than a second one will spend more time in the extraction region and thereby gain more kinetic energy in this region. Both ions gain the same kinetic energy in the second accelerating region. They will enter the drift region, which is free of field, with velocities differing only by the amount determined by the difference of kinetic energies gained in the first extraction region. So that the first ion enters later the drift region but will have higher energy and will catch up with the second ion after some distance *d*. This distance defines the position of the space-focus plane. This space-focus plane is independent of the mass of the ions. It should define the position of the detector. The aim of a dual stage extraction is to move farther the focus plane from the ion source (the cross beam region for us) for preventing that the resolution of the TOF MS becomes too low.

The initial kinetic energy dispersion can be reduced by using a reflectron for instance. Some simulations with SIMION were performed to verify the performance of the TOF MS and to search for solutions to improve its resolution in order to be able to measure fragmentation spectra of heavier molecules of biological relevance. The simplest solution to improve the resolution without changing the dimension of the apparatus is to increase the voltages applied on the electrodes. However, it is not possible to increase the voltages too much to avoid discharges. Replacing the usual voltages $\left(V_{extr} = \pm 150V; V_{drift} = -1836V\right)$ indicated in Figure 2-4 by still reasonably low voltages $\left(V_{extr} = \pm 300V; V_{drift} = -3680V\right)$, ions of masses 315 and 316 amu and mean initial kinetic energy of 0.001eV start to be disentangled on a flat detector. Hence this TOF MS can hardly be used for measuring high mass fragments of heavy molecules.

It is often believed that the advantage of a TOF MS over other mass spectrometer

(like quadrupole, see Part II : Chapter 2.E.I)) is that the extraction and transmission of the ions is close to 100%.The simulation with SIMION revealed that the lightest ions (H^+) are still fully extracted and transmitted up to energies of 1eV. A mass of 50amu is still extracted and transmitted up to initial kinetic energies of formation of 1.5eV. In the case of He^+ (2amu), the initial kinetic energy of formation is much lower than 1eV since the energy transfert in fast heavy ion collisions is very small and all ions are expected to be extracted.

E. Detection and acquisition system

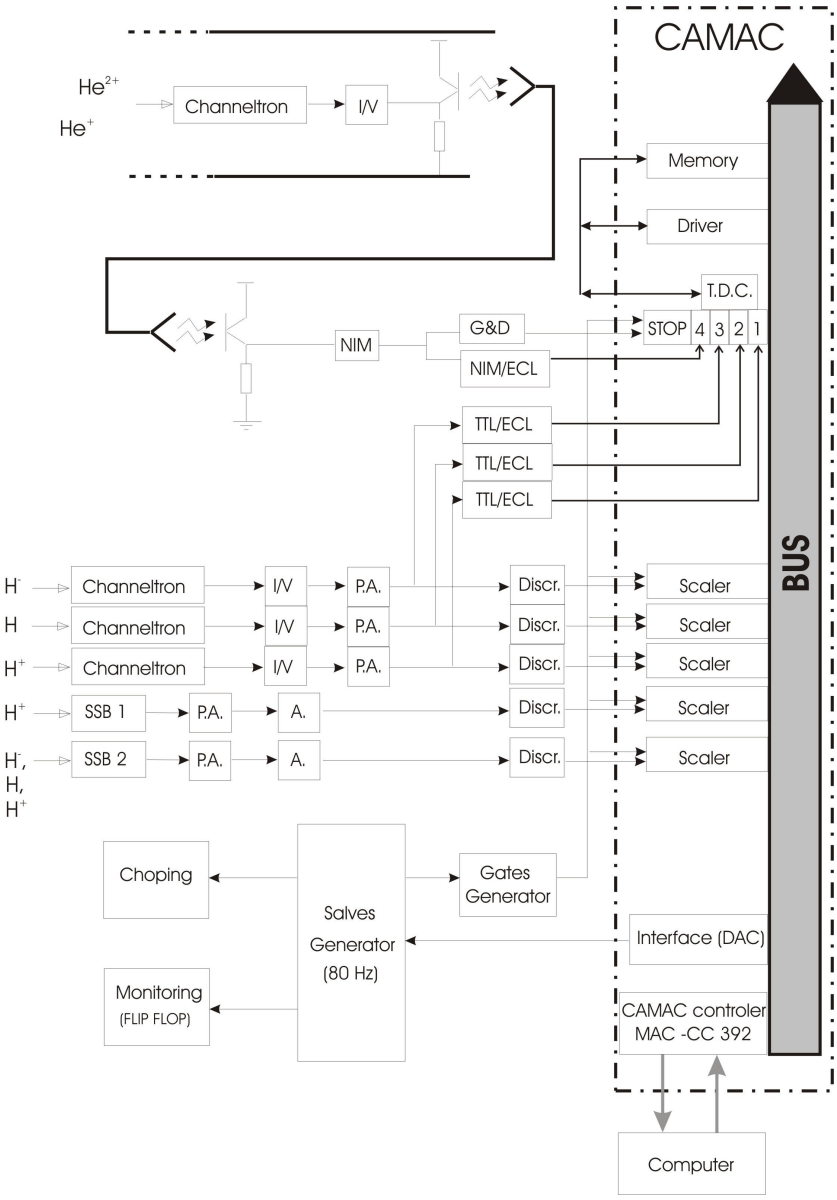

Figure 2-5: Schematic view of the acquisition system.

The machine is equipped with a coincidence system which allows an event by event analysis

of the collisions in the chamber and a simultaneous study of the charge exchange phenomena giving rise to ions in front of the window of the TOF MS.

I) Temporal structure of acquisition

The computer gives the start via the acquisition program to a frequency generator to produce a train of 80 rectangular pulses (= «buse »), this signal is triggered by odd TTL and sent to the generator commanding the voltages of the deflection plates before the chamber (represented by the signal in black on the Figure 2-6, the slope indicates the response of the voltage generator of the plates to the signal, the dashed line shows the original signal from the frequency generator). On another hand, the pulses of the signal from the frequency generator are a bit shrunken by a second generator in order to drive the fast commutators which are chopping the beam (represented by the signal in red on the Figure 2-6, the slope indicates the response of the commutator to the signal), the beam is hence cut during the change of voltages of the second pair of deflecting plates before the chamber. Finally a third generator shrinks the signal even more to form the signal of the "gates" which enables or inhibits the scalers of the acquisition (represented by the blue signal on the Figure 2-6). In this configuration, we are sure to acquire when the beam is set in the wished position (directed towards the chamber or directed towards SSB1) and we also avoid a deviation of the beam during the change of voltages of the plates before the chamber, which would possibly have bad consequences like charging some part of the set-up exposed to the beam.

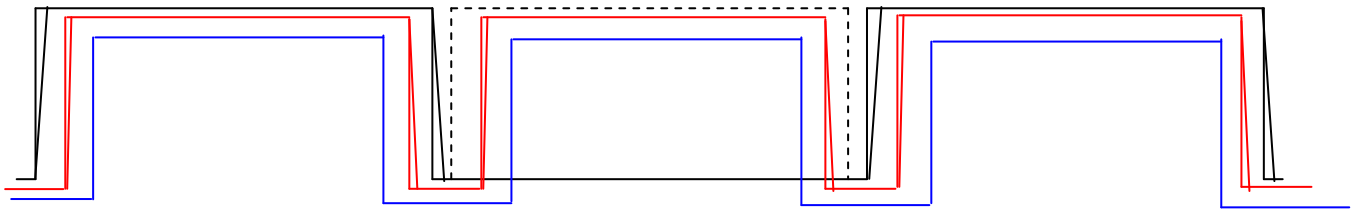

Figure 2-6 : Representation of the temporal structure, signals commanding the experiment (see text).

When the hydrogen beam was formed, the vertical plates before the chamber were constantly deflecting the protons on SSB1. The temporal structure was conserved concerning the chopping of the beam and the acquisition gates.

II) Detection of the projectiles after the chamber

The ion species composing the beam after the interaction with the molecules are separated according to their mass to charge ratios by an electro-magnet in the chamber of analysis placed about 1.5m after the chamber of collisions. Three channeltrons, placed at the end of the main beam line at the corresponding places detect independently the outgoing projectiles (H^-, H, H^+). When a particle is detected in one of the channeltrons, a pulse of 1 mA amplitude and about 10ns width is created, its rising ramp does not exceed 1ns. This signal is sent to a current / tension converter which then delivers the high level of a TTL logic signal. The switching from the low level to the high level is also made in less than 1ns, the high level switches again to the low level after about 10ns. On the one hand, this signal is sent into a discriminator, then into a scaler for counting the projectiles. On the other hand, it is going into a TTL/ECL converter before entering the TDC (Time to Digital Converter, whose functioning will be explained later). The different signals coming from the three channeltrons are going into different gates of the TDC, we can differentiate them during the analysis, and it makes possible the determination of the nature of the projectiles after collisions with the molecules.

III) Detection of the ions in the TOF

The positive ions produced by collision with the beam are extracted into a Time of Flight mass spectrometer (TOF).

All ions detected in the TOF arrive in the same channeltron; their difference of nature is guessed according to their time of flight. At the arrival of one ion, the channeltron delivers a pulse of current which is optically transmitted via a phototransistor to the CAMAC. This proceeding has been chosen in order to decouple the TOF system, put at high voltage, from the rest of the acquisition system at the ground.

The light coming from the optical fibre is converted into a NIM signal via another phototransistor, the arrival of an ion induce the fast switching of the signal (less than 1ns) from 0V (low level) to -2V (high level) for a duration of about 10ns. On the one hand, this signal is sent into a NIM / ECL converter before entering one gate of the TDC. On the other hand, it goes into a “gate and delay” module which introduces a delay of 10µs, this delayed signal enters the gate of the TDC called “STOP”. It gives the size of the window of coincidence after the arrival of a first ion in the channeltron of the TOF. This is the time we

are waiting for possible bigger fragments of a fragmentized molecules. As is explained below, the “STOP” signal is giving an instant of reference for the calculation of the times of flight.

IV) TDC: Code of an event

When a signal arrives on the gate “STOP” of the TDC, the time differences between the moment of arrival of signals on the other gates and this moment of reference is measured.

The TDC is taking into account all signals which has arrived in the laps of time of 32μs before the “STOP” signal arrived on the TDC. This corresponds to the size of the window of coincidence of the system, events are considered to be coincident if they were detected during this lap of time. The different times are measured with a precision of 0.5ns; every time is coded by 2 words of 16 bits. The eight lower bits are used to code the value of the measured time, and the eight higher codes the nature of the species detected in coincidence. A word “header” is preceding this series of double words.

V) Principle of coincidence: functioning of the TDC

The objective is to be able to guess the reactions that occured in the chamber which gave rise to the detection of ions in the TOF spectrometer. For that, we need to determine the nature of the ions that are detected in the channeltron of the TOF MS. According to their mass to charge ratios, ions will fly more or less longer in the flight tube; the difference of time of arrival will reflect their difference of mass to charge ratios. From the detection in the chamber of analysis we can also determine the state of charge of the outgoing projectile, if we are able to link both detections by coincidence in time, we should be able to determine which reaction occurred.

The first ions detected in the channeltron of the TOF will start the search for other signals coming from the detectors of the outgoing projectiles in the chamber of analysis (H^-, H, and H^+) and also for another possible signals from the TOF’s detector due to heavier fragment ions (there should be no fragmentation for experiments with He!); we wait 10μs for future detections and look in the past 22 μs before the first detection in the TOF.

The TDC records every signals in the past 32μs, once the “STOP” signal

arrives, it calculates the times corresponding to the arrival of projectiles by reference to the "STOP" signal. So for every occurrence of a "STOP" signal, the TDC is recording information on the event associated with it, concerning the nature of the projectiles and their measured times of flight, into a "memory" module controlled by a "driver" via a fast ECL bus.

Once a "buse" is finished, the data contained in the "memory" module of the TDC are transferred into the memory of the computer.

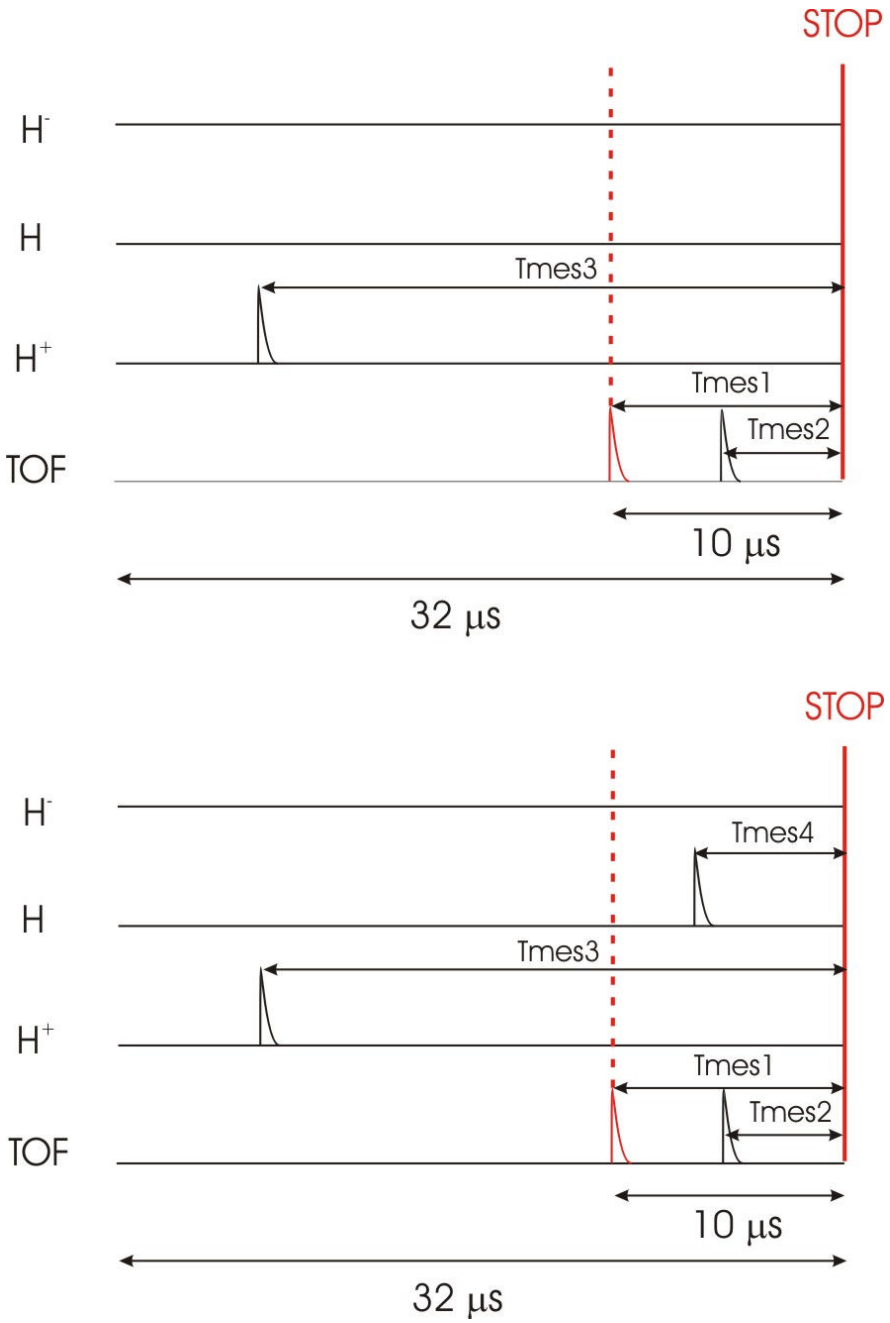

Figure 2-7 : Representative diagram of two examples of coincident events.

The times calculated so far could only tell us about the relative mass differences of the ions arrived in the TOF detector, we need to set a reference time in order to make

comparison of the flight times associated with the different ions species. The most intuitive reference time would be the instant of formation of the ions, but unfortunately we don't have any direct possible determination of this instant. However, we can take as reference the arrival of the projectiles at the end of course since they all fly the same distance with the same velocity until the detection (fluctuations estimated of a few ns between event of the same type, see Part I : Chapter 3.B).

If one proton came to interact with one molecule of the target leading to the formation of 2 fragment ions, the situation can be sketched as in the upper diagram of Figure 2-7: the TDC measures the times Tmes1, Tmes2, corresponding to the arrival of the fragment ions in the detector of the TOF MS, and Tmes3 corresponding to the arrival of the proton at the end of the main line section.

Tmes1 is equal to 10μs within the precision of the "Gate and Delay" module of a few tens of ns, since it corresponds to the arrival of the first detected fragment (the lightest) in the detector of the TOF MS. T1=Tmes3-Tmes1 and T2=Tmes3-Tmes2 are the times of flight of the first and second fragment ion respectively, with respect to the arrival of the proton at the detector of the chamber of analysis. In this way, we also free ourselves from the time fluctuations introduced by the "Gate and Delay" module in the measured times Tmes1, Tmes2, Tmes3.

In the case when several projectiles arrived in the detectors of the chamber of analysis during the time-window of coincidence (rare events since the beam intensity is very low), only one is responsible for the ionization of the molecule whose fragments have been detected in the TOF MS. The TDC measures the time of flight of every projectile but we are confronted with a problem of identification of the projectile having caused the ionization. In most cases, it is still possible to deduce which one of the projectiles was actually responsible for the ionization. There are only a few possible ionization events, and every one is characterized by a typical time of flight. We can identify the projectile having cause the ionization by determining which projectiles has a time of flight corresponding to one of the typical possible time of flights. For instance, it can happen that a neutral projectile (H) was detected during the same coincidence-time-window as the proton responsible for the ionization in the lower diagram of Figure 2-7. An associated time Tmes4 was then measured by the TDC. From the event of coincidence with a single proton shown in the upper diagram of Figure 2-7, we can deduce in the example of the lower diagram that only the proton has a time of flight which can correspond to a projectile having ionize the molecule.

So, it is possible to determine after all which one of the projectiles was most

probably colliding with the target by refering to the spectra of coincidence with a single projectile. The typical time of flight associated with different species of projectiles (H+, H, or H-) do not differ much since the projectile velocity is almost unchanged by the collision and projectiles different species travel almost the same distance until the detectors in the chamber of analysis (see Part I : Chapter 3.B). The characteristic times of flight corresponds to the time of flight of the peaks of the spectra of coincidence with a single projectile. The projectile, whose time of flight falls within the spread of the peaks determined by the latter spectra, is most probably the one responsible for the ionization of the molecule. Ambiguous coincidences, for which several projectiles have times of flight corresponding to some characteristic times of flight of ionization, are very rare and can be neglected.

VI) Formation of the spectra of coincidence

The accumulation of the times of flight of the ions detected in the TOF MS in coincidence with the same species of outgoing projectile (H^+, H or H^-) forms the spectra of coincidence (see Figure 4-1, Figure 4-2).

After reclassification of the “multi coincidence” events, for which several projectiles were detected in the same window of coincidence, almost the totality of the events is taken into account in the spectra of coincidence. We can then directly estimate the relative intensities of the different charge exchange phenomena having formed an ion in the region of extraction of the TOF MS if we look at the peaks intensities of the spectra, every peak of the spectra can be associated with one specific process (see experiment with He).

Chapter 3. Study of the beams

This chapter is presenting a detailed analysis of the composition of the beam: it attests the purity of the beam of protons or hydrogen atoms, which is of uttermost importance for the validity of the identification of the charge changes reaction by the coincidence technique.

A. Beam formation and Composition

Thanks to the display of the total number of counts on every detector of the machine "buse" after "buse", we are able to determine for every "buse" the composition of the beam before and after the interaction in the chamber, as well as its evolution during the experiment (see Appendix examples of beam characteristics profiles at 150keV and 80keV). E5 is the scaler associated with the outgoing H^-, E2 and E6 are associated with the outgoing H^0 and H^+ respectively. E1 is the scaler associated with SSB1.

One "buse" is made of a train of 80 rectangular pulses, 40 "odd" pulses and 40 "even" pulses; during the "odd" pulses the incoming H^+ are deviated onto the surface barrier SSB1, so the total number of counts on SSB1 or on the outgoing-projectiles-detectors during one "buse" is the sum over 40 pulses. Since the duration of one pulse is 0.01s, the total number of counts is given per 0.4s. Intensities indicated on the beam characteristics profiles in appendix have to be multiplied by 2.5 to be given in counts per second (cps).

I) Beam Characteristics Profiles

Six observables have been defined to characterize the beam, which are very useful to follow the evolution of the beam properties during the experiments. Some examples of beam characteristics profiles are presented in Appendix.

From bottom to top are displayed:

- The total intensity of the beam as defined by the sum of the channeltrons associated with the different outgoing-projectiles species (H^-, H^0, H^+), per "buse". (tot=E2+E5+E6)
- The ratio of the total intensity on the outgoing-projectiles channeltrons (tot) over the intensity measured on SSB1 which is the intensity of protons in the beam before the chamber, per "buse". (=tot/E1=tot/BS1)
- The number of detected ions in the TOF MS per "buse".
- The ratio of the counts per "buse" on the channeltron associated with the outgoing H^+ in the chamber of analysis to the total intensity. (=E6/tot=F_1 the fraction of protons in the beam after the collision, as defined in Part I : Chapter 1))
- The ratio of the counts per "buse" on the channeltron associated with the outgoing H^0 in the chamber of analysis to the total intensity. (=E2/tot=F_0 the fraction of hydrogen atoms in the beam after the collision, as defined in Part I : Chapter 1))
- The ratio of the counts per "buse" on the channeltron associated with the outgoing H^- in the chamber of analysis to the total intensity. (=E5/tot=$F\text{-}_1$ the fraction of hydrogen anions in the beam after the collision, as defined in Part I : Chapter 1))

Mean values of these observables were obtained by rough estimations determined from the beam characteristic profiles in Appendix and tabulated in Table 1 energy by energy. It is useful to refer to this table during the following analysis of the composition of the beams. The analysis of the evolution of the composition of the beam as a function of energy using the beam characteristic profiles, gives already a physical appreciation of the charge changes phenomena and an idea of the evolution of their cross sections.

II) Efficiency of the detection

We have to be aware of our detectors detection efficiency. Not enough care was given to the determination of our detectors efficiency. However, in the range of energy considered in this study, it is reasonable to assume that the channeltrons had an efficiency of 100%. Channeltrons have a counting rate tolerance above 10000 cps. Surface barrier detectors

have a lower counting rate capacity: 3000cps should not be exceeded if the significance of pulses intensities as a function of the impinging energy has to be taken into account. Their absolute counting rate capacity is expected to be a bit higher. Attention must be paid to not exceed the limit counting rate of the surface barrier; otherwise we can expect a decrease of the intensity on SSB1 compared to the intensity measured on the channeltrons. However, it seems not to have been the case for the present experiments with helium.

Moreover, the efficiency of the detectors depends also strongly on the energy of the impinging particles. At low energies the amplitude of the pulses arising after the arrival of a particle on the surface barrier detector becomes too small to be disentangled from the noise. As a consequence, a sudden rising of the ratio tot/SSB1 at 27.5keV is observed for the experiments with a beam of protons whereas the composition of the beam determined by the projectiles detectors in the chamber of analysis remains unchanged (see Table 1). Since the amount of neutral in the beam has not been increased, this effect is clearly due to the deficiency of SSB1 observable from that energy.

The final results of our experiments show that the counting rate of the H^- projectiles was too low. It must be attributed to some deficiency of the channeltron associated with the detection of this projectile.

III) Procedure to prepare a beam of H(1s)

During the experiments, the cell of neutralization was always placed on the course of the beam, it was emptied when we wanted to form a beam of protons, and it was filled by Argon or Helium when we wanted to form a beam of hydrogen atoms.

Figure 3-1 gives an idea of the efficiency of the formation of the hydrogen beam. Down to 35keV, we can rely on the detection of SSB1, as said before, the steep rise of the curves at 27.5keV comes partly from the low energy deficiency of the surface barrier detection.

For the formation of the hygrogen beam, the second pair of vertical plates before the chamber was constantly deflecting the charged particle. However, the actual acquisition time structure remained unchanged: the beam was still chopped as a bunch of 80 pulses and the acquisition was still enabled or inhibited in the same way, we were counting only during the “odd gates” even if the beam of hydrogen was also sent into the chamber during the “even gates”.

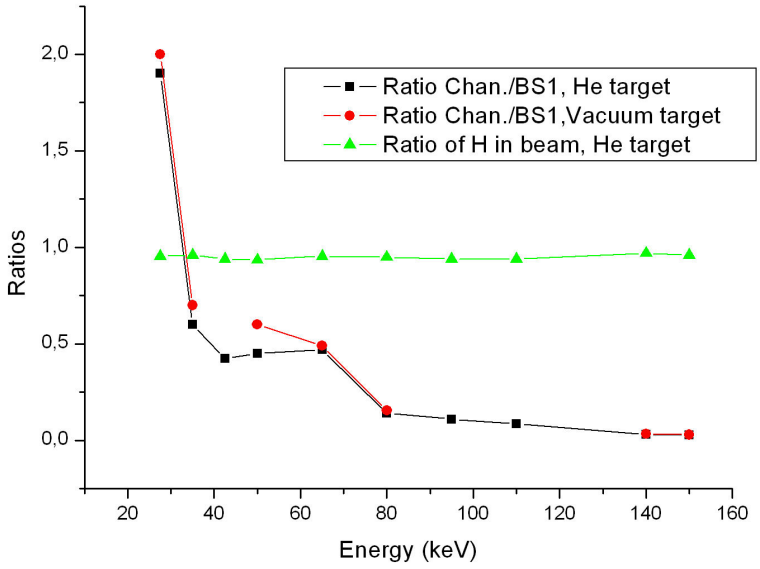

Figure 3-1 : Neutralization by the cell (in the legend, Chan=tot=total intensity of the beam and BS1 is as defined in the text). The rise of the inverse ratio Chan/BS1 (before the collision chamber) is due to the defiency of the surface barrier detector SSB1. As well, is shown the fraction of neutral H^0 in the beam which remained constant.

The deflection plates played also the role of quenching plates. The gas of neutralization was first chosen to be Ar, it was then replaced by He because the formation of metastable hydrogen (H(2s), H(2p) …) was then expected to be less abundant [29,30]. Indeed, hydrogen atoms are formed into various excited states by electron capture, in amounts depending on the energy of the incoming protons and of the target used. The most abundant excited states are H(2s) and H(2p): H(2p) has a short lifetime of 3×10^{-9}s so it almost immediately decays after its formation in the neutralization cell (at 150keV, it can travel 1.65cm in average before decaying), but H(2s) is a long-lived metastable atom (~150ms) because the decay into the ground states H(1s) is optically forbidden. Hence the metastable H(2s) formed in the cell of neutralization are able to survive long enough to interact with the effusive beam target, and influence the determination of cross sections. However, by using an external electric fields we can force the decay to happen faster by mixing the $2s_{1/2}$ and $2p_{1/2}$ states (Stark effect). The time required for the transition $2s_{1/2} \rightarrow 2p_{1/2} \rightarrow 1s_{1/2}$ varies from 20 years in the zero field case to twice the 2p state lifetime for large fields (>100V/cm) [29].

Since the projectiles are going fast (5.5×10^{8} cm.s^{-1} at 150keV), the time remaining between the deviation plates must also be taken into account to estimate the effective decay of the population of metastable atoms: if $\tau\sim6\times10^{-9}$s designates the lifetime of H(2s) under a field strength of 700 V/cm, 70% of H(2s) atoms created in the neutralization cell has decayed to the ground state after 3.3cm, and 99% after 16cm. So, in order to fully quench the metastable

atoms we need deviation plates to be longer than 16cm about in the worst case.

The second pair of vertical plates are 10cm long and a field of 700V/cm (plates distant of 1cm), about 95% of the metastable H(2s) must have been forced to decay to the ground state. Moreover, it is known [30,41] that the fraction of metastable H in the beam becomes negligible by increasing the pressure of the cell of neutralization, we were working with high pressure in the cell, it reduced the formation of metastable H(2s).

In any case, the fraction of the metastable excited hydrogen atoms H(2s) is relatively small since the total electron capture cross section from He is more than 50 times greater than the specific capture into the H(2s) according to the results of [29] (Figure 3-2 (a)), so that the amount of metastable H(2s) in the beam must be less than 2% anyway.

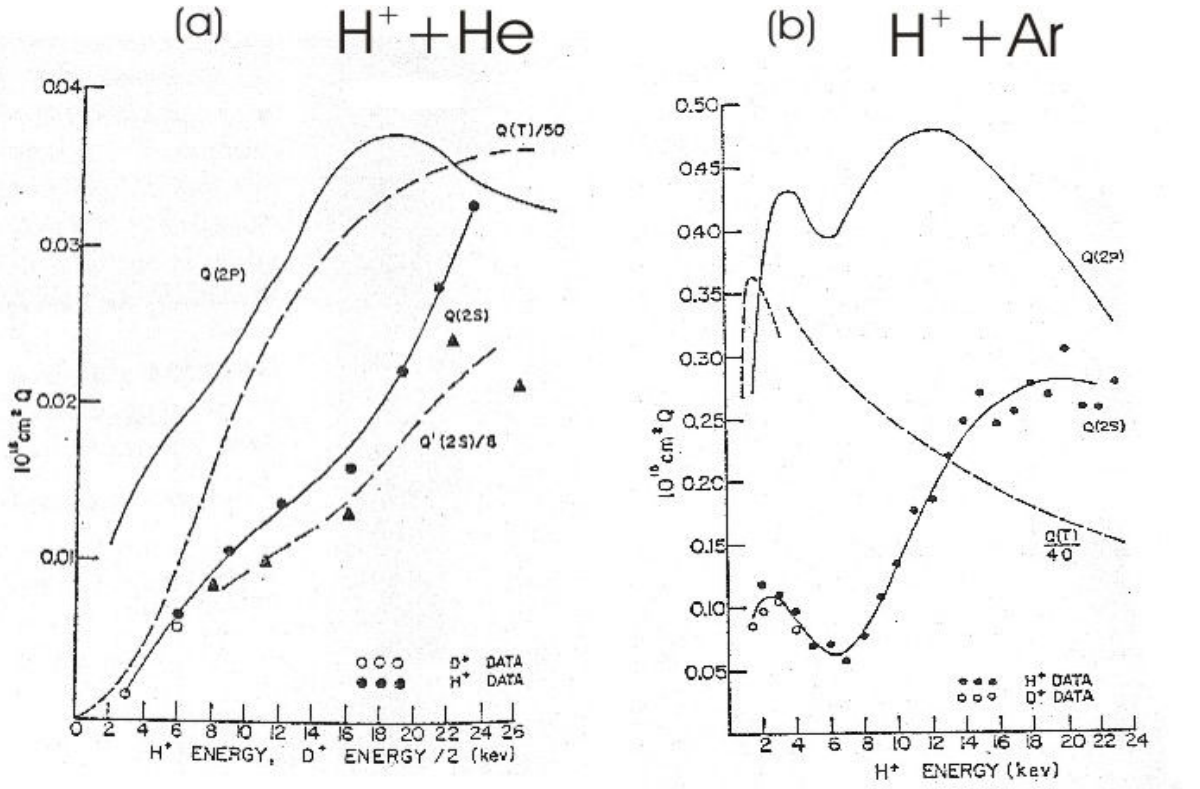

Figure 3-2: Cross sections of single electron capture by protons from He (graph (a)) and Ar (graph (b)), into different excited states of hydrogen atoms H (2s) (=Q (2s)) or H (2p) (=Q (2p)) and total cross section of capture are shown. Results from [29] compared to earlier results.

From the beam characteristic profiles at 150keV in Appendix, we realize that it is much more difficult to form a beam of hydrogen atoms at high energy: according to the ratio tot/BS1, 3% only of the incoming beam of protons was neutralized. A very intense beam of protons of at least 17000cps had to be sent through the neutralization cell for obtaining a beam of some 500cps (the counting rate capacity of SSB1 could be largely exceeded for such high counting rates). It gives an idea of how much dense was the target constituted by the cell of neutralization compared to the target constituted by the effusive beam whose presence is

invisible on the beam profiles at that energy (the residual pressure of 2.10^{-4}mb was measured in the section close to the neutralization cell, the pressure inside the cell was very high).

IV) Dependence of the composition of the beam with the beam intensity

A dependence of the composition of the beam of H^+ with the beam intensity is observable in the beam profiles in Appendix. When the beam intensity is increased, the ratio of H^+ tends towards the value 1 whereas the ratios of the other species H and H^- are lowered. We could believe that the species H and H^- composing the beam are produced by collisions of protons with the residual gases or by stripping on the aperture of the collimator D_1 and D_2; however we notice that the amount of the species H and H^- in the beam seems to be constant. Indeed, an increase of the beam intensity has the effect of increasing the number of H^+ in the beam whereas the respective numbers of the other species (H and H^-) remain unchanged. It gives this "blow-up" effect in the evolution of the fractions F_1=H^+/tot, F_0=H^0/tot and F_{-1}=H^-/tot when the beam intensity (tot) is varied, observable in the beam profiles of a beam of protons at 150keV in Appendix. If H and H^- would originate from charge transfert by collisions with the residual gases or by stripping on the collimators, their amount should also increase with the increase of intensity of the beam of protons, since the target constituted by the residual gas (resp. by the collimators) is expected to be constant.

The origin of the presence of this "neutral background" in the beam (mainly constituted by H) is probably explained by the formation of a constant amount of H and H^- produced inside the magnetic sector field, which can results from collisions on the wall of rejected charged species (H_2^+,H_3^+ …). Therefore we have this observed dependence of the composition of the beam with the intensity of the beam of H^+. As a consequence, the amount of neutralizations by collision with the residual gases can be neglected for experiments with a proton beam, since they are less abundant than the permanent neutral background.

Concerning the beam of hydrogen atoms, its composition remains unchanged at various beam intensities. The plates of deviation before the chamber constantly deflect the incoming charged particles. On the one hand the projectiles H^+ go to SSB1, on the other hand the projectiles H^- are deviated in the opposite direction. Hence projectiles H^+ and H^- which compose the beam after the second pair of deviating plates originate mainly from interactions of the beam with the helium target and the residual gas in the chamber, consequently the ratios of the different species grow together with the intensity of incoming hydrogen atoms

beam. This can be observed on the beam profiles of the hydrogen-atoms-beam in Appendix.

V) Dependence of the beam composition with the projectiles energy

The effect of the crossing of the helium effusive beam target on the composition of the beam of protons is observable at the lower energies (from 65keV) in Figure 3-3: the fraction of protons H^+ in the beam diminish if the helium target is present compared to its value when the helium target is absent. It is due to the increase of the cross section for electron capture by protons when the energy is lowered.

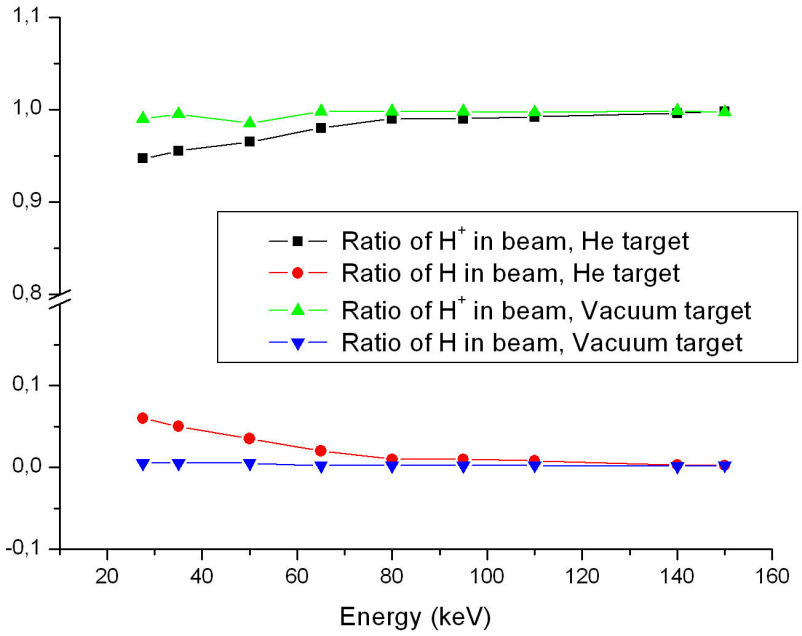

Figure 3-3 : Effect of the presence of the effusive beam target of He on the beam of protons H+.

In comparison, the influence of the lowering of energy is not felt strongly on the composition of the beam of H^0 at lower energies, no important changes are directly measurable in Figure 3-5 if the effusive beam target is flowing or not. And, an important amount of H^+ is constantly present in the beam at the end of course of the projectiles. The beam of hydrogen atoms is made of 95%±1.2% of hydrogen atoms when the effusive beam helium target is crossing the beam and it is made of 96.7%±0.6% when the effusive beam is off; whereas the ratio of protons in a beam of protons was very close to 1 in vacuum (>99.5%), and felt down to 95% at the lowest energies when the effusive target was introduced. So the presence of the effusive beam target is felt in the beam of H, but the

protons of the beam are mostly not formed by collision with the target only. Indeed, the rest of the protons (more than 3%) must be formed by collisions with the residual gas.

The pure electron loss is the process leading to the ionization of the hydrogen atoms, pure electron loss without ionization of the target has the highest cross section in the intermediate range of energy under 100keV, and its magnitude is estimated to be of the order of $10^{-16}cm^2$ in the work of Dubois et al [6]. It is comparable with the order of magnitude of the cross section for electron capture by protons which leads to the formation of hydrogen atoms in the beam of protons. Both cross sections are shown in the Figure 3-4.

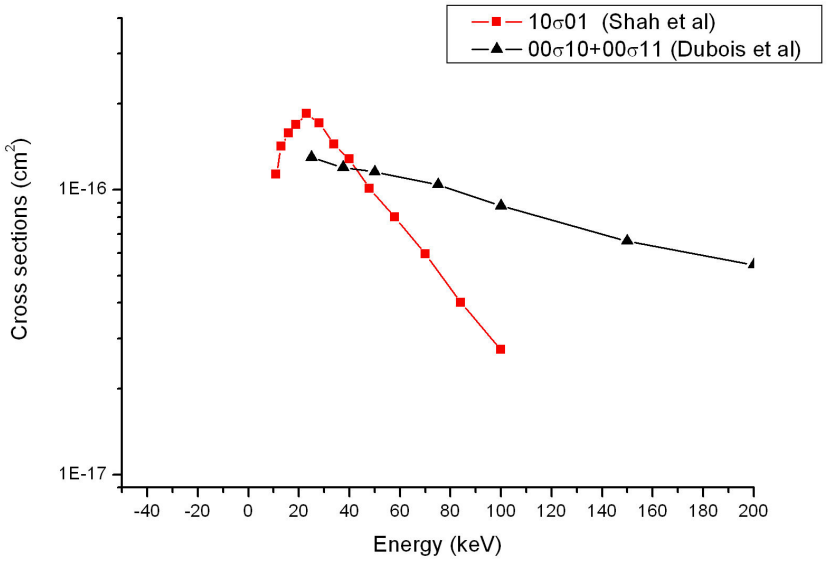

Figure 3-4: Comparison of the magnitude of cross sections of pure electron loss (formation of H^+) in a beam of hydrogen atoms with the magnitude of the cross section for electron capture (formation of H^0) in a beam of protons, in the range of energy of the present study. The results from Dubois et al [6] are used for the hydrogen beams and the results from Shah et al [40] for the beam of protons.

Combined with the fact that the residual pressure was high and was somehow hiding the effusive beam target, the steeper rise of the cross section for formation of H in a beam of H^+ shown in Figure 3-4 is in agreement with the observation that the presence of the target is felt more strongly in the composition of a beam of H^+.

If we take the largest cross section of electron loss at 25keV (Dubois et al, $\sigma(0->1) = 00\sigma10+00\sigma11 = 1.3\times10^{-16}cm^2$) and suppose a pressure of 5×10^{-5}mbar over a distance of 150cm, which is too much since the pressure is only so high in the chamber because of the differential pumping reducing the pressure in the adjacent beam sections (see Part I : Chapter 2.C.I) ; and if π is the number of helium atoms in a volume of section $1cm^2$ (constant

$\pi=2.5\times10^{16}\times P\times l$ taken in the review of Tawara [41]), we get :

$F_1=F(0->1)=\pi\times\sigma(0->1)=2.5\times10^{16}\times P\times l\times\sigma(0->1)=2.5\times10^{16}\times10^{-5}\times150\times1.3\times10^{-16}\sim2.5\%$

It is still under the observed fraction of H^+ in the beam of H at 150 keV (~3%) (Dubois et al, $\sigma(0->1)=6.6\times10^{-17}cm^2$ at 150 keV)!

So it is difficult to explain the important fraction of H^+ in the beam of H only by collisions with the residual gas. However it is the only explanation and it should be remarked that, depending on the range of pressure and the type of gauge, the indication of the pressure gauge might underestimate strongly the actual pressure of helium. Indeed, it is known that the gauge indication needs to be corrected by a factor of 2 or more when measuring specifically helium pressure. The residual pressure in the beam line close to the neutralization cell reached 2×10^{-4} mbar when the beam of H was formed. The differential pumping along the beam line reduces the pressure in the collision chamber but the residual pressure was still high (Pres=5×10^{-5}mbar and estimated in the adjacent sections of about 5×10^{-6} mbar).

Moreover, the fraction of H^+ cannot be due to collisions with some part of the apparatus since it would also have affected the beam of H^+ which was pure at 99.5%.

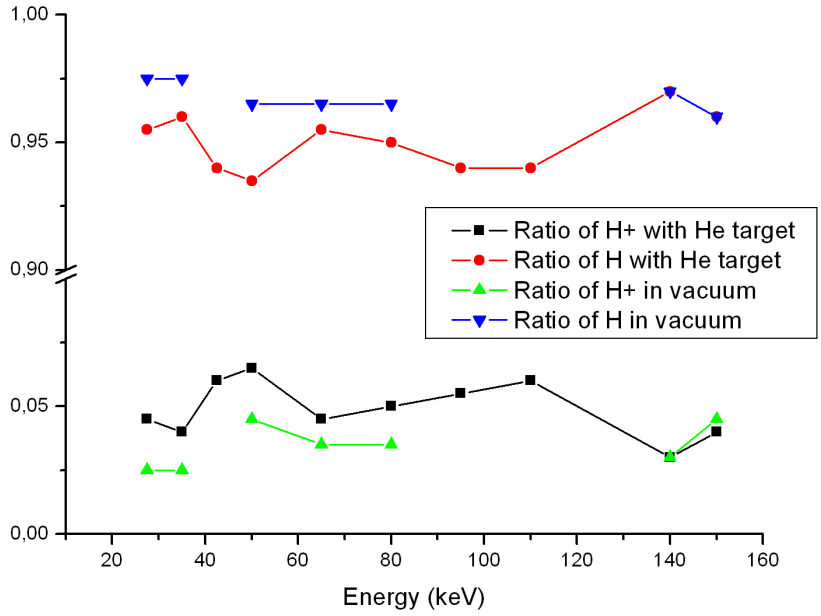

Figure 3-5: Effect of the crossing of the beam of hydrogen atoms by the effusive helium target beam.

Even if the presence of the effusive beam target is somehow hidden by the residual gas and not clearly noticeable on the composition of the hydrogen atoms beam, its presence is however clearly observable on the detection profiles of the TOF MS: the number of ions

formed in the region of detection of the TOF MS coincident with an outgoing projectile is much higher when the effusive beam target is present as we can see on the spectra of the beam characteristics (see Appendix).

VI) Conclusion about the composition of the beam

The beam of protons is made of more than 99.5% of H^+ and less than 0.5% of hydrogen atoms for beam intensities of more than 1000cps, the hydrogen atoms are formed mostly inside the magnetic sector field in a constant amount independent of the beam intensity. The beam of hydrogen atoms is made of more than 95% of hydrogen and less than 5% of H^+, it is so because of the higher residual pressure due to the leak from the cell of neutralization (Pres= 2.10^{-4}mbar when the beam of hydrogen atoms is formed), the H^+ are probably formed during the travel after the deviation plates by ionization in collisions with the residual gases. It is the composition of the beam at the end of the course of the outgoing projectiles; we can expect that the proportion of H in the beam just before the interaction with the effusive beam is less contaminated by protons.

VII) Diluted beam for the coincidence system

By looking at the compositions of the beam, we see that the formation of an He ion in front of the window of extraction of the TOF MS is very probably due to the impact of a proton if we apply a beam of proton, and very probably due to the impact of an hydrogen when the beam of H is applied. It is so because we are in single collision conditions, even if the beam of hydrogen is contaminated by several % of protons. The probability that a proton produced by the collision of a hydrogen atom with some helium atom of the residual gas experienced a second collision in front of the window of the TOF MS is very low. We can verify that we are still under single collision conditions by calculating $\frac{\pi^2}{2}\sigma_{01}(\sigma_{01}+\sigma_{10})$ from Equation 1-7. At 25keV, we have $\sigma_{01}=1.3\times10^{-6}\,\mathrm{cm}^2$ from Dubois et al [6] and $\sigma_{10}\simeq1.5\times10^{-6}\,\mathrm{cm}^2$ from Shah et al [40], π=$2.5\times10^{16}\times$P$\times$l from Tawara [41], we obtain taking P=10^{-5}mbar and l=50cm: $\frac{\pi^2}{2}\sigma_{01}(\sigma_{01}+\sigma_{10})\simeq0.01$

$\frac{\pi^2}{2}\sigma_{01}(\sigma_{01}+\sigma_{10}) \ll 1$, the conditions of single conditions being fulfilled, we can consider that only hydrogen atoms can be responsible for helium ionization in front of the TOF MS window.

It has to be realized that the functioning of the coincidence system requires the formation of very diluted beams, the mean number of protons (or hydrogen atoms) in the window of coincidence must not exceed one, this gives an idea of the maximal intensities we should work with: the intensity must be lower than 1 proton in 32 μs, i.e. 3×10^4 protons per second. Usually we worked with intensities lower than 10^4 cps, so this condition was respected.

		Energy (keV)		150	140	110	95	80	65	50	42.5	35	27.5
Beam of H+	He Target	Composition Ratios	H^+	0.998	0.996	0.992	0.99	0.99	0.98	0.965		0.955	0.947
			H	<0.0025	<0.003	0.008	0.01	0.01	0.02	0.035		0.05	0.06
			H^-	<0.001	<0.001	<0.002	<0.0015	<0.001	<0.002	<0.002		<0.002	<0.004
		Intensity (cps)		2000	3250	1425	1375	3000	2500	1250		1000	750
		Chan./BS1		0.94	1	0.97	1	0.9	1	0.88		0.85	1.6 !
	Vacuum target	Composition Ratios	H^+	0.997	0.9985	0.997	0.998	0.998	0.985	0.996		0.995	0.99
			H	<0.0025	<0.0015	<0.0025	<0.002	<0.002	<0.005	<0.004		<0.005	
			H^-	<0.0015	<0.004	<0.002	<0.0013	<0.001	<0.002	<0.0015		<0.0001	
		Intensity (cps)		1875	7000	1375	2000	2500	3755 to 625	1500		1000	1250 to 10000
		Chan./BS1		0.93	0.97	0.95	0.98	1	1	0.92		0.9	1.5 !
Beam of H	He target	Composition Ratios	H^+	0.04	0.03	0.06	0.055	0.05	0.045	0.065	0.06	0.04	0.045
			H	0.96	0.97	0.94	0.94	0.95	0.955	0.935	0.94	0.96	0.955
			H^-	<0.006	<0.01	<0.006	<0.002	<0.006	<0.005	<0.0012	<0.004	<0.0025	<0.0035
		Intensity (cps)		400	250	450	925	562	500	2500	625	2000	1000
		Chan./BS1		0.029	0.03	0.085	0.11	0.14	0.47	0.45	0.425	0.6	1.9
	Vacuum target	Composition Ratios	H^+	0.045	0.03			0.035	0.035	0.045		0.025	0.025
			H	0.96	0.97			0.965	0.965	0.965		0.975	0.975
			H^-	<0.005	<0.015			<0.005	<0.005	<0.0015		<0.0015	<0.005
		Intensity (cps)		550	162			562	500	2000		2000	625
		Chan./BS1		0.03	0.033			0.155	0.49	0.6		0.7	2

Table 1 : Mean characteristics of the beams profiles for every energy with and without the effusive beam target of He.

B. Relative precision of the definition of energy of the beam

If $T(E_p)$ is the time needed for an outgoing projectiles of energy E_p to reach the end of course detector in the chamber of analysis and d the distance from the cell of collision to this detector, the relation $E_p = \frac{v_p^{\,2}}{2m_p}$ can be rewritten :

$$\sqrt{E_p} = \frac{d\sqrt{m_p}}{\sqrt{2}T(E_p)} \qquad 3\text{-}1$$

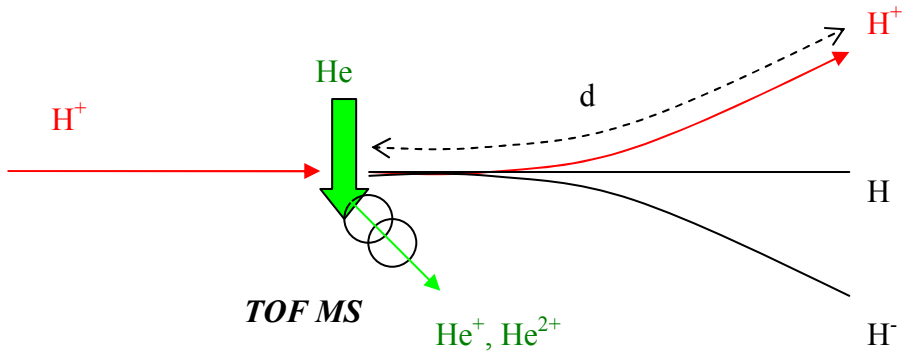

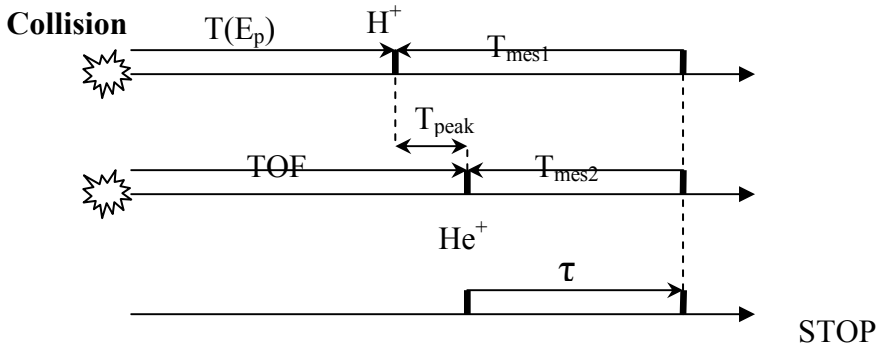

Figure 3-6 : Measure of time of flight and definition of energy.

As was previously explained in Part I : Chapter 2.E.VI), spectra of coincidence are histograms of the times of flight (T_{peak}) of the ions extracted into the Time of Flight mass spectrometer (TOF MS) calculated by reference to the arrival of the outgoing projectile. As shown in the explicative diagram of Figure 3-6, it corresponds to the difference between

the time of flight of the helium ion TOF in the TOF MS and the time of flight $T(E_p)$ of the outgoing projectile of energy E_p until the detector in the chamber of analysis. T_{mes1} and T_{mes2} correspond to the time measured by the TDC of the acquisition system (Part I : Chapter 2.E.IV)) and τ is the constant time delay introduced by the gate and delay module before the STOP signal is sent.

The TOF of the helium ion in the TOF MS is expected to be always the same for a given type of ion (He^+ or He^{2+}), independent of the energy of the incident projectile, whereas the time of flight of the outgoing projectile $T(E_p)$ is dependent of the incident beam energy. It follows that:

$$T_{peak} = T_{mes1} - T_{mes2} = TOF - T(E_p) = cst - T(E_p),$$

which can be rewritten $T_{peak} = cst - \frac{d\sqrt{m}}{\sqrt{2}\sqrt{E}}$ using the relation **3-1**.

So there exists a relation of proportionality between the position of the peaks of the He ions and the inverse of the square of the energy.

We found the expected straight lines in Figure 3-7 and Figure 3-8 by drawing the position of the peaks of He^+ and He^{2+} for the different coincidence channels as a function of $1/\sqrt{E}$. In this way, we could verify the relative precision of the determination of the energy of the incident particle. If we extrapolate the curves to the origin, the intersection with the y-axis gives an estimation of the time of flight of the He^+ or He^{2+} in the TOF MS: the travel of a He^+ to the detector of the channeltron lasts approximately 900ns, and the travel of a He^{2+} lasts about 620ns. We observe a small shift between the curves associated with a same peak but different reaction channels, the time of flight of the helium ions are a bit shorter for the channel coincident with an H^+ compared to those for the channel coincident with a neutral H. According to the diagram of Figure 3-6, this means that the time of flight of the protons before detection is a bit longer than the corresponding time of flight of the H. It is due to the deflected trajectory of the H^+ in the chamber of analysis which is a little bit longer than the straight trajectory of the H to the detector. The shift in flights time is less than 5ns, for a proton of 100keV whose speed is 4.5 10^6m .s-1, it represents a distance of 2.2cm.

The curves obtained by impact of protons superimpose the curves obtained by impact of hydrogen, hence the energies are not altered by the neutralization, more generally the charge exchanges don't affect the energy of the incident particles in this range of energy.

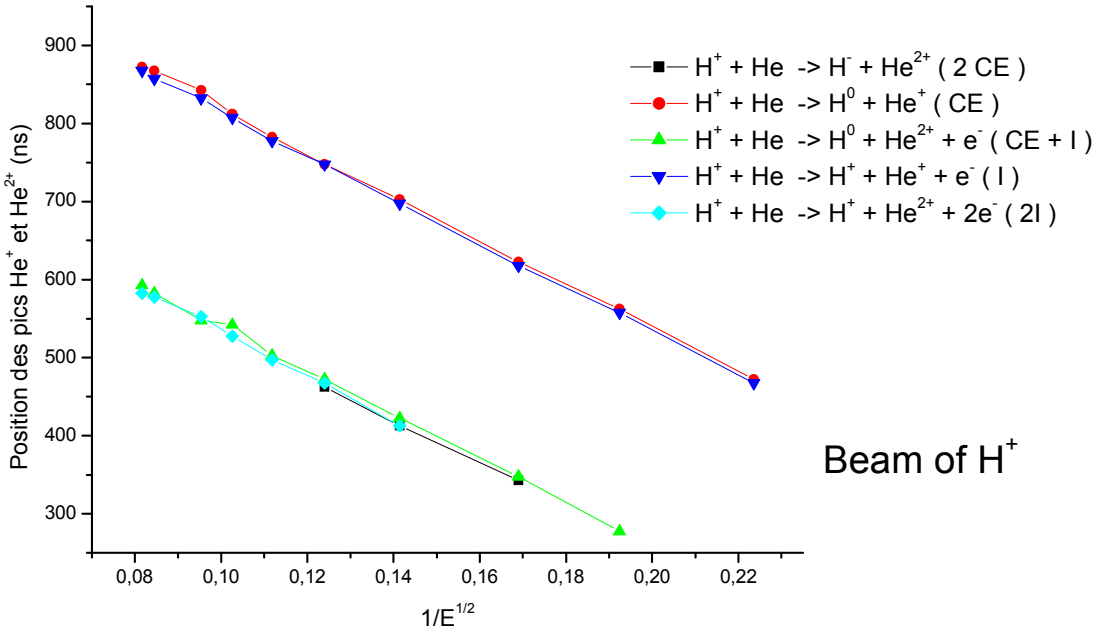

Figure 3-7 : Displacement of the position of the peaks of He^+ and He^{2+} obtained by impact of H+ on He for the different channels with respect to the Energy.

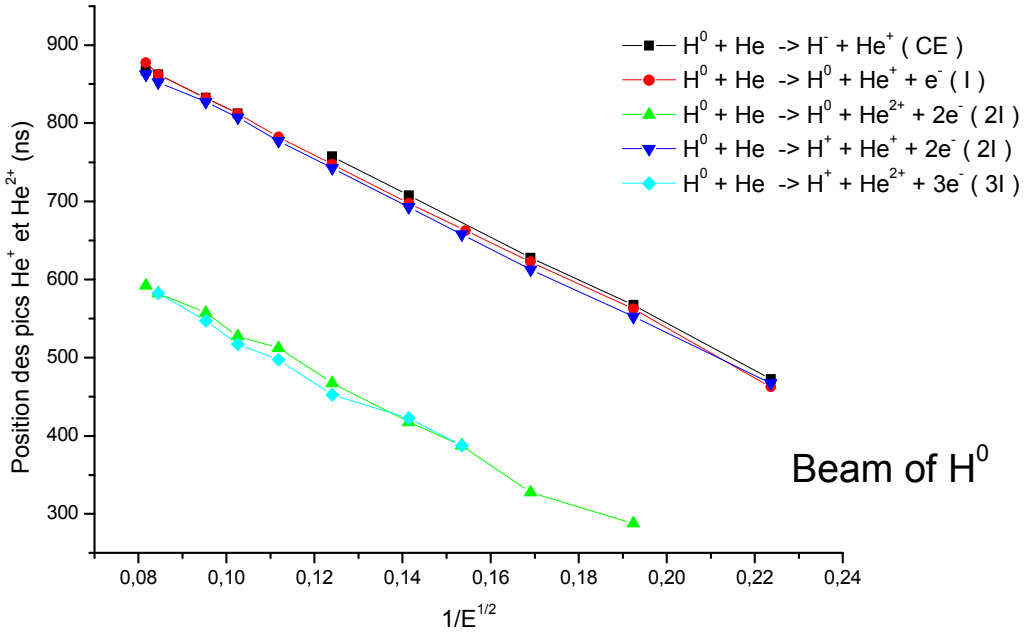

Figure 3-8 : Displacement of the position of the peaks of He^+ and He^{2+} obtained by impact of H on He for the different channels with respect to the Energy.

Chapter 4. Cross sections of Charge changes phenomena in protons and hydrogen atoms impact onto Helium, Results.

In the spring of the year 2002, the machine was used to make experiments of collisions of protons and hydrogen atoms onto a gas target of helium. Following these experiments in the autumn 2002 started their analysis in order to determine new sets of cross sections for charge changes reactions with formation of a helium cation.

A. Branching ratios

I) Analysis of the coincident events

By impact of protons, the following reaction channels were observed:

$H^+ + He \rightarrow H^- + He^{2+}$ (double electron capture=2EC)

$H^+ + He \rightarrow H + He^+$ (electron capture=EC)

$H^+ + He \rightarrow H + He^{2+} + e^-$ (electron capture and target ionization=EC+TI)

$H^+ + He \rightarrow H^+ + He^+ + e^-$ (single target ionization=TI)

$H^+ + He \rightarrow H^+ + He^{2+} + 2e^-$ (double target ionization=2TI)

By impact of hydrogen, the following reaction channels were observed:

$H + He \rightarrow H^- + He^+$ (electron capture=EC)

$H + He \rightarrow H + He^+ + e-$ (pure single target ionization=TI)

$H + He \rightarrow H + He^{2+} + 2e^-$ (pure double target ionization=2TI)

$H + He \rightarrow H^+ + He^+ + 2e^-$ (electron loss and simultaneaous target ionization=EL+TI)

$H + He \rightarrow H^+ + He^{2+} + 3e^-$ (electron loss and simultaneous double target ionization=EL+2TI)

The hardest task of the analysis is the reclassification of the multicoincident events,

some being due to fortuit coincidence of several projectiles detected in the same time-window of coincidence (rare since we were working with “diluted” beam, see Part I : Chapter 3.A.VII) and some being due to systematic errors in the acquisition system which could be understood by the analysis and systematically corrected. This reclassification is performed by a self consistant analysis: among the several projectiles detected in the same coincidence time-window, we determine the one which is most probably at the origin of the He ionization, depending whether its time of flight falls into one of the peaks of the spectrum constituted by the events recorded after coincidence with single projectiles. This task is achieved by the use of a series of fortran90 programs which were developed during this work.

On the basis of an event by event analysis, we can have certainty about the occurance of the precedently-cited reaction channels even if a few numbers of events were associated with them. This is the case for instance for reaction channels $H^+ + He \rightarrow H^- + He^{2+}$ and $H^+ + He \rightarrow H + He^{2+} + e^-$ for which only a few events were registered during the experiments.

Once the reclassification procedure was achieved, about 99% of the total events registered could be attached to one of the coincidence spectra with a single projectile. For every incidence energy of the protons (or hydrogen atoms), we were left with only three spectra of coincidence: the coincidence spectrum with one H^+, the coincidence spectrum with one H and the coincidence spectrum with one H^-. Figure 4-1 shows typical spectra of coincidence obtained by collision of a beam of H^+ onto the gas target of helium at 50keV incident energy. The lower graphs of the Figure 4-1 show events for which an ion was detected in the TOF in coincidence with one H^+ in the chamber of analysis, as well, the middle graphs show the coincidences with one H and the upper graphs show a few events of coincidence with one H^-. Each peak observed in the graphs can be directly associated with one particular reaction channel: the first peak near 400ns contains a few events only, it corresponds to the detection of He^{2+} in the TOF, the biggest peak near 700ns corresponds to the detection of an He^+ in the TOF. For instance, an event associated with the He^+ peak of the middle graphs can be identified with the occurrence of an electronic capture, the reaction $H^+ + He \rightarrow H + He^+$ .The complete histograms are shown in the left graphs; they are redrawn at a lower vertical scale in the right graphs in order to observe the growth of the He^{2+} peaks.

Figure 4-2 shows similar coincidence spectra obtained by impact of hydrogen atoms onto the helium gas target.

We can then determine the branching ratios of one specific reaction channel by counting the events associated with the peak of this particular channel and dividing it by the total number of events recorded during the experiment over the different channels.

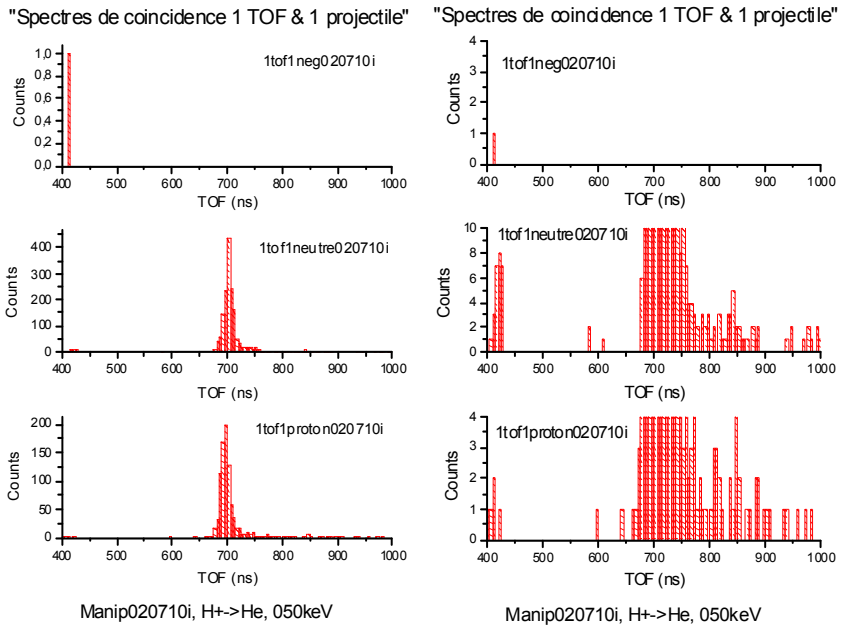

Figure 4-1 : Typical Spectra of coincidence with a single outgoing projectile obtained by impact of H^+ on a target of He: coincidence with an outgoing H^+ (lower spectra), coincidence with an outgoing H (middle spectra) and coincidence with an outgoing H^- (upper spectra). The graph shown on the right represents the same spectrum with a different vertical scale in order to make apparent the peak of He^{2+}.

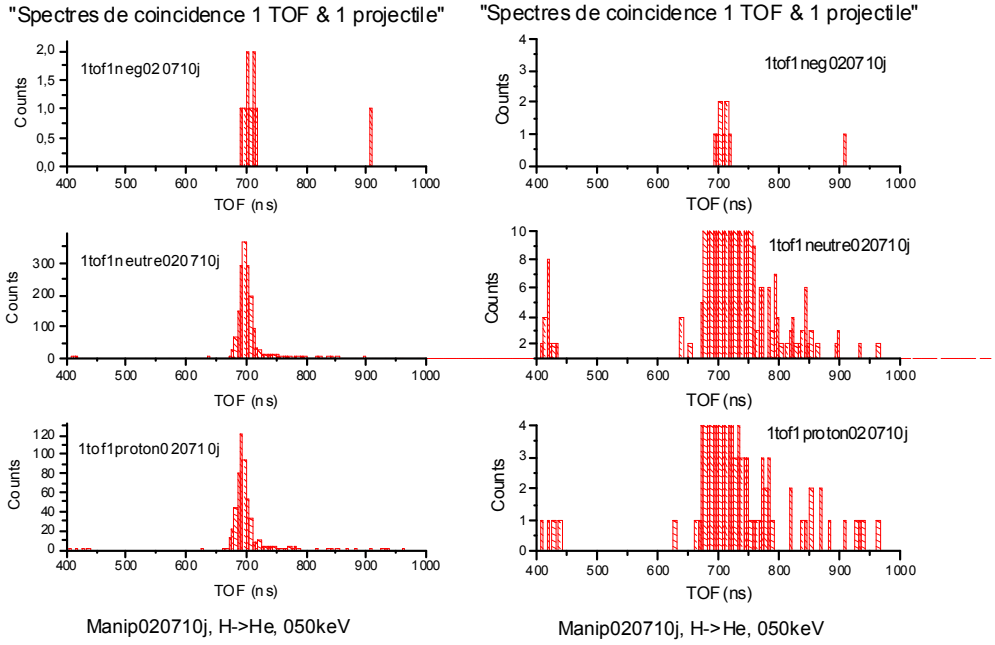

Figure 4-2 : Coincidence spectra with a single outgoing projectile obtained by impact of hydrogen on a target of He.

II) Branching ratios

Figure 4-3 and Figure 4-4 show the calculated branching ratios for the different channels observed. Each experiment was unique in the sense that the target and the incident beam varied from one experiment to the next. We tried to reproduce similar target conditions by maintaining the pressure of helium constant in the reservoir. However, the determination of branching ratios obtained for different beam intensities leads to results of different quality due to the associated statistical errors (see the evolution of the beam profiles intensity during one experiment in Appendix, see also the variation of the intensities from one experiment to another in the Table 1). Typically, at a given energy, one single experiment with incident protons was performed, whereas several experiments with incident hydrogen atoms were repeated in series in order to improve the statistics since hydrogen atoms beam intensities were lower than proton beam intensities. Besides, several experiments were carried out at 80keV and 95keV. In Figure 4-3 and Figure 4-4, the single points outside the curves correspond to the yields of these additional experiments. Regarding the curve, the point at 80keV derived from "manip020710" is preferred because the associated statistical error is relatively low (see Appendix). The errors bars shown in the Figure 4-3 and Figure 4-4 are statistically calculated using the Gaussian relation ($\sigma = \sqrt{Np(1-q)}$, where N is the total number of events all channels together, p is the ratio of the events attributed to a given channel divided by the total number of events)

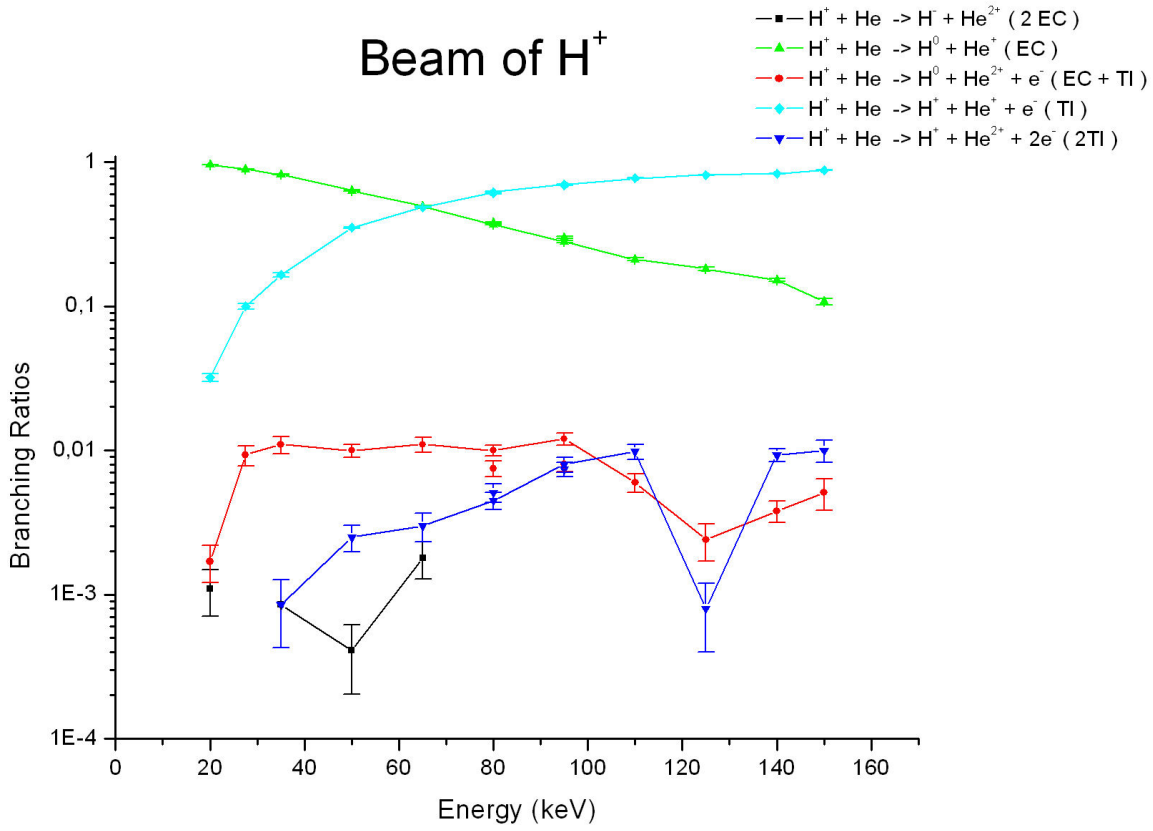

Figure 4-3 : Branching Ratios of the reactions observed by impact of protons. Two points are shown at 80keV and 95keV corresponding to experiments carried out on two separate dates.

Concerning the major processes $H^+ + He \rightarrow H + He^+$ (EC), $H^+ + He \rightarrow H^+ + He^+ + e^-$ (TI) for the proton-incidence and $H + He \rightarrow H + He^+ + e^-$ (TI), $H + He \rightarrow H^+ + He^+ + 2e^-$ (EL+TI) for the hydrogen atoms-incidence, the statistical errors are low and the points at 80keV and 95keV are found in very good agreement, it demonstrates the good reproducibility of the results concerning the relative cross sections.

For the minor processes, the statistical error bars are underestimated since the number of counts is very low: ~1800 reactions were registered in average for one experiment by proton impact, among them 15 counts are attributed in average to the process $H^+ + He \rightarrow H + He^{2+} + e^-$ (red curve in Figure 4-3), 10 counts are attributed in average to the process $H^+ + He \rightarrow H^+ + He^{2+} + 2e^-$ (blue curve in Figure 4-3), 1 or 2 counts only indicate that the process of double capture $H^+ + He \rightarrow H^- + He^{2+}$ does exist at the lowest energies (black points in Figure 4-3). The indication of the single points at 80keV and 95keV shows a good accord within error bars slightly bigger than the one calculated. The point at 125keV is in disaccord with the general tendency, for an unknown reason, very low counts were recorded for the minor processes during that experiment.

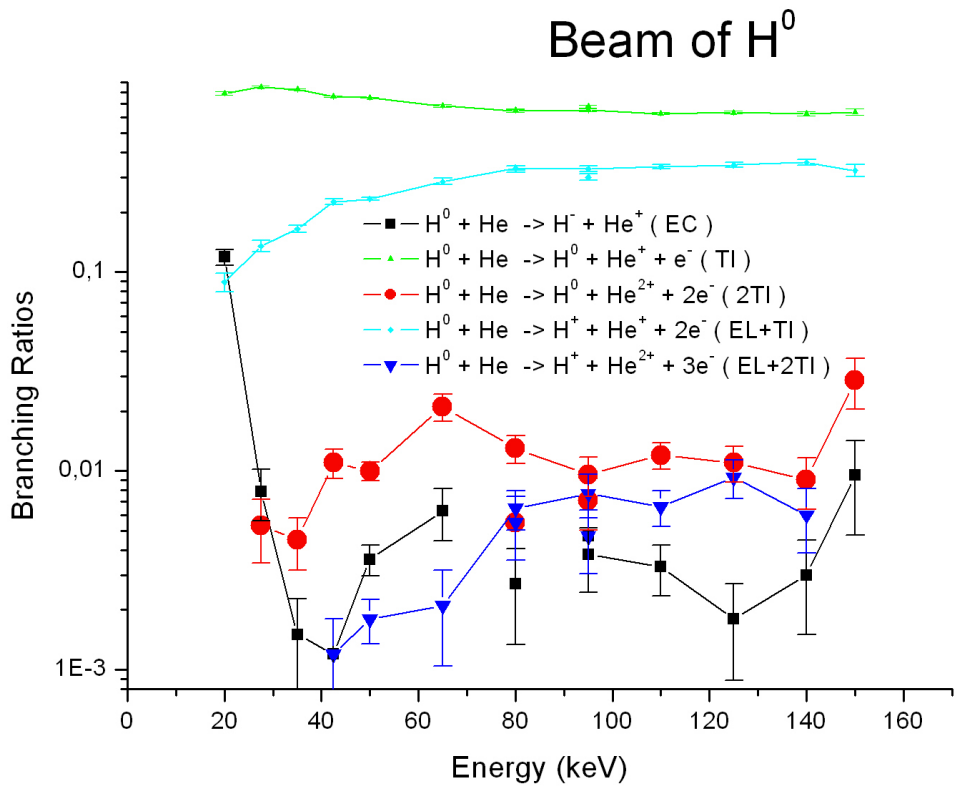

Figure 4-4 : Branching Ratios of the reactions observed by impact of hydrogen atoms. Two points are shown at 80keV and 95keV corresponding to experiments carried out on two separate dates.

The curves associated with the minor processes by hydrogen atoms impact have an erratic appearance due to very low statistics, the statistical errors must also be underestimated: ~620 reactions were registered in average during one experiment by hydrogen atoms impact, 6 counts in average go for the process $H + He \rightarrow H + He^{2+} + 2e^-$ (red curve in Figure 4-4), 2 or 3 counts in average for the process $H + He \rightarrow H^+ + He^{2+} + 3e^-$ (blue curve in Figure 4-4), 4 counts in average go for the process $H + He \rightarrow H^- + He^+$ (black curve in Figure 4-4). The results at 50keV are the most reliable since the intensity of the beam was very high lowering the statistical error for that experiment. At 20keV, the electronic capture process becomes as important as the simultaneous electron loss and target ionisation process ($H + He \rightarrow H^+ + He^+ + 2e^-$), it represents more than 10 per cent of the reactions counted (28 counts over 225 reactions counted in total). At 50keV, the electronic capture (EC) represents only 8 counts over 2225 that is to say 0.36 per cent of the counted reactions.

B. Collisions by protons impact

I) Normalization and Comparison with precedent studies

Published in an article of 1989, Shah et al presented the results of their experiments of proton-impact upon helium in a range of energy overlapping ours (9-100keV). They report high precision cross sections for the individual collision channels by using a cross beam experiment which incorporates a time of flight spectroscopy together with electron-ion and ion-ion coincidence counting of the collision products [40]. The coincidence system of their apparatus is shown in Figure 4-5 and described in more details in [31,32].

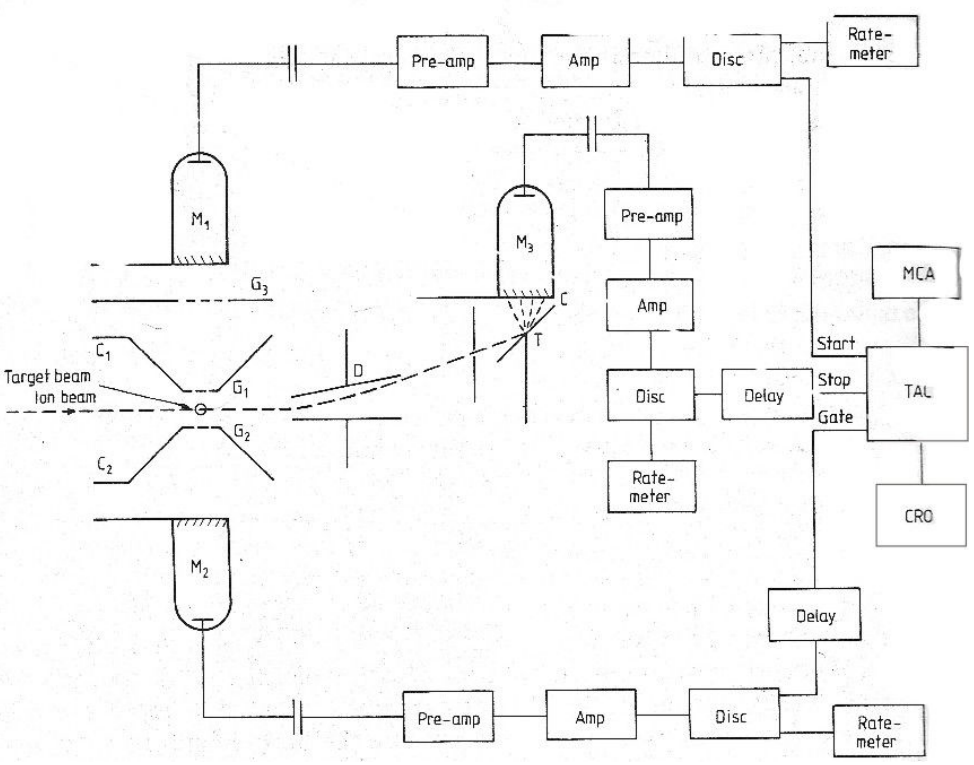

Figure 4-5: Schematic coincidence system of the apparatus of Shah et al [40].

We normalized our branching ratios with their total cross section after having extrapolated their curve for the highest energy values, the results are compared to their results in Figure 4-6. Only a few counts were attributed to the double capture process $H^+ + He \rightarrow H^- + He^{2+}$ in our experiments. This process was not observed by Shah et al and its contribution to the total absolute cross section is negligible. So it could be included in the calculation and an estimation of its magnitude could be obtained with respect to the other processes. The subject of the double electron capture is further developed in the next subsection (Part I : Chapter

4.B.II)).

Shah et al normalised their cross sections to previous high-energy measurements of single and double ionisation of helium by protons (50-2380keV) reported in [32]. The latter measurements were normalized to the well-established absolute cross sections for one-electron capture by protons in helium measured by Stier and Barnett with an accuracy believed to be within 5% [33].

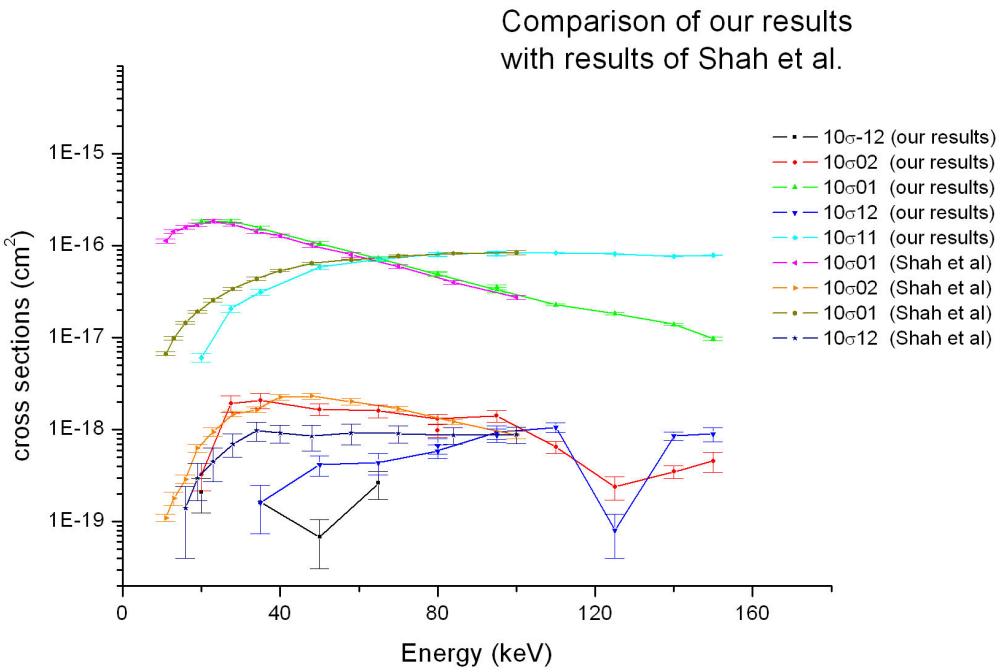

Figure 4-6 : Comparison between our results and the results of Shah et al [40]. The legend uses the usual notation for the processes: for instance, 10σ02 corresponds to the reaction $H^+ + He \rightarrow H + He^{2+} + e^-$ (CE+I).

The processes are compared by decreasing order of magnitude in the next Figure 4-7 and Figure 4-8. The disaccord increases with the decrease of cross section magnitudes due to the decrease of statistic quality. In Figure 4-7, the curves of the main processes $H^+ + He \rightarrow H + He^+$ (EC) and $H^+ + He \rightarrow H^+ + He^+ + e^-$ (TI) crosses at nearly the same point near 60keV. For energies higher than 50keV the two studies are in close agreement, whereas we observe a discrepancy in the results for the lower energies (42, 35, 27 and 20keV), our measurements lowered the yield of the ionization process with respect to process of electronic capture compared to the measurements of Shah et al [40].

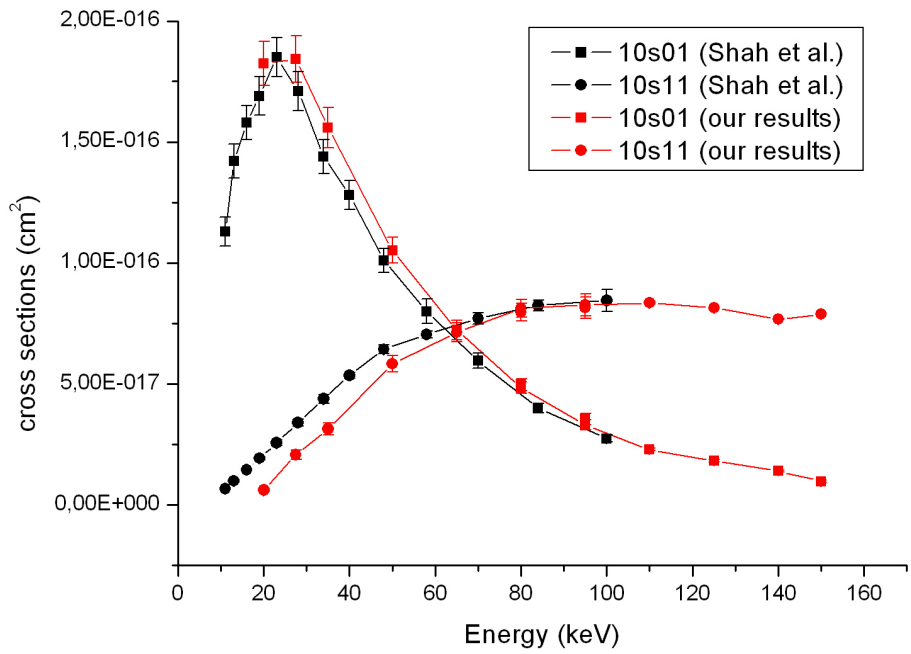

Figure 4-7 : Major processes. Comparison between our results and the results of Shah et al [40].

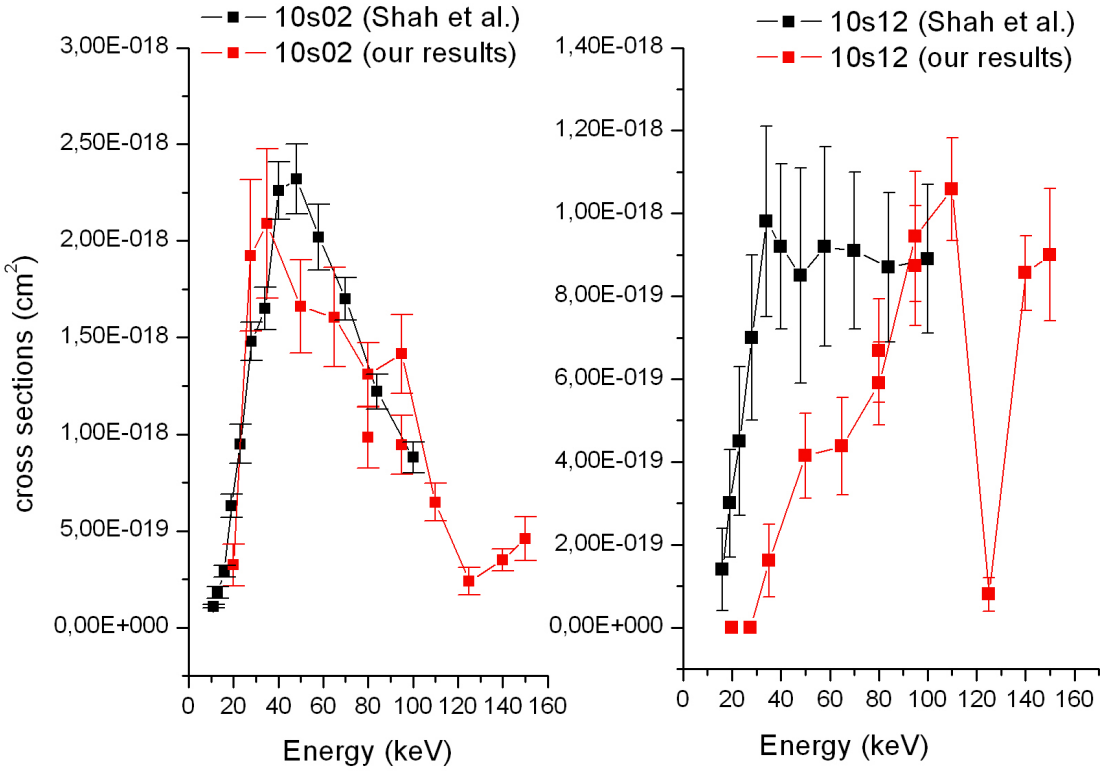

Figure 4-8 : Minor processes. Comparison between our results and the results of Shah et al [40]. The left graph shows the comparison for the process $H^+ + He \rightarrow H + He^{2+} + e^-$ (EC+TI), in the right graph are compared the yields for the process $H^+ + He \rightarrow H^+ + He^{2+} + 2e^-$ (2TI).

The comparison with the previous work of Shah shows good agreement for the channel $H^+ + He \rightarrow H + He^{2+} + e^-$, the red curve (our results) follows the black one (Shah et al) in the left graph of Figure 4-8, although the points of our curve were constituted by low statistics and the error bars are underestimated. We had too low statistics for the process $H^+ + He \rightarrow H^+ + He^{2+} + 2e^-$ (2I) at low energy in order to make a relevant comparison with the work of Shah (in the right graph of Figure 4-8), but the order of magnitude of the results becomes comparable at higher energies. We remark that Shah et al also determined big error bars for this last process.

II) Double electron capture

The events of double electron capture were the rarest during our experiments. In order to improve the statistics for this particular channel, experiments were performed again with a modified acquisition system set up to determine the coincidence between events from the signal received from the detection of H^-. However the results obtained were in agreement with the first one within the error bars. Our results are compared to previous investigations of the double electron capture by impact of protons on helium in Figure 4-9.

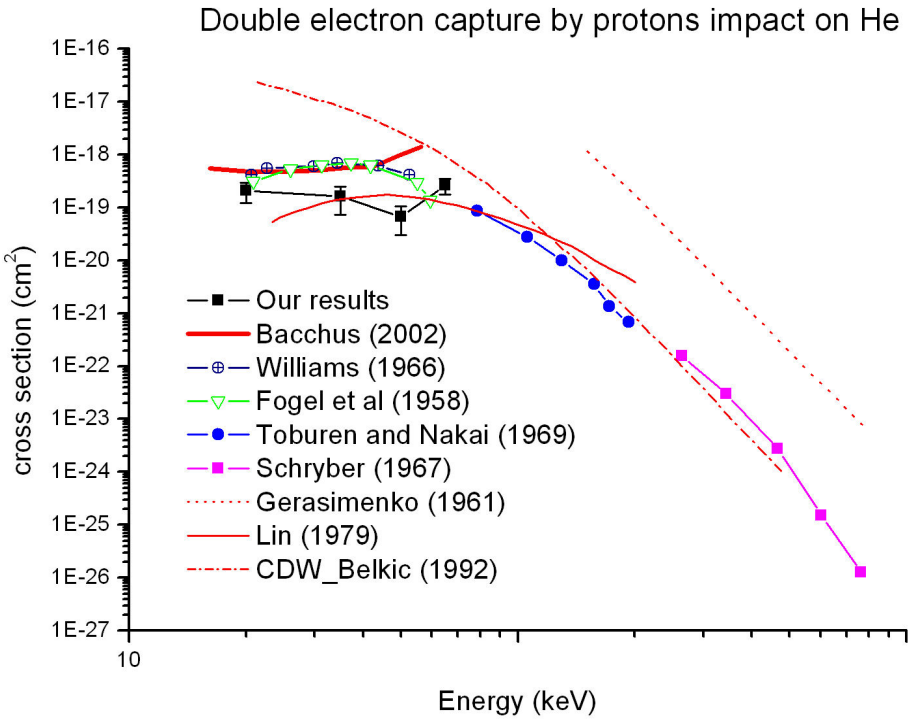

Figure 4-9: Comparison of our results with precedent works on the double electron capture by incidence of protons on Helium atoms. Red lines refer to various theoretical investigations.

A theoretical investigation was performed by M.C. Bacchus from the LASIM[1] with the intention of comparing with our results. Methods used for the calculation are presented in a special issue [34]. The agreement with precedent results from Fogel et al [35] and Williams [36] is very good over the range 20-50keV. Our results lie lower (factor 5) than the precedently cited experimental results [35,36], this underestimation of the process is to relate with the underestimation of the electron capture channel obtained by impact of hydrogen atoms (see Part I : Chapter 4.C.II) and might be due to some deficiency of the H^- detection channel. Other experimental results at higher energies are also shown in Figure 4-9 which reveal to be well described by the CDW model (continuum distorted wave approximation) proposed by Belkic [37]. Also shown in the Figure 4-9, the first theoretical investigation of the double capture was performed by Gerasimenko by the first Born approximation [38], but his results lie several order of magnitude away from the experimental results. As well are given some results of Lin [39], which used a three states two order close coupling approximation, with which our results are in closer agreement, but manifestly, the method of M.C. Bacchus is giving results in better agreement with the more reliable measurements of [35,36] over the range 50-80keV. All details on the various models of approximation cited for the theoretical calculations can be found in the books of Mc Daniel [13,14] and the book of Bransden and Mc Dowell [12].

To conclude, our branching ratios are in satisfying agreements with the branching ratios determined Shah et al. These results encourage us to give an estimation of absolute cross sections for the processes observed by impact of hydrogen atoms.

[1] Laboratoire de spectroscopie ionique et nucléaire.

C. Collisions by hydrogen atoms impact

I) Normalization of the cross sections for hydrogen atoms impact

Due to the quick succession between protons impact and hydrogen atoms impact measurements, it can be assumed that the target width remained constant after passing to collisions by hydrogen atoms impact. Under this assumption, we can write at every energy, $dN_H = N_H \Sigma_H d\varepsilon$ and $dN_{H^+} = N_{H^+} \Sigma_{H^+} d\varepsilon$, where dN corresponds to the total number of events leading to the formation of ionized helium by impact of hydrogen atoms (dN_H) or by impact of protons (dN_{H^+}); and N corresponds to the total number of incident particles of the beam, Σ refers to the total absolute cross sections of helium ionizations by impact of hydrogen atoms (Σ_H) and by impact of protons (Σ_{H^+}) ; if we pose $\alpha = \frac{dN}{N}$, we deduce the relation:

$$\Sigma_H = \frac{\alpha_H}{\alpha_{H^+}} \Sigma_{H^+} . \qquad 4\text{-}1$$

Energy by energy, we normalized our branching ratios calculated for the hydrogen atoms impact channels to the total cross section of ionization Σ_H determined by the relation 4-1 using the total cross section for helium ionization Σ_{H^+} determined by Shah et al in [40], and we can derive for every channel an estimated absolute cross section for the processes by hydrogen atoms impact. The results are tabulated in Table 2 and drawn in Figure 4-10.

Energy (keV)	Σ_{H+} (derived from Shah)	$K=(\alpha_H/\ \alpha_{H+})$	Σ_H (calculated)
20	1,90E-16	0,06494	1,23E-17
27,5	2,07E-16	0,20055	4,15E-17
35	1,90E-16	0,22338	4,24E-17
42,5	1,80E-16	--	--
50	1,66E-16	0,27871	4,63E-17

65	1,46E-16	0,29922	4,37E-17
80	1,31E-16	0,34551	4,53E-17
95	1,18E-16	0,38007	4,48E-17
110	1,08E-16	0,39069	4,22E-17
125	1,00E-16	0,29767	2,98E-17
140	9,20E-17	0,48117	4,43E-17
150	9,00E-17	0,1967	1,77E-17
--	--	--	--
80	1,31E-16	0,42297	5,54E-17
--	--	--	--
95	1,18E-16	0,25133	2,97E-17

Table 2: Table of calculation of the total absolute cross section for the hydrogen impact Σ_H.

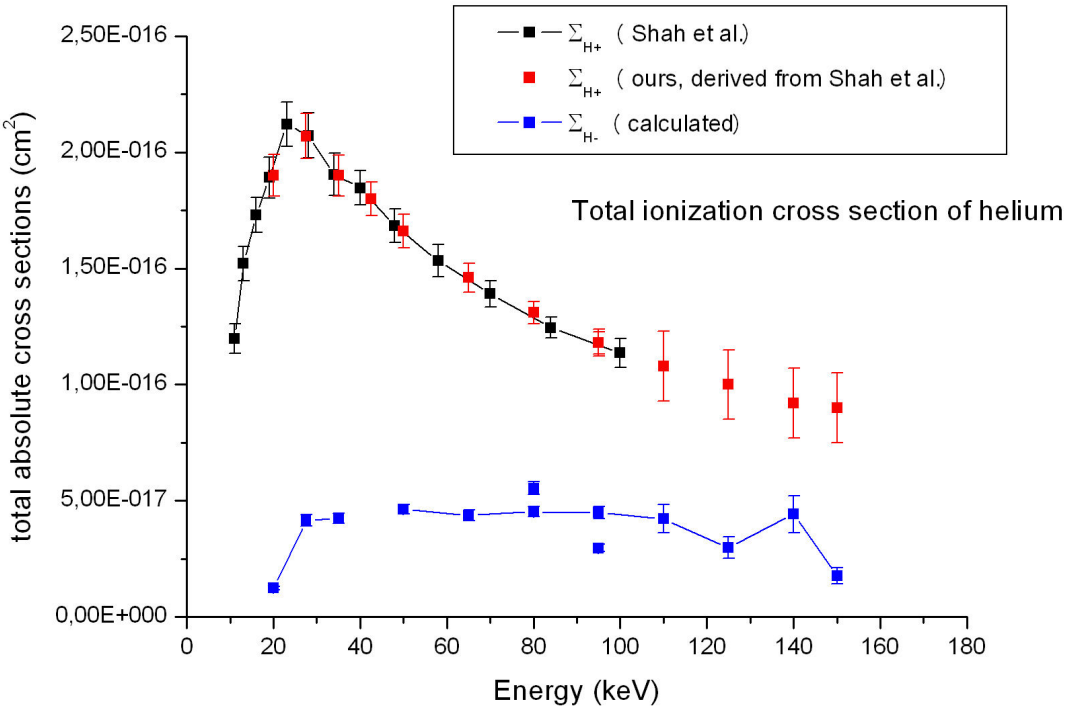

Figure 4-10 : Derivation of the total absolute cross section of helium ionization by impact of hydrogen atoms.

The energy range in the study by Shah et al extends from 11keV to 100keV. Since

our energy range goes until 150keV we needed to extrapolate the curve of total absolute cross section Σ_{H^+} towards higher energies, for the derivation of the total cross section for the processes by hydrogen atoms impact. We put larger error bars for these points (110-150keV) to account for the incertitude of the extrapolation. Statistical error bars were calculated for the derivation of the total cross section for hydrogen impact, the disaccord of the points at 80 and 95keV shows that the error bars are underestimated.

However the general shape of the curve shows a nice regularity. The Figure 4-11 shows the final results of our estimated absolute cross sections for the processes by hydrogen impact.

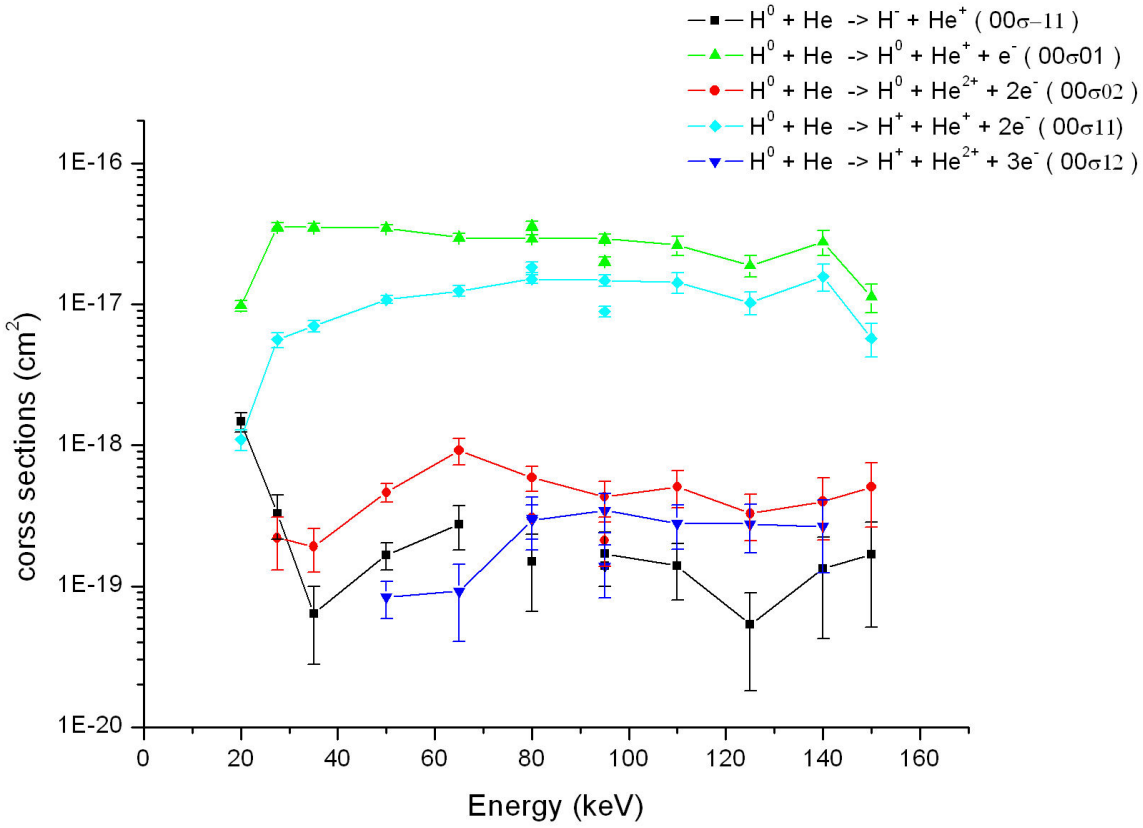

Figure 4-11 : Estimation of the absolute cross sections for the processes registered by impact of hydrogen on a He gas target.

Above 80keV, the magnitude of the processes becomes roughly constant: we found a mean cross section of 2.5×10^{-17}cm^2 (65% of Σ_H) for the single ionisation H + He→ H + He^+ + e^-, an average of 1.3×10^{-17}cm^2 (35% of Σ_H) for the simultaneous electron loss and ionization H + He→ H^+ + He^+ + 2e-. About 1% of the total cross section, i.e. 4×10^{-19}cm^2 represents the magnitude for the reaction H + He→ H + He^{2+} + 2e-. In the same order of magnitude (0.7% of Σ_H), the cross section of the double ionizations with simultaneous electron loss H + He→ H^+ + He^{2+} + 3e- is found near 2.4×10^{-19}cm^2 in average. Finally, the electronic capture becomes

negligible at higher energies; we found an approximate order of magnitude of $1.3\times10^{-19}cm^2$.

II) Comparison with previous studies:

There were some experimental studies on the impact of hydrogen atoms onto helium, but few of them overlap with the range of our study, which extends in the intermediate energy range from 10 to 150keV, most of them were performed at higher energies up to 2Mev. The Figure 4-12 compares the results concerning the total single ionization cross sections obtained by the the different research groups so far, to the extent of our knowledge.

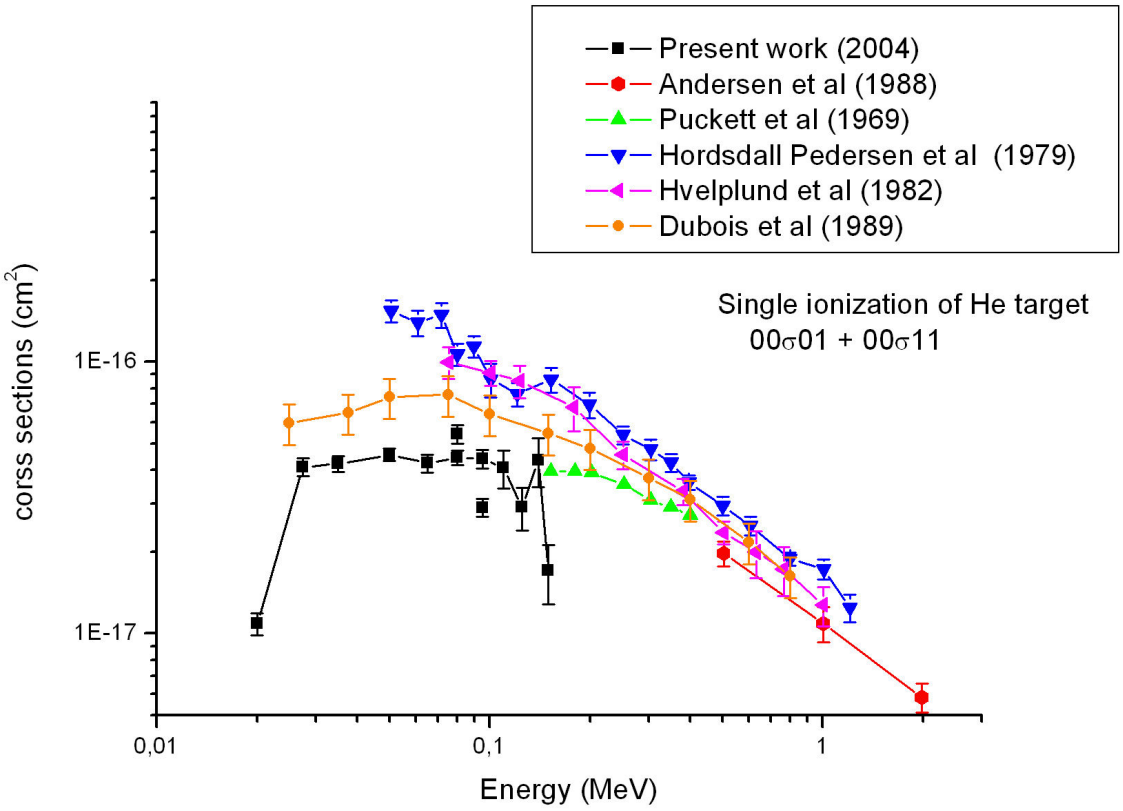

Figure 4-12 : Single ionization of helium target from different authors.

In Figure 4-12, the most evident is that our estimated cross sections are considerably smaller than the cross sections previously determined by Hordsdal Pedersen and al [8] and Hvelplund et al [9] at low energy (20-100keV). We confirm a lower magnitude for the single ionization processes as determined by the latest study from Dubois et al [6]. The estimation of our cross sections lies even lower than those of Dubois by roughly a factor 2/3. However, the estimation of Puckett et al [7] for the energy range 150-400keV is in the continuity of our estimated cross sections.

It is difficult to give the reasons of the discrepancies appearing at low energies

between the studies shown in Figure 4-12. Above 200keV all precedent studies come in better agreement. Dubois et al estimated their experimental uncertainties to 17%, no other studies of the hydrogen atoms impact on helium were found in the literature over the energy range 20-100keV to allow further comparison. All studies presented in Figure 4-12 used a combined time of flight and coincidence technique similar to our apparatus, with the exception of Puckett et al [7] who used the "condenser method" (see [13]) by measuring the current of the primary H beam current as well as electrons and target ions produced in the region of collisions.

Horsdal Perdersen et al [8] they were particularly interested by measuring the simultaneous ionization of the target and projectile in H+He and H+Xe 50-1200keV collisions for a comparison with theoretical work in the high-energy range.

Above a few MeV the negative hydrogen ions are used as a source beam and converted into the neutral hydrogen atom by the stripping reactions whose cross section are considerably larger than those for the electron capture by proton [41]. This technique was used by Andersen et al for their study up to 2MeV.

The latest study was performed by Dubois et al [6], their experiment was very similar to the one performed in Lyon, measuring the target ions in coincidence with the projectile ions yielded relative probabilities for single- and double-target ionization resulting from direct ionization or electron transfert. A schematic drawing of their apparatus is shown in Figure 4-13.

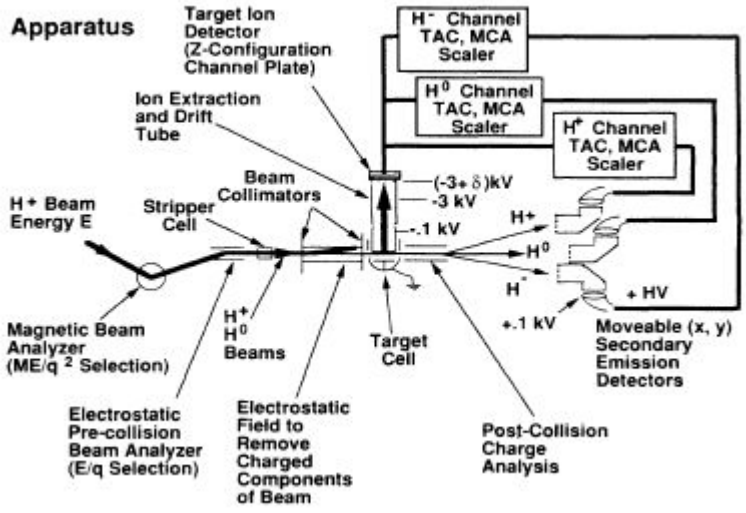

Figure 4-13: Experimental set-up used by Dubois et al [6] for their study of charge changes phenomena in the collision of hydrogen atoms on helium.

Their charge exchange cell placed after the pre-collision beam analyser was filled by

air to a pressure of several mTorr; they mentioned that beam neutralization also occurred in the beamline which had a pressure of (0.2-2) $\times 10^{-5}$Torr depending on the pressure inside the cell of neutralization. They consider that the probability that the projectile-ion charge states were altered due to collisions with background gases was negligible, with regard to the pressure in the chamber <0.01mT. For comparison, we measured a higher pressure of about 1.5×10^{-4}Torr along the beam line close to the neutralization cell during our experiments. We concluded from the analysis of the beam composition done in Part I : Chapter 3.A that collisions with the background gas are frequent in our experiment since the hydrogen beam contained more than 3% of protons probably produced by collisions with the background gas. Dubois et al used air as neutralization gas whereas we used helium for most of the experiments: the cross sections of single electron capture by protons from N_2 and O_2 are slightly higher than from helium, they are compared in Figure 4-14. As a consequence, we had to work at higher pressure of neutralization's cell to compensate for the smaller cross sections of electron capture from helium. We choose helium for reducing the presence of metastable hydrogen atoms H (2s) in the beam of interaction: cross sections for formation of H (2s) at 16keV (~ maxima of the cross sections) by electron capture from various targets were estimated in [30] and the results are given in Table 3.

Target	Ar	He	N_2	O_2
$\sigma(cm^2)$ at 16keV ($\times 10^{-17}\pm 8\%$)	3.10	0.156	3.41	2.86

Table 3: Estimations from [30] of cross sections for capture into the H (2s) state at 16keV for different gases of interest in our study.

Dubois et al used electrostatic field of 400 to 2000V/cm to quench the long-lived excited states of hydrogen atoms formed in the neutralization cell (H(2s)), and they were confident that the hydrogen atoms beam was purely made of H(1s). We also estimated that the fraction of metastable atoms in our beam of hydrogen atoms was very low (Part I : Chapter 3.A.III))

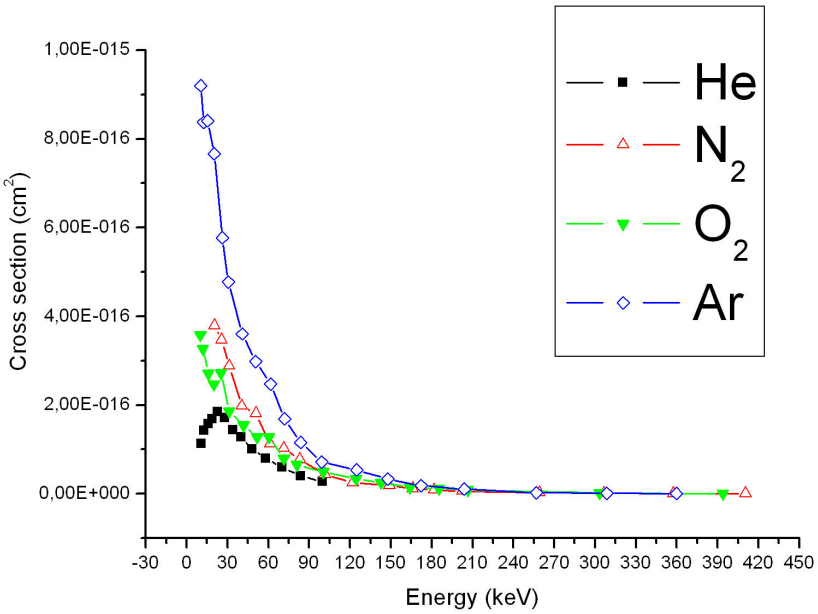

Figure 4-14: Comparison of single electron capture cross sections by protons from different gases of interest for the study.

The location of their deflection plates (used as quenching plates as well) between the beam collimators, lead to contamination of their hydrogen atoms beam by protons (F_1=7%) due to slit edge stripping of the neutral projectiles on the exit collimator. They corrected their determined cross sections by calculating the contribution of the fraction of the protons.

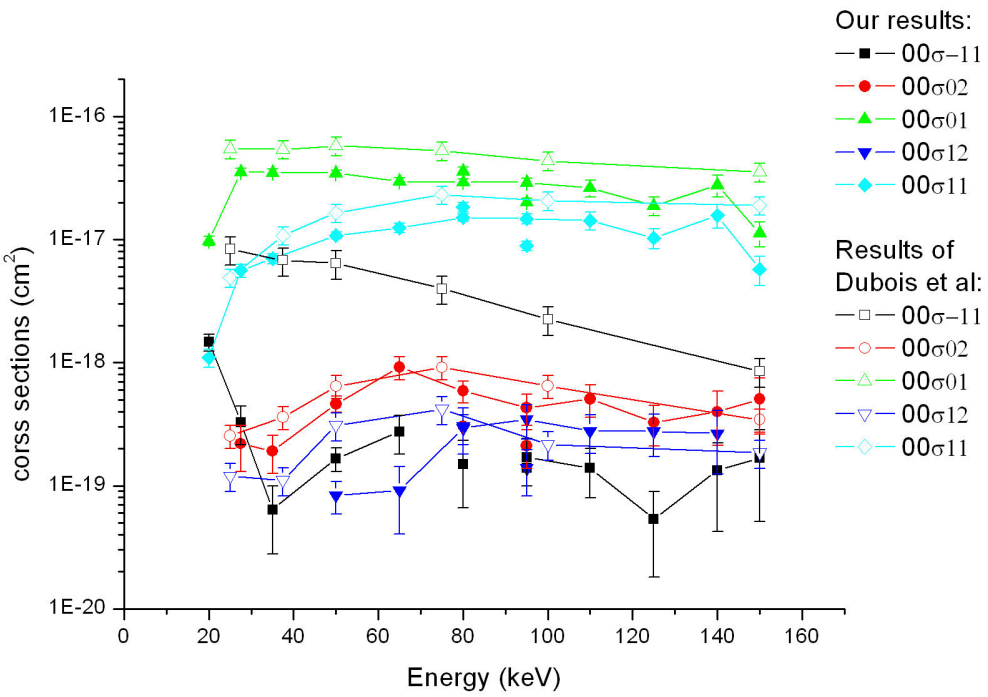

Figure 4-15: Comparison of our results with the results of Dubois et al.

The single ionization of the target with or without ionization of the projectile

constitutes the major processes for the impact by hydrogen atoms. Our results lie systematically under the results of Dubois et al, but have the same tendency.

The most evident from this comparison is that we have underestimated the electron capture channel $_{00}\sigma_{-11}$. It can be probably attributed to a deficiency of the detection of the H^- projectiles generally during our experiments. We could also observe in Part I : Chapter 4.B.II) that we determined double capture cross sections smaller than the results of the other authors probably for the same reason. Moreover, Dubois et al measured processes of electron capture by the incident hydrogen atoms with double ionization of the helium target $_{00}\sigma_{-12}$, which we didn't detect. But we should have detected some since Dubois et al determine a cross section of the order of $2\times10^{-19}cm^2$ for this process.

The other minor processes of double ionization of the target with or without ionization of the projectile ($_{00}\sigma_{12}$ and $_{00}\sigma_{02}$) are in satisfying agreement between the two studies.

D. Conclusion

These studies were performed as a general test of the functioning of the apparatus before going to more complex systems. The satisfying agreement obtained with previous studies of Shah et al [40] and Dubois et al [6] for the impact respectively of H^+ and H on helium is favorable for a pursuit of the studies.

In particular, the processes of ionizations in hydrogen impact on helium is confirmed to have a lower magnitudes than previous older studies by Hordsdal Pedersen and al [8] and Hvelplund et al [9] in the intermediate energy range, as already determined by the latest study from Dubois et al [6].

Examples of beam characteristics profiles

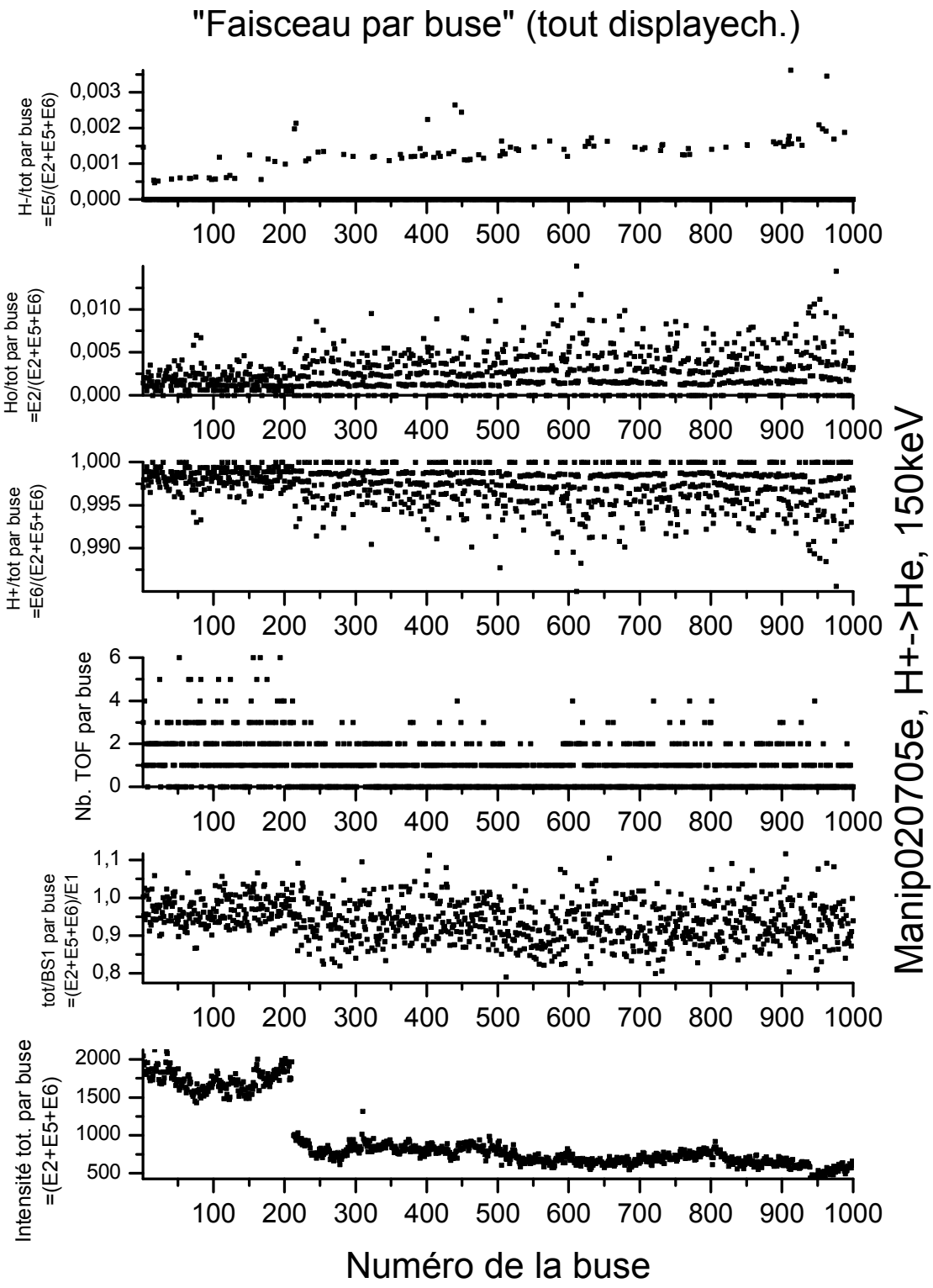

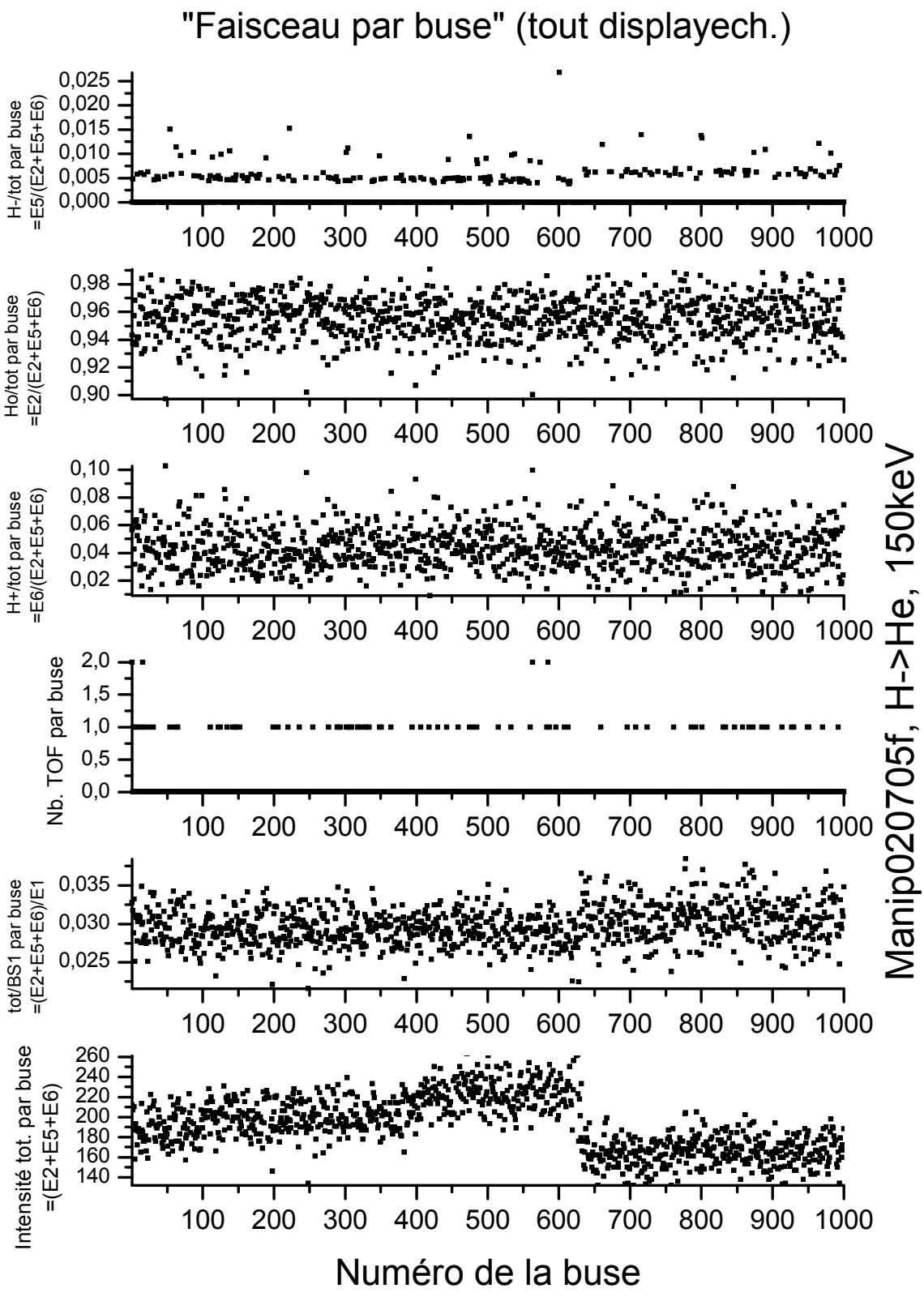
"Faisceau par buse" (tout displayech.)
H-/tot par buse =E5/(E2+E5+E6)
Ho/tot par buse =E2/(E2+E5+E6)
H+/tot par buse =E6/(E2+E5+E6)
Nb. TOF par buse
tot/BS1 par buse =(E2+E5+E6)/E1
Intensité tot. par buse =(E2+E5+E6)
Numéro de la buse
Manip020705f, H->He, 150keV

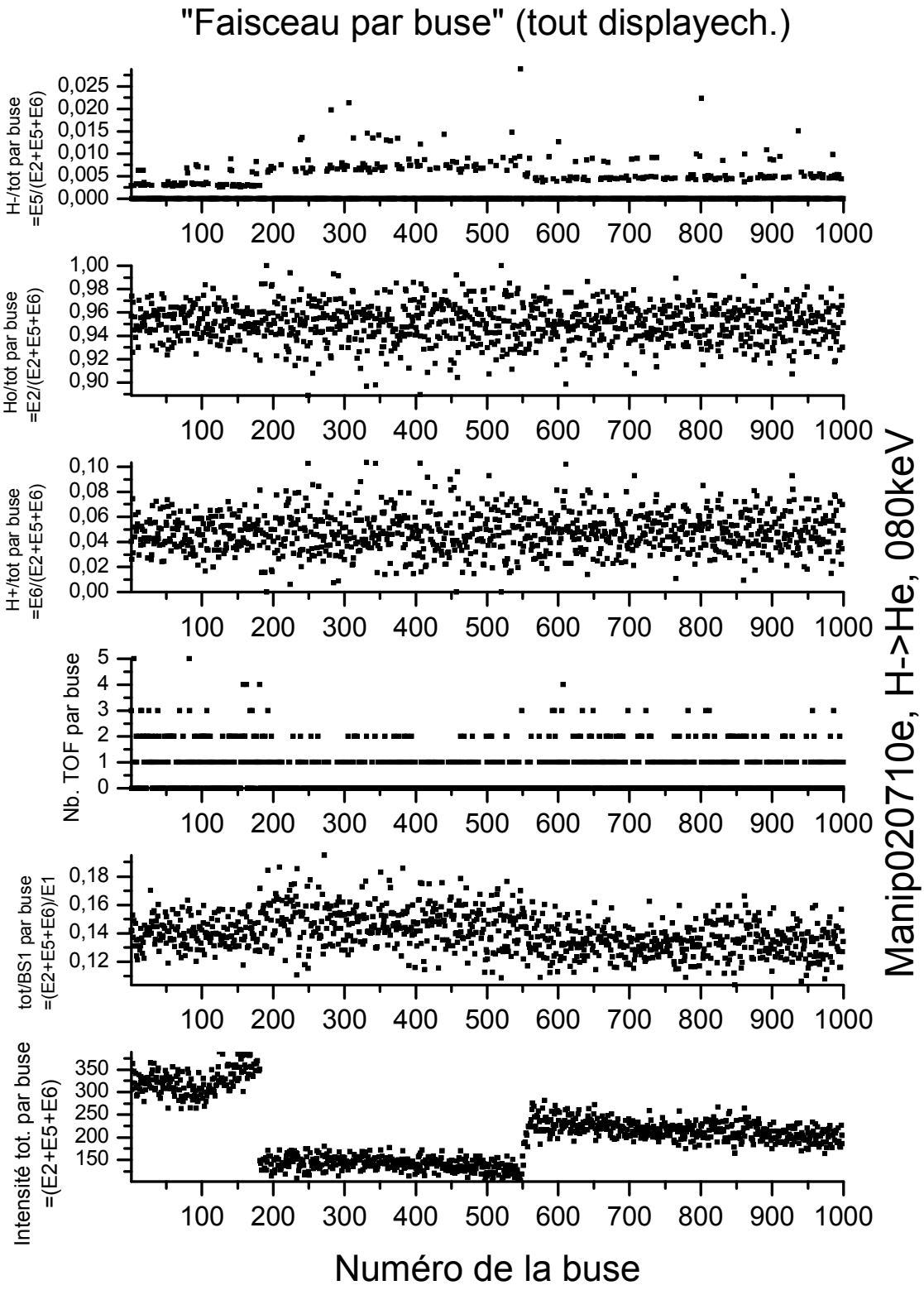
"Faisceau par buse" (tout displayech.)
H-/tot par buse =E5/(E2+E5+E6)
Ho/tot par buse =E2/(E2+E5+E6)
H+/tot par buse =E6/(E2+E5+E6)
Nb. TOF par buse
tot/BS1 par buse =(E2+E5+E6)/E1
Intensité tot. par buse =(E2+E5+E6)
Numéro de la buse
Manip020710e, H->He, 080keV

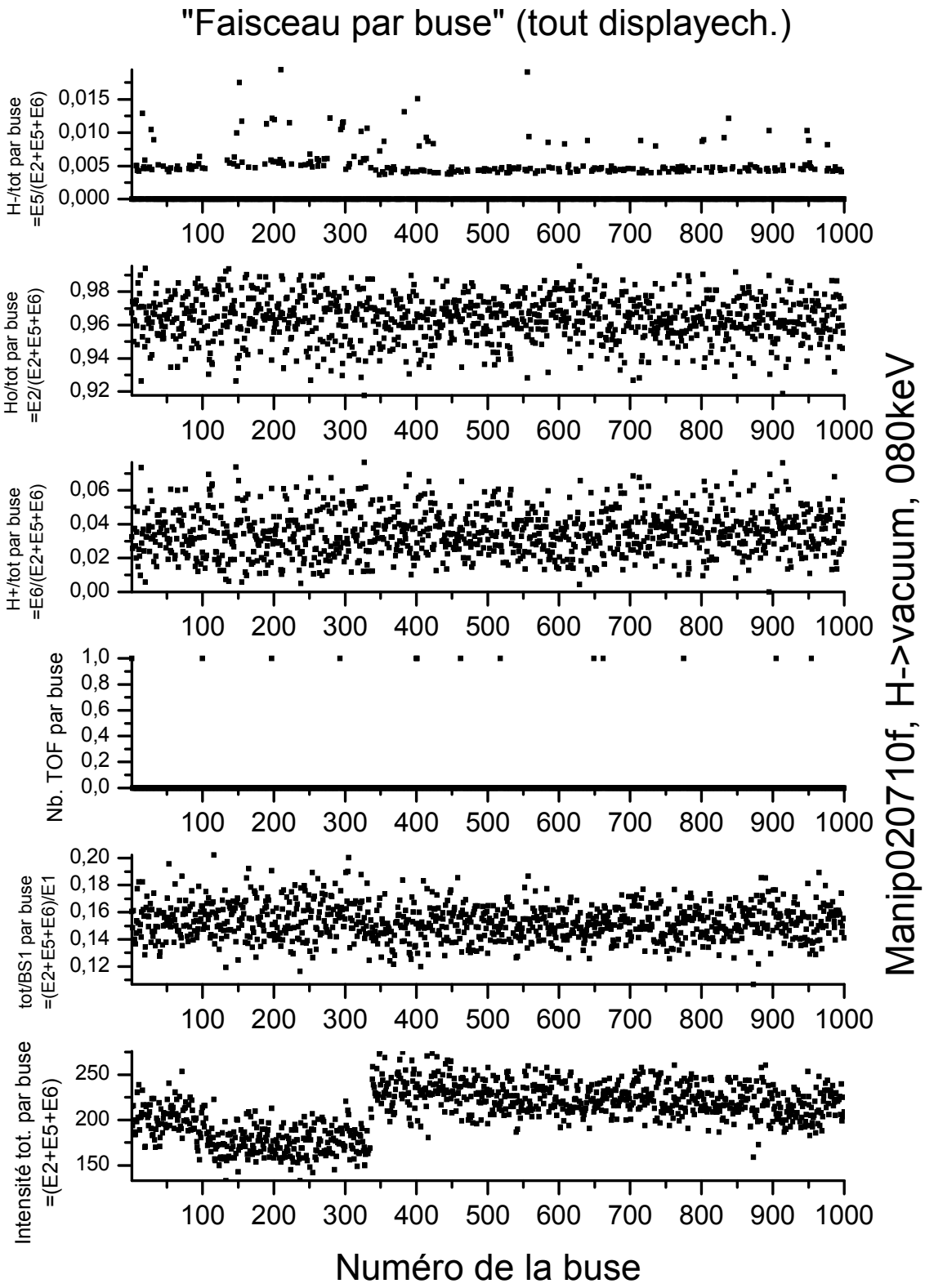
"Faisceau par buse" (tout displayech.)
H-/tot par buse =E5/(E2+E5+E6)
Ho/tot par buse =E2/(E2+E5+E6)
H+/tot par buse =E6/(E2+E5+E6)
Nb. TOF par buse
tot/BS1 par buse =(E2+E5+E6)/E1
Intensité tot. par buse =(E2+E5+E6)
Numéro de la buse
Manip020710f, H->vacuum, 080keV

Results experiment by experiment

- **Experiments at 80keV**

E=80keV, Manip020708k			
Reaction channel	Nb Of events	Branching ratios	Position of Peak
$H^+ + He \rightarrow H^- + He^{2+}$	0		
$H^+ + He \rightarrow H^0 + He^+$	814	0.379	782.5
$H^+ + He \rightarrow H^0 + He^{2+} + e^-$	16	7.5e-3	502.5
$H^+ + He \rightarrow H^+ + He^+ + e^-$	1305	0.608	777.5
$H^+ + He \rightarrow H^+ + He^{2+} + 2e^-$	11	5.1e-3	497.5
Total	2146		

Target: P0~25mb, U0=8.64V;

Total number of incident H^+=446348; α_{H+}=0.0048

Diagnostic of reclassification:

- 0.4 % of events not classified
- 1368 events coincident with H^+
- 848 events coincident with H

E=80keV, Manip020708l			
Reaction channel	Nb Of events	Branching ratios	Position of Peak
$H^0 + He \rightarrow H^- + He^+$	1	2.7e-3	772.5
$H^0 + He \rightarrow H^0 + He^+ + e^-$	236	0.65	782.5
$H^0 + He \rightarrow H^0 + He^{2+} + 2e^-$	2	5.5e-3	502.5
$H^0 + He \rightarrow H^+ + He^+ + 2e^-$	119	0.33	777.5
$H^0 + He \rightarrow H^+ + He^{2+} + 3e^-$	2	5.5e-3	502.5
Total	360		

Target: P0~25mb, U0=8.64V;

Total number of incident H^0=177025; α_H=0.002

Diagnostic of reclassification:

- 0.5 % of events not classified
- 123 events coincident with H^+
- 252 events coincident with H

E=80keV, Manip020710c			
Reaction channel	Nb Of events	Branching ratios	Position of Peak
$H^+ + He \rightarrow H^- + He^{2+}$	0		
$H^+ + He \rightarrow H^0 + He^+$	1144	0.37	787.5
$H^+ + He \rightarrow H^0 + He^{2+} + e^-$	32	0.01	502.5
$H^+ + He \rightarrow H^+ + He^+ + e^-$	1917	0.62	782.5
$H^+ + He \rightarrow H^+ + He^{2+} + 2e^-$	14	4.5e-3	502.5
Total	3107		

Target: P0~30mb, U0=8.9V;

Total number of incident H^+=431318; α_{H+}=0.0072

Diagnostic of reclassification:

- 1 % of events not classified
- 2027 events coincident with H^+
- 1210 events coincident with H

E=80keV, Manip020710de			
Reaction channel	Nb Of events	Branching ratios	Position of Peak
$H^0 + He \rightarrow H^- + He^+$	0		
$H^0 + He \rightarrow H^0 + He^+ + e^-$	478	0.646	782.5
$H^0 + He \rightarrow H^0 + He^{2+} + 2e^-$	10	1.3e-2	507.5
$H^0 + He \rightarrow H^+ + He^+ + 2e^-$	247	0.334	777.5
$H^0 + He \rightarrow H^+ + He^{2+} + 3e^-$	5	6.6e-3	497.5
Total	740		

Target: P0~35mb, U0=8.85V (manip020710d), P0~60mb, U0=9.01V (manip020710e);

Number of incident H^0: N=89487 (manip020710d), N=207831 (manip020710e);

Total number of incident H^0=297318; α_H=0.0025

Diagnostic of reclassification:

- 2.3 % of events not classified
- 270 events coincident with H^+
- 510 events coincident with H

- **Experiments at 95keV**

E=95keV, Manip020711q			
Reaction channel	Nb Of events	Branching ratios	Position of Peak
$H^+ + He \rightarrow H^- + He^{2+}$	0		
$H^+ + He \rightarrow H^0 + He^+$	622	0.28	812.5
$H^+ + He \rightarrow H^0 + He^{2+} + e^-$	27	0.012	532.5
$H^+ + He \rightarrow H^+ + He^+ + e^-$	1570	0.7	807.5
$H^+ + He \rightarrow H^+ + He^{2+} + 2e^-$	18	0.008	522.5
Total	2237		

Target: P0~60mb, U0=9.01V;

Total number of incident H^+=299454; α_{H+}=0.0075

Diagnostic of reclassification:

- 0.8 % of events not classified
- 1653 events coincident with H^+
- 673 events coincident with H

E=95keV, Manip020711r			
Reaction channel	Nb Of events	Branching ratios	Position of Peak
$H^0 + He \rightarrow H^- + He^+$	2	3.8e-3	822.5
$H^0 + He \rightarrow H^0 + He^+ + e^-$	338	0.65	812.5
$H^0 + He \rightarrow H^0 + He^{2+} + 2e^-$	5	9.6e-3	527.5
$H^0 + He \rightarrow H^+ + He^+ + 2e^-$	170	0.33	807.5
$H^0 + He \rightarrow H^+ + He^{2+} + 3e^-$	4	7.7e-3	527.5
Total	519		

Target: P0~70mb, U0=9.05V;

Total number of incident H^0=182798; α_H=0.0028

Diagnostic of reclassification:

- 1.7 % of events not classified
- 177 events coincident with H^+
- 362 events coincident with H

E=95keV, Manip020704o			
Reaction channel	Nb Of events	Branching ratios	Position of Peak
$H^+ + He \rightarrow H^- + He^{2+}$	0		
$H^+ + He \rightarrow H^0 + He^+$	724	0.3	817.5
$H^+ + He \rightarrow H^0 + He^{2+} + e^-$	20	0.008	537.5
$H^+ + He \rightarrow H^+ + He^+ + e^-$	1661	0.69	807.5
$H^+ + He \rightarrow H^+ + He^{2+} + 2e^-$	18	0.0074	522.5
Total	2423		

Target: P0~10 Torr;

Total number of incident H^+=641867; α_{H+}=0.0038

Diagnostic of reclassification:

- 1 % of events not classified
- 1744 events coincident with H^+
- 756 events coincident with H

E=95keV, Manip020704p			
Reaction channel	Nb Of events	Branching ratios	Position of Peak
$H^0 + He \rightarrow H^- + He^+$	2	4.7e-3	812.5
$H^0 + He \rightarrow H^0 + He^+ + e^-$	286	0.68	812.5
$H^0 + He \rightarrow H^0 + He^{2+} + 2e^-$	3	7.1e-3	527.5
$H^0 + He \rightarrow H^+ + He^+ + 2e^-$	127	0.3	807.5
$H^0 + He \rightarrow H^+ + He^{2+} + 3e^-$	2	4.7e-3	512.5
Total	421		

Target: P0~10 Torr;

Total number of incident H^0=443739; α_H=0.001

Diagnostic of reclassification:

- 2.1 % of events not classified
- 133 events coincident with H^+
- 299 events coincident with H

Concluding remarks / Introducing Part II

One of the purposes of this study on the collision system of H^+/H impact on helium was to perform a general test of functioning of the apparatus before investigating more complicated systems. Indeed, collisions with molecular target involve fragmentations, which are more difficult to handle experimentally, due to the greater complexity of the coincident events when the molecules splits in several fragments and the kinetic energy released during the fragmentation. The helium atomic target avoids these difficulties.

The agreement with the works of Shah et al [40] and Dubois et al [6] are satisfying, and we found explanations for the eventual disagreements. So the first objective of the study was successful.

Furthermore helium was chosen for this study because there have been very few previous studies carried out upon hydrogen atoms collisions with helium by the techniques of coincidence. The study of Dubois et al [**6**] is the only found in the literature which covers the intermediate energy range (20-150keV). Indeed, the range of energy of our experiments goes from 20 to 150keV, coinciding with the domain of energy of the Bragg peak but also the range of energy giving the more difficulties to the theoreticians. Our measurements provide another set of cross sections of reference which can constitute interesting information for the theoreticians since the system H + He is already a complex system (2 nuclei and three electrons) difficult to handle theoretically in particular in this energy range.

However, as already discussed in (Part I : Chapter 1.C.V)), the simple collision systems are of phenomenological interest and many results, which can be studied theoretically only for these systems, can be extended to more complex systems. To some extent it is even possible to derive some scaling laws between cross sections of various systems (Toburen, [1]).

In this first part of this thesis we considered the conjugated ionizing action of proton and hydrogen atoms on single atoms of helium in the gas phase. When such a charged particle enters a solid, it produces by its primary ionizing action a distribution of excited atoms and molecules, ions and secondary electrons. These latter species are created in large quantities and carry most of the energy of the fast primary radiations. Secondary electrons have low energies with a distribution lying essentially below 70eV and a most probable energy around 10eV (Bernardi [42], Sanche [43]). At those energies electrons have their highest cross

sections for interaction with atoms and molecules. Hence they interact rapidly in the irradiated medium, where they generate very reactive species which initiate chemical reactions.

Water is of particular interest for the radiobiology since it is the principal constituant of our organisms. The electron attachment to water molecule occurs in the energy range 5 to 15eV, corresponding to the most probable range of ejected electrons following the primary collisions of primary heavy ion radiations. The dissociation of the water molecule follows immediately the electron attachment, according to three dissociation channels leading to the formation of ions H^-, O^- and OH^-. By ion-molecules reaction other molecule of water, H^- and O^- form hydroxyl ions OH^- and free radicals $OH^\bullet$ which diffuse and might attack the macromolecules in the cells. This indirect effect of the primary radiation is dominant for the diffusion of the ionizing radiation in the cells of our organism.

A review of the dissociative electron attachment to water was undertaken at the University of Innsbruck motivated by the existing discrepancies between old studies on the same subject. For this study we used the trochoïdal monochromator of the University of Innsbruck. A beam of effusive water vapor was crossing a monochromatized beam of electrons in the energy range 5-15eV. The determination of the electron energy distribution is of fundamental importance for this apparatus and is the subject of the first chapter of this study. The ions resulting from the beam crossing region were then extracted into a quadrupole mass filter, and then detected. The liberation of high kinetic energy fragment ions (H^-, O^-, OH^-) from the dissociation of water necessitates giving a particular attention to the problem of discrimination in the trochoïdal monochromator used for this study. It is developed in chapter 2. Our final results and other investigations on the dissociative electron attachment to water and heavy water are discussed in the chapter 3.

Part II : Study of the dissociative electron attachment to water with the trochoïdal electron monochromator (Innsbruck)

Chapter 1. Trochoïdal electron monochromator.

A. Overview

The experimental Set-up is called a trochoidal electron monochromator (TEM), it has been designed to study the ions yield from the interaction between a gaz of molecules and a beam of electron having a definite energy within a narrow resolution (~ 0.1eV).

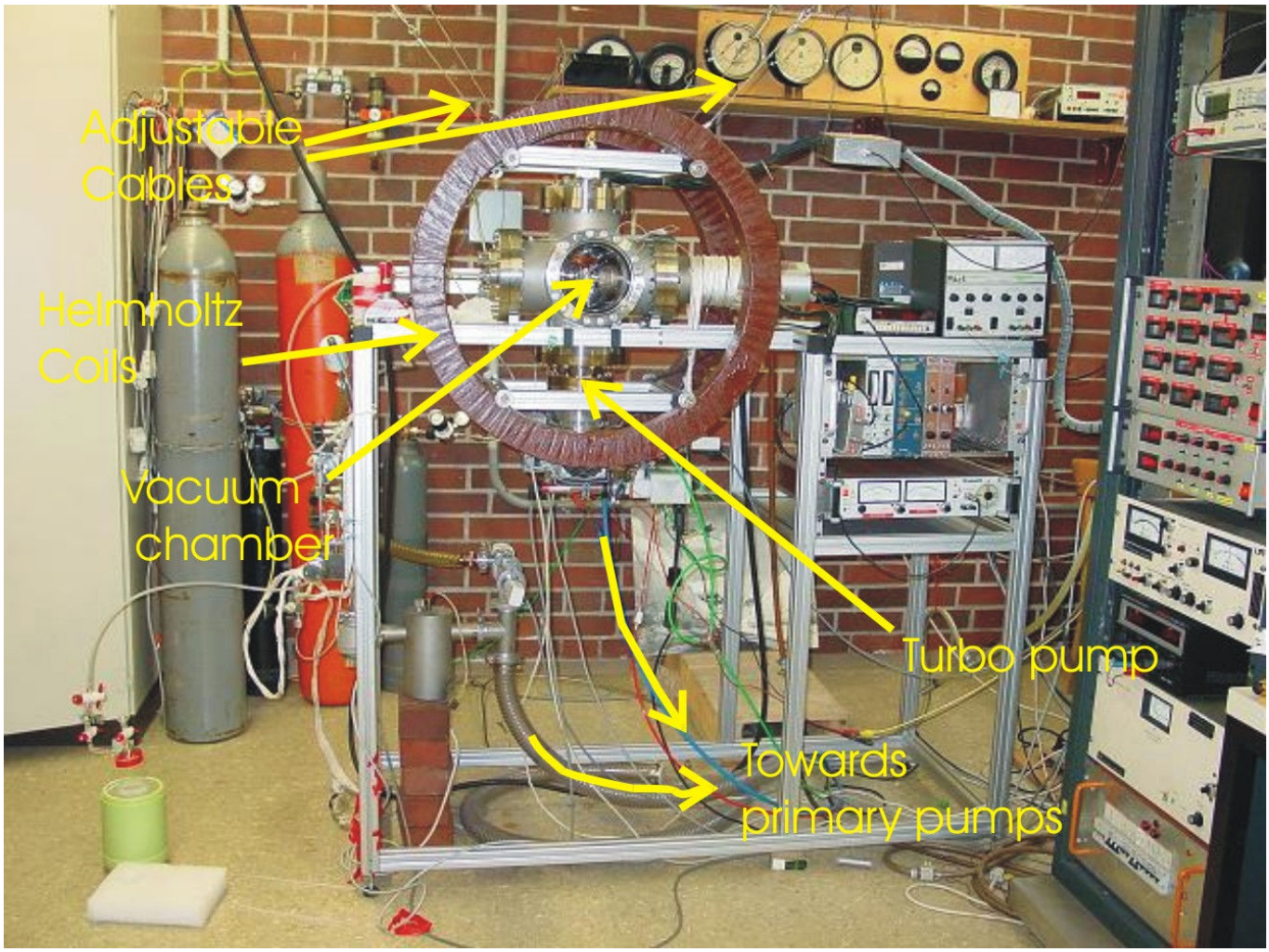

Figure 1-1: **Overview of the experimental setup.**

The photo of Figure 1-1 shows the complete setup.

The monochromator is placed inside a vacuum chamber. A molecular turbo pump with a pumping speed of 300 l/s maintains a vacuum down to 10^{-8}mbar inside the chamber, the primary pumps are installed in the next room to avoid noise nuisance.

Specifically, the gas inlet will be described in the last chapter in the part describing the experimental realization of the experiments with water, the monochromator and its functioning will be described in the following of this chapter, the detection system and the quadrupole mass filtering will be described in the next chapter concerning the study of the discrimination along the way to detection.

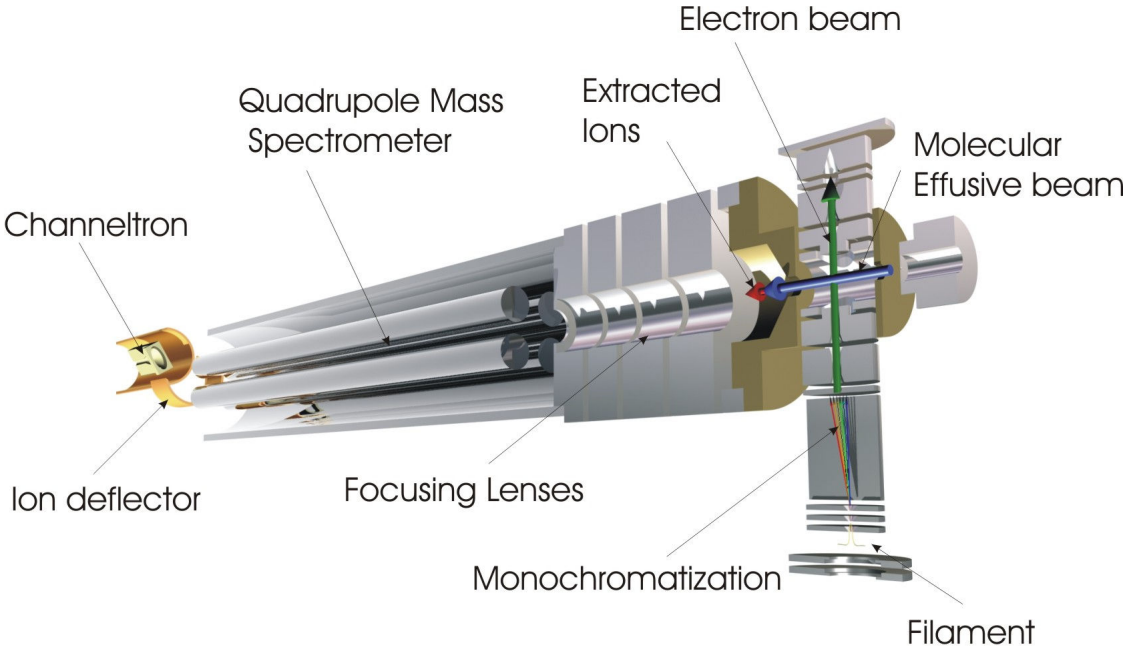

Figure 1-2: **Inside the vacuum chamber, the monochromator is mounted onto the detection ensemble constituted by the focusing lenses, the quadrupole mass spectrometer and the channeltron.**

The electrons are emitted from a wire tungsten hairpin filament, heated by a current of 2.3A to a temperature of 2700K [44] and the initial energy spread of the electrons is about 700meV. Hence, the assembly of emitted electrons has an initial mean kinetic energy of about 1 to 1.5eV. Despite its rather broad emission energy spread, this tungsten filament has been chosen for its resistance to the chemical attack, since many of the gases studied with this instrument are corrosive.

A magnetic field is created by two large Helmholtz coils of 70cm diameter (Figure 1-1), which are attached to the ceiling by four adjustable cables, giving the possibility to adjust the alignment of the magnetic field with the axis of the monochromator. The coils, alimented by a current of 5A, give rise to an almost uniform magnetic field in the centre of the collision cell of

roughly 50G, which is nearly 100 times more intensive than the ambient earth's magnetic field. The magnetic field has the double role of collimating the electrons along the axis of the monochromator, and, combined with a normal electric field in the dispersive element, it deviates the electrons in a plane according to their forward kinetic energy.

Indeed, by the action of the magnetic field the electrons have trochoïdal trajectories giving its name to this type of monochromator. Electrons are hold in a circular motion transverse to their translational movement imposed by the accelerating potential which is exerted along the axis of the monochromator, and become in this way less sensitive to stray electric fields even when they are slow. It is the advantage of this type of monochromator over the so-called hemispheric monochromator which is purely electrostatic, and whose electrons get easily lost due to stray electric fields when their energy becomes less than some eV.

If the magnetic field is properly aligned with the axis of the TEM, electrons are well collimated in a beam traversing the monochromator. The misalignment of the magnetic field has bad consequences like the drifting of the electrons which leads to a wrong determination of the electron current in the collision cell for instance. Without magnetic field, or if the alignment is really wrong, the deviation in the dispersive zone would not occur, and no current would be measured in the faraday cup.

The first lenses (entrance1 and entrance2) of the monochromator prepare the beam for the entrance in the dispersive element: they are used to reject electrons emitted with a too large angle with respect to the magnetic field axis (large traces of the impact of electrons on the surfaces around the holes of the first lens (entrance1) constitute a proof of this rejection, Figure 1-7), and also serve to accelerate or decelerate the electrons before the entrance into the dispersive element. The dispersive element is the place where electrons are deviated according to their forward kinetic energy and selected by an aperture in the exit lens (exit1). Afterwards, electrons can be subjected to a retarding field potential created between the lenses called exit1 (austritt1) and exit2 (austritt2) which can stop the electrons with the slowest forward motion. The accelerating field, which determines the electron energy (Ee-), is applied between the lens exit2 and the first shielding lens of the chamber. The lens exit2 is thick in order to prevent both coupling of the accelerating and retarding fields. As well, the two shielding lenses before and after the collision cell are thick in order to isolate the collision cell from penetrating fields. In the chamber, the monochromatized beam is interacting with an effusive beam of molecules under study. After the chamber, a retarding potential field can be created between the second shielding lens and another thick lens (retarding

field lens) in order to determine the forward kinetic energy distribution of the electrons. A last electrode before the faraday cup is usually set at a slightly positive voltage (~2V) with respect to the faraday cup in order to re-conduct backscattered electrons.

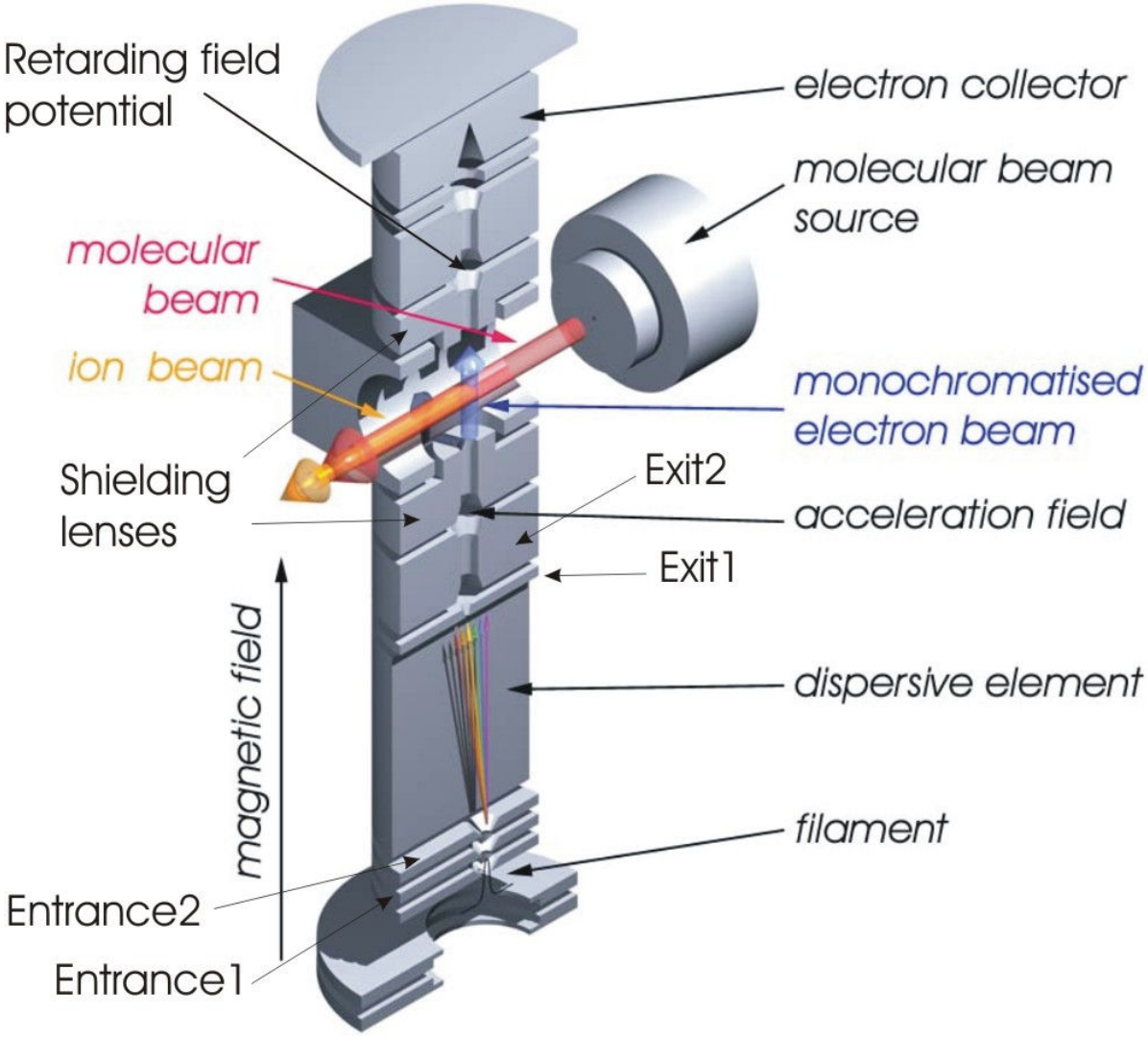

Figure 1-3: Schematic Cut of the monochromator.

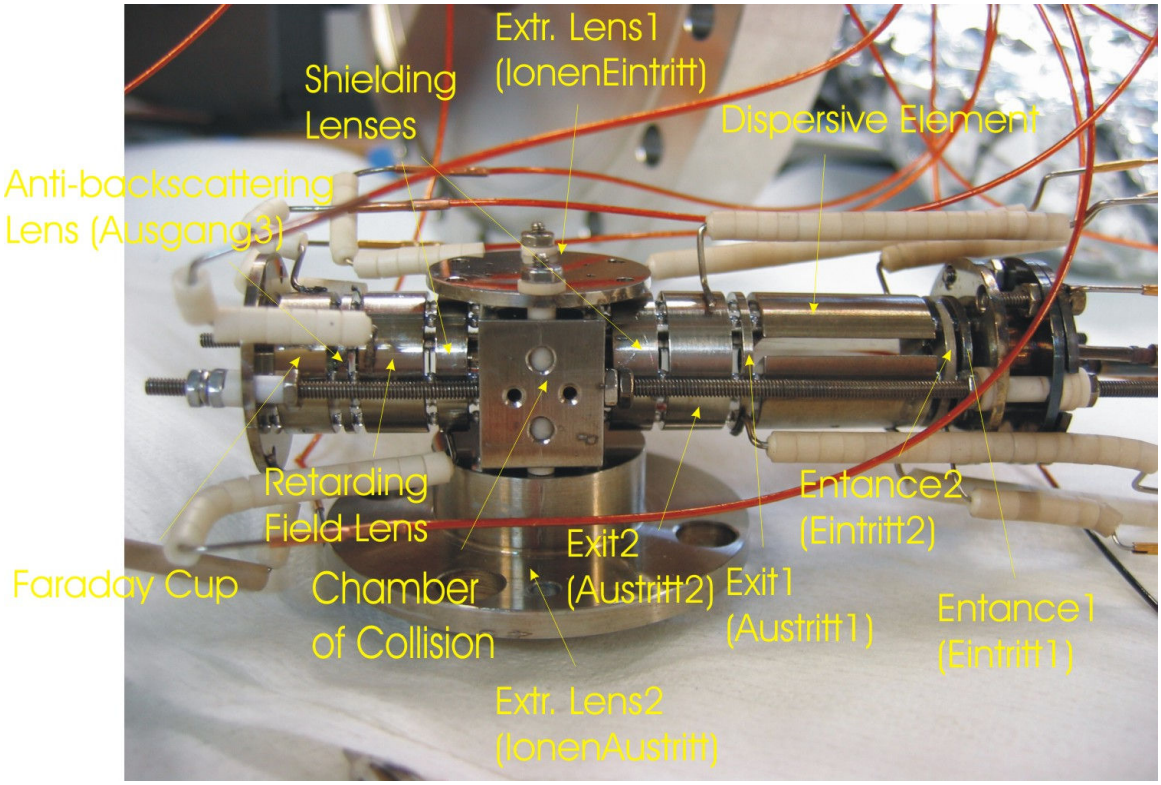

Figure 1-4: Photo of the monochromator.

The principle of the trochoïdal monochromator was first used as an energy analyser for electrons produced in a plasma (Barr and Perkins [45]), Stamatovic and Schulz were the first to use the principle of a combined axial $\vec{B}$ field and a perpendicular $\vec{E}$ field to disperse electrons in a plane with respect to their forward velocity in order to obtain a beam of definite energy after selection by a small aperture (1968, [46]). Recently, the principle of the old monochromator was revisited by V.Grill et al (2000, [48]), they improved the stability of the resolution with regards to the change of electron energy. The newly built monochromator was not designed to improve particularly the resolution; it was conceived to gain stability against the change of energy. We can find some examples were it works satisfactorily (for instance the example of Figure 1-14). But, still, in many cases, the determination of the 0eV-energy distribution by CCl_4 does not coincide with the energy distribution derived by the Retarding Field Potential (RFP) method at higher Ee-. The first part of this study presents the monochromator with emphasis on the importance of the rotational transverse motion of electrons; the second part is concerned with the examination of the methods of determination of the energy scale and resolution of the apparatus.

B. Principle of the Trochoïdal Electron Monochromator (TEM)

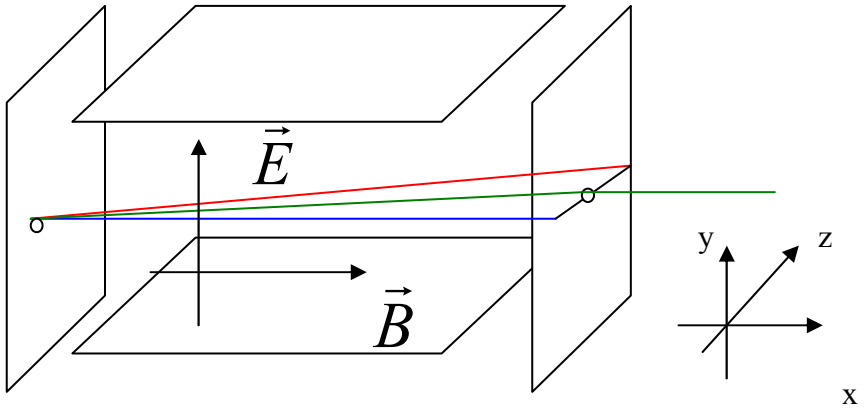

The force acting on a charged particle in presence of a magnetic field $\vec{B}$ and an electric field $\vec{E}$ is the force of Lorentz; for the electron, it can be written $\vec{F} = -e\vec{E} - e\vec{v} \otimes \vec{B}$. If we separate the components of the velocity with respect to the direction of $\vec{B}$, we can write $\vec{v} = \vec{v}_{yz} + \vec{v}_x$, and the equation of Lorentz reduces to $\vec{F} = -e\vec{E} - e\vec{v}_{yz} \otimes \vec{B}$. At first sight, it is astonishing that the application of this force results in a deviation in the (z;x) plane since the electric field exerts a force along the y-axis. The energy provided by the electric field in the y-direction is converted into the z direction by the magnetic field $\vec{B}$.

A simple picture helps a lot to understand the motion of an electron when electric and magnetic field are combined: the following drawing depicts the trajectory of an electron in a $\vec{B}$ field in presence of a normal electric field as indicated. The electron goes in circles around the magnetic field axis, its velocity tends to decrease when it goes against the electric field and, vice-versa, tends to increase when it goes in the same direction as the electric field. Having in mind the simple rule that fast electrons draw smaller circles, and slow electrons make larger ones, we can infer the resulting drift in the trajectories.

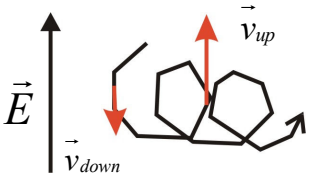

The proper way to describe the motion of the electrons in the dispersive element is to rewrite the equation of Lorentz in a cinematic form:

$$m_{e^-}\frac{\partial}{\partial t}\begin{pmatrix} v_x \\ v_y \\ v_z \end{pmatrix} = -e\begin{pmatrix} 0 \\ E \\ 0 \end{pmatrix} + -e\begin{pmatrix} 0 \\ v_z B \\ -v_y B \end{pmatrix} \qquad 1\text{-}1$$

The solution of this equation leads to the equation of motion for the electron inside the dispersive zone:

$$x = v_{x_0} t + x_0, \qquad 1\text{-}2$$

$$y = -\left(\frac{v_{z_0} + E/B}{\omega}\right)\cos\omega t + \left(\frac{v_{y_0}}{\omega}\right)\sin\omega t + y_0, \qquad 1\text{-}3$$

$$z = \left(\frac{v_{y_0}}{\omega}\right)\cos\omega t + \left(\frac{v_{z_0} + E/B}{\omega}\right)\sin\omega t + \left(z_0 - \frac{E}{B}t\right), \qquad 1\text{-}4$$

Where $\omega = \frac{eB}{m_{e^-}}$ is the cyclotron angular frequency of the electron (for a field of 50 Gauss, $\nu = \frac{\omega}{2\pi}$ ~140MHz), i.e. it is the angular frequency of the rotational motion of an electron in the magnetic field $\vec{B}$, and it is unchanged inside and outside of the dispersive element.

The equation (4) reveals the drift induced by the combination of the mutually perpendicular electric and magnetic fields in the dispersive zone (comparable to the drift in a cyclotron), the drift is given by $-\frac{E}{B}t$ after a time t. If the time $T = L/v_{x_0}$ corresponds to the time an electron takes to pass through the dispersive zone, the total deviation it has experienced at the exit of the dispersive zone is given by $D = \frac{EL}{Bv_{x_0}}$. Hence, the dispersive element separates electrons spatially according to their forward kinetic energies in a similar way like a prism does for the light. Some calculated trajectories are shown inFigure 1-5; the aperture of selection in the centre exit lens,

displaced of approximately 2.2mm with respect to the entrance aperture in our monochromator, is represented by the shaded area.

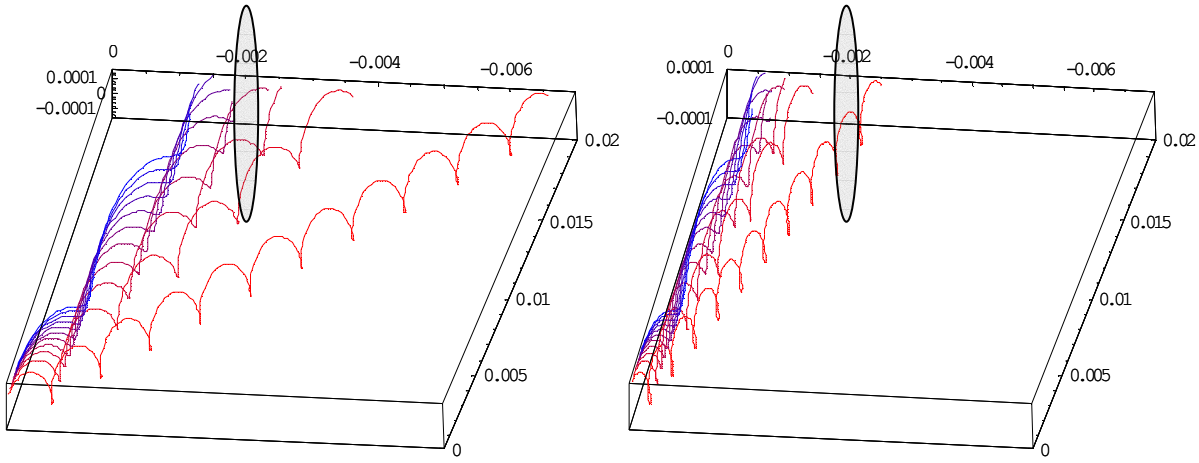

Figure 1-5: Calculation of electron trajectories inside the dispersive zone for two different intensities of Electric field applied (V_{ABQ}=0.8V for the left picture and V_{ABQ}=0.3V for the right pictures), the dimensions are indicated in meter. It gives an idea about the drift of the electron trajectories. The forward velocity is changed from 0.2eV to 5.2eV in step of 0.5eV; the fastest electrons have blue trajectories, the slowest red trajectories. An initial transverse kinetic energy $v_{y_o z_0}^2 / 2m_{e^-}$ of 0.01eV was set giving rise to gyrations with radii of 0.1mm (0.0001m). The position of the exit aperture is indicated by the ellipse in Gray (the ellipsoid form is due to the difference of scale in y-z directions).

V_{ABQ} stands for the potential set by the generator called Ablenker Quer (deflector in german), V_{ABQ}=0.3V gives rise to an electric field of about E ~160 V.m^{-1} and V_{ABQ}=0.3V gives rise to E ~ 430 V.m^{-1}.

C. Transverse kinetic energy of collision

The particularity of the electrons trajectories of this monochromator is the trochoïdal motion. In this section, we examine some consequences of this particularity. Notably is of importance the transverse kinetic energy carried by the electrons when they arrive in the region of collision, especially for the study of resonances at nearly 0eV collision energy.

Enlargement of the gyroradii in the dispersive element

Equations 1-2, 1-3, 1-4 show that the entrance into a region of a combined electric field perpendicular to the magnetic field as in the dispersive element cause an enlargement of gyroradius of the trajectories. The rotational movement of radius R becomes one with a larger radius R':

$$R^2 = \frac{v_{yz_0}^2}{\omega^2} = \frac{v_{y_0}^2 + v_{z_0}^2}{\omega^2} \rightarrow R'^2 = \left(\left(\frac{v_{y_0}}{\omega} \right)^2 + \left(\frac{v_{z_0} + E/B}{\omega} \right)^2 \right) = \frac{v_{y_0}^2 + v_{z_0}^2}{\omega^2} + \frac{\left(E^2/B^2 + 2v_{z_0} E/B \right)}{\omega^2} \qquad 1\text{-}5$$

Calculations of the gyroradii of trajectories have been tabulated in Table 4. R designates the radius before the entrance in the dispersive element and R' is the radius inside the dispersive element. The increase of gyroradius is especially important at small transverse kinetic energies. For instance, the radius becomes 10 times larger for an initial transverse kinetic energy of 0.0001eV. The difference is more and more reduced as the transverse kinetic energy increases. One can note also that the radius of the trajectories of electrons with small transverse kinetic energies (0.0001eV) inside the dispersive zone is already of the order 100µm, which represents 1/2 of the radius of the exit aperture (in lens exit1). Therefore, the enlargement of the gyroradii should be taken into account when we are considering the selection by the exit aperture of the dispersive zone.

As we see from equation 1-5, the radius of gyration also depends on the initial intensity of the velocity in the z-direction at the entrance of the dispersive zone. An incoming electrons of 0.01eV transverse kinetic energy will experience different gyroradius enlargements depending on the initial direction of its transverse velocity at the entrance of the dispersive element: if the velocity is pointing entirely in the z-direction the radius R' has for value $R'\left(\frac{v_{z_0}^2}{2m_{e^-}} = 0.01\text{eV} \right) = 0.000165\text{m}$, whereas its value becomes $R'\left(\frac{v_{z_0}^2}{2m_{e^-}} = 0\text{eV} \right) = 0.000119\text{m}$, if the initial velocity is entirely pointing in the y-direction; this gives a difference of 46µm which might result in big differences in the characteristics of the trajectories of electrons having identical energetic properties. The significance of this difference is immediately clear after comparison with the size of the aperture of selection (lens exit1) in the range of 400 µm only (see below Figure 1-6).

V_{ABQ}=0.8V / V_{ABQ}=0.4V	K = mean kinetic energy in the z- or y-direction (eV) (2K is total transverse kinetic energy)											
	0.0001		0.0005		0.001		0.005		0.01		0.05	
	(Ky=0, Kz=2K)	(Ky=2K, Kz=0)	(Ky=0, Kz=2K)	(Ky=2K, Kz=0)	(Ky=0, Kz=2K)	(Ky=2K, Kz=0)	(Ky=0, Kz=2K)	(Ky=2K, Kz=0)	(Ky=0, Kz=2K)	(Ky=2K, Kz=0)	(Ky=0, Kz=2K)	(Ky=2K, Kz=0)
R(µm)	9.54		21.3		30.1		67.4		95.4		213	
R'(µm)	107 58	98 50	119 70	100 53	128 79	102 57	165 116	119 83	193 144	137 107	311 262	235 219

V_{ABQ}=0.8V / V_{ABQ}=0.4V	K (eV)					
	0.1		0.35		0.7	
	(Ky=0, Kz=2K)	(Ky=2K, Kz=0)	(Ky=0, Kz=2K)	(Ky=0, Kz=2K)	(Ky=2K, Kz=0)	(Ky=2K, Kz=0)
R (µm)	302		564		798	
R'(µm)	399 351	317 306	662 613	573 566	896 847	804 799

Table 4: Calculations of the radii of the electrons trajectories before the entrance in the dispersive zone and inside the dispersive zone. Calculations of gyration radii in the dispersive zone are given for both extreme configurations: (Ky=0,Kz=2K) when the transverse velocity is pointing in the z-direction at the entrance of the dispersive zone, (Ky=2K,Kz=0) when the transverse velocity is pointing in the y-direction (2K is the total transverse kinetic energy). The gyration radii have to be compared with the size of the aperture of selection (Ø 400µm). The initial energy spread from the filament emission is of 0.7eV. V_{ABQ} designates the potential difference between the electrodes of the dispersive zone, giving rise to the normal Electric field.

The application of potentials between the lenses of the monochromator can modify in several ways the forward velocity v_x of the electrons before and during the passage in the dispersive zone, but the transverse velocity v_{yz} is only influenced by the intensity of the electric field in the dispersive zone. Neither is the transverse kinetic energy altered after the dispersive element. Indeed,

setting $R'^2 = \frac{v_{y_0}^2 + v_{z_0}^2}{\omega^2} + \frac{\left(E^2/B^2 + 2v_{z_0} E/B \right)}{\omega^2} = R^2 + \Delta R^2$, we note that the enlargement ΔR of the gyroradii experienced at the entrance of the dispersive zone depends on the ratio E/B. Table 4 gives the results of the calculations performed for different entrance configurations and different electric fields applied in the dispersive zone. The range of initial transverse kinetic energies (0.0002 to 1.4eV) should be close to the expected distribution of emission from the filament. This order of magnitude is confirmed by the traces of collisions of electrons found on the surface of the electrodes (see below).

Besides, the gyroradii reveal to have a magnitude of a few hundreds of µm close to the size of the selection aperture of the exit lens (exit1). As a consequence, the aperture does not only select electrons of a given forward kinetic energy, but also cut a part of the electron distribution in dependence with the gyroradius of the trajectories. The discrimination of trajectories by the aperture also depends on the wavelength of the trajectories as illustrated by the schematic drawing of Figure 1-6. An electron with a given gyroradius can pass the exit lens or not, depending on its forward velocity: the slower it goes the harder it is to pass the aperture as shown on the schematic drawing of Figure 1-6.

V_{ABQ}=0.8V V_{ABQ}=0.4V	T= forward kinetic energy (eV)						
	0.2	0.5	1	2	3	4	5
D(mm)	6.48 3.24	4.10 2.05	2.90 1.45	2.05 1.03	1.67 0.84	1.45 0.73	1.30 0.65
λ(mm)	1.90	3.00	4.24	5.99	7.34	8.48	9.48

Table 5 : Some order of magnitude of the Drift experienced by the electron in the dispersive zone (D) and of the wave length of the trochoïdal trajectories (λ). The drift has to be compared with the offset distance of placement of the exit aperture (2.2 ±0.2mm).

The Table 5 displays the results of calculations of the wavelengths and drifts of some trochoïdal trajectories for various forward kinetic energies of order of magnitude close to the

energies in use in our monochromator. The wavelengths appear to be much longer than the width of the exit lens (1.15mm), allowing trajectories with large gyroradii to pass the aperture of the exit lens (see Figure 1-6).

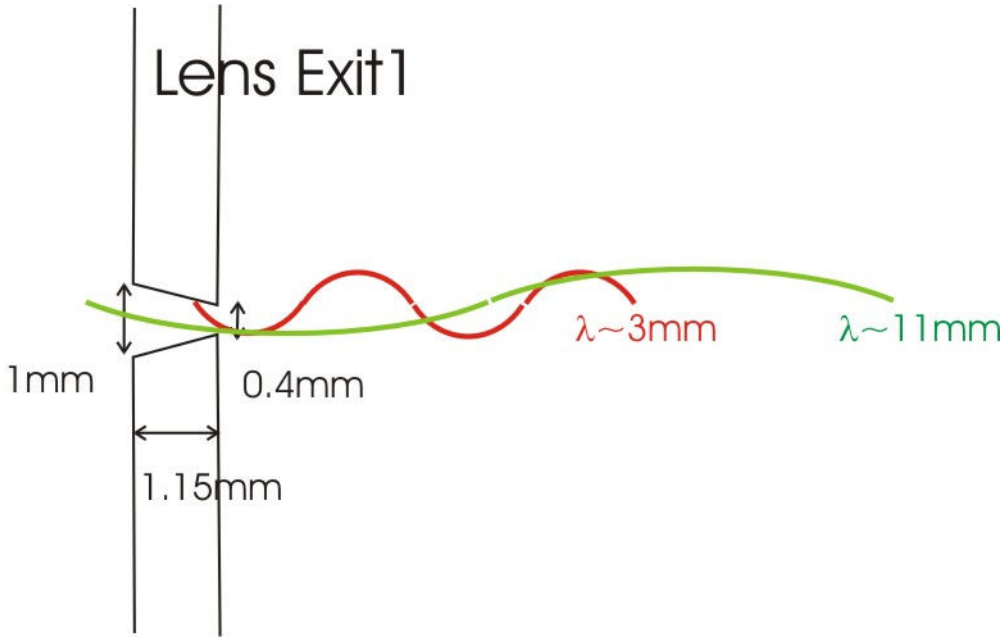

Figure 1-6 : Passage through the exit aperture in dependence with the forward velocity of electrons. Both trajectories have the same gyroradius (corresponding to transverse kinetic energy of 2K~0.2eV) but different forward velocity, the electron with the fastest forward speed can pass the aperture, the other is rejected.

To summarize, at a given intensity of electric field $\vec{E}$ (normal to $\vec{B}$), the aperture selects electrons of a given range of forward kinetic energies ([0.35eV, 0.55eV] for V_{ABQ}=0.4V and [1.45eV, 2eV] for V_{ABQ}=0.8V), associated with a given range of wavelength ([2.5mm, 3.1mm] for V_{ABQ}=0.4V and [5.1mm, 6mm] for V_{ABQ}=0.8V). It appears to be more interesting to work with lower normal electric field because the range of selection of the electrons should be finer. These electron distribution defined by these range of energy are however not fully transmitted, but further discriminated in dependence with the gyroradii i.e. the transverse kinetic energies. The larger is the wave length, the greater is the acceptance of larger radius. The faster the selected electrons are going, the larger is the allowable transmitted transverse kinetic energy. As well, electrons of forward velocities out of the determined range of selection can be transmitted if they are fast enough and have a large enough gyroradius.

On the right of the page are shown photos of the inward sides of the exit (exit1) and entrance (entrance2) lenses of the dispersive zone (photo1 and photo2 respectively). The appearance of black traces on the lenses where the electrons are impinging on the surfaces is due to some carbon residuals deposited after burning of molecules containing carbon atoms like hydrocarbons CH_4, C_2H_6 … It gives the possibility to trace where the electrons are impinging on the surface. The spread of the observable deviation around the aperture of the exit lens is of roughly 1.2mm: this gives an estimation of the drift in agreement with the results of calculations presented in Figure 1-5.

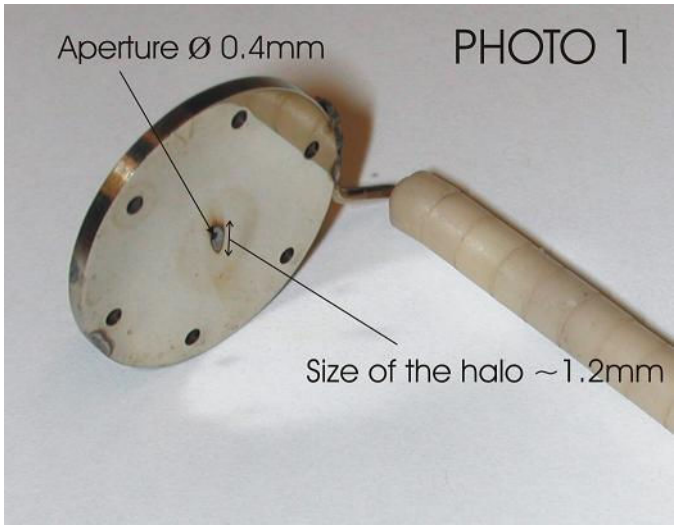

Likewise, the plane of deviation of the trajectories in the dispersive zone comes to be observable on the side of the entrance lens inwards the dispersive zone (photo2). These traces are most probably due to the impact of electrons reflected by the surface of the exit lens (exit1): after reflection, the electrons drift in the opposite direction which they took when they flew forwardly. The spread of the deviation is much larger than the one experienced in the forward direction, we can deduce that the electrons have lost a part of their energy during the reflection on the surface of the exit lens: the spread of the traces is about half the lens diameter (~ 8mm), it corresponds to the drift that would experience reflected electrons with a velocity down to v_x ~0.08eV. However, the place of impact of the fastest electrons is identifiable where the dark trace is more pronounced. It was mentioned in [48] that a part of the electron distribution can be constituted by electrons reflected twice from the surfaces of the dispersive element. These slower electrons can form a second peak in the energy distribution.

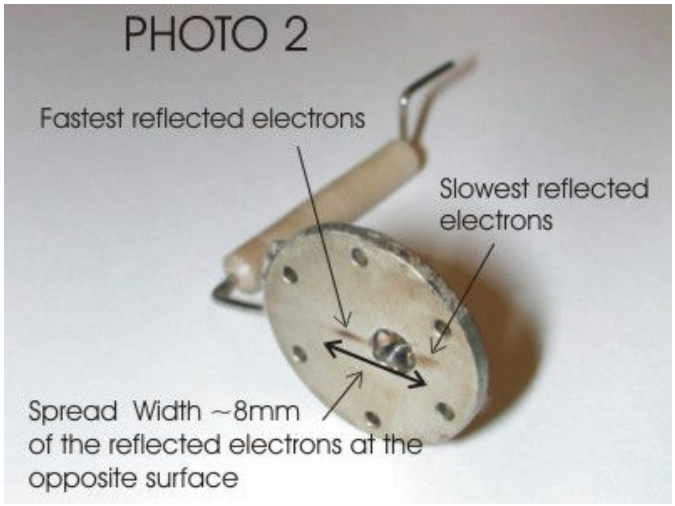

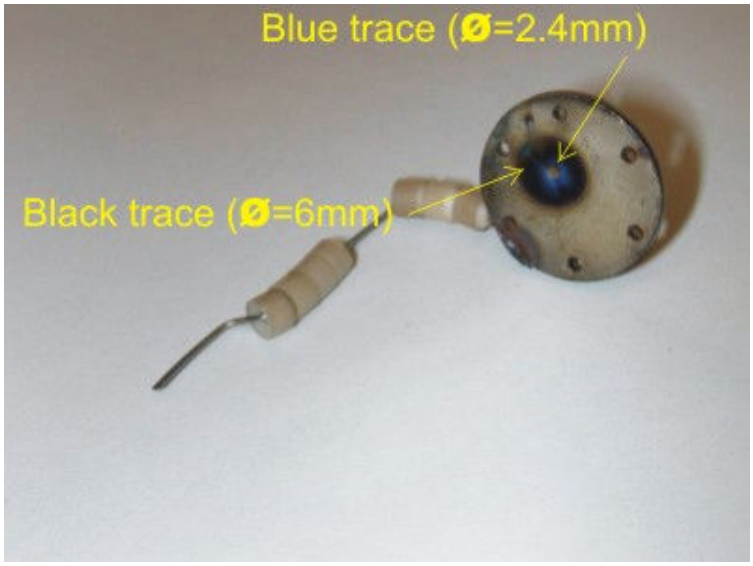

Figure 1-7: Photography of the first entrance lens (entrance1) responsible for the rejection of trajectories with large gyroradii.

The photo of Figure 1-7 shows the first entrance lens placed right after the filament aperture, the black trace has a diameter of 6mm, it is larger than the aperture from which electron are emitted (diameter 1.4mm). It is much too large for being due to electron impact; the transverse energy of the electron required for such gyroradii would exceed 6eV. Most probably it is due to the emission of tungsten particles from the filament. However, the blue trace close to the aperture of the lens could be identified with the impact of electrons; its size of roughly 2.4mm diameter could correspond to the impact of an assembly of electrons of mean transverse kinetic energy ~1.3eV and 0.7eV energy spread emitted from an aperture of 1.4mm, which is close to the initial kinetic energy distribution expected for the emitted electrons. Indeed, we determine a maximum gyroradius of ~1 mm for an electron of transverse kinetic energy of ~2eV arising from an extremity of the 1.4mm diameter exit aperture of the filament box.

If there is a doubt about the origin of these traces as due to impinging emitted electrons, the traces found previously in the dispersive zone can however not be due to the deposition of tungsten particles since those particles would not experienced the deviation observed in the dispersive element.

At the end of the dispersive zone, typically, electrons have a forward kinetic energy of several eV. The spread of the electron beam is rather small as we observed on the photo of the exit lens (photo1): the size of the halo does not exceed 1.2mm. From that point of view, the diameter of

the aperture of 0.4mm is too large for performing a real selection of the forward kinetic energy. According to the simple calculation from the drift, the range of forward energies selected has a width of 0.2eV for V_{ABQ}=0.4V and 0.55eV for V_{ABQ}=0.8V. On the other hand, it is small if we consider the gyroradii of the trajectories which can reach 165µm for a typical intensity of electric field of 430V.m^{-1} (V_{ABQ}=0.8V) and an initial transverse kinetic energy of 0.01eV only. Therefore it might limit the transmitted electron current. Taking the entrance aperture as limit size for the gyroradius of trajectories entering the dispersive zone, up to 0.35eV-electrons can enter the dispersive zone.

At the emission we have an important spread of the electron kinetic energies. Due to the collimating magnetic field, the transverse kinetic energy is transformed into rotational motion. This transverse kinetic energy available in the rotational motion is only altered inside the dispersive zone. Electrons with low initial transverse kinetic energies at the entrance of the dispersive zone acquire non negligible gyroradius with respect to the size of the selection aperture in the exit lens. Electrons of transverse kinetic energies up to several tenth of eV are allowable (maximal radius corresponding to the size of exit aperture corresponds to a transverse kinetic energy of 0.35eV).

This study reveals that the transverse kinetic energies of the electrons out of the dispersive element might be generally underestimated and can play a role for the existence of true 0eV-electrons in the collision cell, since the transverse motion is not altered by the accelerating voltages between the dispersive element and the collision cell. A detailed study of the transmitted transverse kinetic energy distribution should be made to shed some light on this problem.

These considerations are of importance when we are concerned with the minimal energy which electrons are carrying when they arrive in the collision cell. The estimation of the transverse kinetic energy carried by the electrons in a TEM (Table 4) is of great importance especially for the study of electron-molecule collision at very low energy, for which the transverse kinetic energy can not be neglected. The attachment to CCl_4 occurs mostly for electrons with less than 0.05eV. In particular it might explain some disaccords observed between the methods of determination of the energy distribution of electrons in the chamber.

D. Acquisition system and electronics

This machine has been designed to produce a beam of electrons of a definite energy within fine energy resolution. This section poses the question of the reliability and accuracy of the determination of the electron energy distribution of the beam in the cross beam region of the monochromator. The heated tungsten filament emits electrons with an initial spread of 700meV. Hence, electrons are emitted with a mean velocity of about 1 to 1.5eV. The overall accelerating potential experienced by the electron from emission until the collision cell is modified by the electron energy scan generator and the electron energy offset generator shown on the schematic drawing of the Figure 1-8. The uncertainty on the initial kinetic energy and on the potential of emission makes the energy determination by the two electron energy generators a relative one. Hence the energy scale must be calibrated.

Two distinct methods of determination of the electron energy distribution are at our disposal: one method makes use of a gas test presenting some sharp onset of ionisation at a known energy (ex: H2, NO, CO) or some peaked resonances (ex: CCl4, SF6); the other method is made by a retarding field analysis after the cell of collision. For the experiments with CELIA, CCl_4 is usually used to calibrate the energy scale from its s-wave resonance at 0eV.

The following study of the energy distribution of the apparatus was occasionally done during the experimental study of the DEA to water. As a consequence, in all examples shown below, the apparatus was tuned to provide a high electron current at the price of making the energy distribution rather rough (>200meV). It was difficult to work with much finer resolution since the electron current needed to be at least 100nA in order to be able to measure processes with low cross section (OH^- channel). It is usually possible to work with a resolution under 100meV (CCl_4) for an electron current of some tens of nA.

At first, the acquisition system and electronics of relevance of the apparatus are described in Part II : Chapter 1.D.I), then the functioning of the retarding field potential analysis is further detailed in Part II : Chapter 1.D.II). The use of the two methods of determination of the electron energy distribution is discussed in the last section (Part II : Chapter 1.E).

I) Acquisition system in Celia

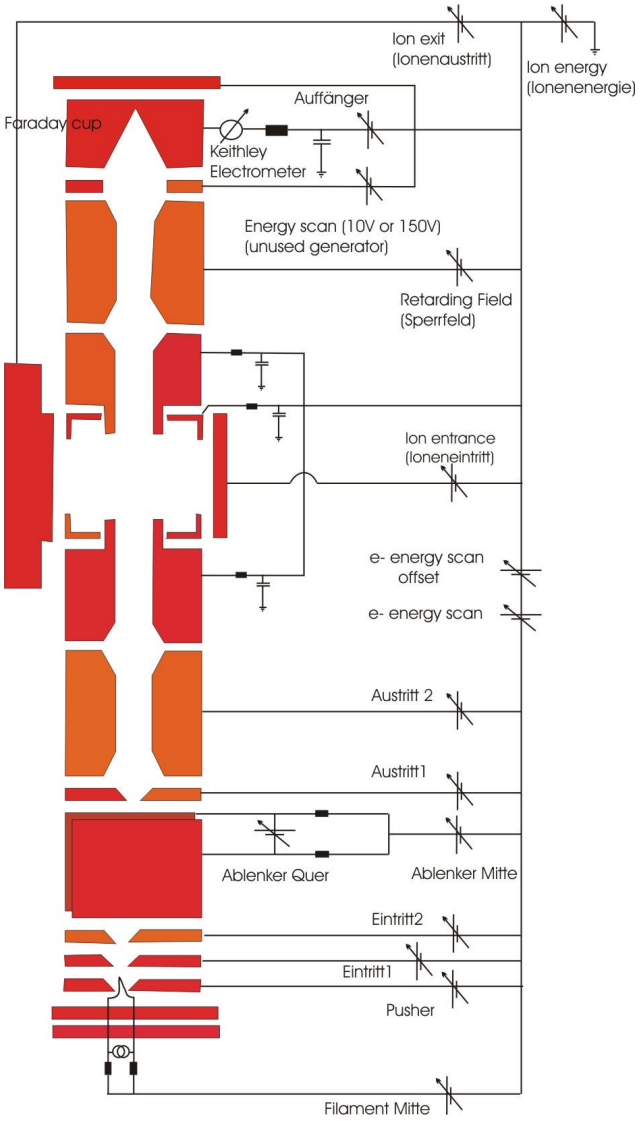

Figure 1-8: Electric diagram of the monochromator.

We are using a MCS-plus card to count the pulses from the channeltron after filtering, amplification and discrimination. It can have an input counting rates up to 100MHz. For the scanning purposes the MCS-plus card provides an analog ramp output with 14 bits resolution. The PC-lab card is a multi-function data acquisition card, it has 16 A/D input channels with a resolution of 12 bits, 2 A/D output channels with a resolution of 12 bits. Usually the energy and mass scan are computer-driven via the MCS-plus card, there is namely also the possibility to drive them via the PC-lab card if we want for instance to measure the current as a function of the electron energy. The monitoring is passed alternately to the PC-lab card or to the MCS-plus card by a switch controlled

by the digital output DO0. To overcome the difference of potential between generator and ion signal on one side and grounded computer on other side, isolation amplifiers are needed.

We also use it to drive the scan voltages of the generator. The PC-Lab card can only measure analog signal, it is used to measure the electron current from the faraday cup.

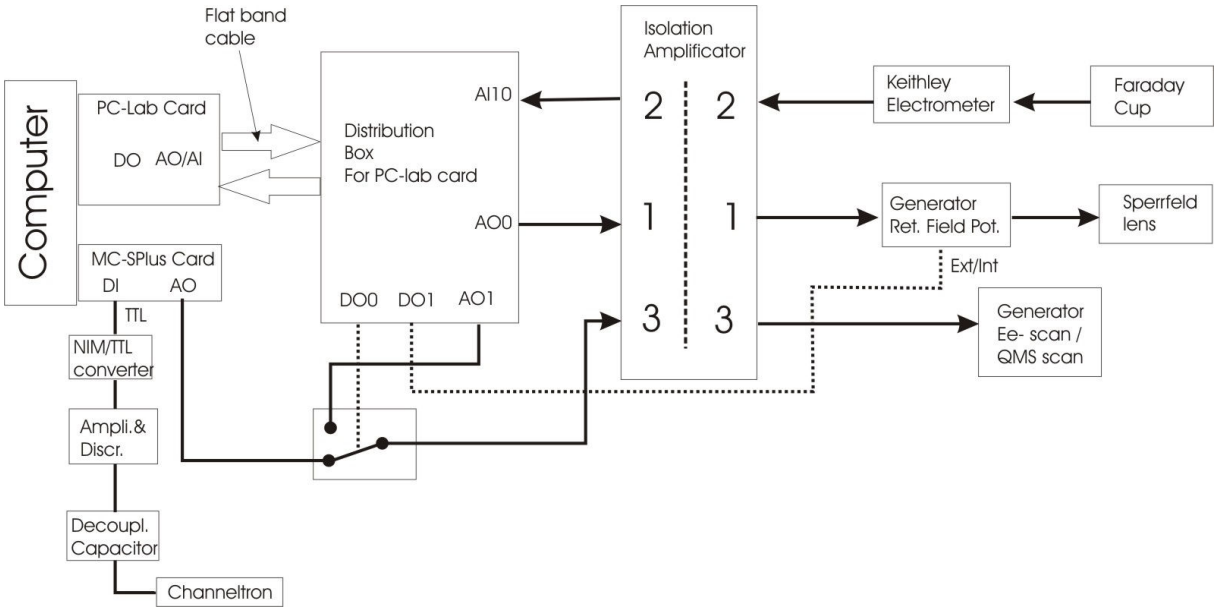

Figure 1-9: Schematic electronic diagram of the apparatus.

(1) Retarding field potential

A Labview program has been written to command the PC-lab Card which sets the value of the retarding field potential and measure the charge (per sec.) collected in the faraday cup via the Keithley electrometer. The drop of the current so measured is further smoothed and derivated to obtain the shape of the electron distribution (see the electric diagram of the monochromator, Figure 1-8 and Figure 1-9).

(2) Keithley Electrometer

(a) Response time of the electrometer

The limitation comes from the electrometer since the generator delivering the tension applied on the Sperrfeld lens has a linear response time of 10ms/V. Hence it needs 50μs for a usual increase step of the retarding field potential which is negligible in regard to the response time of the electrometer.

The Keithley electrometer is converting the measured current into an analog voltage delivering 1V tension when the full range is reached. The response time of the electrometer is depending on the selected range: a longer time is needed to measure smaller current; the delay to wait is indicated in the Table 6. It gives a minimum interval time to wait between two successive voltage steps when the retarding field potential is swept.

Range (A)	Delayed Response τ
10^{-6}	2-3 ms
10^{-7}	5 ms
10^{-8}	15-20 ms

Table 6: Response time of the Keithley.

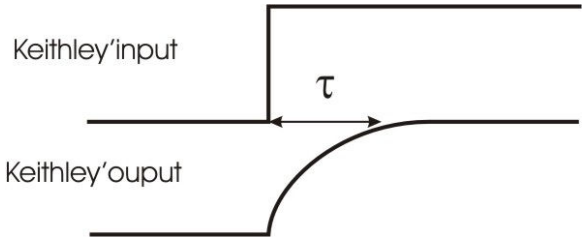

(b) Relative intensity of current

We must stress out that the current intensity is measured by the PC-card relatively to the scale chosen for the electrometer; no absolute measured is delivered by the electrometer, every time the range must be noted. The voltage range of the analog input channel of the PC-lab card has been chosen to be +-5V. The amplifier preceding the A/D converter was set to a gain of 2, so that the resolution of the intensity could be improved as shown on the schematic drawing of Figure 1-10.

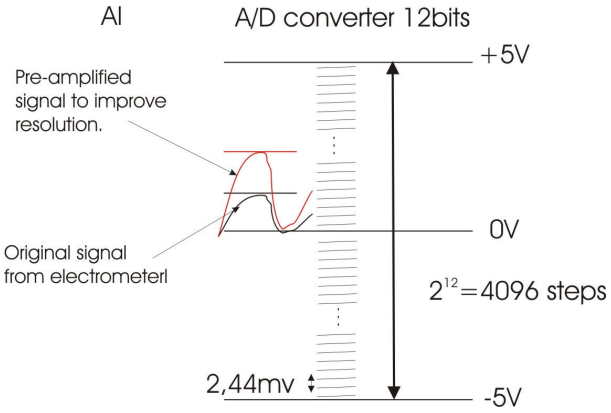

Figure 1-10: Schematic drawing of the digitalisation of the signal entering the analog input channel of the PC-lab card. The measured current from the electrometer is resolved maximally by 2^{12}bits.

The measured current from the electrometer is resolved by maximally $2^{12}/2*G/5=819$ since the gain of amplication before the A/D conversion was chosen G=2. The resolution could be increased by a factor of 2 (G=4), G=8 would lead to saturation effect because it would exceed the AI range of the PC-lab card (5V).

(3) Supplementary generator for the RFP analysis

The generator used to perform the retarding field scan is limited to -10V, therefore we add an offset potential with an additional generator (maximal range 32V DC), in order to perform an extended retarding field range which gives the possibility to determine the resolution of the electron beam for higher electron energies (most of the ionisation phenomena's threshold of interest are located happen under 20eV).

The output scan has a 12bits-resolution and a range of 0-10V has been chosen. The usual resolution selected by the program is 11bits which gives a voltage step for the scan of $10/(2^{11}-1)= 4.89$ mV . It is sufficient to resolve the peaks of the electron energy distribution which are usually in the best case of the order of 100mV.

II) Retarding field potential analysis

The energy of an electron is the energy that we need to stop this electron.

When we proceed to a retarding field potential, care must be taken to switch off the unused scan generator since it is connected to the small lens coming right after the sperrfeld lens (called in anti-backscattering lens in Figure 1-4) as shown in the electric scheme of Figure 1-8, and it might influence the current collected in the faraday cup. Generally the lens "anti-backscattering lens" is set to a slightly positive potential in order to prevent the losses due to secondary emission when the electrons are impinging the surface of the faraday cup.

As for tuning the monochromator with the retarding field potential, it can be done as follows: it is usually wished to have the highest intensity of current with the best resolution, as well as a nice stability of current over a given range of energy. This range extends from 5V to 15V in the case of the study of the DEA to water. The tuning can be achieved the most easily by looking at the evolution of the drop of current when changing the potentials of the lenses of the monochromator. Since all three important characteristics of the electron energy distribution are observable at once when looking at the drop of current. Indeed, the sharpness of the drop tells about the resolution, the height tells about the intensity of the current and the regularity of the plateau tells about the stability of the current intensity over the range of energy.

For the retarding field analysis to be reliable, the magnetic field needs to be properly aligned with the monochromator axis otherwise the electron energy distribution cannot anymore be determined by the drop of current.

Illustrative examples are given in the Figure 1-11 and Figure 1-12:

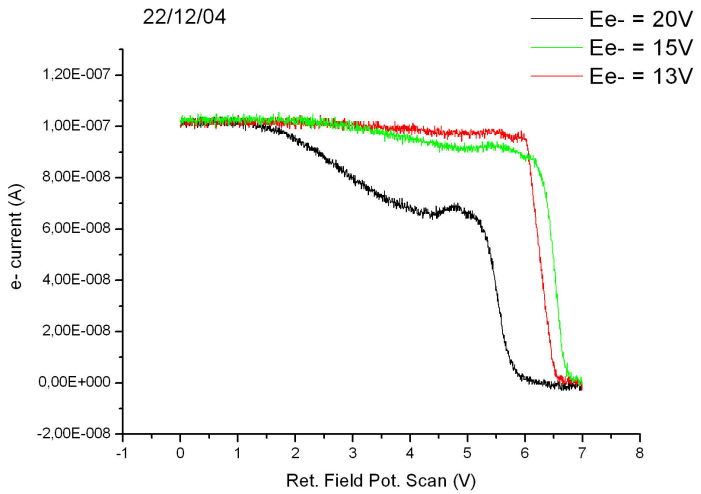

Figure 1-11: Effect of the misalignment of the magnetic field.

The Figure 1-11 shows an example of the effect of misalignment of the magnetic field, the current doesn't drop sharply at Ee-=20V, the current drops slowly over several volts before the sharp drop occurs. Hence, a part of the electron energy distribution is progressively changed into slow electrons. The non alignment induces a drift (comparable as the drift in the dispersive element) which is dependent on the intensity of the $\vec{E}$ field normal to the $\vec{B}$ field.

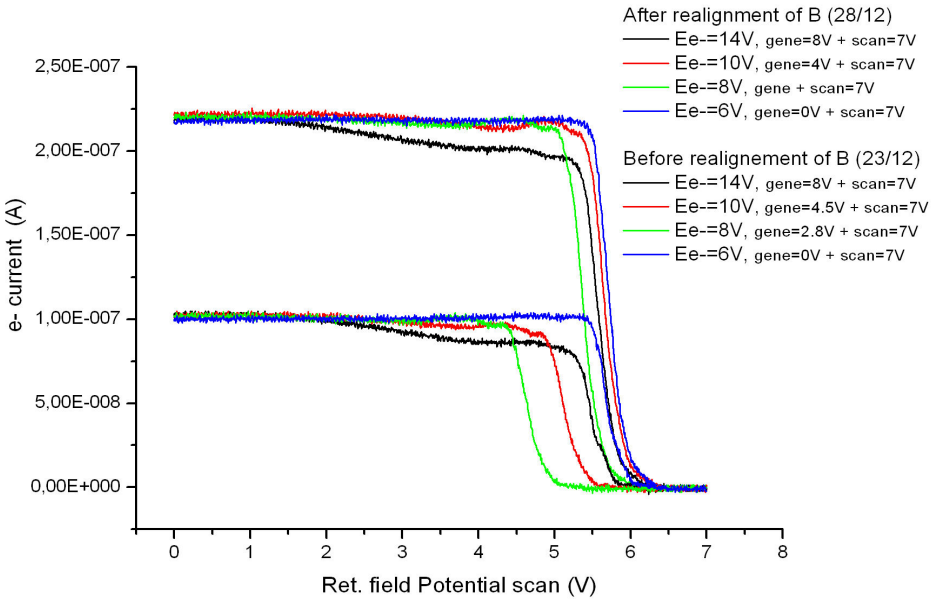

Figure 1-12: Comparison of drops of current obtained by application of the retarding potential before and after a realignment of magnetic field $\vec{B}$.

The second Figure 1-12 shows a comparison of the current drops after realignment of the $\vec{B}$ field, we notice the improvement of the stability of the current and especially the important gain in electron current. The curves are shifted one from another since the additional generator was only set approximately since we were only interested in observing the drop of current close to the end of the 7V-scan.

Thanks to the additional generator we can look at the evolution of the distribution up to very high energies (max of additional generator of 32V + 10V_scan of PC-lab card = 42V). It gives the possibility to stop electrons up to energy of 40 V. Figure 1-14 gives an example of evolution of the distribution with electron energy from Ee-=0.77V up to Ee-=15V. The associated drops of current are shown in Figure 1-13.

The distribution of forward kinetic energy of the electrons is obtained after derivation of the smoothed (or filtered) drop of current. The details of the distributions obtained depend on the choice of the smoothing procedure. The interval time between two successive measurements of the current is also of importance, we saw that it is necessary to wait 2-3ms when the electrometer is measuring in the range 10^{-6}A. Actually, a longer interval time would be needed to make the measurements independent: in the range 10^{-6}A it can be estimated to be of the order of 13ms. However the analysis proves that an interval time of 2ms is sufficient to draw the main features of the distribution, and the correlation between successive measurements acts like a first filtering of the distributions signals. Some examples of distributions, obtained after a 10-points adjacent smoothing of the current drop, are shown in blue in the Figure 1-15 to be compared with the corresponding distributions obtained with the usual filter implemented in the Labview program.

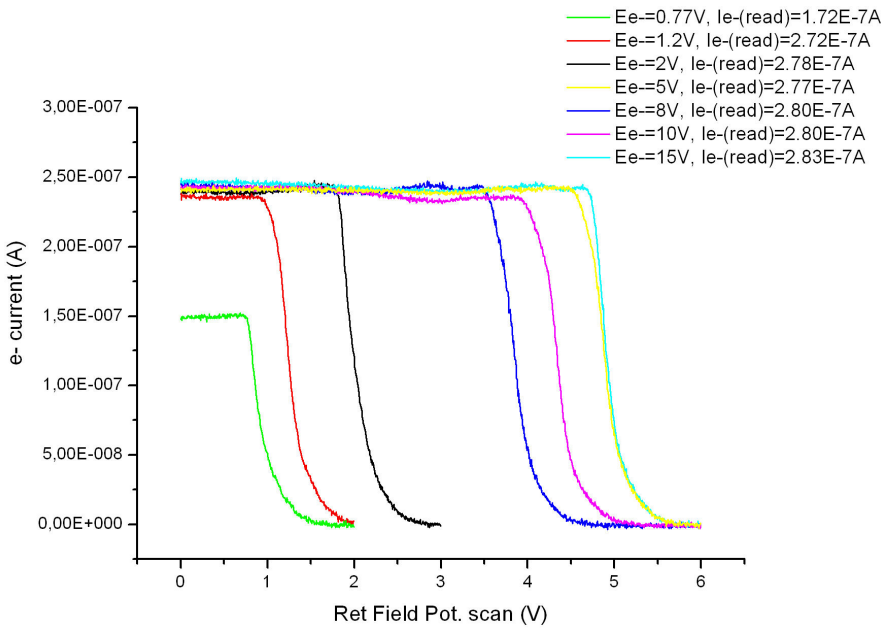

Figure 1-13: Drops of current associated with the distributions of Figure 1-14. The current remained very stable from Ee-=1.2V to Ee-=15V.

In the examples of Figure 1-13, the stability and current intensity were even more improved. A remark should be made about the current intensity: the value of the intensity of the current indicated on the scale corresponds to the intensity read by the PC-lab card. It proves to be systematically lower than the value read on the electrometer i.e. $Ie^{-}(\text{read}) = 1.15 \times Ie^{-}(PC-lab \text{ card})$. It is of importance if the absolute determination of the current is required. In the Figure 1-13, the corresponding values of the current for the different Ee- are indicated in the legend.

Here we come to realize the importance of the alignment of the magnetic field especially when we want to make quantitative study like measuring cross sections. If the magnetic field is misaligned, we cannot know how many of the electrons are lost between the collision cell and the faraday cup, and the number of electrons of a given energy which come to interact with the target molecules in the collision cell is undetermined. So special care must be taken to prevent misalignment, and the alignment can be easily checked by a long scan of the retarding field potential at high electron energies.

The distributions derived from the current drops of Figure 1-13 are very regular; the corresponding mean FWHM at a given energy indicated with the associated standard deviation σ calculated from a sample of N distributions (N is given in bracket). FWHM is the width at half of the height of the peak; it is calculated by the Labview program as the difference in abscissa of the first point at half of the height (upwards) and the next point at half of height (downwards). For this example the determination of FWHM is reliable since the distribution is regular, it can become a wrong determination of the actual width of the peak when the peaks have a structure and a point at half of the height downwards is encountered too early.

The evolution of the distribution with the electron energy can be considered in Figure 1-13, from Ee-=0.77V up to Ee-=15V, the width of the distribution remains rather stable around 260mV FWHM with the exception of the very low energy 0.77V where it is finer (195mV, only a part of the distribution reaches the chamber) and at 8V where the distribution becomes wider. The current varies of less than 4% over the range 1.2V to 15V, for such a high current, experience shows that it is a good resolution.

However if we consider the associated measured distribution of Cl^- from CCl_4, it is clearly wider than the distributions determined by the RFP method over the whole range of energy.

Very frequent disagreements are obtained between the distribution determined by Cl^- and the one determined by the RPF analysis. We will return to this point in the next section on the comparison between the two methods of determination.

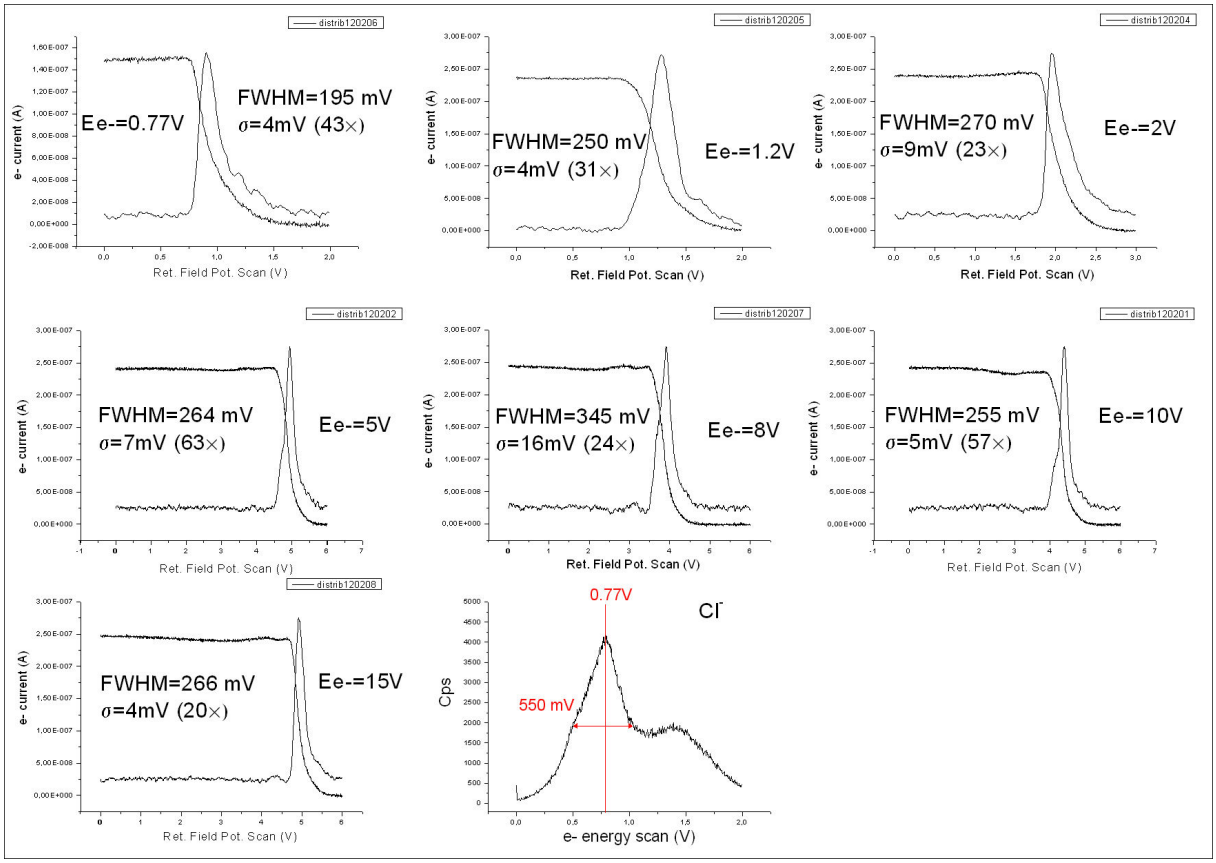

Figure 1-14: Example of determination of the electron energy distributions at various electron energies (Ee-) with the RFP method. On this example, the resolution of the apparatus remains very stable over the entire range.

On the next example of Figure 1-15 is shown another example of evolution of the distributions over a longer range, from Ee-=1.41V, up to Ee-=20V. The three last distributions in blue presented in this figure results from the use of another filtering before derivation which shows more detailed distribution, especially we can notice the more pronounced peak structure for the distribution at Ee-=1.41, or the variation of intensity of the peak at Ee-=20V. However as said before the main features of distributions are displayed in the smoothest distribution (2ms time interval for the range 10^{-6}A) determined by the program online.

As before the FWHM calculated from a sample of N distributions (N×), is indicated on every graph and one of the distribution of the sample is drawn in example. However in this example its value is not always representative of the actual width of peaks since the distributions can be rather irregular, leading to underestimations of the width of the distribution by this systematic calculation (FWHM is the difference in abscissa of the points at half peak's height); for example at

Ee-=2V the width of the peak is underestimated since the distribution becomes much broader under half of the maximum height. But this determination of FWHM can be generally taken as a good indicator of the width of the peaks.

With this example of Figure 1-15 we see that the evolution of the distributions with the electron energy can be non trivial, the shapes of the peaks knows a lot of changes and the resolution is not stable contrarily to the first example given of Figure 1-14.

The maximal current before the drop is indicated on every graph of Figure 1-15. This series of distribution were obtained from the derivation of drops taken the same day as the drops shown in Figure 1-11. As a consequence, at the highest energies, the measurements were plagued by the misalignment of the magnetic field. So, the distributions shown in Figure 1-15 correspond to the sharp final drop of current only without including the long drop produced by the lost of the electrons due to the drift induced by the misalignment. The decrease of the maximum current for the highest value is indicative of it.

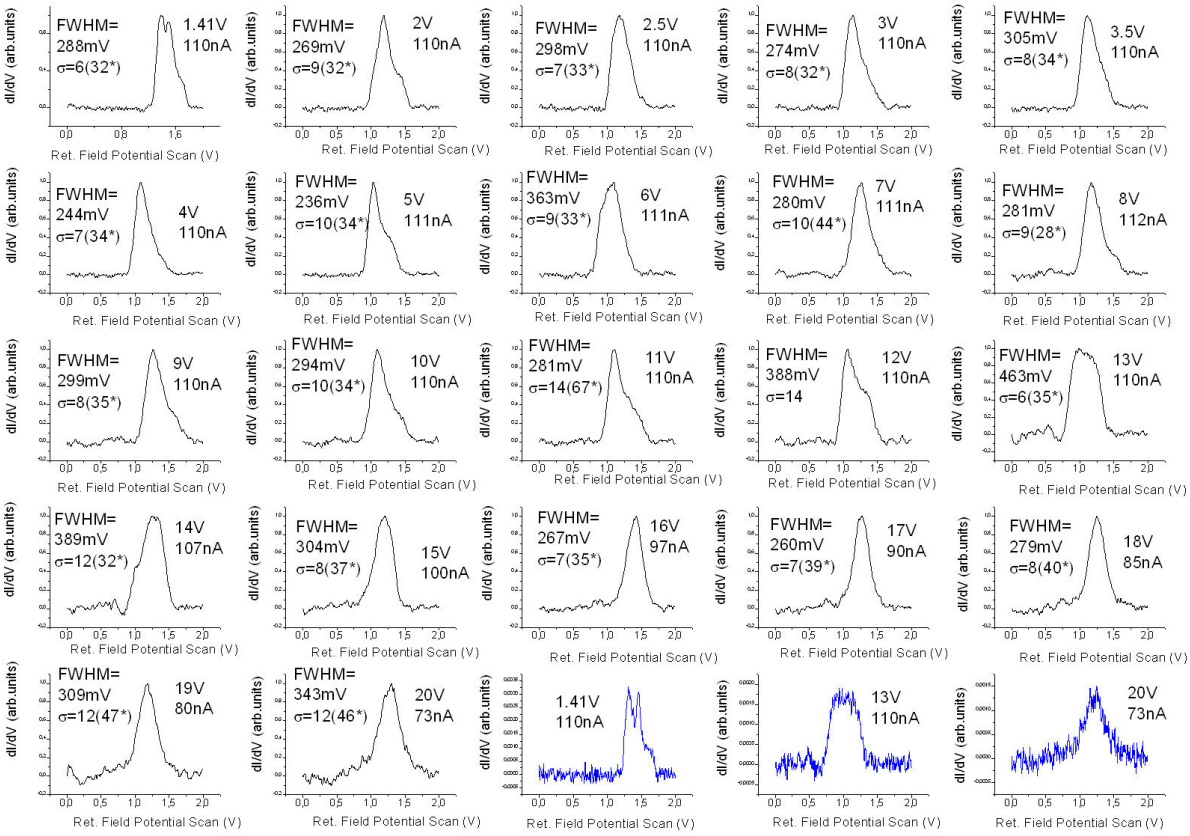

Figure 1-15: Example of evolution of the energy distributions with the increase of electron energy (Ee-).

Corresponding distributions of Cl-, taken before and after the series of measurements of Figure 1-15 are shown in Figure 1-16. The distributions of Cl- were regular and remained stable during the series of measurements of drops of current. It proves that obtaining a regular distribution of Cl^- does not imply that the energy distribution remains stable at higher energy or that the methods do not agree in the determination of the energy distribution.

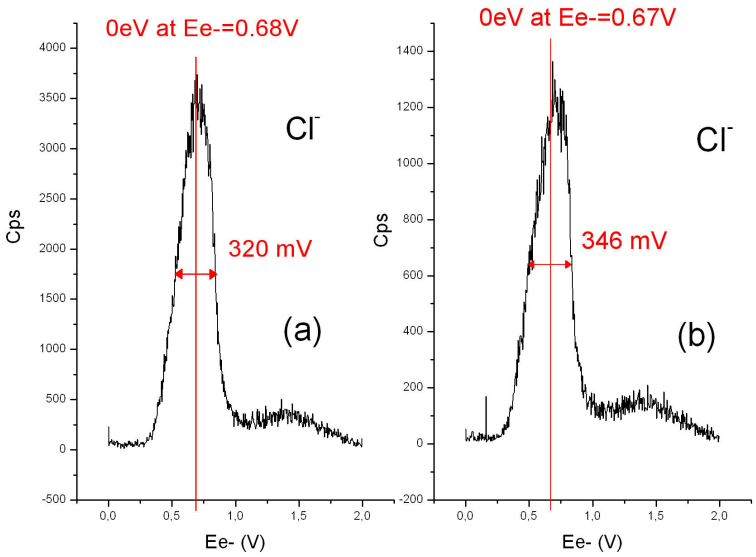

Figure 1-16: Corresponding distribution of Cl- taken before (a) and after (b) the series of measurements of the Figure 1-15.

E. Determination of the energy resolution and calibration of energy scale

This study was initiated after the observation of frequent disagreements between the results of the gas test method (CCl_4) at 0eV energy and results of the RFP method at various Ee- energies. The RFP method is the only method able to give the evolution of the distribution over a wider range of energy. Since a reliable determination of the energy scale and energy resolution is of greatest importance for this apparatus, it is worth to re-examine both methods procedure in details.

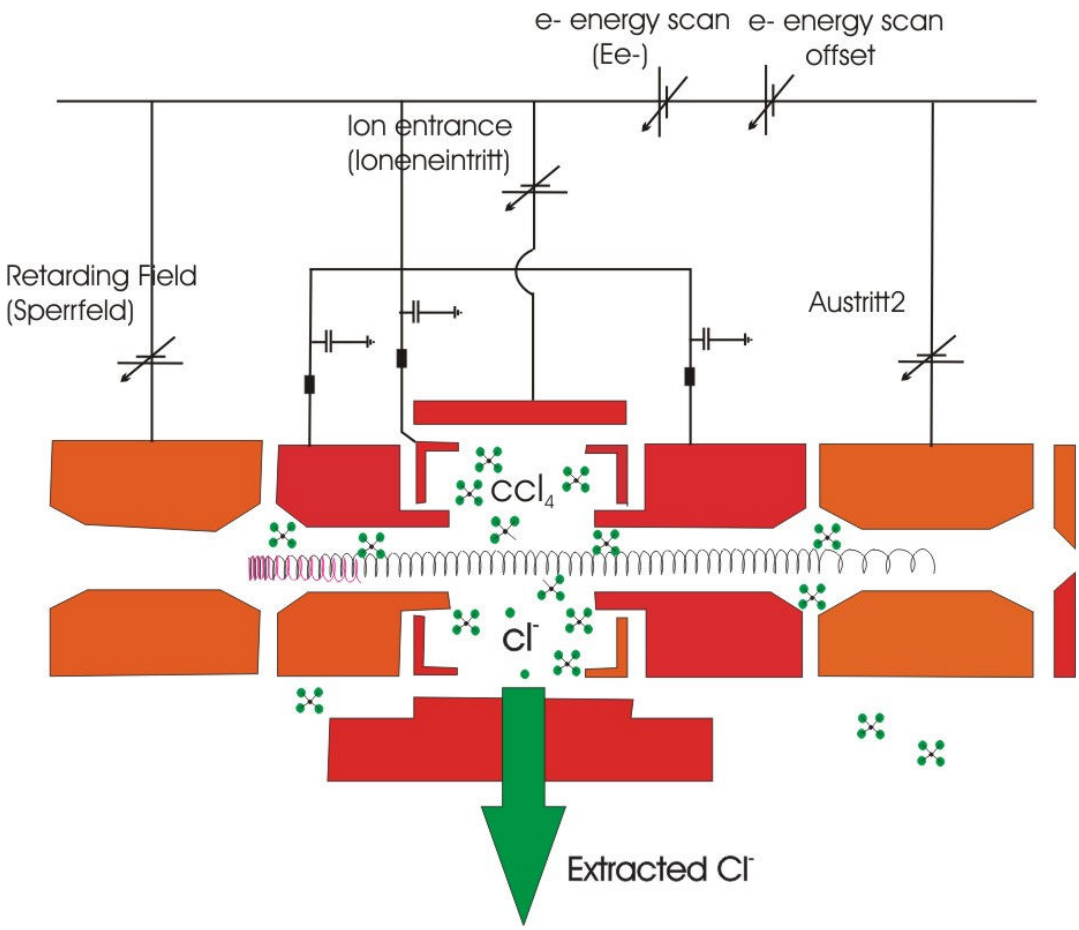

I) Description of the electron beam

Slow electrons are very sensitive to stray electric field, the magnetic field $\vec{B}$ is holding them in the axis of the monochromator (if the $\vec{B}$ field is aligned with this axis), but on the other hand it gives rise to trochoïdal paths for the electrons, which makes the physics more complicated.

The slower electrons go in the trochoïdal monochromator, the more important becomes the rotational component of their movement. The upper picture is schematically showing the imaginary trajectory of an electron. Usually the Ee- offset is used to shift the energy scale towards negative potentials in order to start the start of the energy scale before the incoming of the electron i.e. before the 0eV position, so that we can observe the appearance of the Cl^- resonant peak at the 0eV position. So usually before 0eV, the electrons coming out of the dispersive element are slowed down and repelled by the first shielding electrodes before the entrance into the collision cell as shown in the picture. As the electron energy Ee- is increased, the fastest electrons can overcome the

negative potential barrier, the wave length of their trajectories is decreased by the barrier and it results in a movement of slow forward motion combined with fast rotation. The transverse movement is not affected by a change of Ee- (in the case of perfect alignment with the magnetic field). If the electrons are close to 0eV, we can expect that most of their energy is contained in the rotational component of the movement. The electrons reach then the retarding field electrode (sperrfeld in German) after traversing the chamber. If their forward kinetic energy is less than the negative potential barrier applied between the second shielding electrode and the RFP electrode, electrons are repelled as illustrated (this effect was checked by observing the doubling of intensity of the yield of Cl- from the DEA to CCl_4 when the electrons are repelled by the retarding field). If their forward energy is sufficient they are slow down by the retarding field potential but continue their course until the faraday cup.

However their forward energy is very low and the rotational movement contains the major part of energy according to the analysis of Part II : Chapter 1.C.

II) Two methods of determination of the electron energy distributions

There are two ways of measuring the electron energy distribution of the monochromator. We can make use of a calibration gas with a known cross section shape, usually CCl_4 which shows a s-wave resonance at very low energies (~0eV, Hotop [47]) (see theoretical description of the s-wave resonance to CCl4 in chapter III theory and figure):

$CCl_4 + e^-(E) \xrightarrow{\sigma(E)} Cl^- + CCl_3$, $\sigma(E) \propto E^{-1/2}$ if $E < 55$ meV

In this way, we have a reference energy from which the rest of the energy scale is determined by translation of Ee-.

The second method uses the retarding field analysis which was presented in Part II : Chapter 1.D.II).

III) Comparison between the two methods

It is often believed that it is sufficient to determine the characteristics of the energy distribution from the yield of Cl^-. This distribution is expected to be conserved at higher energies: this problem was studied before especially in [48] for the special case of this trochoïdal monochromator which was rebuilt to improve the stability of the distribution over a longer range of energy. It is believed that both determination of the energy distribution should coincide.

These beliefs rely on the assumption that the rotational motion of the electrons is negligible. In fact, some simple recalculation in Part II : Chapter 1.C and the reading of [49] tell us that it might not be negligible. And even if it is very small, when considering the distribution of electrons near zero energy it is to be expected that the transverse component of the movement does not remain negligible. Due to the transverse motion it might be true that 0eV-electrons can not be achieved with the trochoïdal monochromator, and we cannot avoid missing a large part of the actual distribution when we use Cl^- for determining the electron energy distribution. It is a matter of fact that discrepancies in the determination of the distributions by the two different methods arise. Two examples were already given in the previous paragraphs which illustrate this point: in the first example of Figure 1-14, the energy distribution determined by the RFP was nicely conserved all over the range considered, but the distribution determined with Cl^- was much broader than the one determined by the RFP analysis. In the second example of Figure 1-15 and Figure 1-16, the distribution determined by the RFP knows various changes along its evolution with the energy, whereas the regular distribution determined by Cl^- at 0eV did not let envisage such an evolution.

The retarding field potential provides the energy necessary to stop electrons with a given forward velocity; it doesn't affect the transverse movement of the electrons. The transverse motion is amplified in the dispersive element (Part II : Chapter 1.C), but is not altered otherwise.

First there is no reason that both methods give identical results since the two methods do not probe the same energy components of the electron motion. The retarding field method only probes the forward kinetic energies, whereas the molecules of CCl_4 are sensitive to the total energy of the colliding electrons, including the transverse kinetic energy.

For an apparatus like the hemispherical monochromator where the electrons fly in straight trajectories, the electron energy distribution given by the two methods should be the same.

If we consider that the magnetic field is perfectly aligned with the axis of the monochromator, we can write:

$$G(E) = \int_0^{Et} g(Et) \times f(E - Et) dEt$$

Where *Et* is the translational energy provided by the electron energy generator (Ee-), $g(Et)$ designates the electron energy distribution in the forward direction, *f (E)* designates the electron energy distribution of the transverse rotational motion. The integral energy distribution is given as the convolution of these two energy distributions. It is now easier to identify the energy distributions probed by the two methods: we can expect that the distribution obtained from the Cl^- yield corresponds to the distribution of integral energy *G(E)*, whereas the electron energy distribution probed by the RFP method is *g(E)*.

IV) Effective comparison on an example

The yield of Cl^- reveals the 0eV-distribution of electrons entering the collision cell by progressively increasing the electron energy Ee-. Usually, it is assumed that the distribution at higher energy can be obtained by simply translating the 0eV-distribution. This study was initiated after the observation of frequent disagreements between the results of the gas test method (CCl_4) at 0eV energy and results of the RFP method at various Ee- energies. The RFP method is the only method able to give the evolution of the distribution over a wider range of energy. Since a reliable determination of the energy scale and energy resolution is of greatest importance for this apparatus, it is worth to re-examine both methods procedure in details on an example and show more concretely the appearance of discrepancies between the methods.

Energy distributions determined by the use of CCl_4 are presented in Figure 1-17. The distribution (a) was taken before a series of measurement of electron current drops by the RFP method, from which the distributions shown in Figure 1-18, Figure 1-19, Figure 1-20, Figure 1-21, Figure 1-22, were derived. And the distribution (b) of Figure 1-17 was taken after the series of RFP measurements. We notice that the yield of Cl- was almost unchanged during the time of experiment. Figure 1-18 to Figure 1-22 show the evolution with the Ee- of the energy distribution as determined by RFP; the Figure 1-21 gives reliability to the reproducibility of the RFP determinations by returning to low Ee-.

(1) Mirroring of the RFP distributions

In order to make the comparison, the distributions obtained by RFP must be mirrored with respect to the y-axis. Indeed, the distribution as determined with CCl_4 is first constituted by the faster incoming electrons followed by the slowest. It is the other way around with the retarding field method: first are the slowest electrons stopped by the potential barrier then are the fastest electrons stopped. As a result, the distributions of Figure 1-18 to Figure 1-22 have been mirrored in order to be properly compared to the distributions determined by the yield of Cl^-.

(2) Determination of 0eV

It is fundamental to calibrate properly the energy scale of the apparatus. Both methods can be used for this purpose. If we use the retarding field method, the energy of an electron is the energy needed to stop it. If we use the yield of Cl^-, the first moment of the distribution (of the first peak) gives the average position of 0eV, from which the rest of the energy scale can be calibrated by translation.

In Figure 1-18 to Figure 1-22:

Close to Ee-=0.35V start the current to flow through the collision cell and the Cl- to be formed in the chamber. The full current is reached at nearly Ee-=1V, it also corresponds to the end of the Cl^- distribution.

Below Ee-=1V, the full current is not reached and only a part of the complete electron distribution is analysed by the retarding field potential. From the position of RFP distribution mean a calibration for the energy scale can be derived. Some results of exact calculations are shown on some examples of Figure 1-18, Figure 1-19, Figure 1-22. These results are typical of the 0eV-determination made by RFP method on several other examples and reveal a discrepancy about the 0eV-determination obtained by the two methods.

The following observation can be made from the results of 0eV-determination by RFP:

Under $Ee^- \sim 0.85V$, the energy distribution do not follow the accelerating voltage decrease and remains invariably at the same mean position as if electrons would have the same forward

kinetic energy as they enter the collision cell whatever Ee- is applied (we see it on figure). I don't understand why!

Above Ee- ~ 0.85V, the energy distribution moves with the increase of Ee- as we can observe it from Ee- ~1V. From Ee-=1.6V, an arbitrary additional voltage was supplied by the added generator, so that the exact position of distribution is unknown. However for Ee-=3.54V, 4V and 6V, using a scan of 7V without additional voltage of the generator, we can observe the tendency of the 0eV-position to increase (+0.25V at Ee-=6V) with the energy Ee-.

More work is needed to understand the discrepancy between the determinations of 0eV from the two methods. However, something seems to be wrong with the RFP determination: the electron current start to flow through the collision cell when the Cl- ions start to be detected, and the full current is reached for an Ee- which is close to the energy marking the end of the Cl- distribution (of the first peak), indicating that the actual 0eV should be properly given by the Cl- distribution.

(3) Comparison of shapes and widths of distributions

The 0eV-distribution determined by CCl_4 in Figure 1-17 has a special peak shape. This feature makes it easier to recognize among the distributions.

It is a fact that the energy distribution determined by RFP resembles the most the 0eV-distribution determined by the yield of Cl- when the full current is reached at Ee-=1V (Figure 1-19). A proper comparison between the distributions can not be made before this value of Ee- since only a part of the full distributions is then probed by the RFP at lower electron energies. Hence, so far, the agreement is very satisfactory, and both methods agree in this case on the shape of distribution.

However, the RFP distribution knows many changes at higher energies and does not continue to match the 0eV-distribution! It was also observable on the precedent examples: the Figure 1-15 and Figure 1-16 showed that a regular distribution determined by the gas test method at 0eV (Figure 1-16) can give rise to a non trivial evolution at higher energies (Figure 1-15). So that if we can rely on the determination by the RFP, we can conclude that a determination of the resolution by means of CCl_4 is not sufficient to ensure that the energy resolution will remain stable at higher energies. And the verification of the stability of the resolution should be made every time at higher energies as well.

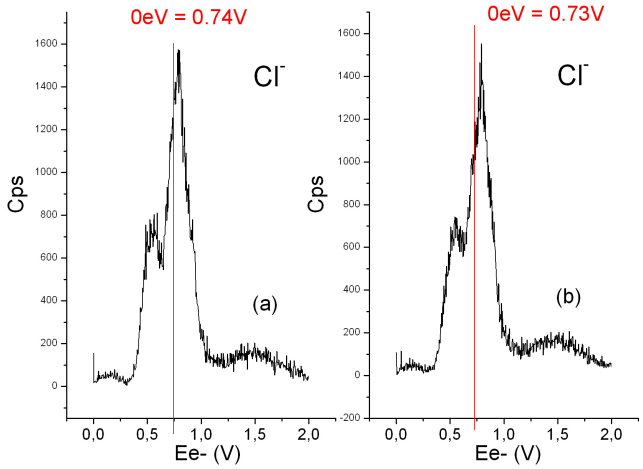

Figure 1-17: Distribution of Cl^- before (a) and after (b) the series of measurements of electron current drops from which the distributions of the next figures are derived. Hence, the determination by the gas test method is stable and the location of 0eV remained constant during the series of RFP measurements.

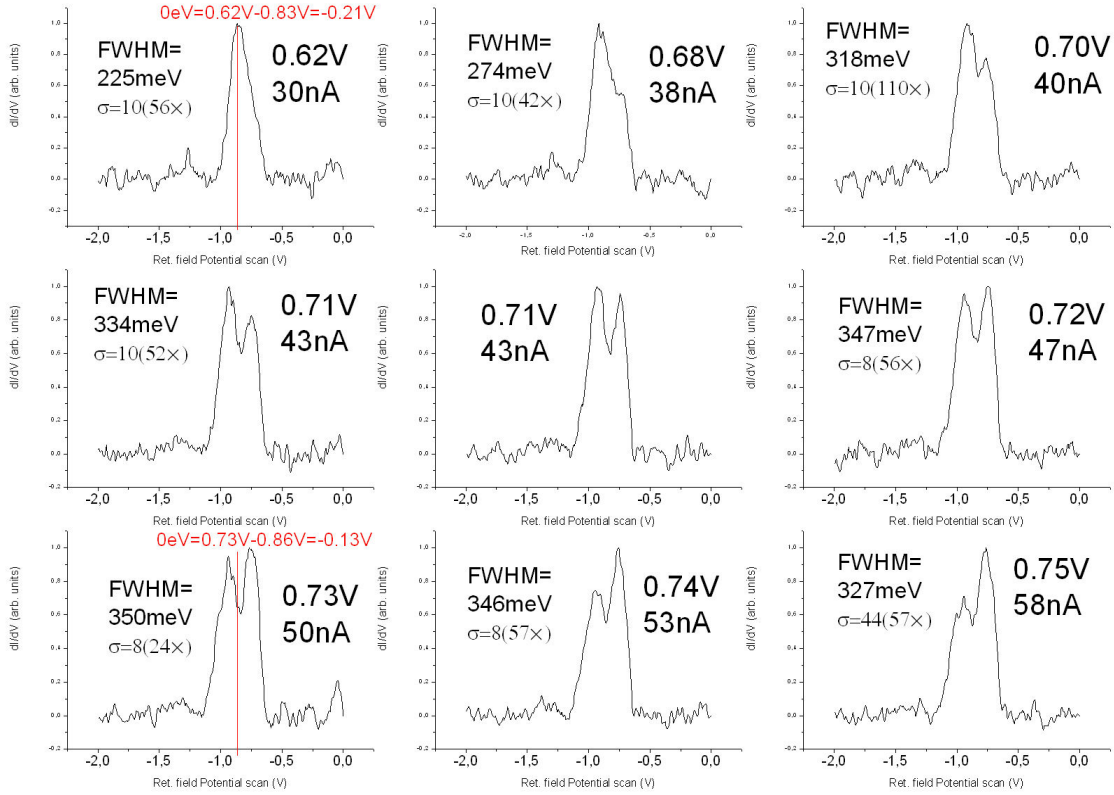

Figure 1-18: Distributions determined by the RFP for the lowest Ee-. The two distributions at Ee-=0.71V give an idea of the fluctuations from one distribution to another at one given energy. As before, the mean FWHM is determined from a set of of such distributions taken at the given energy. A RFP scan of 2V was used to derive these distributions; the additional generator was switched off. It gives the possibility to determine some mean of the distribution to obtain 0eV position from these distributions.

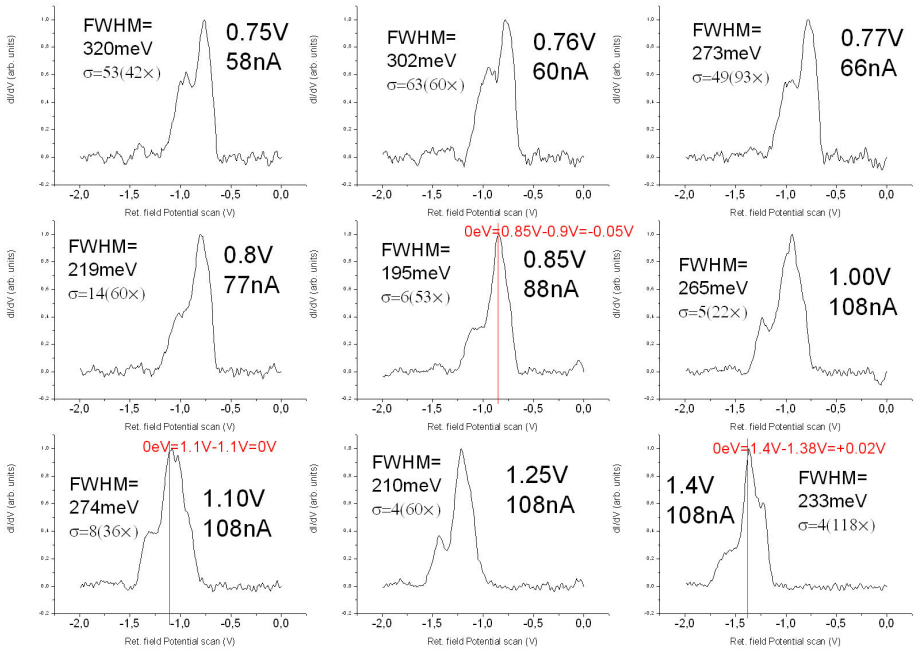

Figure 1-19: Distributions determined by the RFP for intermediary Ee-. The 2V-RFP scan was used only, and the additional generator was switched off until Ee-=1.4. It gives the possibility to determine some mean of the distribution to obtain 0eV position from these distributions.

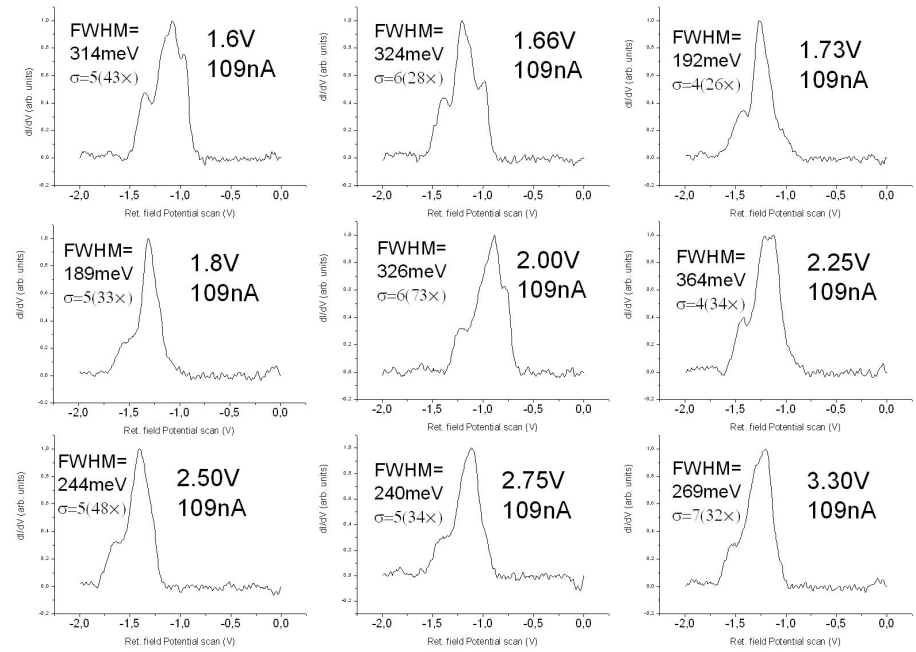

Figure 1-20: Distributions determined by the RFP for intermediary Ee-. The additional generator was switched on from Ee-=1.6V, without exact determination of the potential added, the determination of 0eV could not be performed for these distributions, only the shape of distributions can be taken into account.

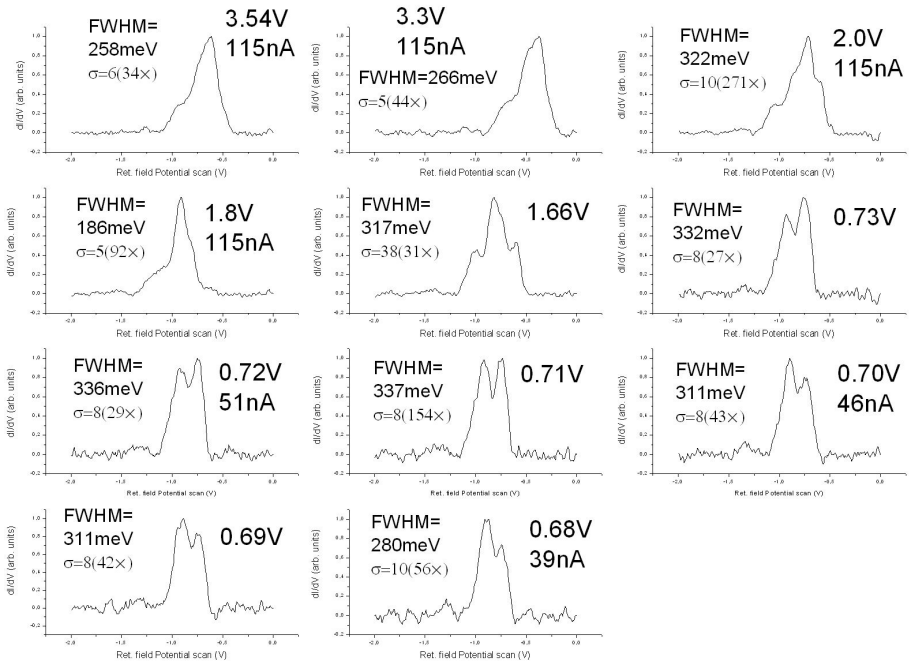

Figure 1-21: Distributions determined by RFP. Return to the lowest distributions in order to show that to any Ee- can be attributed a given energy distribution. These distributions must be compared with the first distributions obtained in the precedent figures; we notice that the general shapes are reproduced and that the mean FWHM are the same within the calculated standard deviations. It proves the reversibility of the evolution with Ee-.

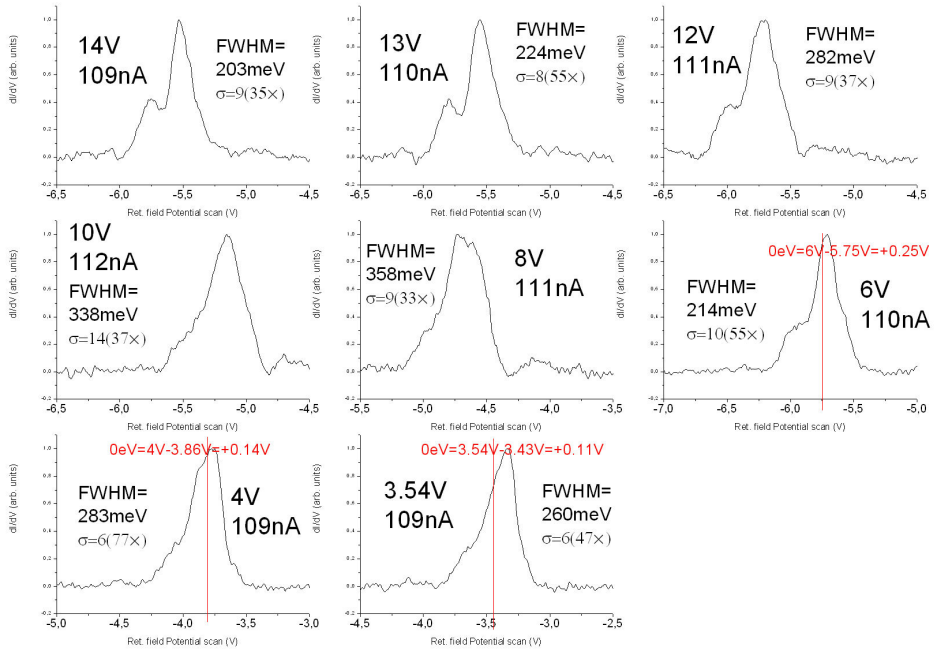

Figure 1-22: Distributions determined by the RFP method for the highest energies. A 7V- RPF scan was used, the additional generator was switched off for Ee- until 6V, making possible a determination of the 0eV position for the three lowest values of Ee-

V) Effects of extraction field

The study of the chapter 2 will show that the ion yield can be dramatically transformed by the influence of ion extraction and ion optics settings chosen. The yield of Cl- makes no exception and can also show a strong dependence as in the example chosen of Figure 1-23. In this example the distribution is broaden and a double peak structure appears when the extraction field is switched on (Figure 1-23 (b)).

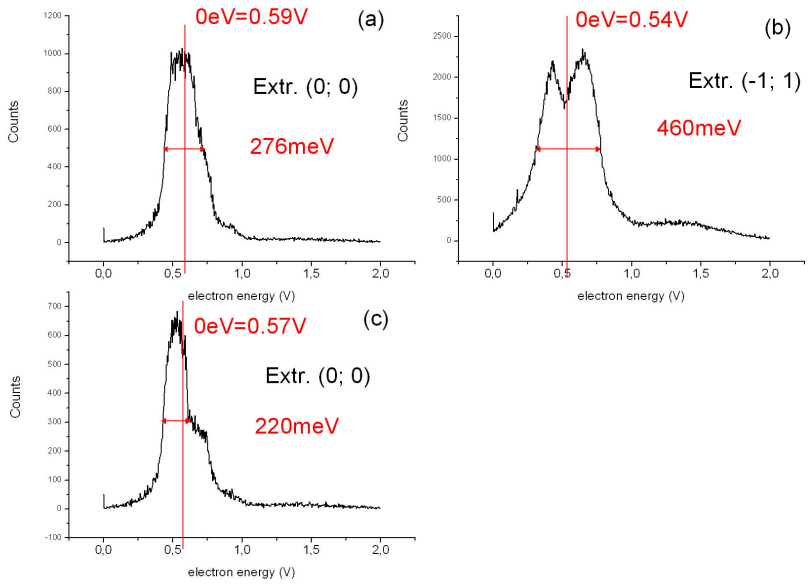

Figure 1-23: Dependence of the Cl- yield with Extraction. On this example the resolution determined from the peak of Cl- depends dramatically on the extraction applied. (a) Taken without extraction, (b) taken with (L1;L2**)= (-1;+1) extraction at identical ion optics and quadrupole settings and (c) after measurements of the current distributions of** Figure 1-24 **and** Figure 1-25 **by RFP and retour to (0;0) extraction.**

On the other hand, the distributions determined by RFP remained unchanged in position and shape when the same extraction field (L1;L2)=(-1V; +1V) was applied as shown in Figure 1-24 for Ee-=0.57V.

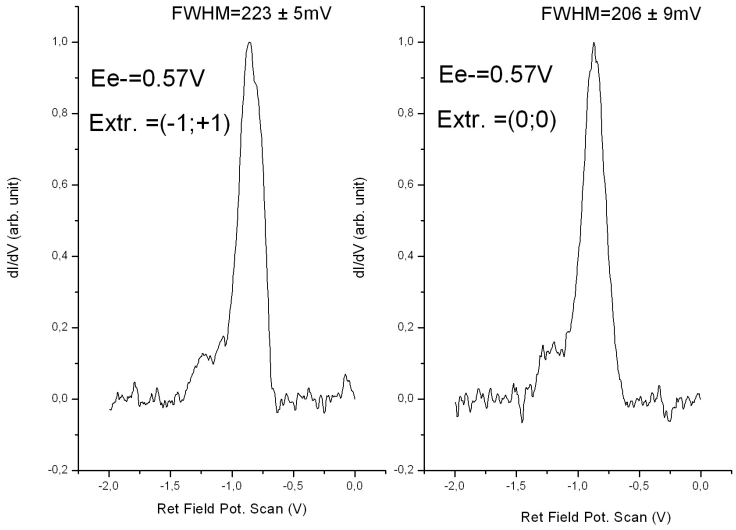

Figure 1-24: The position and width of the distributions determined from the drop of current remain unchanged after application of the extraction field (L1;L2)= (-1;+1).

However the maximal electron current intensity is largely influenced by the extraction field when electrons are slow as shown in Figure 1-25. The series of electron current drops of Figure 1-25 were taken between measurements (b) and (c) of Figure 1-23; surprisingly, the current collected in the faraday cup is enhanced when the extraction is switched on.

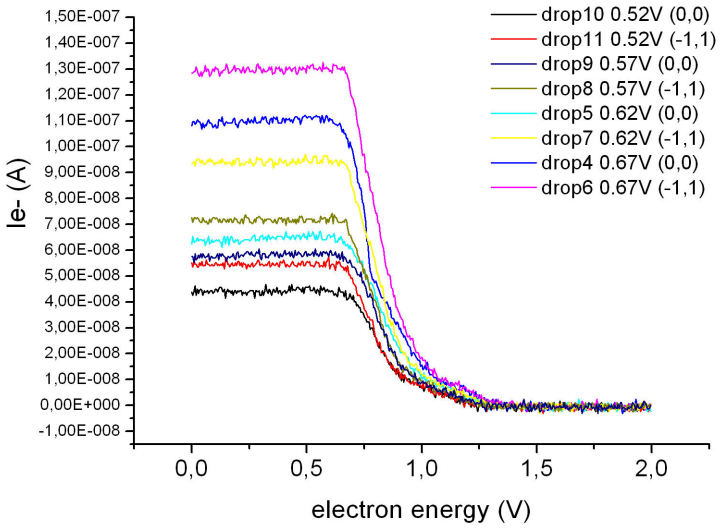

Figure 1-25: Drops of current for slow electrons.

The extraction field gives rise to a deflection of the electron beam similar to the deviation occurring in the dispersive element; slow electrons are more deflected than fast electrons. In this

case it leads to an increase of the electron current because the deflection produced might correct the trajectories of electrons which would get lost if the extraction field is not applied.

Taken another day, Figure 1-26 (b) shows again that the electron current is enhanced when the extraction field is increased. But the distributions derived from these drops (not shown) remained unchanged in position and width as for the examples of Figure 1-24 and Figure 1-25.

However, the curves of Figure 1-26 (a) taken at higher electron energy Ee-=7V, demonstrate that the influence is null when the electrons are fast enough. The mean FWHM are given in Figure 1-26 (b) for the case of slow electrons to ascertain for the stability of the distribution's width.

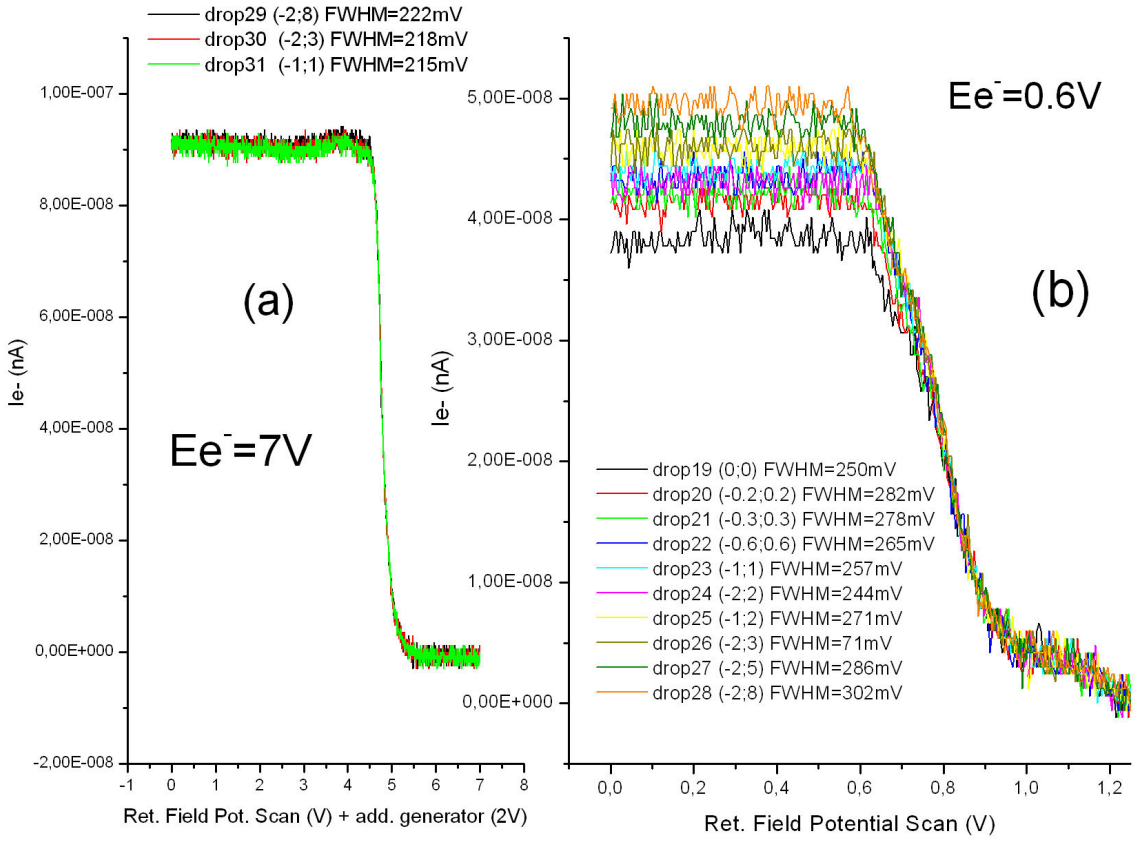

Figure 1-26: Electron current drops (27/12). Slow electrons are more influenced by the extraction lenses (b), whereas the influence is reduced when the electron energy is more important (a).

It shows that the determination of resolution from the width of the Cl^- distribution might be erroneous due to the discriminative influence of the extraction field (see chapter 2), while the determination from the RFP method shows more stability with respect the influence of the

extraction field. These observations also show that the electron current of slow electrons is influenced by small extraction fields only ((L1;L2)=(-1V;1V) in Figure 1-26 (b)), while even high extraction fields ((L1;L2)=(-2V;8V) in Figure 1-26 (a)) seem to have no influence on the fast electrons.

The conclusion of these observations is that we cannot always rely on the determination of the resolution of the apparatus by means of the gas test method using the s-wave resonance of CCl_4, which might be plagued by discriminative effects due to the use of extraction fields and during the travel inside the quadrupole mass filter.

F. Conclusion

Can we really understand the discrepancies in the determinations of electron energy distributions by the fact that the gas test method is probing the integral motion while the retarding field method only probes the forward energy of the electrons?

Both methods should lead to an agreement in the position of 0eV-energy. More work is needed to examine the determination of energy of electrons by the retarding field method.

There are agreements and disagreements between the methods and more work should be done to understand them.

Very often we are interested to have a good energy resolution in a given energy range, and, from the precedent observations, it is doubtful that the simple determination of the distribution by means of the gas test method (CCl4) is enough to ensure the determination of the distribution in the range of interest. The method of the RFP is the only which can determine the resolution of the apparatus at non zero electron energies.

The general procedure for the determination of the energy distribution should combine both previously described methods: obtaining a fine determination of 0eV energy position from the yield of Cl- since it seems to be the most reliable method for this purpose and verify that the distribution is regular and stable at higher energies with RFP method (especially verify the alignment of magnetic field).

The accuracy of the energy scale is then given by the finesse of the 0eV-peak of Cl^-.

In the chapter 3, the study of the dissociative electron attachment to water will reveal that the determination of the energy scale by use of the gas test method with CCl_4 gives excellent results. The agreement with other studies from other author is very good, and the determinations among our experiments are consistent. We performed experiments over several months in various conditions.

This study constituted first steps in the examination of this problem, which should be further examined by detailed simulations of the transformations of kinetic energy distribution in the monochromator.

Chapter 2. Study of the Discrimination in the trochoïdal monochromator

A. Introduction

During the preparation of a review on "cross sections for electron collisions with water molecules", N. Mason and Y. Itikawa [50] realized that the measurements of cross sections of dissociative electron attachment to water were 30 years old. Since it is known that many of the earlier experiments of dissociative electron attachment were plagued by discriminative effect of high kinetic energy ions, a re-measure of dissociative electron attachment cross sections to water was initiated in Innsbruck for which special care was taken to handle the problem of ion discrimination along the way to detection.

At three resonant energies, the attachement of electrons to water molecules lead to the dissociation of the water molecule according to three dissociation channel (see chapter 3). Measuring the cross sections of these processes consists in determining how many ions of a given decay channel were formed by the crossing of a beam of monoenergetic electrons with an effusive beam of water vapour. How many H^- ions were formed by the decay $H_2O^- \xrightarrow{\sigma_{H^-}} H^- + OH$, or how many O^- by the decay $H_2O^- \xrightarrow{\sigma_{O^-}} O^- + 2H$, or OH^- by the decay $H_2O^- \xrightarrow{\sigma_{OH^-}} OH^- + H$.

But, there are other processes which might interfere with the processes under consideration, and which have to be taken into consideration when determining cross sections:

- Ion- molecule reactions: the ions formed can react afterwards with another atomic or molecular species and be transformed before detection. When the pressure is high enough, the occurrence of ion-molecule reactions becomes probable: $H^- + H_2O \rightarrow OH^- + H_2$
  or $O^- + H_2O \rightarrow OH^- + OH$. OH- could be the product of ion-molecule reaction, but this question will be assessed in the next chapter.
- Electron attachement to impurities or background gases: these processes can produce similar ions and contribute to the ion yields. As an example, for our study, O^- can be formed by dissociative electron attachment to O_2 at electron energies close to the energy threshold of the first resonance of the DEA to water. As a consequence, the amount of O_2, always present in the air-background of the chamber, should be reduced to avoid the entanglement of processes.

- Electron attachment to cluster of water: the formation of water cluster cannot be excluded under the present conditions of introduction of the water vapour by the effusive beam source. This can lead to a wrong determination of the cross sections of the DEA to water, since the cross sections of the DEA to water clusters may be different in many aspects from the corresponding cross sections of the DEA to water.

The use of high vacuum conditions and care to introduce the gas under study in highest purity make it possible to overcome most of these difficulties by isolating the phenomena under study. But even when all these different production channels are taken into consideration, there are still difficulties.

This chapter deals essentially with the examination of transmission and discrimination effects arising along the way to detection in our apparatus. If we want to be able to make a quantitative study of the phenomena, we need to determine how many ions are lost along the way to detection. Indeed, most of the ions get lost in the apparatus before having being driven into the detector. In particular the extractionof the ions from the ion source into the quadrupole can be problematic.

In some experiments, extraction is used to collect all ions formed in a given collision volume. However, strong extraction is not permitted in the present apparatus since it would affect too much the beam of slow electrons from the monochromator. Therefore, only weak extraction fields can be used to enhance the amount of ions collected. Unfortunately, with such weak extraction fields, ions will get discriminated according to their kinetic energies and it can lead to significant deformation of the measured cross section curves. The influence of extraction field on the cross sections of the DEA to water will be discussed in Part II : Chapter 2.C.

Once the ions have been extracted from the chamber, they will traverse the quadrupole mass filter; where the ions are subjected to additional discrimination. Discrimination in the quadrupole however reveals to be less important than in the extraction process and it might be possible to cope with it if care is taken to properly tune the ion optics and quadrupole settings.

The focus of this work is to give an estimation of these effects and draw some general conclusions concerning the capacity of the apparatus concerning in determining absolute cross sections. If it is difficult to determine truly absolute cross sections which require a clear knowledge on the loss of ions from production to detection, it still may be possible to determine relative cross sections, which only requires that the sensitivity of the apparatus remain the same for all ions. An inspection of the different processes by which the transmission is altered was undertaken and will be discussed in this chapter.

B. Overview of the detection system

Ions are extracted from the collision chamber by a weak electric field; once repelled by the second extraction lens L_2, three focusing lenses guide then the ions toward the optical axis of a quadrupole analyser which filters the ions according to their mass to charge ratios. At the exit of the quadrupole is placed a repeller for deviating the ions into a channeltron which has been placed off-axis to avoid that neutral particles from the effusive beam contribute to the detection signal.

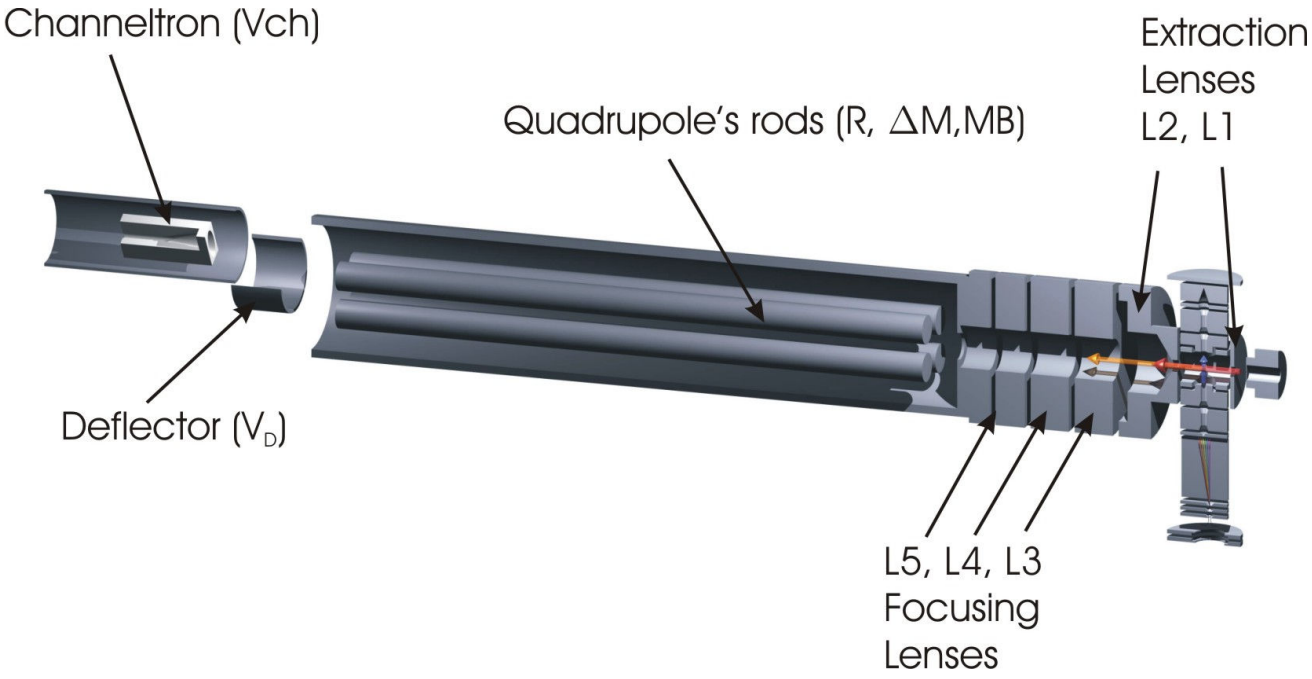

Figure 2-1 : 3D Schematic View of the Apparatus. From this view the role of the different elements of the ion optics becomes evident. The dimension of the monochromator with respect to the rest of the apparatus becomes more apparent having in mind that the quadrupole's rods are 20cm long. The monochromator is directly mounted on the system of detection.

Figure 2-1 gives a complete overview of the detection system.

I) Element by element

L1 and L2 are the extraction lenses; a weak extraction field can be applied by their intermediary to extract the ions from the collision chamber. L2 is determining the ion energy (IE) gained by the ions between the exit of the chamber and the entrance of the quadrupole set at ground potential.

L3, L4, L5 are the focusing lenses, they are operated as an einzel lens. Their role is to focuse the beam of ions towards the entrance of the quadrupole. Ions should be injected into the quadrupole as close to the optical axis as possible. They also influence the transverse velocities of the ions.

Moreover it is possible to apply perpendicular fields in the normal directions by the intermediary of the Lenses L3 and L4, which have been splitted for this purpose, in order to correct an eventual bending of the ion beams. This possibility was not needed during our experiments.

The parameters R, ΔM, MB define the resolution in the quadrupole. R and ΔM are parameters corresponding to the buttons on the control panel of the extranuclear power supply. R determines the slope of the operating line in the stability diagram and ΔM has the effect to translate the operating line towards a higher or lower resolution region in the stability area (see Part II : Chapter 2.D.I)). MB designates the mass button of the control panel of the power supply. Its position is crucial when a cross section is taken as it defines the exact position of the point of functioning in the stability area.

V_D designates the voltage of the deflection plate. Placed before the detector, its role is to deflect the ions exiting the quadrupole into the channeltron.

Vch designates the high voltage applied between the entrance and the end of the channeltron. Besides its role to polarize the detector, Vch creates a deep potential well which attracts the ions. Vch was set to very high value of 0.7×4kV=2.8kV during our study because the detection of OH^- ions was too low otherwise.

Hence, a 10-tuple is completely defining the ion optics of the apparatus:

(V_{L1};V_{L2};V_{IE};V_{L3};V_{L4};V_{L5};V_D) is given as indication of the ion optics conditions under which an experiment was performed. The other parameters (R;ΔM;MB) are given independently when it is necessary and V_{CH} remains almost always constant at 2.8kV. V_{L1}, V_{L2}, V_{L3}, V_{L4}, V_{L5}, designate the potential applied to the extraction lenses L1 and L2, and to the focussing lenses L3, L4 and L5. V_{IE} designates the potential of L2 with respect to the ground, it corresponds to the ion energy (IE). And, V_{L2} designates the potential of L2 with respect to the other part of the monochromator and L1 in particular. V_D is the potential of the deflection plate at the exit of quadrupole.

II) Definition of two types of ion optics settings for the study

We can define two different types of settings for the focussing lenses: settings of the type “retarding einzel lens” (RET) and the settings of the type “accelerating einzel lens” (ACC). The definition of these type of settings are related to the analogy between our three lenses of focussing and an einzel lens: according to [51], an einzel lens is made of a retarding (or accelerating) tubular electrode that is sandwiched between two other tubular electrodes both of which usually are at

ground potential. More generally, the first and last electrode do not have to be at the same potential: "such a lens would achieve an overall ion acceleration or deceleration in the z-direction defined by the potential difference between the first and last electrode and a lateral focusing in the x- and y-direction which is mainly controlled by the potential of the centre electrode." This describes the case of our three focalisation lenses L3, L4, L5 connected to independent generators which can deliver voltages between -150 and +150 volts.

The Figure 2-2 shows an einzel lens of the "retarding type" (for positive ions). The focusing forces are more effective for tise setting since the ions are slower in the middle of the lens, so that, overall, the retarding lens is focusing. If one would inverse the polarity of the lenses, one would obtain an einzel lens of the "accelerating type": inversely, the focusing forces would act in the side regions and the defocusing forces in the centre. Since, however, in this case the ions move slower in the side regions, the focusing forces are again more effective than the defocusing forces and the "accelerating einzel lens" is overall focusing as well.

It is a matter of fact that we can always optimize the ion signal by setting the focusing lenses L3 , L4, L5 to resemble an einzel lens of the retarding type (.,-,.) or of the accelerating type (.,+,.) (for negative ions). However, the ACC type of focusing gives a larger ion signal than the RET type. Therefore, we will refer in the following of this chapter to the ACC type of focusing when the configuration $(L3, L4, L5) \equiv (...,+,...)$ resembles the more an einzel lens of the accelerating type and to the RET type of focusing when it resembles an einzel lens of the RET type as $(L3, L4, L5) \equiv (...,-,...)$.

The transmission in a quadrupole depends strongly on the initial conditions of the entrance of the ions. The role of the focusing lenses L3, L4, L5 is to focus the ions as close as possible to the center of the quadrupole's entrance with as little transverse kinetic energy as possible. However depending on the quadrupole settings (R;ΔM;MB), the sensitivity of the quadrupole to the initial conditions varies, and thereby the influence of focusing. The change of focusing from the "ACC" type to the "RET" type represents important changes for the focusing even if both correspond to a local optimization of the ion signal. Even if optimized ion signal settings can be found for both type of focusing, it is expected that the focusing differs in many aspects in each case, and as a result that both settings bring the ions into different initial conditions at the entrance of the quadrupole. It is the effect sought after for systematically testing the influence of ion optics on the cross section yield. In fact, ions with very different transverse kinetic energies will not be focussed in the same conditions at the entrance of the quadrupole by the same ion optics settings. In regions of high sensitivity regarding the initial conditions the influence of ion optics settings should be felt more strongly than in regions of less sensitivity. These effects will be discussed in (Part II : Chapter 2.E.V)).

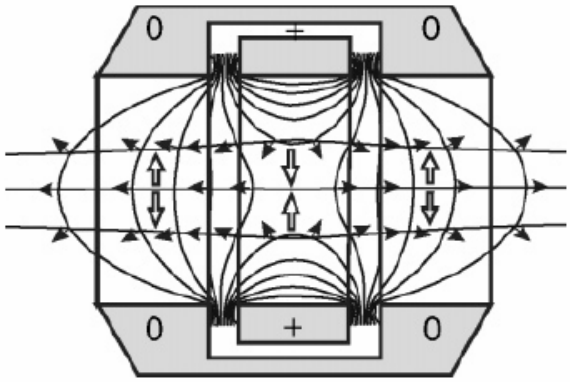

Figure 3. A 'retarding Einzel lens' built from three concentric tubular electrodes held at different potentials. The main effect of the Einzel lens shown is that the ion velocity is drastically decreased in the first half of the lens and then drastically increased again in the second half. The decelerating and accelerating forces are illustrated by small black arrows which indicate the directions of the forces on positively charged ions. These forces have small components perpendicular to the optical axis, the *z*-axis. In the first and the last section of the Einzel lens, these forces are defocusing and drive the ions away from the optical axis, while in the middle region these forces drive the ions toward the optical axis and thus are focusing. The overall effect of these forces is indicated by the hollow arrows. Since these forces toward and away from the optical axis are of comparable magnitude, they are most effective in the middle region where the ions are slow and consequently spend most of their time. For this reason the lens shown is overall focusing. Note here also that the potential of the middle electrode must be close to the potential of the ion source if the lens is to be effective.

Figure 2-2 : Taken from [51]. It illustrates the principle of functioning of an Einzel Lens.

C. Extraction from the collision cell and discrimination

In this section we look at the influence of the extraction field on the cross section, particularly we are concerned with the strong discriminative effects able to deform the measured cross section in some conditions.

The ion extraction efficiency from the collision cell of our apparatus has been studied previously in [52]: simulations of ion trajectories using the program SIMION were performed. The creation of the ions was assumed to take place in the middle of the collision cell and the initial kinetic energies of the ions were distributed isotropically (step of 0.5°, range of initial kinetic energy went from 0-10eV). Figure 2-3 displays the result of the simulations for O^- and O_2^- ions: the influence of the mass is negligible, similar results were obtained for ion masses up to 100amu.

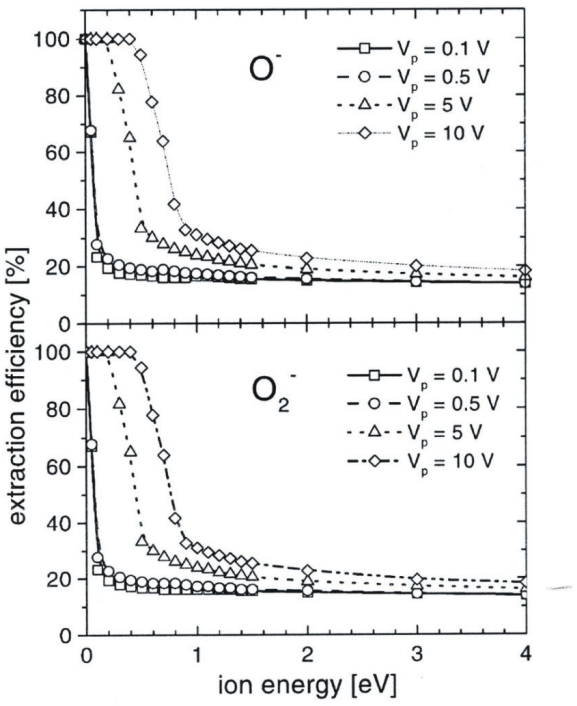

Figure 2-3 : Taken from [52]. Simulated Extraction efficiency for different extraction forces ($Vp=V_{L2}-V_{L1}$) as a function of the initial ion kinetic energy.

It is only possible to extract all ions of up to 0.4eV kinetic energy when the maximal extraction voltage is applied. However, the kinetic energies released by the ions can easily exceed 0.4eV (at least in the case of O^- ions produced by the DEA to water), and the application of strong extraction voltages will lead to deformation of the measured cross sections due to discriminative effects as will be observed in the following paragraph. Strong extraction fields also have a large influence on the monochromatized electron beam, as they deteriorate the energy resolution and hence such conditions should be avoided in any cases.

Therefore, the cross section will be plagued by discriminative effects as soon as we are going to apply an extraction voltage and ions will be extracted or not according to their initial kinetic energies. This means all slow ions will be extracted whereas fast ions will most probably finish their course in the wall of the collision cell except if they are flying inside the solid angle determined by the exit (i.e. if their initial kinetic energy of formation is pointing inside the solid angle determined by their position of formation and the exit aperture of the lense L2).

To minimize the effect of discrimination one should use no extraction voltage at all, which means collecting only the ions flying naturally towards the exit aperture. The disadvantage of zero extraction voltage is at the price of reducing considerably the ion signal. The ratio of extracted ions to all ions produced is estimated to be a bit less than 20 % when the extraction is switched off

according to the simulations of [52]. We can expect to detect even less ions in the real experiment since the ions are formed along a line across the collision cell determined by the electron beam and not in the middle of the cell as it was supposed in the simulation.

I) The Lense responsible for extraction

The lenses designed in the present experimental-set-up to control the extraction of the ions from the production region are L1 and L2 (see Figure 2-1). However, it can be shown that L2 is the only lens which really determines the extraction force.

It can be shown (Figure 2-4) that L2 is the only lense which predominantly determines the extraction force: in the example of the measured ion yield of O^- produced by DEA to heavy water, several experiments were performed successively to study the effect of the extraction lenses L1 and L2. Almost no difference in the ion yield could be observed after changing the voltage of L1 from -1 to 0 Volt while keeping L2 at +1Volt, and only a slight difference was observed passing from (L1;L2)=(-2V;+2V) to (L1;L2)=(0V;+2V). This demonstrates that the lens L1 is almost ineffective in comparison to L2.

This shows also that the extraction voltage cannot be defined as the difference between the potential of L1 and L2.

Also at lower extraction forces, the influence of L1 on the extraction is negligible i.e. changing L1 from (L1;L2)=(-0.2V;0.2V) to (L1;L2)=(0V;0.2V) in Figure 2-4. However, we have seen in the previous chapter that L1 has a rather strong influence on the electron beam.

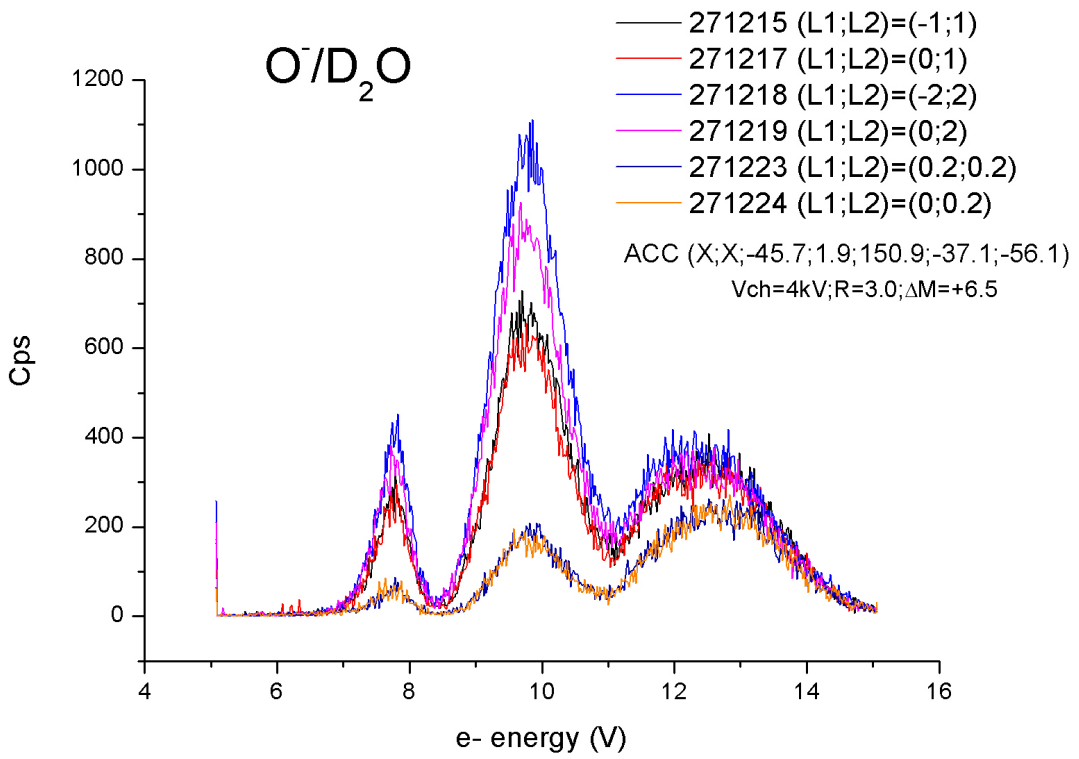

Figure 2-4 : Lens L1 which should repel the ions is almost ineffective: the two curves taken at (L1;L2)=(0.2V;0.2V) and (L1;L2)=(0V;0.2V) exactly superimposed, almost no difference in ion yield observed by changing from (L1;L2)=(-1V;1V) to (L1;L2)=(0V;1V), and only a small difference could be observed by changing (L1;L2)=(-2V;2V) to (L1;L2)=(0V;2V).

The deforming effect of the extraction conditions on the measured cross section curves as observed in Figure 2-4 is the subject of the next paragraph.

II) Effect of extraction conditions on the cross section

This paragraph presents the study of the influence of extraction conditions on the measured cross sections for the formation of O^- and OH^- (resp. O^- and OD^-) from the DEA to H_2O (resp. D_2O).

(1) Influence on the measured cross sections of the DEA to H_2O.

Figure 2-5 shows the evolution of the relative intensities of OH^- resonances attributed to the DEA to H_2O. The conditions of electron current and water pressure were stabilized during the whole experiment, so that a direct comparison of yield intensities is possible.

The first resonance is fast increasing with the increase of the extraction force: already a small extraction (L1;L2)=(-0.2V;0.2V) doubles the height of the first peak. A similar effect of a small extraction force on the shape of the measured cross section can be seen in this paragraph for several examples.

We observe in Figure 2-5 that the intensity of the third peak doesn't change from (L1;L2)=(-0.4V; 0.4V) independently on the extraction force no more ions were extracted. This may be the case because we have already extracted all ions formed or because we cannot extract more ions even when increasing the extraction force. By considering the yield without extraction of Figure 2-5 (a) which should represent roughly 20% of the total ions formed in the chamber according to [52], we conclude that we cannot extract more ions because their kinetic energies are too high and the extraction force available is not strong enough.

Figure 2-6 shows the relative increase in ion intensity for the three different resonances shown in Figure 2-5. We can observe that the peaks grow faster at the beginning (L2<0.5V) and that a regime of slower constant increase starts after this short fast increase. The slope of the curve can be associated with the average kinetic energy of the OH^- ions composing the peak. The bigger the slope, the easier we can extract more ions, thus the lower is the average kinetic energy of the ions. The extraction force is measured by indicating only the voltage applied on the lens L2 since this lens determines almost completely the force of extraction as we have seen in the previous paragraph.

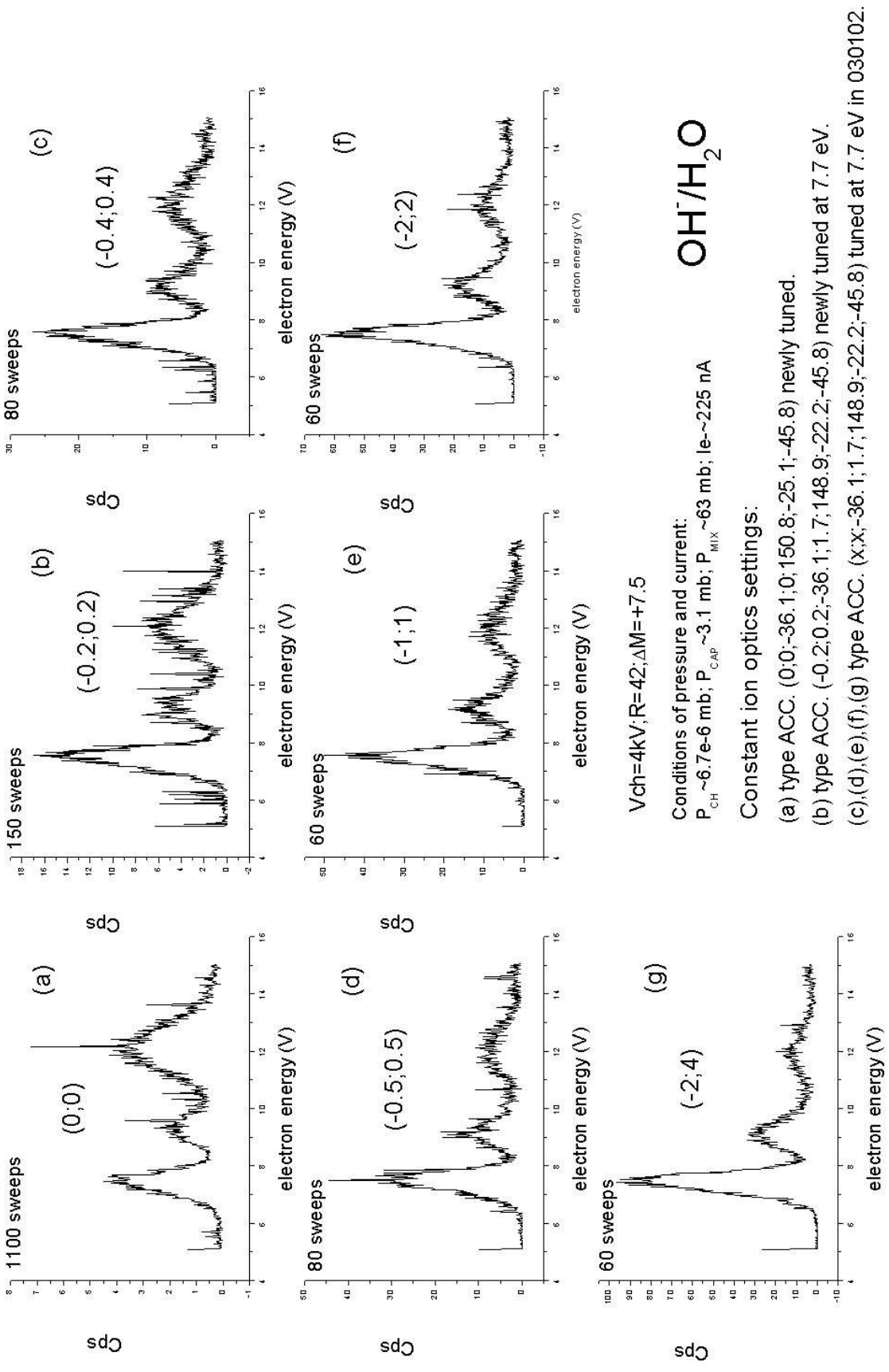

Figure 2-5 : Variation of peaks intensities due to the change of extraction forces for OH-.

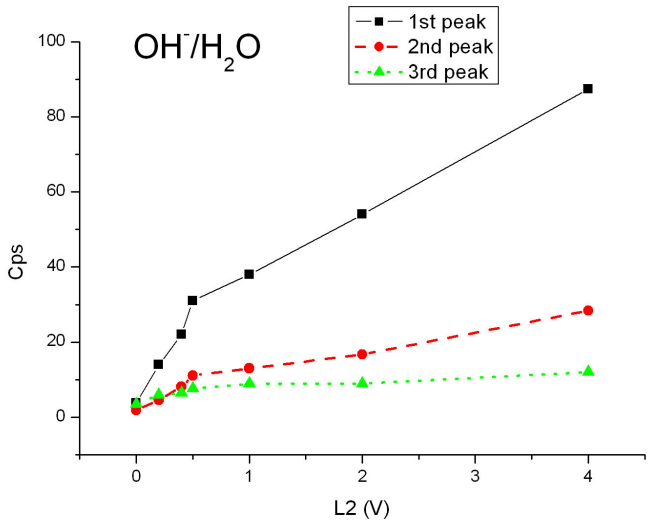

Figure 2-6 : Growth of the OH^- resonant peaks when the extraction force is increased.

Similarly, Figure 2-7 displays the evolution of peaks intensities of the O^- resonances of the DEA to water. Again we notice that the third peak is almost constant once we have reached the extraction force (L1; L2) = (-0.5V; 0.5V). This reveals that this peak is made by ions released with a high kinetic energy at their formation, exceeding the available extraction power.

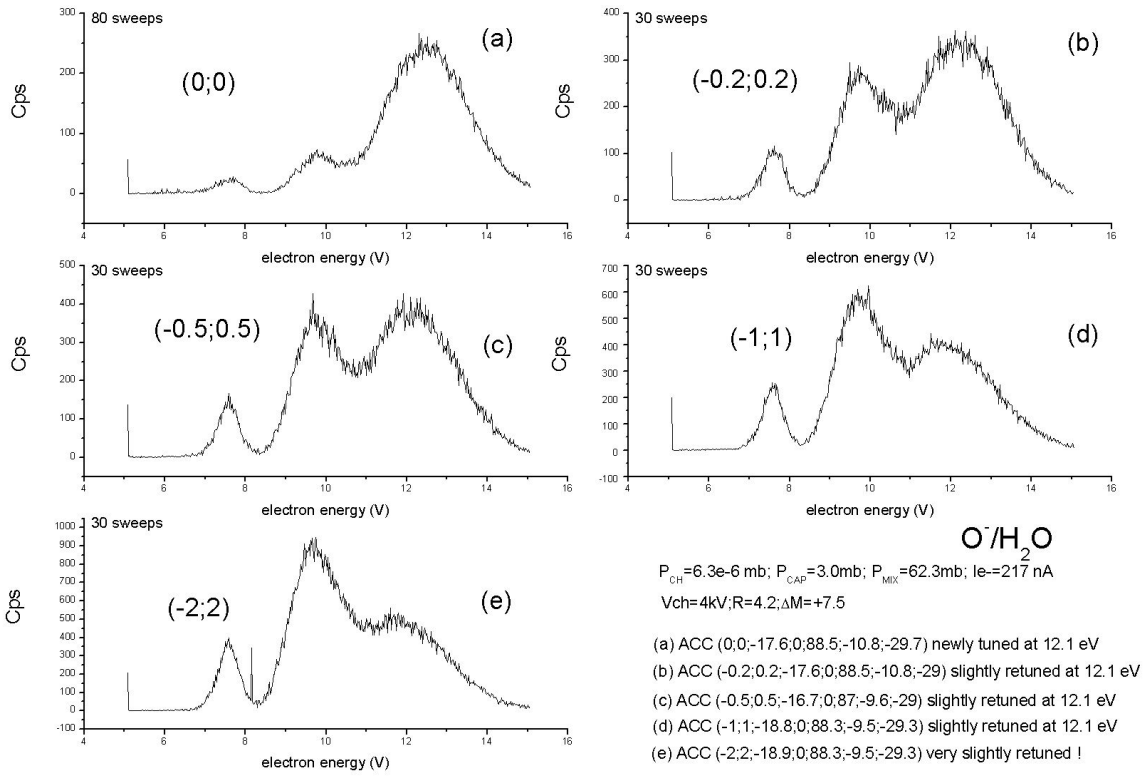

Figure 2-7 : Variation of peaks intensities due to the change of extraction forces for the yield of O-.

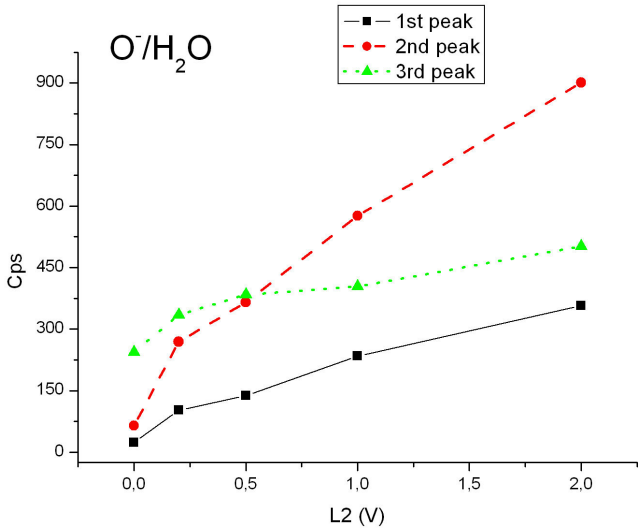

Figure 2-8 : Growth of the O^- resonant peaks when extraction is increased.

In Figure 2-8, the growth of peak intensities as a function of the extraction force is shown for O^- from H_2O, it reveals different energy contents than for the OH^- resonances: the third peak is again the most difficult to extract because the ions have too high initial kinetic energies, while the second peak is easier to extract than the first peak revealing that the average kinetic energy associated is lower than the average kinetic energy associated with the first one.

(2) Influence on the measured cross sections of the DEA to D_2O.

Figure 2-9 shows the deformation of the measured cross section for the OD^- yield attributed to the DEA to heavy water. Figure 2-10 shows the associated curves of the evolution of the peaks intensities.

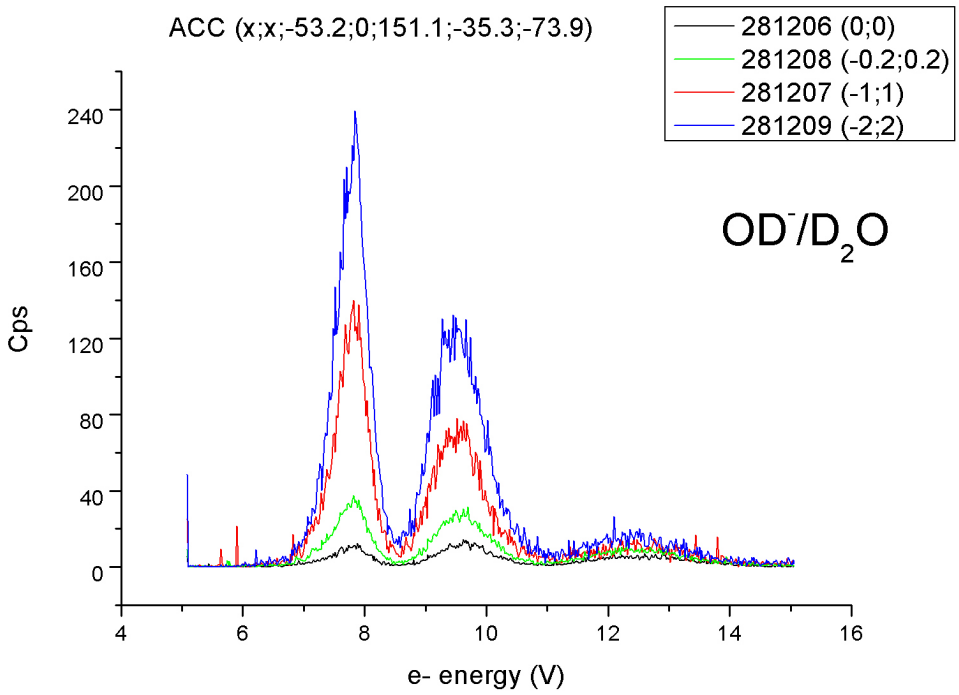

Figure 2-9 : Variation of peak intensities due to the change of extraction forces for the yield of OD-.

The results are similar to the results obtained for the normal water. The fast growth of the peaks for low extraction force seems to be less apparent for the deuterated water, as can be seen in Figure 2-10.

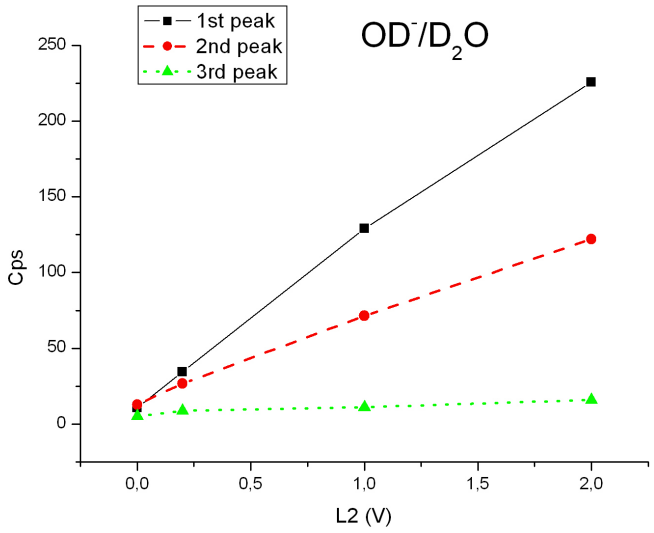

Figure 2-10 : Growth of the OD- resonant peaks when extraction is increased.

In the following the influence of the extraction field on the O- yield from heavy water is discussed.

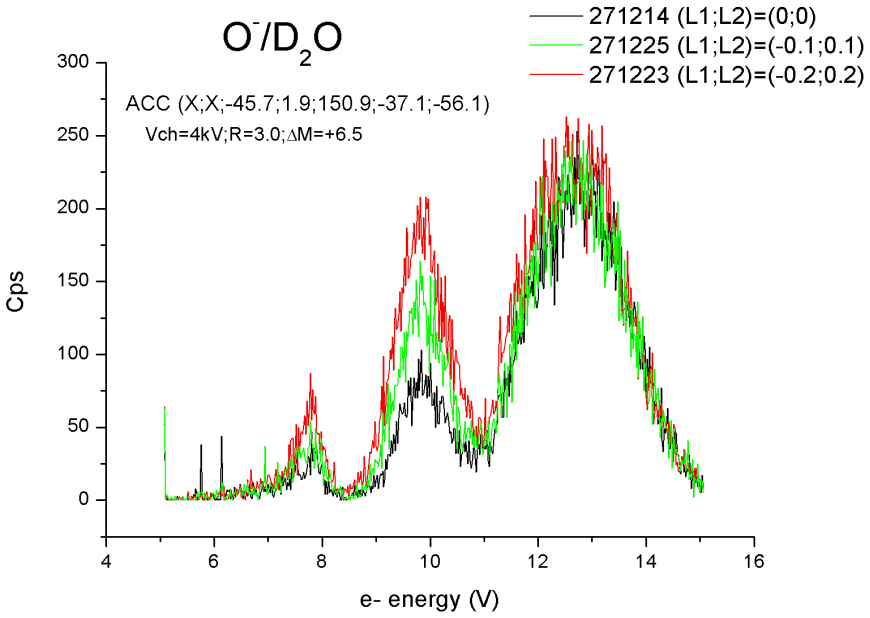

Figure 2-11 : Even small extraction fields applied deform significantly the cross section.

Figure 2-11 shows that even small voltages applied to extract ions can modify the cross section measured. The second peak doubles its initial height when an extraction voltage of only (L1; L2) = (-0.1V; 0.1V) is applied. As a consequence, the extraction should be switched off when measuring cross sections for the purpose of measuring more faithful cross sections, the extraction must be switched off.

Figure 2-12 displays the evolution of the cross sections as a function of extraction force. The growth of the peaks is similar as in the case of normal water.

Figure 2-13 shows the evolution of peak intensities, the range of the extraction force is longer than in the study of normal water (Figure 2-8). From the evolution shown in Figure 2-13 two rates of growth are distinguishable, a fast one for low extraction forces until (L1; L2) = (-2V; 2V) and a slower one for higher forces. This change of rate could not be observed in the case of normal water in Figure 2-8 (O- from water) since in this experiment the extraction was varied till (L1; L2) = (-2V; 2V). It might be a characteristic of such curves but more work is needed to know what information we could extract from Figure 2-6, Figure 2-8, Figure 2-10, Figure 2-13.

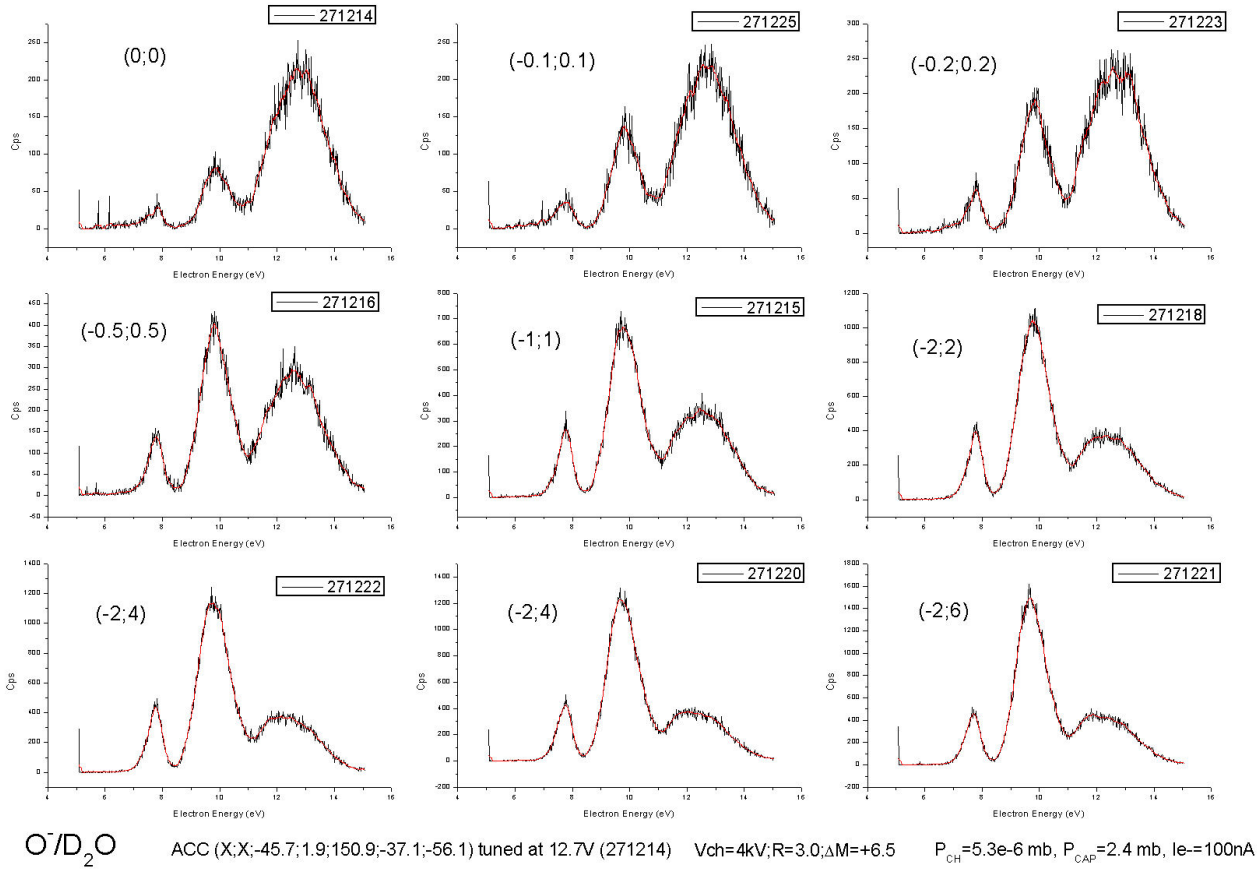

Figure 2-12 : Variation of peaks intensities due to the change of extraction forces for the yield of O^- from D_2O.

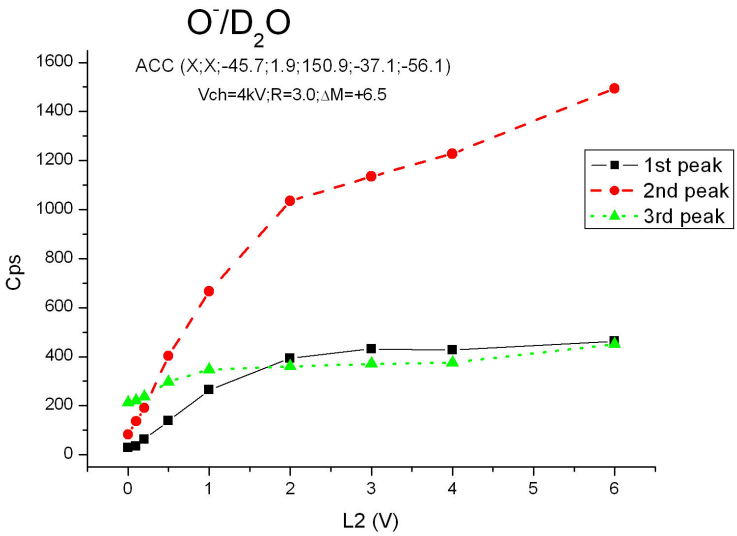

Figure 2-13 : Growth of the O^- resonant peaks from D_2O when extraction is increased.

If the curves of Figure 2-13 reflect the kinetic energy content of the peaks we can say that from L2=2V on more ions products of the first and third resonance can not be more extracted because their kinetic energy is too high, whereas the ion intensity of the second peak still increases with increasing extraction forces, indicating that the kinetic energy release of its product ions is lower.

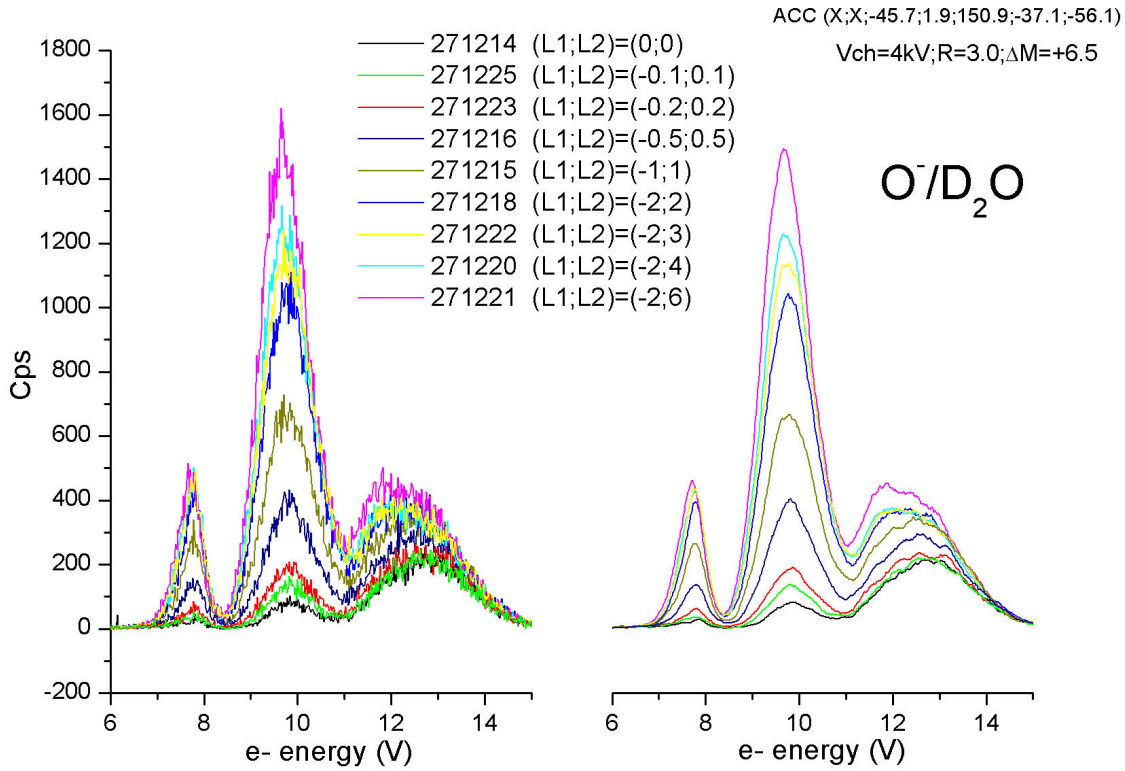

Figure 2-14 : Comparison of the peak shapes as a function of extraction. The smoothed yields are redrawn in the right graph for better reading.

In Figure 2-14 we observe the change of the shape of the third peak when the extraction force is increased: the intensity at the low energy side of the peak is slightly more enhanced at higher extraction than at the high energy side. This effect is due to the overlap with the second peak which contributes to the beginning of the third peak.

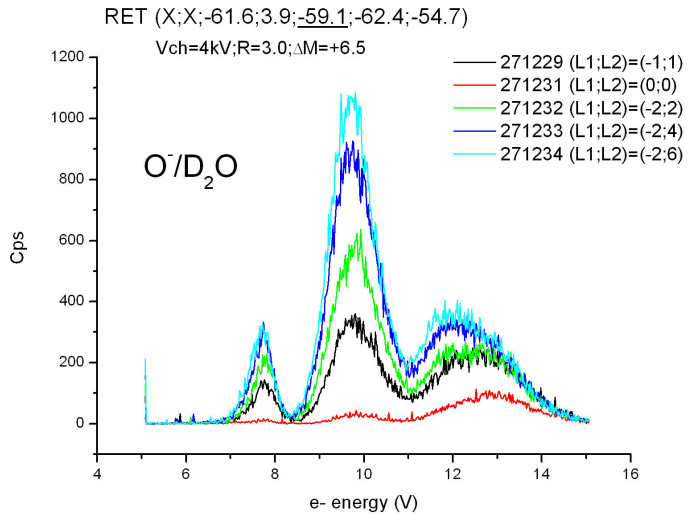

Figure 2-15 : Variation of peak intensities due to the change of extraction force for the yield of O^- from D_2O using RET type of focusing, to be compared to results obtained with the ACC type.

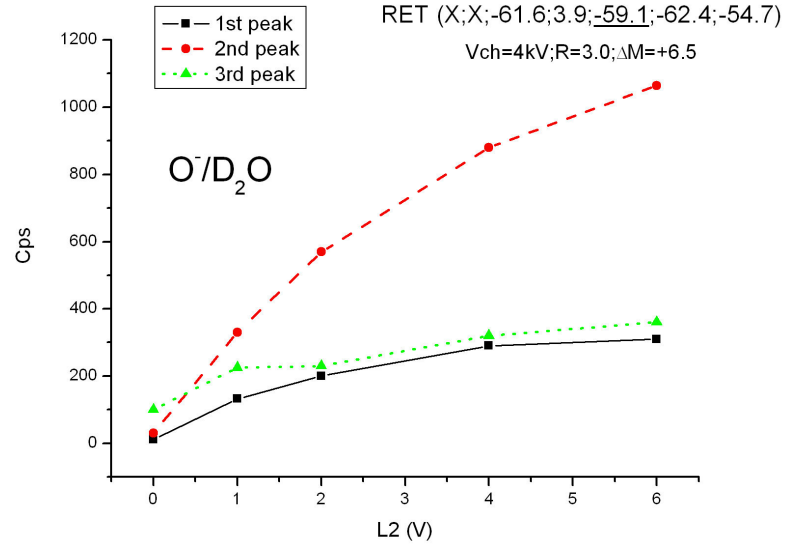

Figure 2-16: Growth of Peaks height of O^- from D_2O when using RET type of focusing. Similar results as for the focusing ACC type.

The change of ion optics to the RET type of focusing does not seem to have a great influence on the rate at which peaks are growing when the extraction is increased: Figure 2-16 shows an evolution of peak intensities which is similar to the one of Figure 2-13 for the ACC type of focusing.

However, differences in the evolution exist when the ion optics is changed. Cross sections obtained at identical extraction force and identical quadrupole settings but with different ion optics are shown in Figure 2-17. Extraction brings ions in different initial conditions with greater transverse kinetic energies at the entrance of the quadrupole mass filter, so that the discriminative effects might

be stronger when the extraction is used. As a consequence the influence of the ion optics is expected to be greater when extraction is used as illustrated in Figure 2-17. Unfortunatly, the position in the stability area of the quadrupole (see section Part II : Chapter 2.D.I)) was not fully determined at the time when this study of the influence of ion optics on cross sections as a function of extraction was done. Therefore, we are unable to estimate how strong the effects shown in Figure 2-17 depend on the position in the stability area and if they could be reduced.

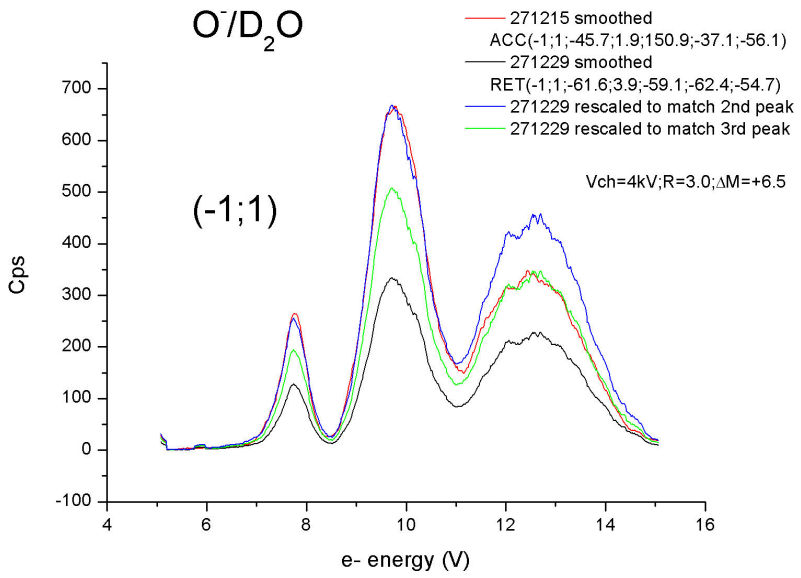

Figure 2-17 : Example of the influence of ion optics on the cross section when extraction is applied.

The significance of Figure 2-6, Figure 2-8, Figure 2-10, Figure 2-13 and Figure 2-16 concerning the kinetic energy distribution of ions is unclear. The influence of the discrimination in the quadrupole must be taken into account. If the quadrupole resolution settings and ion optics are well tuned, it might be possible to minize the discrimination as will be shown in Part II : Chapter 2.E.V)(2) and determine if less dependence on ion optics settings can be achieved. In such case, a study of peaks intensities with extraction could be more reliably related to the kinetic energy of the ions. Anyway, cross sections undergo less dramatic changes due to discrimination in the quadrupole than those observed by the application of extraction fields. And we can expect that the peaks intensities as a function of extraction give an indication of the differences of kinetic energies released between the resonant processes.

The discrimination occurring in the quadrupole is complex and will be analysed in details in the rest of this chapter. For the rest of this study, it must be stressed out that the results of Figure 2-7 and Figure 2-8 concerning the yield of O^- from H_2O were obtained with a constant effort to readapt the ion optics to the changes of extraction force applied whereas the measurement of O^- yields from D_2O of Figure 2-15 and Figure 2-16 were performed at constant ion optics. Nevertheless nearly the same evolution with increasing extraction force was observed in both cases. However, the precise

position in the stability area was also unknown for the measurements of Figure 2-7 and we might have been positioned at the border of the stability area (see Part II : Chapter 2.D.II)(1)). Further results on the dependence of cross sections on ion optics settings when the extraction is applied are given in Part II : Chapter 2.D.III)(2).

(3) Conclusion

In order to have an equal sensitivity for all types of ions, extraction must be switched off, otherwise the measured cross sections can be dramatically deformed.

More work is needed for the interpretation of Figure 2-6, Figure 2-8, Figure 2-10, Figure 2-13 and Figure 2-16 concerning the ion kinetic energy distribution of the resonances. But tendencies can be determined which constitute already precious information on the phenomena.

D. Discrimination in quadrupole

I) Theory of Quadrupole mass spectrometer

(1) Principle of functioning of the quadrupole: theory

The principle of a quadrupole mass spectrometer is to exert the combination of a high-frequency and a low-frequency field by the intermediary of four hyperbolically shaped electrodes on a bundle of incoming ions in order to drive them into unstable or stable trajectories according to their mass to charge ratio. Indeed, if we define the potential as being $\Phi(t) = (U - V\cos\omega t)$ on one pair of opposite electrodes, and $-\Phi(t) = -(U - V\cos\omega t)$ on the other pair of electrodes; rf-only quadrupoles (U=0) act as high-pass mass filters that eliminates all low-mass ions. Adding, however, to the AC-voltage V of the electrodes also a DC-voltage U, all very high-mass and all very low-mass ions are sent into unstable trajectories which finally end on one of the electrodes. The Figure 2-18 shows the hyperbolic potential lines formed by the application of the potential $\Phi(t)$ on the electrodes.

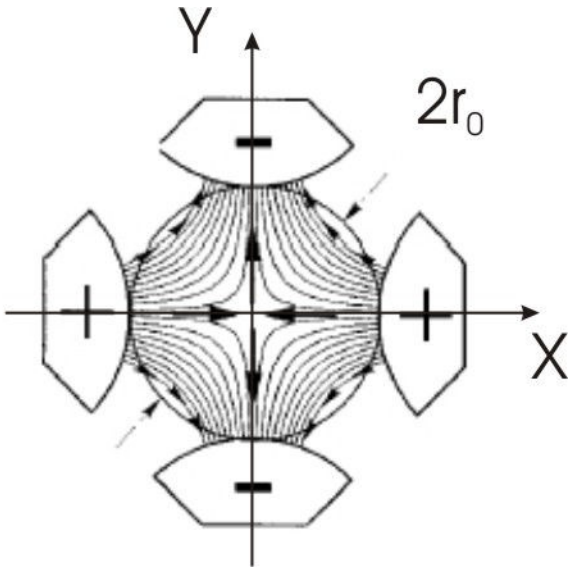

Figure 2-18 : Cross section through an electrostatic quadrupole lens. The focusing and defocusing forces acting on a positive ion are indicated by the black arrows: at a given time, the quadrupole exerts, in the transverse plane, a focusing force in one direction and a defocusing force in the perpendicular direction. Reproduced from [51].

In the transverse plane of motion, the potential formed by hyperbolically shaped electrodes is equal to:

$$\Phi(x,y,t) = \frac{(U - V\cos\omega t)(x^2 - y^2)}{2r_0^2} \qquad 2\text{-}1$$

The resulting force applied on the charged particles is derived by $\vec{F} = q\vec{E} = c\left(-\frac{\partial\Phi}{\partial x}\vec{e}_x - \frac{\partial\Phi}{\partial y}\vec{e}_y\right)$.

Hence the equations of motion of a charged particle entering the quadrupole field are:

$$m\ddot{x} + (U - V\cos\omega t)\cdot 2c\frac{x}{r_0^2} = 0 \qquad 2\text{-}2$$

$$m\ddot{y} - (U - V\cos\omega t)\cdot 2c\frac{y}{r_0^2} = 0 \qquad 2\text{-}3$$

$$m\ddot{z} = 0 \qquad 2\text{-}4$$

r_0 is the radius of the inscribed circle between the rods, its value in our quadrupole is 4.11mm, c designates the charge of the particle and m its mass, x and y are the coordinates in the transverse plane as indicated in Figure 2-18, z is the coordinate along the optical axis of the quadrupole.

By making the change of variable $\frac{\omega t}{2} \to \theta$ and introducing a generic variable X= x or y, the equations 2-2 and 2-3 are put in the form which is called Mathieu's equation:

$$\frac{\partial^2 X}{\partial^2\theta} + (a_X - 2q_X\cos 2\theta)X = 0 \qquad 2\text{-}5$$

Where the coefficient a_X and q_X have the values:

$$a_X = a_x = -a_y = \frac{4cU}{m\omega^2 r_0^2} = a \qquad 2\text{-}6$$

$$q_X = q_x = -q_y = \frac{2cV}{m\omega^2 r_0^2} = q \qquad 2\text{-}7$$

r_0^2 and ω^2 remain constant during the operation of our quadrupole, ω is the pulsation of the rf-voltage determined during the procedure of matching of the resonant frequencies of the different parts of the quadrupole system (when the High-Q-Head of the quadrupole is changed for instance), and held fixed afterwards.

The solution of the Mathieu's equation can be written in the form:

$$X = k_{+} e^{i\beta\theta} \sum_{p=-\infty}^{+\infty} C_{2p} e^{2ip\theta} + k_{-} e^{-i\beta\theta} \sum_{s=-\infty}^{+\infty} C_{2p} e^{-2ip\theta} \qquad 2\text{-}8$$

When β is real the series will converge, giving stable solutions, which correspond to oscillatory trajectories for ions in the quadrupole field. A complex value for β, on the other hand, results in divergent (unstable) solutions, corresponding to exponentially increasing amplitudes of the trajectories.

k_+ and k_- are integration constants determined by the initial conditions $x_0, y_{0,} \dot{x}_0, \dot{y}_0$ and the phase of the rf-field when the ion is entering the field. On the other hand, the constants β and C_{2p} do not depend on the initial conditions but only on the parameter values a_X and q_X: it is an important property of the solutions of the Mathieu's equation that the nature of the ion motion (stablility or unstablibility) depends only on the parameters a_X and q_X. As a consequence, a diagram of stability of the ion trajectories can be drawn in the (a, q) plane. The (a_x, q_x) values which give rise to non divergent motions in the x-direction are represented by the shaded area in Figure 2-19. The corresponding stability diagram in the y-direction is obtained by symmetry of the stability diagram in the x-direction with respect to the q-axis. The requirement for the motion to be simultaneously stable in the x- and y-directions necessitates taking the intersection of both stability diagrams.

The intersection of the two stability diagrams determine four quasi-triangular regions near the origin, which are all mirror images and we can pass from one to another by changing the polarity of the voltages U and V (see relations 2-6 and 2-7). The (a>0, q>0) quadrant is doubly shaded in the Figure 2-19, and shown in more details in the Figure 2-20 and Figure 2-25.

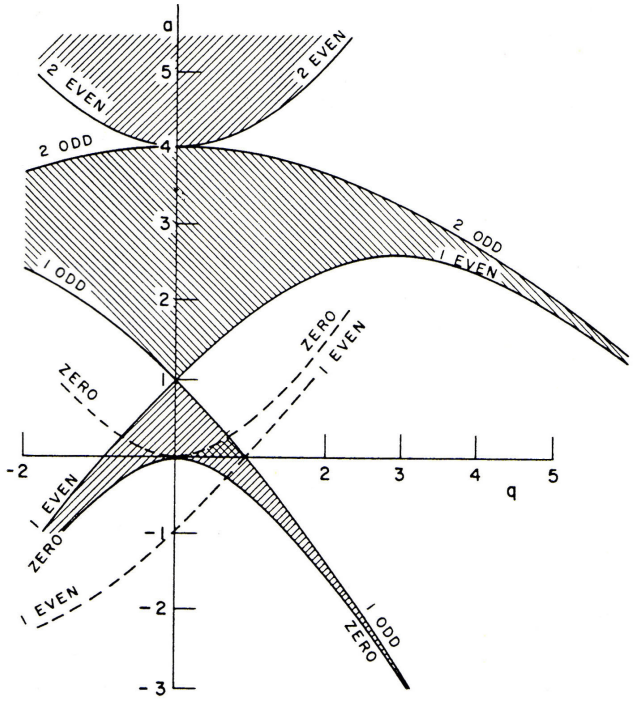

Figure 2-19 : Diagram of stability of the solutions of the Mathieu's equation. The shaded areas represent the regions of stability along the x-direction, the intersection of the stability regions for both motions in the x- and y- directions near the origin is doubly shaded, and it corresponds to the region of interest for the quadrupole mass filter. Reproduced from [58].

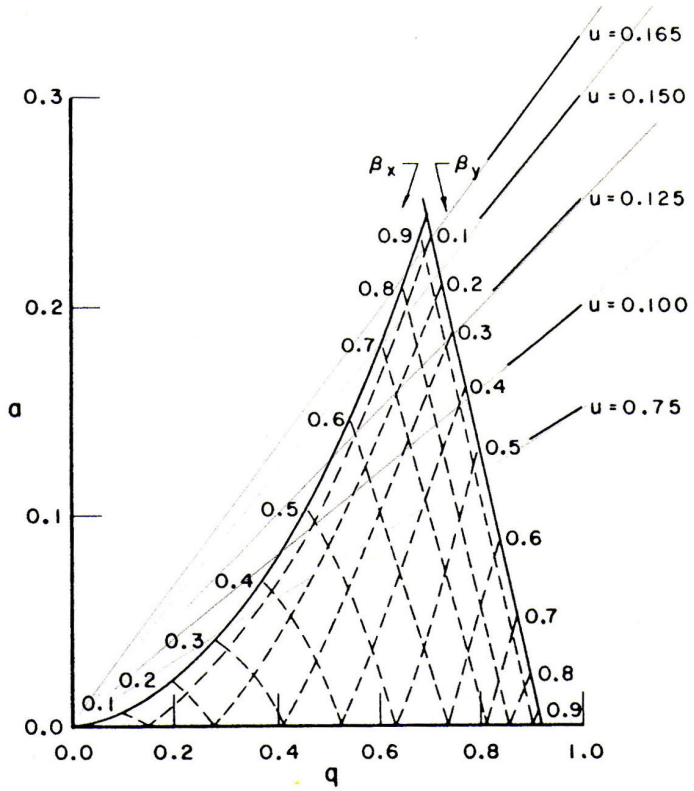

Figure 2-20 : The quasi-triangular zone of intersection of the two stability diagram of the solutions of the equations of motion inside the quadrupole field.

From the equations 2-6 and 2-7, we see that a given set of applied voltages U and V uniquely determines the relative values of a and q. Different straight lines of constant slope

$u = \frac{|U|}{|V|} = \frac{a}{2q}$ are shown in Figure 2-20, these straight lines are called the operating lines, since the usual mode of operation of a quadrupole consists in sweeping the mass to charge value to filter by altering the voltages U and V, while maintaining their ratio constant.

The portions of these lines passing through the regions of stability determine the range of mass to charge ratios for which ions will have stable trajectories. As u, the slope of the operating line increases, the traversed portion of the stability diagram becomes smaller, it corresponds to an improvement of the resolution; we can show easily from relation 2-7 that $\frac{\Delta m}{m} = \frac{\Delta q}{q}$.

A modification of the button "R" on the control panel of our Extranuclear quadrupole amounts to change the voltage ratio $\frac{|U|}{|V|}$, increasing or decreasing the slope u of the operating line (see Part II : Chapter 2.D.II)(3).

The Figure 2-21 shows a series of stability diagrams in the (U, V) plane associated with successive mass to charge values. The operating line intersects successively the stability areas and thus leads to the successive detection of the different mass to charge ratios. The Figure 2-21 is illustrating the fact that rf- only quadrupole act as high-pass mass filters: if the DC field is switched off (U=0), the point of operation characterized by the amplitude V_0 of the AC voltage belongs to all stability diagrams for higher masses than m_3, and it lies out of the stability diagrams of all lower masses (m_1, m_2). In Figure 2-21, the application of the rf- only voltages with "zero to peak" amplitude V_0 will suppress the lower masses m_1 and m_2 and allows all higher masses to pass through the quadrupole.

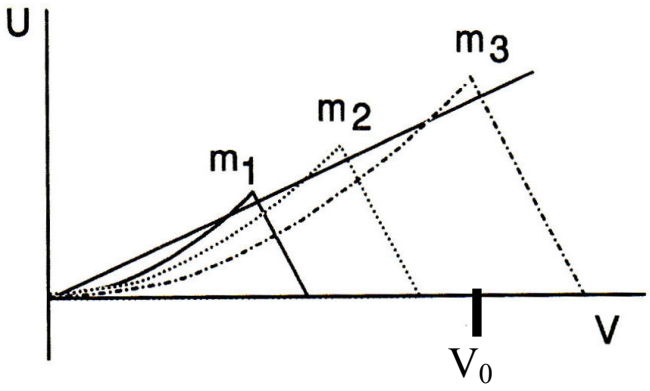

Figure 2-21 : Example of operating line intersecting the successive stability diagrams of different masses (m1 < m2 < m3). Taken from [53].

(2) Description of the extranuclear quadrupole

Our quadrupole system is constituted by the quadrupole control and radiofrequency source, a High-Q Head and the quadrupole filter itself (Figure 1-22). The high-Q Head is mounted near the vacuum system in order to minimize the length of the leads which transport the AC voltages, and thus the capacitance of the leads from the High-Q Head to the quadrupole mass filter.

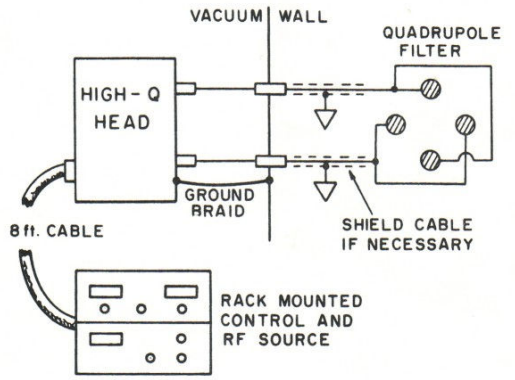

Figure 2-22 : Schematic of the Installation of our Extranuclear quadrupole.

This installation necessitates a initial procedure of tuning of the resonant frequency of the installation: the frequency of our quadrupole is determined at the time of change of High-Q Head by matching the resonance frequency of the entire system in order to maximize the reachable power and in the same time maximize the highest measurable mass, the frequency is then held constant and only the voltages applied on the rods are changing.

$$f_0 = \frac{1}{2\pi\sqrt{LC}} \qquad 2\text{-}9$$

The resonant frequency of the installation is f_0. It is determined by the equivalent inductance and capacity of the High-Q Head and the quadrupole rods. The quadrupole rods represent a given capacitance C which is fixed. We have different High-Q Head and leads at our disposal to vary the range of frequency accessible with the system, and thereby the maximal range of zero-to-peak voltage Vmax accessible giving the maximum mass accessible with the installation (equation 2-27).

Different High-Q Head were used during the study of the DEA to water covering the range 1-18amu and the range 10-180amu for the filtering of light H^-/D^- ions and of heavier O^-, OH^-, OD^- ions respectively.

During all this study on the discrimination in quadrupole, only one High-Q Head was used (range 10-180amu), tuned at the beginning and remained untouched.

The parameters R, ΔM determining the resolution of the quadrupole are relative to this

initial tuning of the frequency matching, but also dc-balance tuning and coarse resolution setting which belong to the initial tuning of the quadrupole installation.

Furthermore the calibration of the mass scale is performed by peak recognition.

II) Discrimination occurring in the quadrupole:

(1) Theoretical estimation of the effect of initial conditions of ions at the entrance of the quadrupole

In the precedent subsection introducing the principle of functioning of the quadrupole, the stability of the solutions of the equations of motion for a quadrupole unlimited in size were considered. Now, taking into account the finite size of the apparatus, we must determine whether the ions will pass through the quadrupole or not depending on their initial entrance conditions. Indeed, not all ions which have stable trajectories succeed to pass through the quadrupole with finite aperture. Some of the trajectories may acquire amplitudes larger than r_0, and thereby be discriminated. Refering to equation 2-8, the maximum amplitude acquired by an ion with a stable trajectory is determined solely by:

i. Its initial conditions on entering the field: these are its coordinate and velocities in the transverse plane $x_0, y_0, \dot{x}_0, \dot{y}_0$.
ii. The phase of the applied rf-cycle, ωt_0, at which it enters the field.
iii. The position in the stability diagram corresponding to the particular value m/c.

These factors determine the conditions for the occurrence of discrimination in the quadrupole and are examined in more detailed in this paragraph. Depending on the rf-phase when they enter the field and the (a,q)-position in the stability area, two ions of the same mass to charge ratio entering the quadrupole field at different positions (and/or) with different transverse kinetic energies might have different fates: one being rejected by the quadrupole whereas the other can pass. Figure 2-23 shows two graphs displaying the combined effect of the previously mentioned factors i), ii), iii) on the amplitude of the oscillatory motion. In the first graph (a), the effect of an entry off axis is plotted as multiples of the initial displacements x_0, y_0. The second graph (b) shows the effect of initial transverse velocities when the ions are entering on the optical axis.

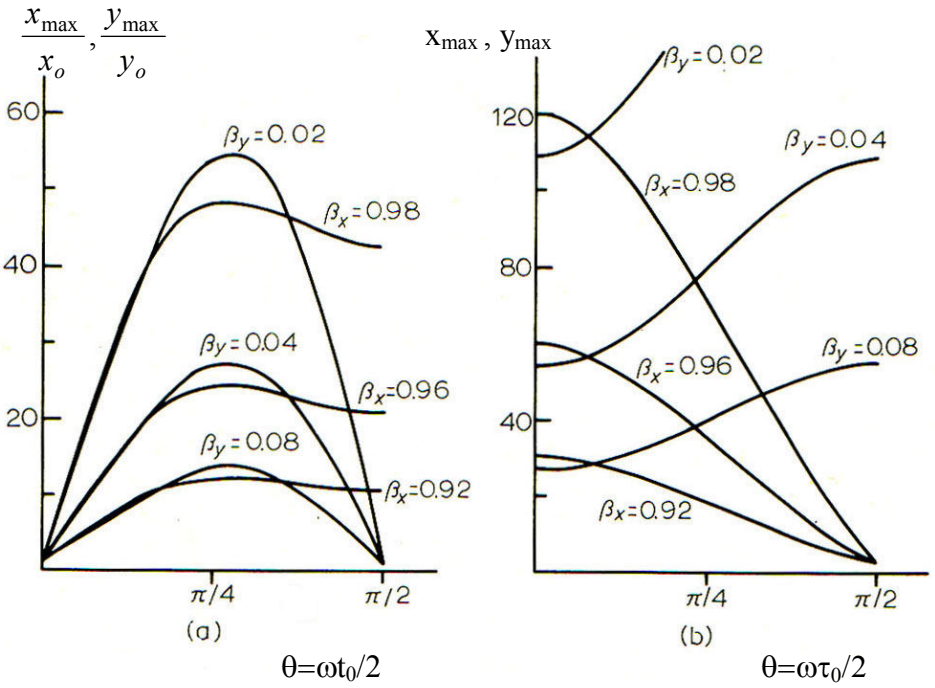

Figure 2-23 : Taken from [54].Maximal amplitudes of ion oscillation for various βx and βy values near the apex of the stability diagram as a function of the initial phase of the field at ion entry. (a) shows the case when the ions enter off axis and without velocities, (b) the ions enter without displacement but with initial transverse velocities $\left(\left.\frac{\partial x}{\partial \theta}\right|_0 = \left.\frac{\partial y}{\partial \theta}\right|_0 = 2 \right)$**.**

A certain displacement from the axis in one direction amounts to a certain increase of the transverse kinetic energy in the same direction. Ellipses of acceptance can be drawn in the $(X, \dot{X})$ planes which connect points resulting in the same maximum amplitude to determine the equivalent conditions of entrance for the quadrupole.

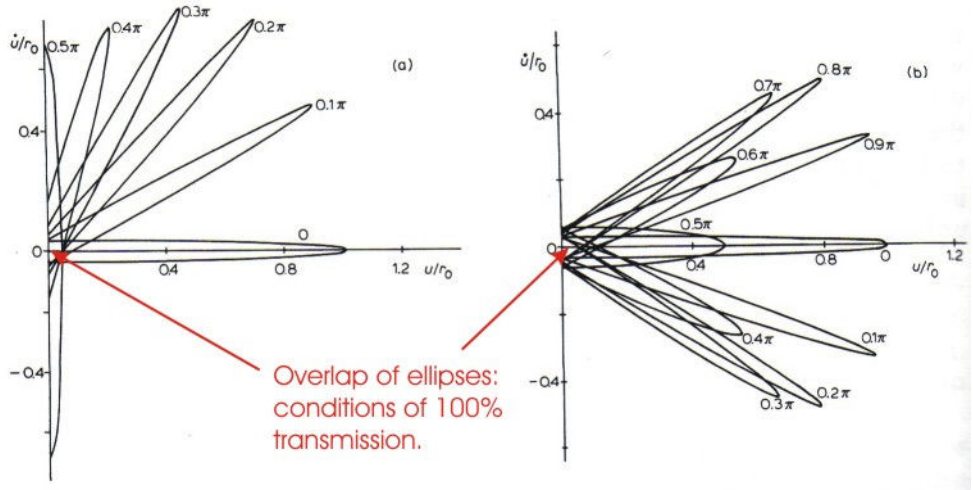

Figure 2-24 : Taken from [54]. Acceptance ellipses for (a,q)=(0.2334,0.706) in the x-direction (left) and in the y-direction (right). The plane $(X, \dot{X})$ **is designated by** $(u, \dot{u})$ **in the figure.**

Ellipses of acceptance obtained for different phases of the rf-voltage when the ions enter the field are shown in Figure 2-24. Their overlap defines a small area which corresponds to the

conditions under which the transmission is 100%. The influence of the ion optics has already been envisaged in Part II : Chapter 2.B.II). Tuning the lenses of focusing before the quadrupole entrance consists in finding the best match of the acceptance area for the incoming ions.

Figure 2-23 as well as Figure 2-24, show the important variations of the quadrupole's sensitivity to initial conditions in dependence on the phase of the rf-voltage at which the ions enter the field. It results in a modulation of the transmitted signal predicted by simulations [59,54] and observed experimentally in [55] (see Part II : Chapter 2.E.I)).

What are the consequences for the stability area?

The loci of the constant β considered in Figure 2-23 are close to the boundary of the stability zone (see Figure 2-20): we observe that the closer we are to the border of the stability area the more drastic becomes the conditions for passing through the quadrupole. According to the initial entrance conditions of the ions the stability area shrinks more or less. Looking only at the displacement from the axis in Figure 2-23 (a), only ions whose initial displacement from the axis is less than ($x_0, y_0 \leq r_0/15$) can be transmitted by the quadrupole when the operating line goes beyond the lines βx=0.92 and βy=0.08. r_0 equals to 4,11mm in our quadrupole so that ions must be focused in a beam of radius 0,274mm to be fully transmitted in this region. This corresponds to only a small fraction of the beam at the entrance which is expected to be several mm wide according to some simulations of ion trajectories presented in [52] (the extraction aperture from the collision chamber as well as the entrance aperture into the quadrupole field have a radius of 2mm~0,5r_0). The further we move away from the border of the stability area the less important the limitations due to the amplitude of the trajectories becomes. The lines βx=0,92 and βy=0,08 define a small band along the borders of the stability area in Figure 2-20, but these proportions should be reconsidered in the apex of the stability zone where the operating line is usually crossing the stability area. Indeed, the quadrupole is a low resolution mass spectrometer; for most of the operating lines traversing the stability area the resolution is too poor to be useable. For instance, a resolution of 20, sufficient to separate the masses in the mass range of our experiments with water (spectra from 14 to 20amu), was achieved with an operating line whose slope was calculated to be u=0,156 in the study of the resolution of our quadrupole (Part II : Chapter 2.D.II)(3), R=45 in Figure 2-32 and Figure 2-33). So, in order to have a resolution better than 20, the operating line had to cross the stability area in its apex (Figure 2-20). 20 is a rather low-resolution hence the useable part of the stability area is restricted to a small region close to the apex of the triangular stability area. The bands defined by βx=0.92 and βy=0.08 are almost completely covering the area of this region, only a small fraction of the incoming beam can be transmitted (r_{beam}<0.274mm) in the working range of our quadrupole. The apex of the stability area is represented in Figure 2-25; successive bands of restriction of the transmissivity are indicated with the

associated maximal amplitudes of the ion trajectories expressed as multiples of the initial displacement. We could think that these restrictions are underestimated since the transverse kinetic energies of the ions also have a contribution which was not taken into account in the diagram of Figure 2-25. The effect of the transverse velocities of ions entering the quadrupole on axis was envisaged separately by Paul et al in their earlier study [59] (Figure 2-23 (b)). More recently, similar diagrams as Figure 2-25 were determined taking into account the combined influence of the displacement and transverse kinetic energy of the ions at the entrance [56]. The author found astonishingly that the bounds on the initial displacement and transverse velocity at entry are higher (meaning less restriction) when both of them are non-zero than when either of them is zero (individual effects) indicating that the interaction effects are favourable to the transmission of ions. They refer to [57] for the experimental observation of this phenomen.

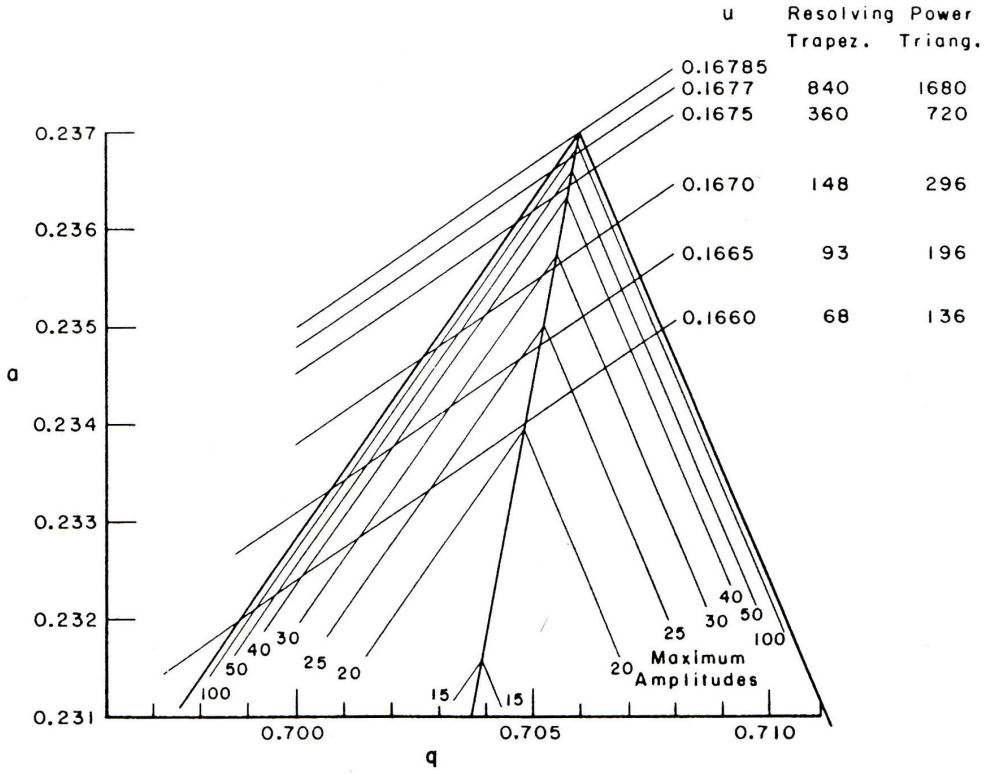

Figure 2-25 : Apex of the quasi-triangular stability region. Some examples of straight lines of constant voltage-ratios intersecting the apex of the stability region are shown. The ultimate value u=0.16785 determines the position of theoretically infinite resolution. The maximal amplitudes of the motion of a given β expressed as multiples of the initial displacement are also indicated in this diagram. Reproduced from [58].

In [59], Paul et al derived the following useful relationship to give, for a given resolution $\left(\frac{m}{\Delta m}\right)$, orders of magnitude of the maximal allowed displacement from the axis and the maximal transverse kinetic energy at the entrance for still having 100% transmission at the peak

maximum.

When ions are injected parallel to the optical axis (no transverse velocity), the maximal amplitude x_m corresponding to an initial displacement x0 is limited by $x_m < 1{,}8x_0\left(\frac{m}{\Delta m}\right)^{\frac{1}{2}}$. This leads to the approximate relationship for the maximal size of the displacement allowed, when the maximal amplitude can be r_0:

$$r_{\max} = \frac{1}{1{,}8} r_0 \left(\frac{\Delta m}{m}\right)^{\frac{1}{2}} \cong \frac{2}{3} r_0 \left(\frac{\Delta m}{m}\right)^{\frac{1}{2}} \qquad 2\text{-}10$$

The other relationship to estimate the maximal transverse kinetic energy that an ion injected on the axis can have if its transmission is to be insured, is:

$$Et_{\max} = \frac{1}{2} m f^2 r_0^2 \left(\frac{\Delta m}{m}\right) \qquad 2\text{-}11$$

The explicit calculations for our case are as followed:

$$r_{\max} = \frac{2}{3} \times 0{,}411 \times \left(\frac{1}{20}\right)^{\frac{1}{2}} = 0{,}0613 \text{ cm}$$

$$Et_{\max} = \frac{1}{2} \times 16 \times 2{,}5^2 \times 0{,}411^2 \times \left(\frac{1}{20}\right) = 0{,}422 \text{ eV}$$

Indeed, in the working range of our experiments (10-32.5amu), the resolution went from 15 to about 120 (Figure 2-32, based on measurements of positive mass spectra with ion optics settings defined by (0;0;15;0;0;-15;30)). The measurements with water were performed at a resolution close to 20 in order to maximize the ion signal, but still ensure a separation of the masses. The mass 16 corresponds to O^-, it is the lightest mass considered in this work on the discrimination along the way to detection. Moreover cross sections of O^- dissociation channel display the greatest kinetic energy heterogeneity at the ions formation by the DEA to water and thereby should show the greatest discriminative effects.

$r_{\max}$ is the same for all ions, but the maximum transverse kinetic energy $Et_{\max}$ allowed becomes really small for H- and D- ions ($Et_{\max} = 0.026$eV and 0.053eV respectively for $\left(\frac{\Delta m}{m}\right) = 20$), this is the reason for the high discrimination that occurs for these ions in the quadrupole. The restriction becomes less drastic for the higher masses.

For $\left(\frac{\Delta m}{m}\right) = 60$, we obtain for O- ions $Et_{\max} = 0{,}14\,\text{eV}$ and $r_{\max} = 0{,}0354\,\text{cm}$, which is of the order of the previously estimated $r_{\max} = 0{,}0274\,\text{cm}$ in the apex of the stability zone (Figure 2-25). In Part II : Chapter 2.D.II)(3), this resolution could be achieved with R=60 calculated to correspond to a slope u=0.161 for the operating line, situated in the middle of the apex of the stability area according to the diagram of Figure 2-25. However, we are concerned here with negative ions whereas the results of Part II : Chapter 2.D.II)(3), were obtained with positive ions. We will realize in Part II : Chapter 2.D.III)(1) that the correspondence between resolution and the quadrupole settings R and ΔM is modified when passing from positive ion to negative ion detection.

Another interesting calculation is to prove that an ion with as much transverse kinetic energy as 0.5eV can be transported from the collision chamber into the entrance of the quadrupole. Suppose that an ion O^- experience a voltage drop of about 20V (average Ion Energy during the experiments of water) from the extraction to the entrance of quadrupole distant of about 10.5cm. This means that the ion have a mean velocity along the axis of $\bar{v} = \frac{1}{105}\int_0^{105} 9{,}8226967 \times \sqrt{\frac{2x \times (20/105)}{16}}dx \cong 10\,\text{mm} \cdot \mu\text{s}^{-1}$ (making use of the formula $v = 9{,}8226967 \times \sqrt{\frac{2\bar{K}}{\bar{m}}}$ determined by Wollnik in [51] to calculate the velocity of an ion of mass $\bar{m}$ amu and $\bar{K}$ eV kinetic energy) and it takes about 10μs for an O^- ion to travel until the entrance of the quadrupole if the focusing lenses were switched off. Making use of the formula of Wollnik once more, we determine the transverse velocity for O^- with a transverse kinetic energy of 0,5eV to be $v_t = 9{,}8226967 \times \sqrt{\frac{2 \times 0{,}5}{16}} = 0{,}04\,\text{mm} \cdot \mu\text{s}^{-1}$. During 10μs, the ion will only go 0,4mm in the transverse direction. This means that we can expect O^- ions with such a transverse kinetic energy to be able to reach the entrance aperture of the quadrupole. Nevertheless, the transverse kinetic energies of the ions is expected to be transformed significantly by the focusing lenses before the entrance into the quadrupole.

Conclusion: the problem of discrimination according to the conditions of entry was sketched in this paragraph and we could determine some orders of magnitude. Only in the apex of the stability area is the resolution good enough, but this region is plagued by the discrimination of ions entering the quadrupole off axis (or/and) with too much transverse kinetic energy. It is difficult to estimate the transmission of ions through the quadrupole: Figure 2-24 shows that there is a region of phase space for which the ions are fully transmitted. But are we able to focus the ions sufficiently with sufficiently low transverse kinetic energy at the entrance to match this small region? It is improbable according to the order of magnitudes determined and discriminative effects can be expected. In

particular, it must be difficult to find some focusing action adapted to measure cross sections when the ions formed have very heterogeneous kinetic energies. However, there is hope to find out a region of full transmission when we lower the resolution of the quadrupole. Indeed, at low resolution the intersection of the stability area is broader and a region of full transmission could be revealed.

.

(2) Discrimination and shape of the peaks of the mass spectra: theory

The true relation determining the operating line in our experiments can be written as

$$|U| = \gamma |V| + \delta \,, \qquad 2\text{-}12$$

where γ is the slope of the operating line (previously called u in the absence of δ), and δ is an added DC voltage which results in translating the operating lines at constant slope towards higher or lower regions of the stability diagram (see Figure 2-28 and Part II : Chapter 2.D.II)(3)). Hence, it also moves the operating line towards a region of better or worse resolution region of the stability area. Buttons (or parameters) "R" and "ΔM" on the control panel of the quadrupole are each controlling the slope γ and the offset δ of the operating line respectively. According to the manual of our Extranuclear power supply, the resolution of the quadrupole is given by the formula:

$$\frac{m}{\Delta m} = \frac{0{,}126}{0{,}16784 - U/V} \qquad 2\text{-}13$$

It corresponds to the formula 2-14 determined by Paul et al in [59] by careful analysis of the details of the stability tips. The reference [59] is a fundamental article on the subject of quadrupole mass filter, which was developed in parallel with the quadrupole ion trap by Wolfgang Paul who received the Nobel Prize in 1989 for this work.

$$\frac{m}{\Delta m} = \frac{0.178}{0.23699 - a_{0.706}} \qquad 2\text{-}14$$

In the formula 2-13, 0.16784 is the value of the slope u_{max} for which the operating line crosses the end point of the tip of the stability zone, where the resolution becomes theoretically infinite. (0.23699; 0.706) are the coordinate of this point in the (a; q) plane.

In our particular case of the Extranuclear quadrupole, we must adapt the formula to the relation 2-12 which gives:

$$\frac{m}{\Delta m} = \frac{0{,}126}{(0{,}16784 - \gamma) - \delta / V} \qquad 2\text{-}15$$

This is the formula which was used to fit the experimentally determined resolution of our apparatus in the series of experiments described later. It was also used to localize the position of crossing of the operating line in the stability area during these experiments and to make the correspondence with the instrumental values of R and ΔM.

Considering the prediction of the Figure 2-25, if we suppose that the ions enter the quadrupole in a beam of radius $r_0/30$, the section of an operating line between its intersection with the lines $x_m=30x_0$ and $y_m=30y_0$ corresponds to the range of ionic mass numbers attaining to 100% transmission. The other two segments of the operating line, which are still in the region of stability, will correspond to ionic mass numbers only partially transmitted. Two broad regions can be defined for the resulting peaks of the mass spectra: when portions of the operating line lie within the 100% transmission region the peak shape is trapezoidal ($u<0.1670$ in the Figure 2-25). At higher values of resolution, where full transmission cannot be achieved, the peaks shape is triangular ($u>0.1670$ for the example considered in Figure 2-25 and Figure 2-26). The theoretical resulting peaks are shown in the Figure 2-26.

In Figure 2-25 some calculated resolutions (resolving power) are shown which were determined by various operating lines crossing in the apex of the stability area (Figure 2-25). For every line, the authors of [58] have calculated the resolution by supposing a peak shape of the trapezoidal type or of the triangular type. When the formula 2-13 is used to determine the resolution the transmission is supposed to be 100% everywhere in the stability area. Clearly this formula should be revised when the resolution is enhanced; in [58], the authors gave formulae adapted to the calculation of resolution in the broad trapezoidal region or in the triangular region, taking into account the discrimination occurring due to the initial entrance conditions. In the broad trapezoidal region, the resolution should be given by:

$$\frac{m}{\Delta m} = \frac{0{,}146}{0{,}16784 - U / V} \qquad 2\text{-}16$$

and in the region of triangular peak shape the corresponding formula becomes:

$$\frac{m}{\Delta m} = \frac{0{,}292}{0{,}16784 - U / V} \qquad 2\text{-}17$$

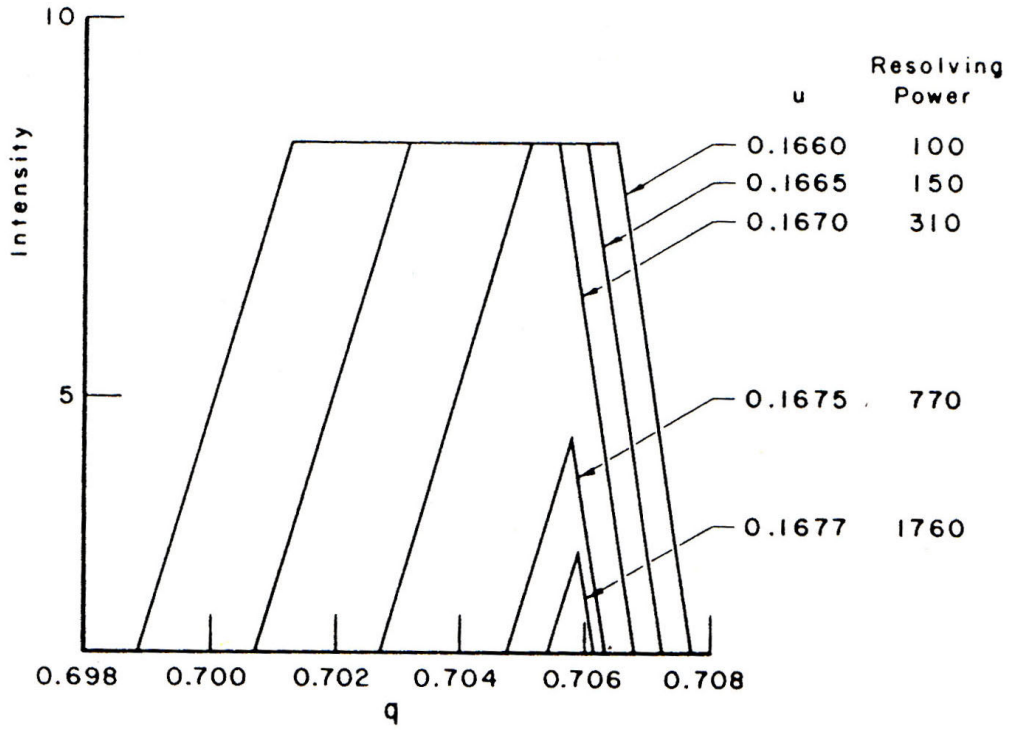

Figure 2-26 : Theoretical shapes of the mass spectrum peaks obtained by sweeping along the operating lines shown in the Figure 2-25**. When portions of the operating line lie within 100% transmission region the line shape is trapezoidal. At higher values of u, where full transmission is not achieved, the line shape is triangular. To be compared with shapes obtained by changing the parameters R and ΔM in the experimental mass spectra.**

Actually the determination of the constant 0.146 and 0.292 are arbitrary, but this procedure can be generalized and another parameter k can be introduced, which could measure the importance of discriminative effects affecting the transmission of the quadrupole:

$$\frac{m}{\Delta m} = \frac{k}{0.16784 - U/V} \qquad 2\text{-}18$$

We are interested to know if we can really tell whether discriminative effects occur, simply by watching at the mass peak shape. Can the triangular peak shape be a signature for the occurrence of discriminative effect? Is the transmission really 100% when the peak shape is trapezoidal?

(3) Some experimental investigation of the mass peaks shape and its correlation with discrimination

These were theoretical investigations showing that it is somehow possible to estimate the sensitivity to the initial conditions of the quadrupole according to the shape of the mass spectra. Now comes an attempt to characterize experimentally the discrimination occurring in the quadrupole, and a measure of the influence it has on the later measured cross section of water. An experimental study of the evolution of the mass spectrum of heavy water with the variations of the parameters "R" and "ΔM" is shown in Figure 2-27 and Figure 2-29.

A series of positive mass spectra were taken at a roughly constant background gas pressure of 1.1×10^{-6} mbar measured in the chamber and a constant e^--current of 70nA: the steady conditions of pressure and current give the possibility to compare directly the intensities of the curves between them. Furthermore, these measurements were made at constant ion optics settings (0; 0; 15; 0; 0; -74; 30) and V_{CH}=4kV. So, briefly, the conditions of measurement were steady and the only parameters changed were the settings of the quadrupole resolution "R" and "ΔM".

Looking at the evolution of the mass spectra presented in the graph a) b) c) d) of the Figure 2-29, the evolution of the peaks shape is analogous with the peaks shape evolution expected from the theory in Figure 2-26: in graph a) and c) the shape of the peaks is more or less trapezoidal and we don't have evidence for a transition towards the triangular region. On the contrary, the evolution of mass peaks shown in graph b) and d) exhibits a transition of the peak shapes from the trapezoidal to the triangular region.

Before continuing, we must consider in more details the effect of the button ΔM on the operating line. Commercial quadrupoles are almost never operated in a constant resolution mode, rather they are generally operated with a mass resolution that increases linearly with increasing masses (i.e. at constant peak width).

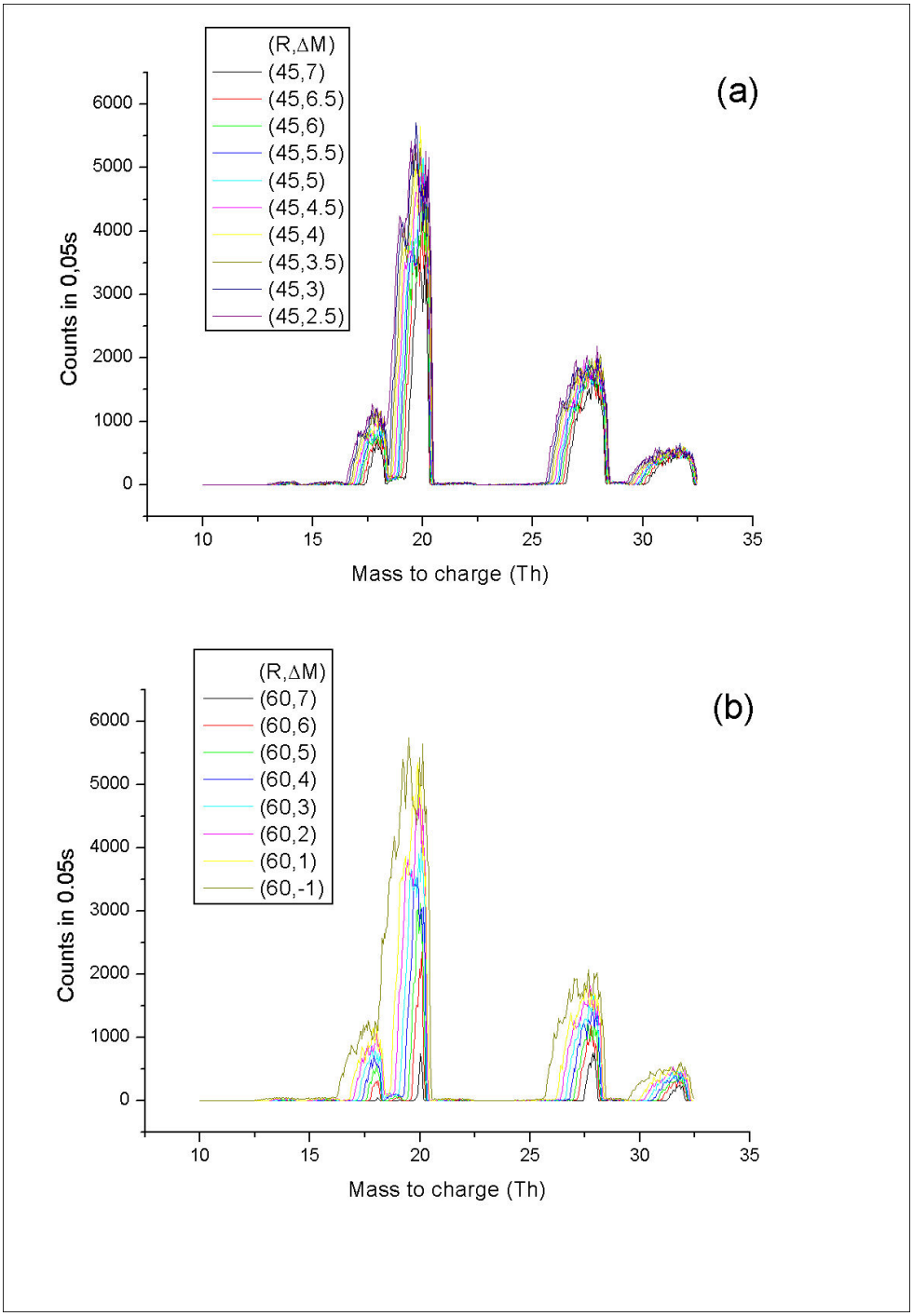

Figure 2-27 : Evolution of 10-32,5 amu-D_2O-Mass spectra as a function of the parameter ΔM for R=45 (a) and R=60 (b). We expect a transition to the triangular region leading to an enhanced sensitivity of the quadrupole to the initial consitions of ions i.e. enhanced discriminative effects. The transition to the triangular region of stability is evident in the graph (b) for R=60, whereas it doesn't seem to occur for R=45 on this example, it looks like we are not quitting the trapezoidal region.

The theory was presented in Part II : Chapter 2.D.II)(1) with operating lines at constant ratios u=U/V, whereas the operating lines of our instrument have more freedom due to the additional DC voltage δ. In the manual of our quadrupole is mentionned that the values of the parameters δ and γ are set by the "R" and "ΔM" buttons respectively, and that the formula 2-15 should account for the

evolution of the resolution with the variation of δ and γ.

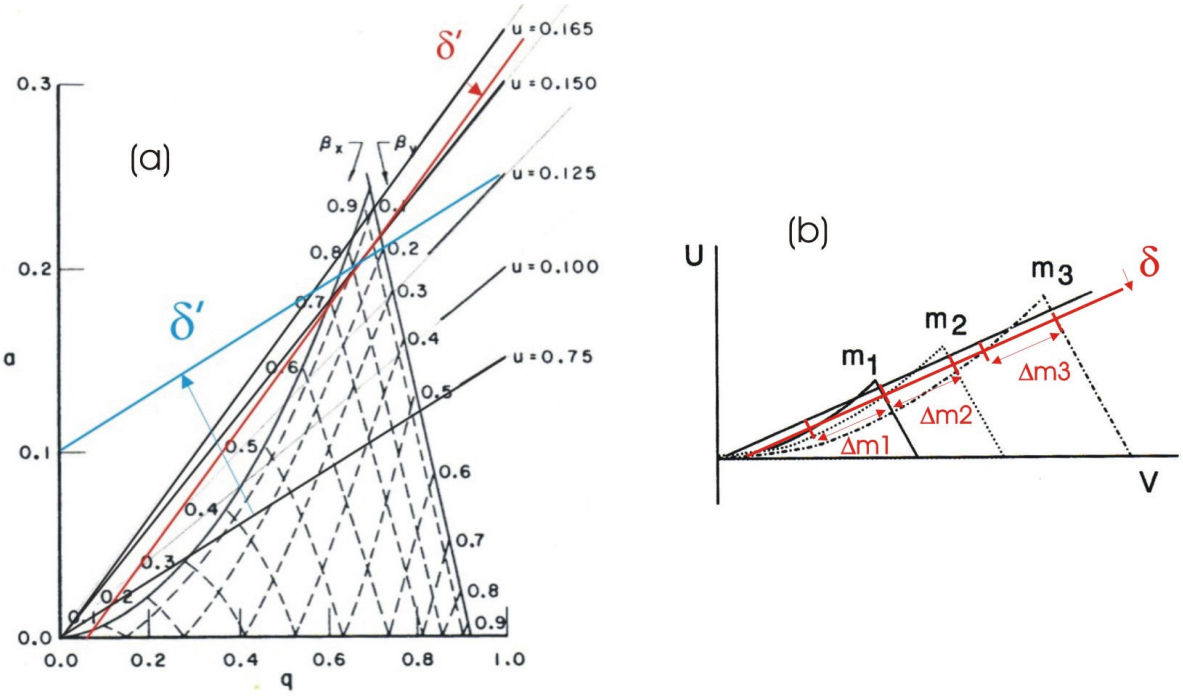

Figure 2-28 : (a) Display of the variation of the operating lines $a = 2\gamma + \delta'$ in (a,q) plane corresponding to the variation of $|U| = \gamma|V| + \delta$ in the (U,V) plane. The variation of the line in blue is exaggerated on purpose to emphasize the difference in making vary the slope γ or the intercept of the y-axis δ. (b) shows that it is possible to achieve a constant peak size Δm over a certain range of masses by slightly translating the operating line thanks to the additional δ DC potential.

We can see the difference of evolution of mass spectra when "ΔM" is swept at constant "R" (graph (a) and (b) Figure 2-29) or when "R" is swept at constant "ΔM" (graph (c) and (d) Figure 2-29). The additional DC voltage has been introduced to give the possibility to achieve a constant Δm mode over a certain range of masses; it is illustrated by the graph (b) of Figure 2-28: a slight translation of the operating lines equalizes its intersections with successive areas of successive masses.

In both cases the peaks are growing towards the low masses, this is even more pronounced when δ is varied due to the particular triangular shape of the stability area since the proportion of the intersection of the stability area grows faster towards the low masses than towards the higher masses. This makes it possible to equalize the peaks size Δm over a certain mass range (Figure 2-28) and it results in an observable difference in the growth of the peaks (Figure 2-29).

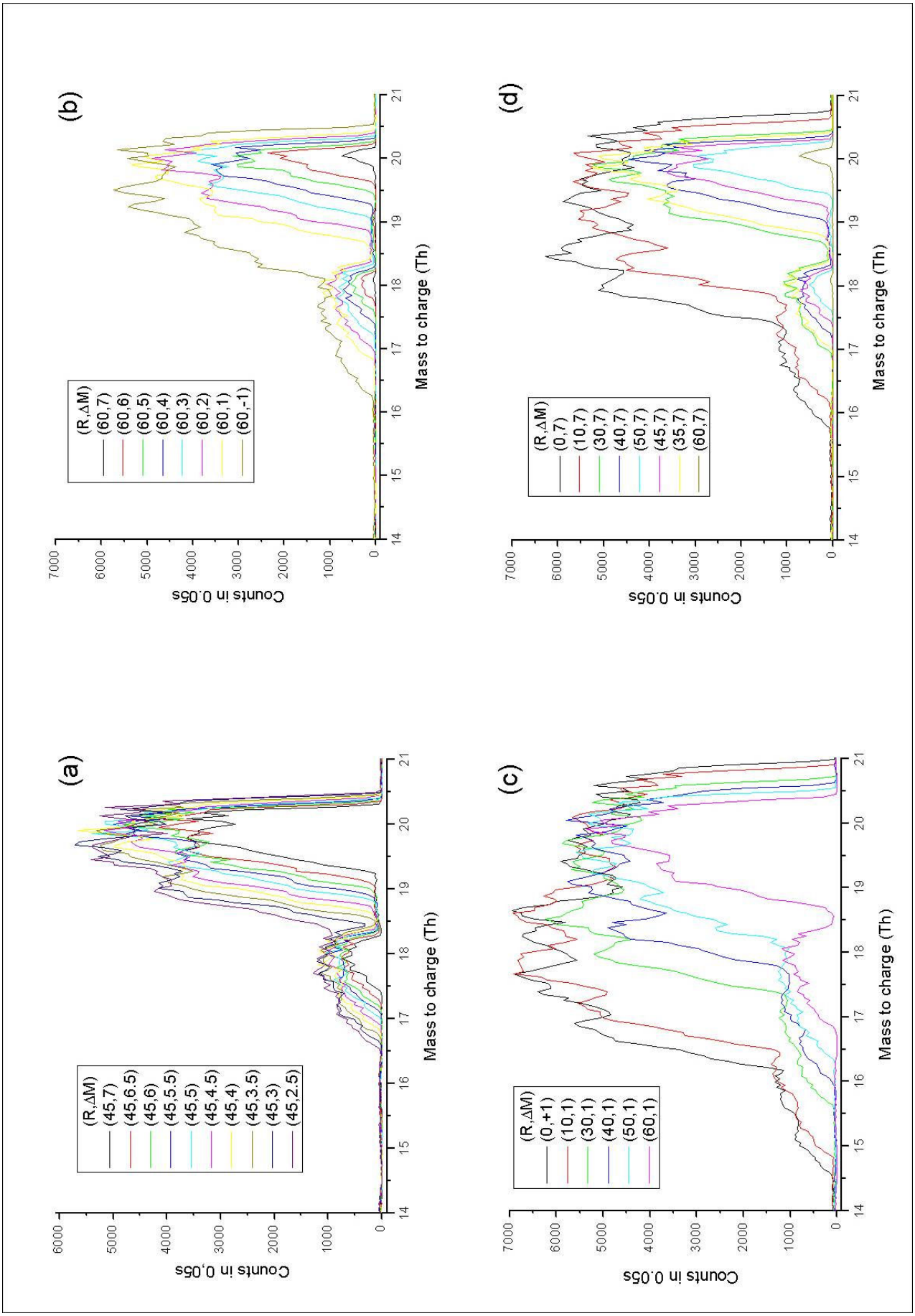

Figure 2-29 : Evolution of mass peaks at 18, 19, 20 amu with the variation of control buttons "R" and "ΔM".

If we look at the graphs of Figure 2-29, we notice that the intensity of the trapezoidal peaks at the lowest resolutions is roughly constant with peak maxima close to 6000 counts per 0.05s, except for the peaks of graph (c) whose intensities is higher in the region of overlap. This gives a hint that the full transmission was achieved when the resolution was low. But, on the one hand, the mass peaks are modulated, which was not predicted by the theory so far, and, on the other hand, the transition towards the triangular peaks shape is not evident to determine from the change of shape only. For instance, peaks at (R,ΔM)=(60,5),(60,6),(60,7) in graph (b) of Figure 2-29, which are obviously in the triangular region since their intensities started to decrease significantly with respect to lower resolution peaks, also look like having trapezoidal shapes.

The purpose of this study was to determine more clearly the evolution of the mass spectra with the parameters "R" and "ΔM". It also serves the purpose to check if our quadrupole behave in the way predicted by the theoretical formula given by the formula 2-15, and to estimate where we are positioned in the stability area. To know this position is useful for the rest of the study. So in the following a fitting procedure is described which will allow us to determine the correspondence between the theoretical parameters and the read values on the buttons of the control panel. However, care must be taken since the study was done with positive mass spectra, whereas the rest of the study will deal with negative mass spectra, and it will be realized in Part II : Chapter 2.D.III)(1) that the resolution changes significantly from positive mass spectra to negative one. Besides, R and ΔM are no absolute parameters; they are relative to the complete tuning of the quadrupole (see Part II : Chapter 2.D.I)(2)). However, for the study of discrimination of this chapter, the rest of the quadrupole settings remained untouched.

Figure 2-30 and the following 3D-representations show the experimental determination of the width of some mass peaks Δm as a function of "R" and "ΔM". They display the useable working range of our quadrupole for positive ions of 15eV injection energy which corresponds to an intermediate velocity between fast and slow injection speed (see Part II : Chapter 2.E.IV)(2)) if the resolution becomes higher some peaks of the mass spectra are vanishing, and if we reduce the resolution more the separation of masses becomes too rough. We can realize from this observation that the quadrupole is a low resolution mass spectrometer, allowing with difficulty a disentanglement of the masses (Δm=1) without loss of transmission. Besides, U. von Zahn [59] determined experimentally a relationship between the maximal attainable resolution and the number of rf-cycle the ions remain in the quadrupole (see Part II : Chapter 2.E.IV)(2)): $R = n^2 / 12.25$, where n= 20 is the number of rf-cycles experienced in our quadrupole by 15eV-ions and it gives R=112 which is in good agreement with the results of Figure 2-32 (b) displaying a maximal attainable resolution of about 120.

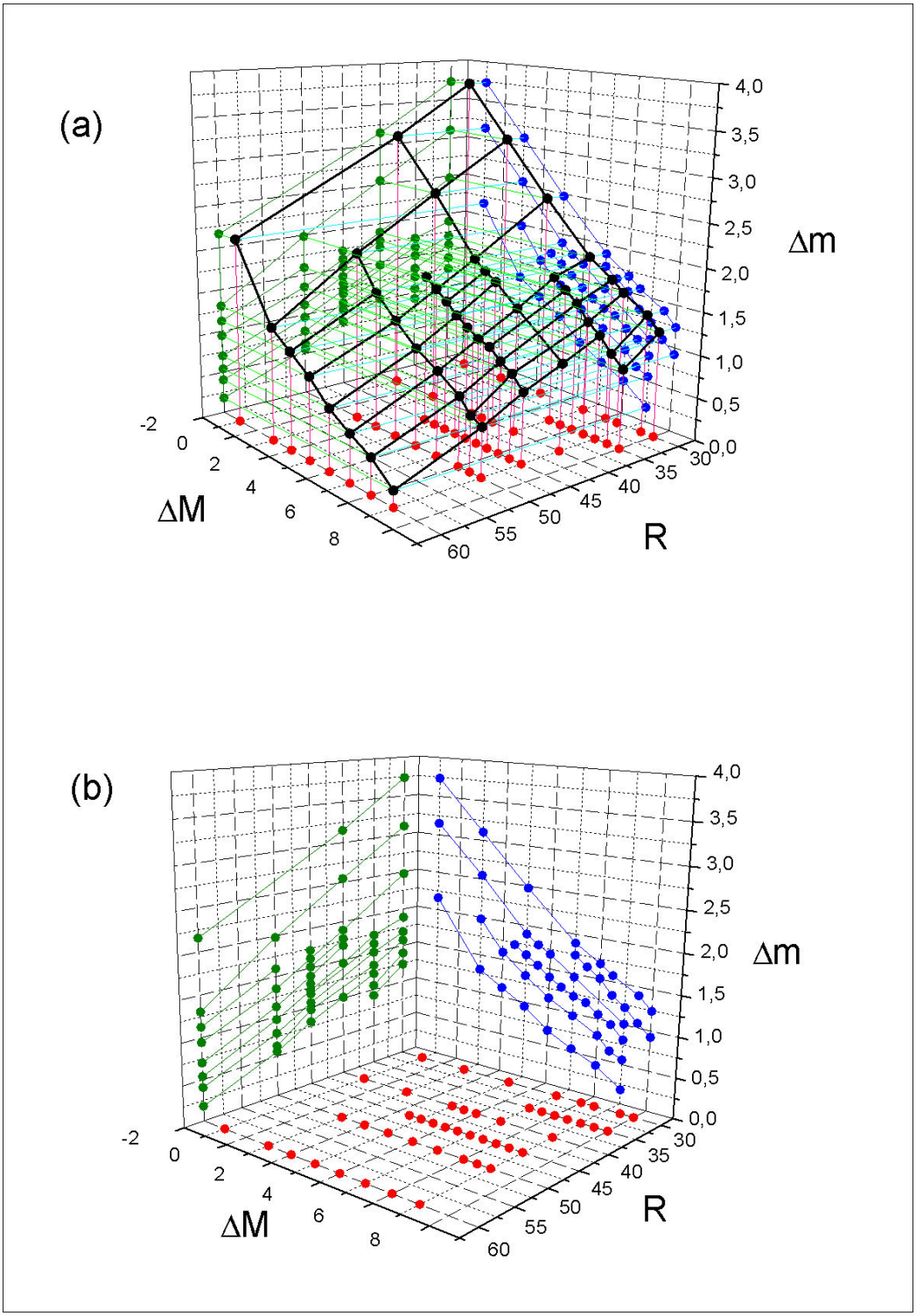

Figure 2-30 : Evolution of the width of the peaks as a function of R and ΔM for the mass 20 (D_2O+). For clarity, the projections are shown alone in the lower graph (b).

Influence on one mass peak

The Figure 2-30 studies the variation of the width of one mass peak as a function of R and ΔM: the upper graph (a) shows the surface in the space (R, ΔM, Δm) representing the experimental width Δm of the 20amu-mass-peak (D_2O^+) as a function of the parameters R and ΔM ; the lower

graph (b) shows for the purpose of clarity the projections of the surface onto the plane (ΔM, Δm) and (R,Δm). The parameters γ and δ defined by the formula 2-12 are some functions of R and ΔM respectively, according to the manual of the control panel of our Extranuclear quadrupole. According to the formula 2-15, we expect the following relation to hold for Δm, γ and δ:

$$0{,}126 \times \frac{\Delta m}{m} = 0{,}16784 - \gamma - \frac{\delta}{V}, \qquad \textbf{2-19}$$

which is the equation of a plane in the space (γ,δ,Δm).

The lines drawn on the planes (ΔM, Δm) and (R,Δm) are connecting the projections at constant R and constant ΔM respectively; they show experimental evidence of linear dependence of Δm on the parameters R and ΔM respectively:

$$\Delta m = a(\Delta M)R + b(\Delta M), \qquad \textbf{2-20}$$

$$\Delta m = c(R)\Delta M + d(R). \qquad \textbf{2-21}$$

The lines are parallel hence the slopes are constant:

$$a(\Delta M) = cst = a \text{ and } c(R) = cst = c. \qquad \textbf{2-22}$$

Moreover, the lines (2-20) (2-21 resp.) are equidistants for equal changes of ΔM (R resp.), and hence we have:

$$b(\Delta M) = e\Delta M + f, \qquad \textbf{2-23}$$

$$d(R) = gR + h, \qquad \textbf{2-24}$$

for some e,f,g,h constants.

We deduce a=g, e=c, f=h and find:

$$\Delta m = aR + e\Delta M + f. \qquad \textbf{2-25}$$

Therefore, the resulting surface of the width Δm of the 20amu-mass-peak (D_2O^+) as a function of the parameters R and ΔM in Figure 2-30 is the portion of a plane in the space (R, ΔM, Δm).

The following fitting procedure (see equation 2-28 below) will show that R and ΔM are affine functions of γ and δ respectively:

The influence on two masses

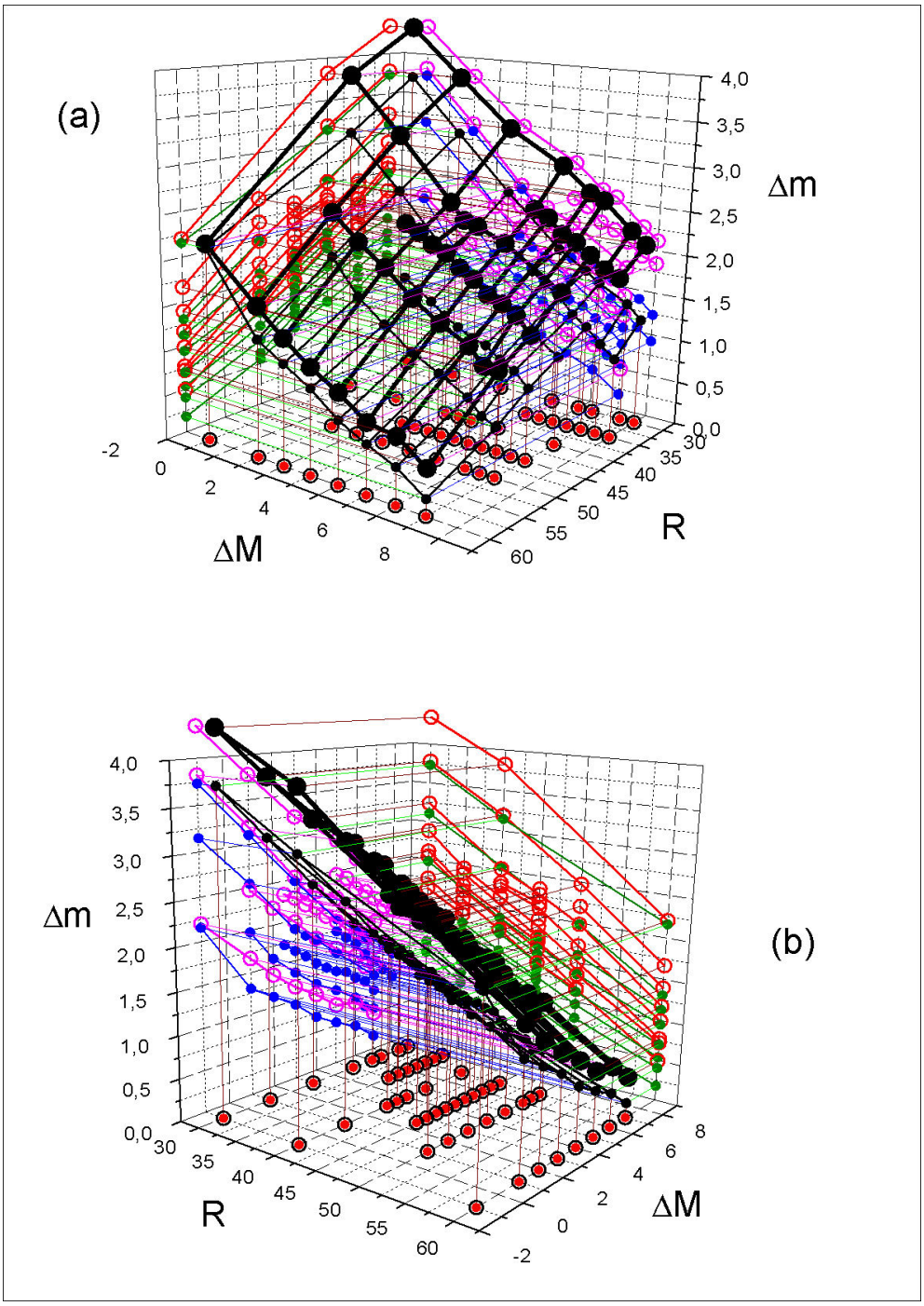

Figure 2-31 : Planes associated with masses 20amu (small dot) and 28amu (bigger dot) in the space (Ṛ,ΔṂ,Δm). The planes are not parallel but do not intersect in this range of parameters, the plane corresponding to the larger mass is moved towards larger peak width Δm at equivalent resolution settings of the control panel. This gives some experimental hint that the relation 2-19 is holding.

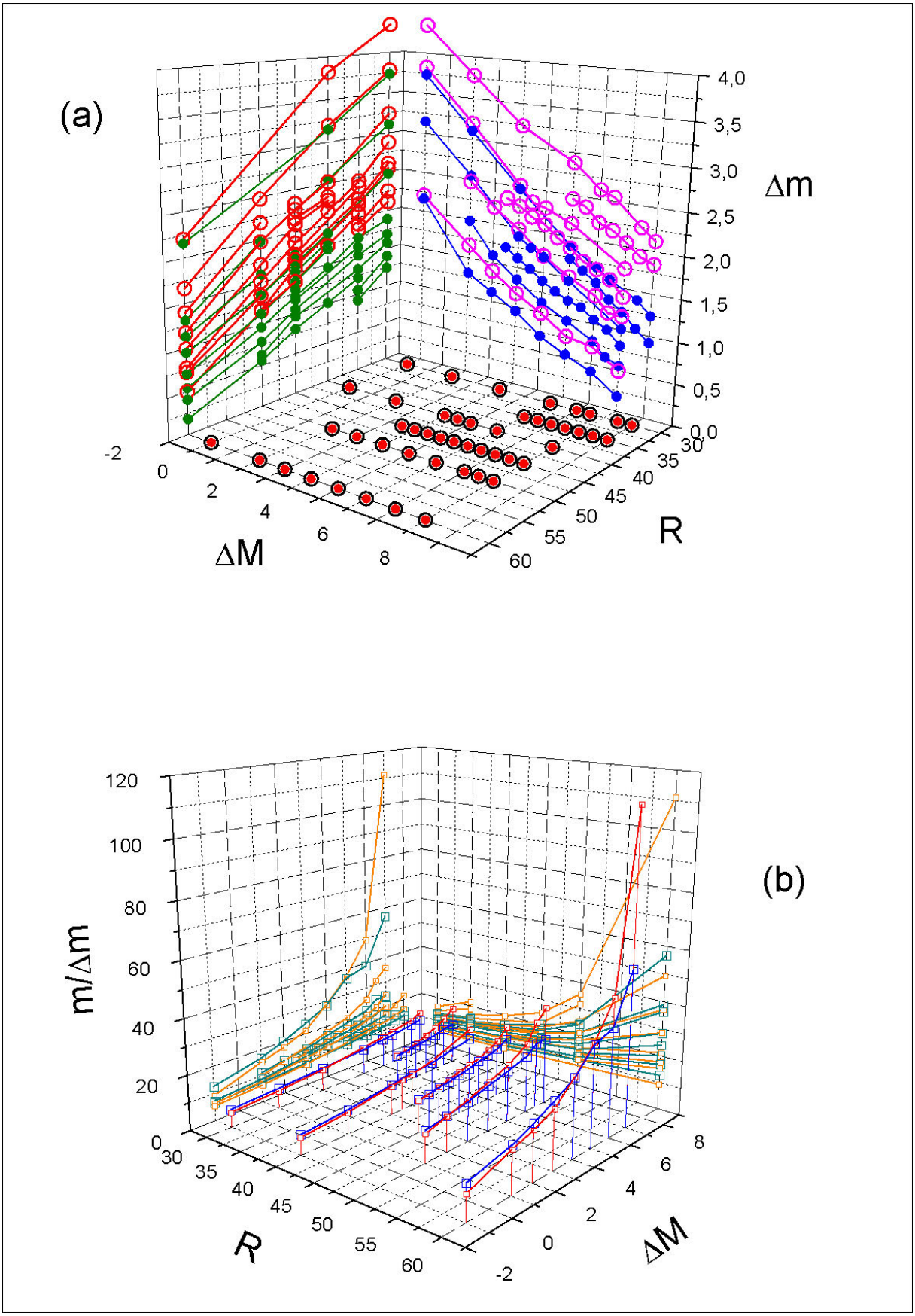

Figure 2-32 : Linearity and display of resolution.

The spectra (a) and (b) of Figure 2-27 show examples of the complete spectra of masses

observed in the range 10 to 32.5 amu, as R and ΔM are varied. By noting the width of the different mass peaks corresponding to m=14,16,18,20,28,32 amu as the control parameter R and ΔM are varied, we obtain a set of data which can give estimations of the parameter γ and δ once fitted by using the relation 2-19 which should hold for our instrument according to the Extranuclear manual.

At constant rf-frequency, V is proportional to m. Using the formula given in the Extranuclear manual:

$$V = 7.219 \times \overline{r_0}^2 \times \overline{f}^2 \times m, \qquad 2\text{-}27$$

where $\overline{r_0}$ (=0.411cm) is the radius in centimeter of the inscribed circle between the rods and $\overline{f}$ (=2.5MHz) is the rf-frequency in MHz. This formula is derived from the equation 2-7 by choosing the ultimate position at the top of the stability area at q=0.706, as reference for the position of the mass peak.

The relation 2-19 can be rewritten:

$$\Delta m = \frac{(0.16784 - \gamma)}{k} \times m - \frac{\delta}{k \times 7.219 \times \overline{r_0}^2 \times \overline{f}^2} \qquad 2\text{-}28$$

In this way we can perform a simple linear fit in order to determine the values of the parameters γ and δ, since, at constant R and ΔM, γ and δ are constants as well.

The results of the fitting procedure are shown in Figure 2-33 and Figure 2-34. Firstly, k=0.126 was chosen which corresponds to the value suggested in the Electronuclear manual (Formula 2-15). In addition to the linear fit, some rational fit were performed also shown in Figure 2-33 for k=0.126, and they give results in agreement with the linear fits which are anyway more accurate than nonlinear fits whose determination depend on the initial parameters values. The results of Figure 2-33 show the validity of the formula 2-28 to describe the resolution of our quadrupole: at constant R=35 and R=45, the value of γ is constant within the error determined from the fit, for R=35 the larger fluctuations might come from a wrong estimation of the width of some mass peaks. The effect of change the value of k, from k=0.126 (black curves) to k=0.146 (blue curves), is to translate the curves to some lower values of δ. However, at R=60, the red curve corresponding to the value k=0.146 at R=60 has the tendency to increase from the constant value of δ determined by the lowest values of ΔM (ΔM=1, 2, 3), whereas the blue curves associated with R=35 and R=45 remain constant over the range of ΔM. It gives a hint that the transition towards the region of triangular mass peaks shape is starting which also announces the occurence of discriminative effects.

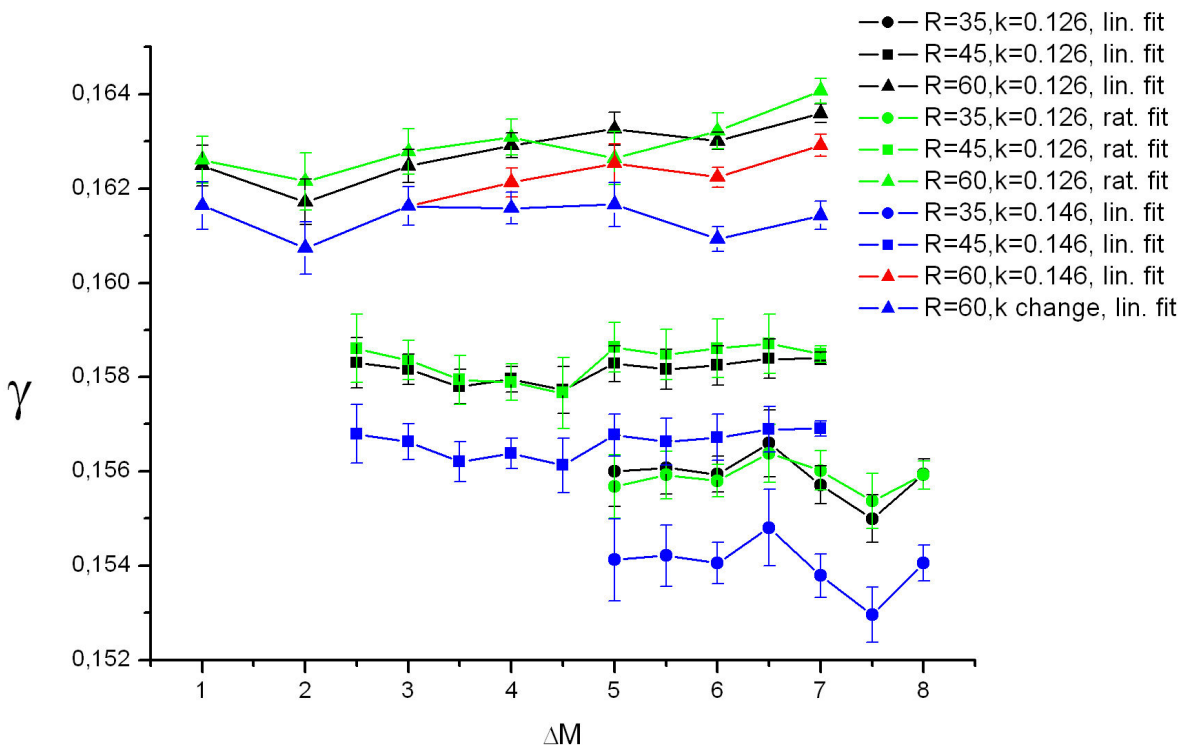

Figure 2-33 : Resulting values of γ from fits of mass peaks width as a function of the mass at constant R and ΔM.

The blue curve corresponding to R=60 has been obtained by varying the parameter k to higher values as suggested in [4] in order to take into account the transition towards the triangular peak shape region. The comparison with the evolution of mass peak shapes is in agreement with this observation of the need for the increase of k, which can be taken as an indicator for the transition to the region of discriminative effects: the mass peak shapes shown in Figure 2-29 (a) at R=45 clearly remain trapezoidal, whereas the transition towards the triangular region seems to occur at R=60 shown in Figure 2-29 (b). However the distinction of the region is not so drastic, and a slow change of the value of k is more adapted to describe this transition and give good results (Figure 2-33), the value k=0.292 suggested in [4] would lead to a deviation from the constant value of γ.

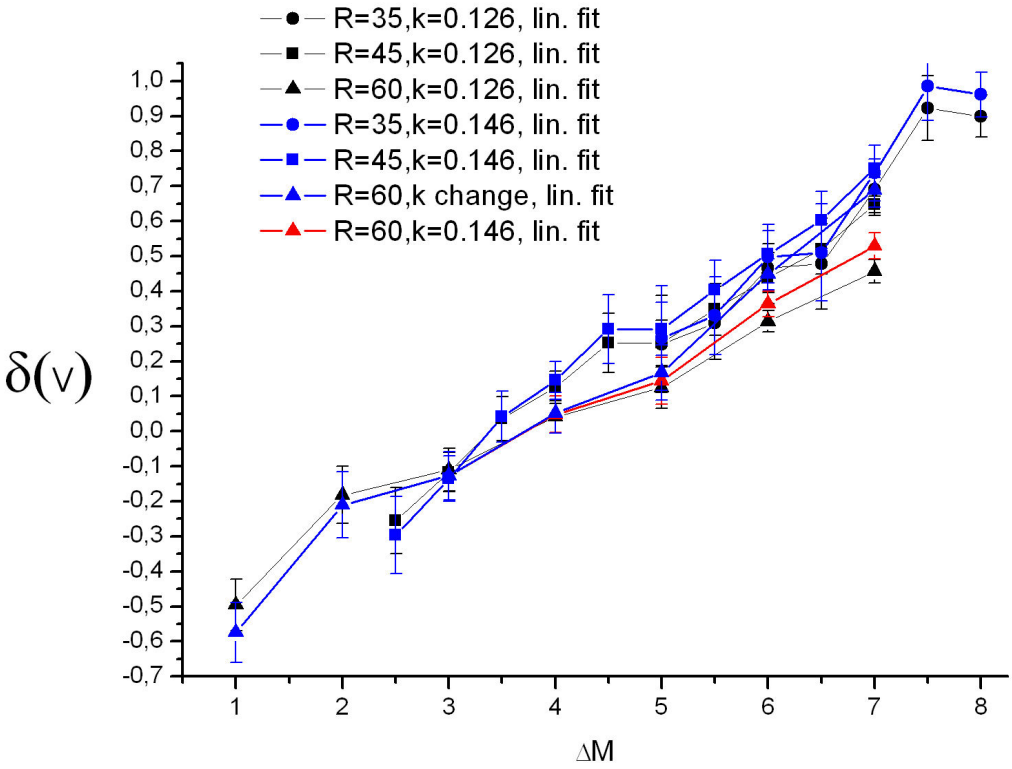

Figure 2-34 : Resulting values of δ from the fit of mass peaks width Δm as a function of the mass at constant R and ΔM.

The Figure 2-34 gives the values of δ determined by the fitting procedure. An inversion of the sign of δ occurs at about ΔM=4, so that we find out that δ is an affine function of ΔM. Above ΔM=4, the operating line is shifted towards better resolution compared to the line at δ=0, under ΔM=4 the operating line is shifted to worse resolution (see Figure 2-28). We also notice that a voltage as small as 0.5V compared to the zero to peak voltage V of several hundreds of volts is sufficient to induce important changes of the quadrupole resolution. We also observe here that the correction obtained by increasing slowly k for the highest values of ΔM improve the agreement between the values of δ obtained at R=60 (blue triangles), R=35 (blue dots) and R=45 (blue squares) as it should be.

This paragraph has shown the validity of the formula 2-28 giving the resolution of the quadrupole as a function of parameters γ, δ and k. It has been shown that the value of k can be taken as an indicator for the progression towards the triangular peak shape region. We could also estimate the position of the operating line in the stability area: R=35 corresponding to $\gamma=0.154 \pm 6\times10^{-4}$, R=45 corresponding to $\gamma=0.1566 \pm 3\times10^{-4}$ and R=60 corresponding to $\gamma=0.1614 \pm 4\times10^{-4}$. By taking reference to Figure 2-25 and Figure 2-26, we notice that the order of magnitude of these calculations are not too far from the theoretical values proposed in [4]: γ=0.1614 at R=60 is close to the transition towards the triangular shape region predicted by the ideal calculation of Figure 2-26, also the values

γ=0.1566 and γ=0.154 a fortiori are situated in the trapezoidal region as we observed experimentally (Figure 2-29 (a)).

III) Research for an effect of discrimination due to the quadrupole on the cross section of water

Another series of experiments were made with the purpose of determining when discrimination effects arise in the cross section of water in correlation with the transformation of peaks of the negative mass spectra from the trapezoidal region to the triangular region.

(1) From positive to negative mass spectra

A positive ions mass spectrum, at an electron energy of 70 eV to 100 eV able to ionize all species, is usually taken as reference to tell about the composition of gas inside the chamber and in order to define the quadrupole settings of resolution adapted to the envisaged study. However this paragraph shows that a negative mass spectrum is better suited for the study of processes with negative ions.

If the quadrupole has been properly tuned, it should filter the ions independently of the sign of their charges. However, the series of graphs in Figure 2-35, Figure 2-36, Figure 2-37 and Figure 2-38 shows that important changes occur when switching from positive to negative mass spectra.

The calibration of the mass scale is slightly shifted as shown in Figure 2-35, and the peak widths are also modified. A shift towards the higher masses is observable, indeed: the spectra of Figure 2-35 were taken successively after reversing the polarity of the instrument i.e. change the ion energy from positive to negative voltages in order to repel negative ions, invert the polarity of the focusing lenses (L2, L3, L4) and change the polarity of the channeltron high voltage; besides extraction was used to enhance the ion signal of negative ions and the complete ion optics settings were retuned to maximize the signal. As a consequence of the reduction of peak width we notice that the quadrupole resolution is improved by going to negative ion detection, even if the corresponding quadrupole settings (R; ΔM)=(42;7.5) were locating the operating line in a region of worse resolution than the settings (R; ΔM)= (60;6) chosen for the positive mass spectrum. This change of resolution from positive to negative mass spectra is also evident when comparing mass spectra of Figure 2-37 and Figure 2-38: at (R; ΔM)=(42;7.5) the mass peaks are overlapping for positive ions, while they were fully disentangled at identical quadrupole settings for the negative ions.

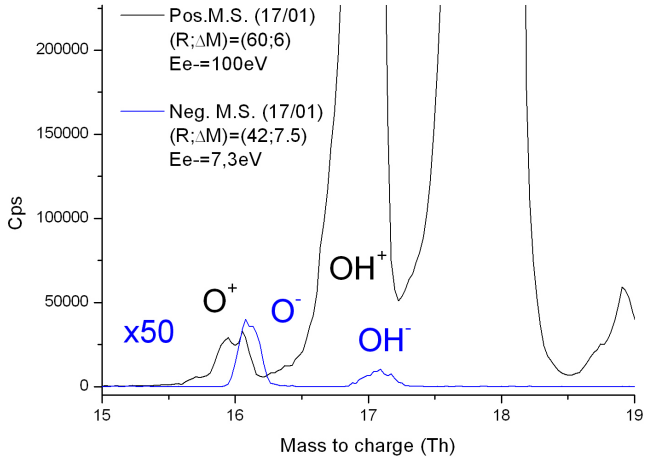

Figure 2-35 : From positive to negative mass spectra. The yield of O- from the DEA to water is extremely low compared to the yield of O+ from ionization at 100eV; it was magnified 50 times for the comparison.

In order to justify the comparison made between the mass spectra taken on different days, the Figure 2-36 show the nice agreement between mass spectra taken at identical quadrupole resolution settings (R; ΔM)= (60;6) but on different days: the black spectrum is the positive mass spectrum of Figure 2-35 taken on 17/01 and the blue spectrum magnified in red for the comparison was taken on 02/01. It is the occasion to stress out that the quadrupole resolution is not usually much influenced by the extraction and ion optics. As it will be shown in (Part II : Chapter 2.E) the resolution is mostly influenced by the injection speed of ions into the quadrupole, by the position of the operation point in the stability area i.e. the quadrupole resolution settings (R; ΔM), and, apparently, it depends for our system on the charge of ions. The reason for this is to find in the exchange of the role of the x- and y- filtering directions when we pass from positive to negative ions, more details can be found in Part II : Chapter 2.E.I).

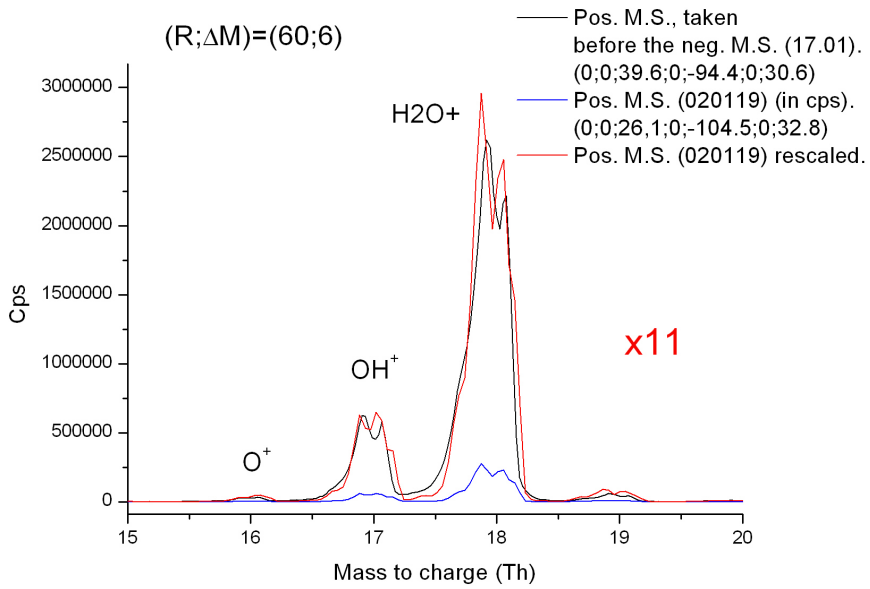

Figure 2-36 : Comparison of positive mass spectra taken at different dates to show the relevance of the comparison of positive and negative mass spectra of Figure 2-37 and Figure 2-38.

Figure 2-37 shows positive mass spectra taken at 100eV at different quadrupole settings (R; ΔM) on the 02/01/2005; Figure 2-38 shows corresponding negative mass spectra taken at identical quadrupole settings taken on the 17/01/2005. The mass spectra of Figure 2-37 were taken during the preparation of the apparatus for measuring the DEA to water whose low cross sections (especially for the yield of OH^-, $\sim 10^{-20} cm^2$) require that we look for an optimization of the separation of the peaks without too much loss of signal intensity. Masses 16 and 17 (O^+, OH^+) were just disentangled at (R; ΔM)=(42;7.5), but the limit values (R; ΔM)=(42;7) could still have been acceptable to ensure a quasi independence of the measurements of O^+ and OH^+ yields. However, at identical quadrupole settings (R; ΔM)=(42;7.5), the corresponding negative mass peaks O^- and OH^- of Figure 2-38 were too largely disentangled even for (R; ΔM)=(42;7) since the peaks O^- and OH^- starts to overlap at the value (R; ΔM)=(42;5) only. It was sufficient to choose resolution settings (R; ΔM)=(42;5) to achieve the separation of the negative mass peaks O^- and OH^-. The traditional reference to positive mass spectra led to a loss of ion signal for this study.

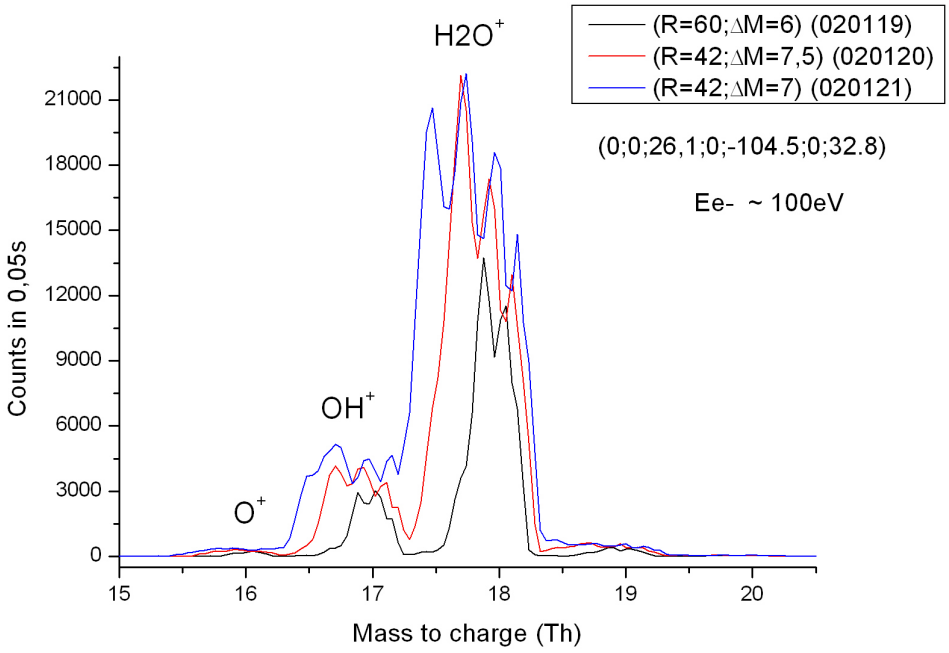

Figure 2-37 : Positive mass spectrum of H2O.

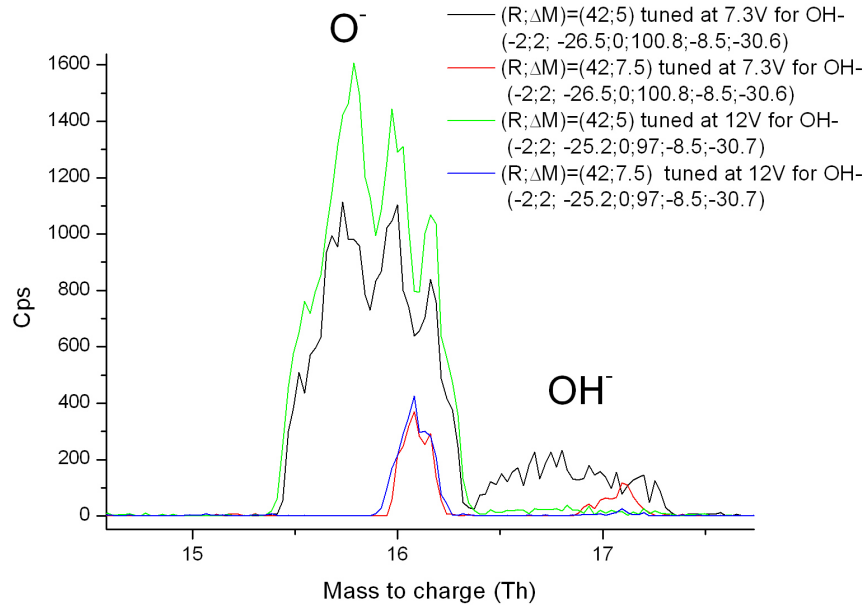

Figure 2-38 : Negative mass spectra of H2O.

Conclusion:

It is recommended to take negative mass spectra for choosing the quadrupole resolution settings when we want to study negative ions. It is better always to have the closest look at any experimental study.

(2) Importance of the position of mass button (MB)

The results of the first investigations on the appearance of discriminative effects as a function of the increase of quadrupole resolution are shown in Figure 2-40 in correlation with the transformation of peak shapes in Figure 2-39. The conditions of pressure and current during the experiment were very stable giving the possibility to make a direct comparison between the intensities of the curves.

The parameter R was kept fixed and ΔM was varied so the operating line was translated at constant slope towards higher resolution. Up to ΔM=6.5, the change in relative intensity is not observable: the cross section cs11 in red at (R;ΔM)=(45;6.5) is in close agreement with cs6 in black at (R;ΔM)=(45;4) once it is rescaled to match its second peak. However, cs9 and cs10 at (R;ΔM)=(45;7) and (R;ΔM)=(45;7.2) respectively, rescaled in the same manner to match the second peak of cs6 are not matching its first and third peak. This is an evidence for discriminative effects occurring when the resolution becomes too high and resonant peaks start to be discriminated according to the average transverse initial kinetic energies of formation of their associated O- ions. Curve cs11 at ΔM=6.5 was measured after cs10 at ΔM=7.2, hence we returned as expected to the undiscriminated cross section when the resolution is lowered again.

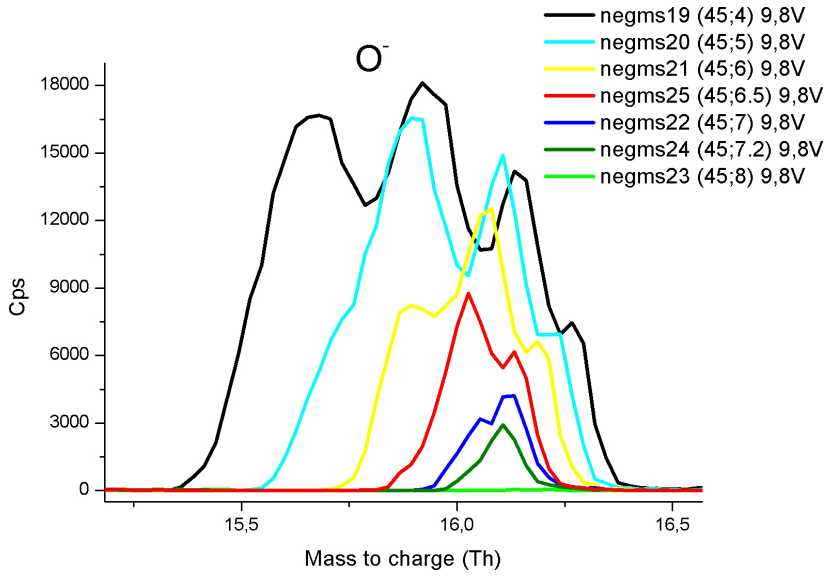

Figure 2-39 : Evolution of the O- peak of the mass spectrum associated with the cross section measured for the same series of quadrupole settings (R;ΔM).

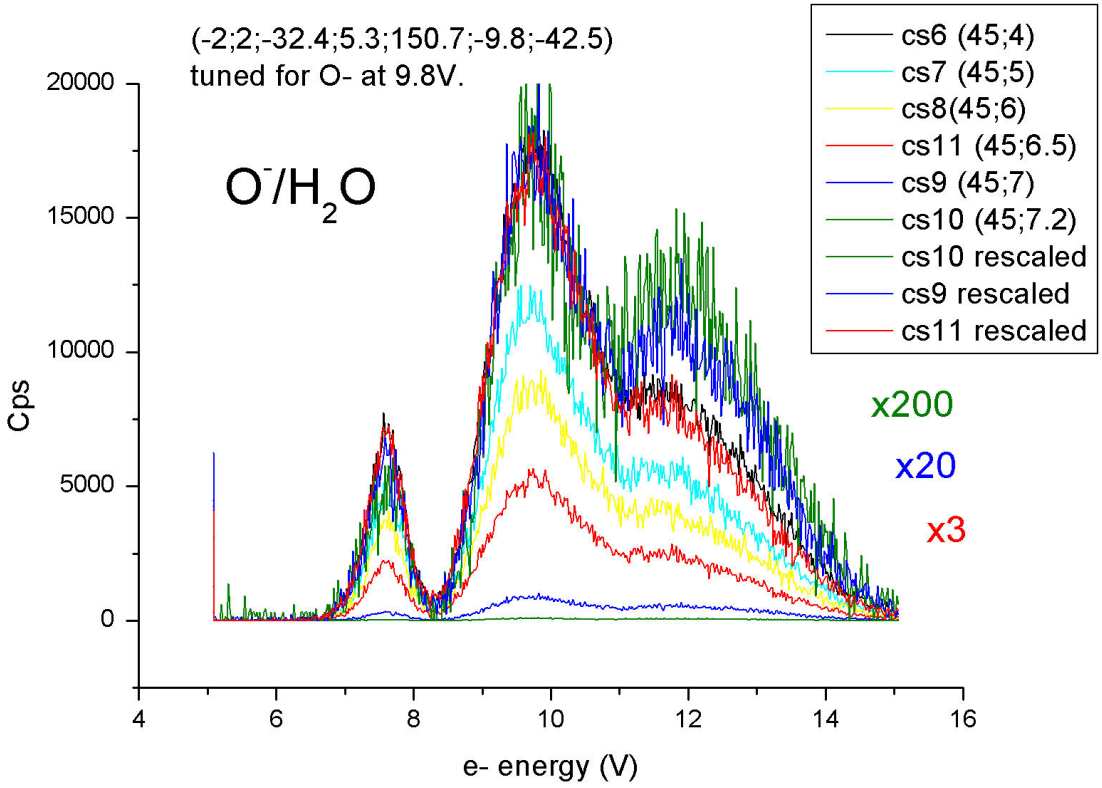

Figure 2-40 : Evolution of cross sections for O- production as a function of (R;ΔM). The curves cs11, cs9 and cs 10 at the highest resolution ((45;6.5), (45;7), (45;7.2) respectively) are rescaled to match the second peak of the curve of cs6 (45;4). There is evidence of an effect due to the discrimination occurring in the quadrupole when we enter the triangular region: look at the Figure 2-39 where the corresponding evolution of negative mass spectra is shown.

The measurements were performed at constant ion optic settings because we were looking for the influence of quadrupole resolution settings (R;ΔM) only. The extraction was used because it was expected that discriminative effects would be more apparent: still it is not possible to be sure on this point, and a study of the discrimination occurring as a function of extraction should be made along with a full determination of the position in the stability area. Up to now, it was not defined along the q-axis which seems to have the greatest influence on discriminative effects.

This study reveals that the triangular mass peak shape is not necessarily indicative of the appearance of discriminative effects, but only tells that we are approaching a region where discriminative effects could start. The occurrence of discrimination is also related to the heterogeneity of kinetic energy distributions associated with the resonances: the O^- yield was chosen for this study because of the great difference in the average kinetic energies of formation of O^- ions existing betwen the second and the third resonant peak. However discriminative effects start to be evident in the example of Figure 2-40 only when the ion signal is vanishing. This experiment would tend to indicate that discriminative effects only occur in extreme conditions and that it is not necessary to care too much about them! Unfortunatly, because it is a low resolution mass filter, we are often very close to extreme conditions with a quadrupole: at (R;ΔM)=(42;7.5) for instance, the

intersection between an operating line and the stability area is rather narrow, about 0.2amu for the RET type of focusing (see Part II : Chapter 2.E.V)(2), it is enough to move slightly the mass button (MB) to have huge changes in yield intensity. Figure 2-42 shows results of a study of the effect of ion optics on the O^- cross section from water as a function of extraction. A slight change in position of the mass button MB might have happened during the first series of measurements using the RET type of focusing; the ion yield intensity became suddendly huge between measurements 030114 and 030115.

Figure 2-41 illustrates the change δm induced by a change in position of the mass button (MB): a change of position of the mass button corresponds to a change of "zero to peak"voltage V; at constant rf-frequency and mass m, V is proportional to q (equation 2-7). So, the mass button positioned the operating point along the q-axis in the stability area.

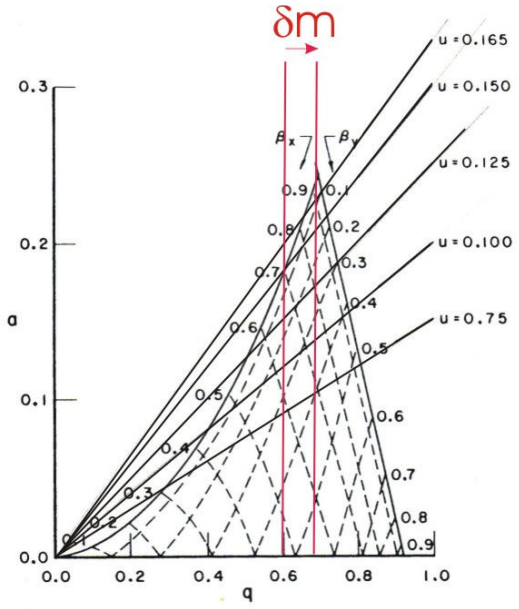

Figure 2-41 : When taking a cross section the position along the q-axis is determined by the manual mass button. By modifying the quadrupole resolution (R;ΔM), at a given mass button position (MB), we move along a vertical line in the stability area. A slight modification of the position of the mass button can have a huge effect on the ion signal intensity.

Many of the first experiments of this study were plagued by the uncertainty of the position of the operating point in the stability area. Indeed, no special care was taken for the choice of the exact position of the mass button (MB): it revealed afterwards actually to be crucial to fully determine the position in the stability area along the q-axis. The experiment of Figure 2-40 gives a typical example of what can happen: we can notice that the maxima of cross sections cs9 and cs10 fall under 1000cps and 100cps respectively whereas the corresponding mass peaks in Figure 2-39 have maxima of intensity up to 4000cps and 2900cps respectively. The reason of these discrepancies is to find in the reduction of mass peaks towards higher masses when the resolution is increased,

whereas the position of mass button (MB), determined at lower resolution, was kept fixed along the experiment. The ion signal was vanishing for ΔM=7.2 because the operating point was then located at the border of the stability area for MB=16amu (Figure 2-39).

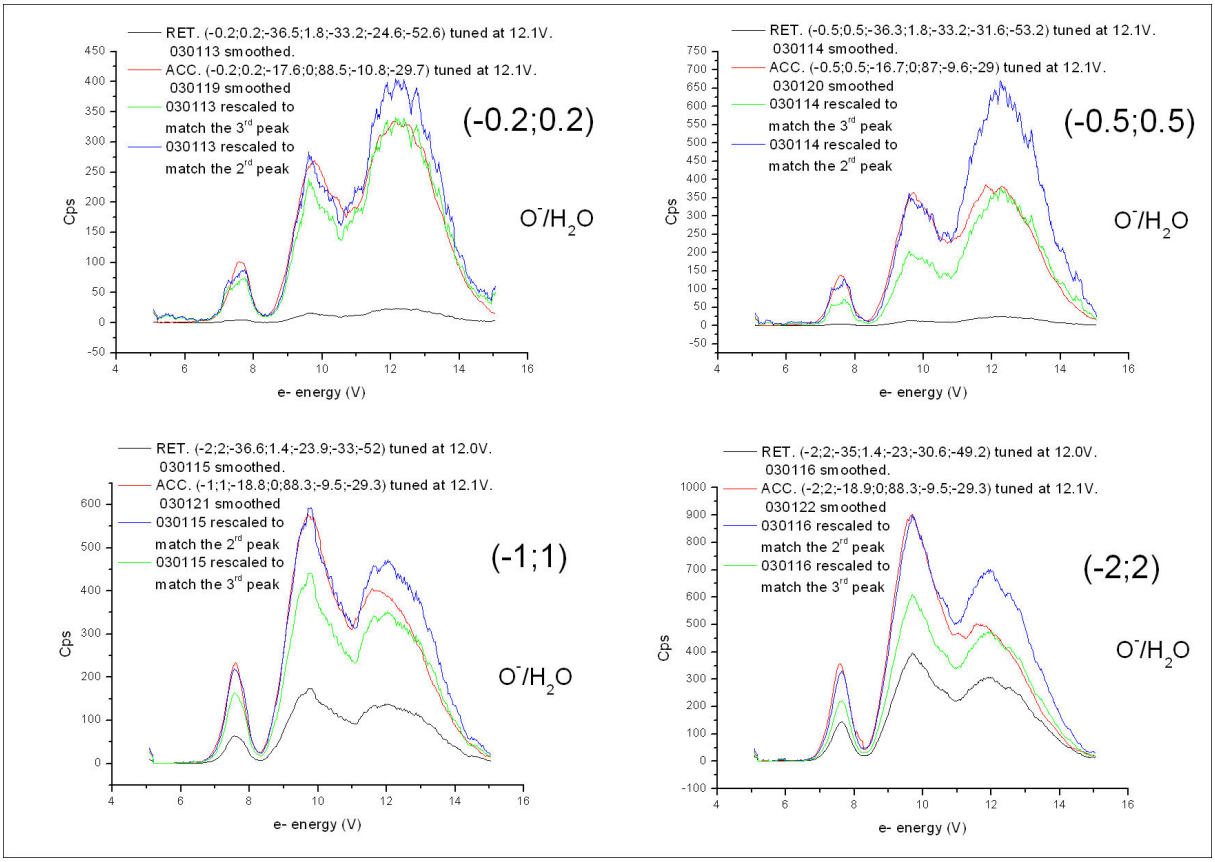

Figure 2-42 : Study of the effect of ion optics with the increase of extraction, possibly plagued by a slight change of MB position. The quadrupole resolution settings were (R;ΔM)=(42;7.5), the intersection of the operating is narrow at this resolution, about 0.2amu with the RET type of focalization.

Another effect of importance is to be remarked in Figure 2-39: the existence of modulation wave on the top of the mass peaks modifying locally the yield intensity. In Figure 2-39 they represent huge fluctuations of the intensity (1/3th to 1/4th of the full intensity). We can wonder where they come from and how they influence the measured cross section: it should make a difference when the operating point is set in a dip or on a top of these modulations.

For these reasons, the choice of position of mass button appears to be crucial for the measurement of cross sections. A full study of the evolution of the cross section when the operating point is moving across the stability area will be presented at the end of the chapter, as well as a study of the modulations observed on the mass peaks.

E. Quadrupole related effects on the cross sections of water

Modulations of mass peaks were observable in every mass spectra presented so far. It is not evident a priori to tell the origin of these observed structures on mass peaks since many causes can have similar effects. The research for the origin of these modulations led us to consider deviations from ideality of the quadrupole: among them, the existence of fine structure of the stability area due to the use of circular rods was a good candidate, as well as the mechanical misalignment of the quadrupole ensemble. By investigating the variations of these modulations under different conditions of measurements we should be able to identify the origin of these mass peak modulations. Their understanding is of fundamental importance since the fluctuations of intensity can be huge and we are concerned about the faithful determination of cross section yields with this apparatus.

What should be a normal peak shape? We already consider this question in (Part II : Chapter 2.D.II)(2) from a theoretical point of view. Normally we expect peak shapes as shown in Figure 2-43 and Figure 2-44. Mass peaks of Figure 2-43 are the results of simulation performed by Dawson [54], the mass peaks shape were obtained by summing the transmission over all phases for various points along a scan line, the ions were considered to be injected uniformly in a squared beam without transverse kinetic energies.

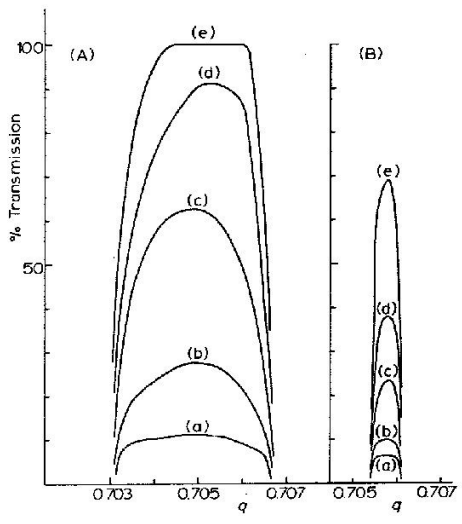

Figure 2-43 : Ideal peak shape from simulations. Taken from [54]. Varying the entrance apertures (100% = $4r_0^2$): a)4% b)1% c)0.25% d)0.11% and e)0.04%. (A) Resolution 225 (trapezoidal shape). (B) Resolution 1100 (triangular shape).

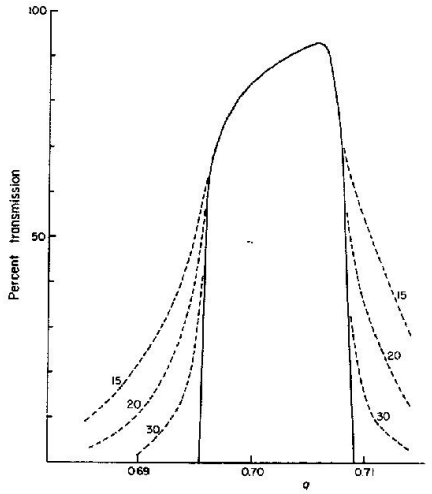

Figure 2-44 : Taken from [54]. Effect of fringing field of 2 rf-cycles long on peak shape calculated by simulations as a function of finite length of quadrupole indicated by the number of rf-cycles spent by ions inside.

We observe in Figure 2-43 that the transmission is rapidly decreasing when the entrance beam of ions (aperture) is increased as predicted in (Part II : Chapter 2.D.II)(2). The mass peaks shown in Figure 2-44 should be even more realistic. They include the presence of fringing fields at the ion entrance of the quadrupole and it shows how the finite length of the real mass filter can account for the "tailing" on the side of peaks observed in our mass spectra (especially towards lower masses).

I) Transmission in quadrupole

The stability of trajectories has been studied theoretically and the stability diagram gives the conditions under which ions in a perfect quadrupole field of unlimited dimensions can pass. The physical realization imposes limitations; the quadrupole must have limited sizes: the radius size limits the trajectories in amplitude and thereby gives their importance to the initial conditions of entrance i.e. the initial position of entrance, the initial transverse velocity and initial entrance phase which determine the amplitude of the trajectories. The stability diagram shrinks with respect to these considerations as shown in Figure 2-25. Besides, because the aperture radius limits the ion motion equally in every direction, the difference of filtering with respect to the entrance angle arises. Limitation of the length of the quadrupole implies the existence of borders and thereby the existence of fringing fields at the entrance and exit of the quadrupole, as well as a finite time of transit for the ions, and thereby the dependence on the speed of injection arises. Other limitations in the realization lead to deviations from a perfect quadrupole field: they are due to geometrical approximation or defaults in the construction of a quadrupole as well as defaults in the potential applied to the rods or simply to local disturbances caused by contamination of the rods. The influence of some of these limitations on the transmission will be envisaged in this section.

Different concepts have been introduced to deal with the problem of transmission in a quadrupole: the transmission itself designates the ratio of the number of ions exiting over the number of ions entering the quadrupole. Very often, since we don't know how many ions are formed in the chamber since this is actually what we are looking for, another concept, the sensitivity, has been introduced [54] which designates the ion yield response of the apparatus for a given introduction of gas in the ion source. Besides, the transmission depends on the initial conditions of ions when they enter the field (see Part II : Chapter 2.D.II)(1)). A related concept has been introduced [62], the available cross section (ACS), which designates the distance from the axis of the quadrupole beyond which an ion cannot penetrate the QMF without being rejected by the quadrupole field. We find a direct illustration of the ACS in

Figure 2-43 (A). The ACS corresponds to 0.04% of entrance aperture giving a flat top peak with 100% transmission (curve (e)). The ACS becomes smaller than 0.04% when the resolution is increased since the curve (e) of Figure 2-43 (B) still does not reach 100% transmission.

However, the concept of ACS can lead to confusion because it disregards the dependence of transmission with the direction of entrance of the ions, as well as the rf-phase and the transverse velocities at the entrance.

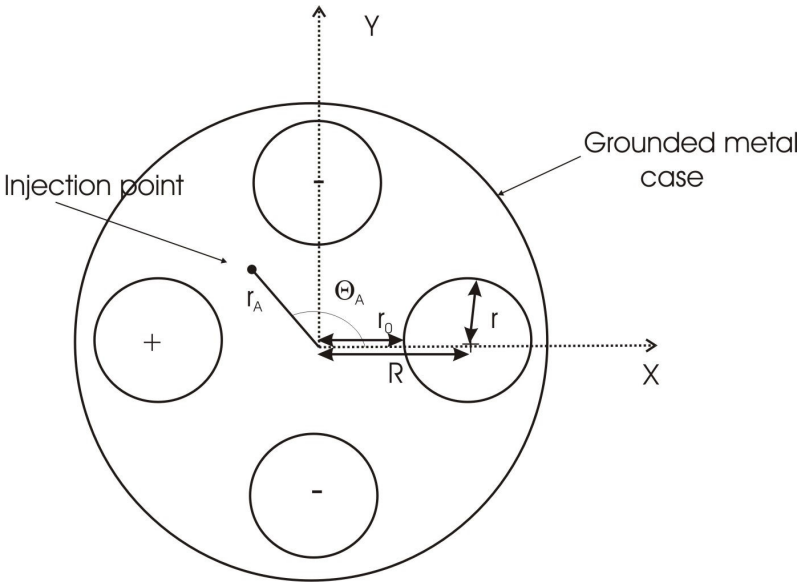

Figure 2-45 : Schematic cut of the quadrupole. r_0 is the radius of the inscribed circle between the rods, r is the radius of a rod, and $R = r+r_0$. The injection point is defined by r_A and Θ_A, which are the radius and angle of aperture respectively, defined in [8] for the study of the available cross section as a function of entrance angle.

The direction x and y defined in Figure 2-45 are defined by the pair of rods. The direction x and y are not equivalent because the potentials applied on them are different: in the x-direction the potential $\Phi(t) = (U - V\cos\omega t)$ is positive in average, whereas in y-direction the potential $-\Phi(t) = (-U + V\cos\omega t)$ is negative in average (see Part II : Chapter 2.D.I)(1). Due to the difference of response to the alternating field, lighter positive ions are rejected along the x-direction, whereas heavier positive ions are rejected alond the y-direction. Hence the field in the x-direction plays the role of a high mass pass filter whereas the field in the y-direction acts as a low mass pass filter, and both combined gives a pass-band mass filter (see [54], p13). As a remark, passing from positive to negative ions is equivalent to change the role of the directions.

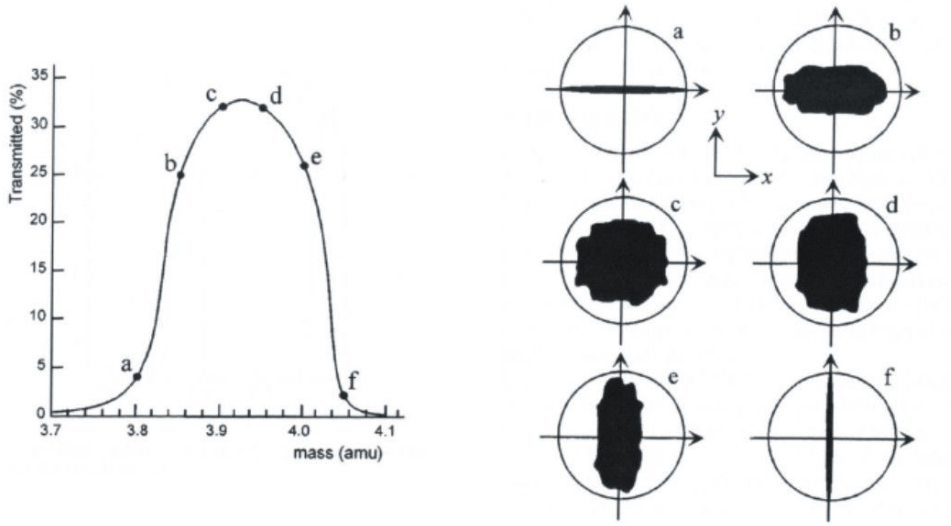

Figure 2-46 : He^+ ions remaining 26 cycles in a finite quadrupole. On the right contour maps are showing where the ions transmitted by the filter originate mostly. The contour maps show that ions contributing to the low mass side of the peaks originate from the region close to the x-axis and ions of the high mass side originate from the region close to the y-axis. The circle designates the original size of the beam at entrance [60].

Variations of sensitivity as a function of the aperture's angle are of importance for us if we consider that the ions are mostly formed in our chamber along the direction of the electron beam. As a consequence we can expect the beam of ions focused at the entrance of the quadrupole to be favorably distributed in one direction. We find here the reason for the shift and change of resolution of the negative ions mass peaks with respect to the positive ions mass peaks observed in Part II : Chapter 2.D.III)(1). The role of the direction is interchanged after the change of ion charge whereas the direction of distribution of the ion beam is unchanged. Positive ions were favorably distributed along the x-axis and the negative ions were favorably distributed along the y-axis. It is illustrated in Figure 2-46 showing the results of simulations which were tracing the origin of He^+ ions transmitted by a finite quadrupole previously emitted uniformly and randomly from a circular source area (represented by the circle on the right graphs) at random instants (random rf-phase), without transverse kinetic energies[60].

In [64], the authors used a program solving the Mathieu equation in two dimensions for a finite quadrupole mass filter. They were interested to examine the effect of finite length of the quadrupole, as well as the effect of variation of the ion source aperture, especially the variation of angle aperture.

The results of [64] show the dependence of the available cross section (ACS) of N_2^+ in a hyperbolic quadrupole field of finite length (38 rf-cycles) as a function of the entrance angle Θ_A and aperture radius r_A defined in Figure 2-45. In Figure 2-47, the transmission of N_2^+ can be truly 100% in the y-direction only if the beam radius is less than 0.1mm. In the

best case, the transmission falls under 10% when the beam radius exceeds 1mm. Hence, the ACS is very dependent on the entrance angle of the ions and rather small: less than 0.1mm for a total aperture radius of 2.75mm in the example of Figure 2-47. We can expect these results to be generic and the transmission for O- must be more favorized in one direction than the other.

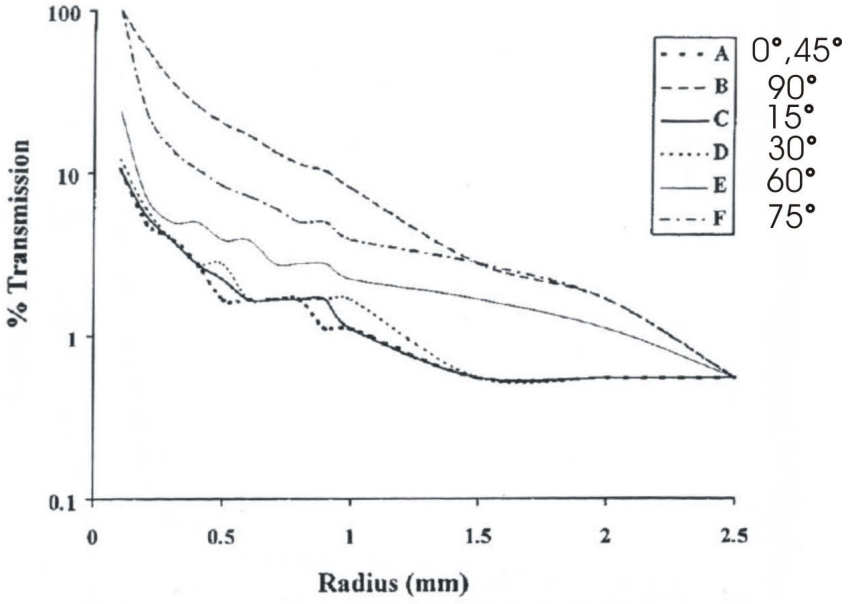

Figure 2-47 : The figure shows the simulated percentage of ions successfully transmitted, plotted against aperture radius, taken from [8]. The curve labeled A represents coincident curves for the aperture angle Θ_A =0°, 45°, 135°, 180°, 225° and 315°. The curves labeled B represents coincident curves for aperture angle Θ_A =90°, 270°. Curves labeled C represents Θ_A =15°, curves labeled D, Θ_A =30°, curves labeled E and F, Θ_A =60° and Θ_A =75° respectively. The transmission is symmetric with respect to the x-axis and y-axis (defined in Figure 2-45**). The field was supposed to be an ideal hyperbolic field, but it gives an idea of the strong dependence of the transmission on the place of injection. Ions remain for N=38 rf-cycles in the quadrupole (long time), the rf-voltage applied is sinusoidal (V=123.5V, U=20.5V, f=2MHz), r_0 was chosen to be 2.75mm.**

It is difficult to take into account all possible effects, which modify the transmission in our quadrupole. For instance the discussion of the effect of finite length in Part II : Chapter 2.E.IV)(2) will reveal to be beneficial in some conditions and detrimental in other: fringing field can strongly defocused the ions if they are too slow or too fast but can on the other hand be beneficial and flatten the dependence with the rf-phase if a proper speed of injection is chosen. As well, the finite length can increase the transmission (at the detriment of the maximal attainable resolution). Other effects as the deviation from an ideal quadrupole field are able to produce important modulations of the intensity under some conditions (high resolution and slow ions) and some will be examined as being the possible cause for the modulations observed on the mass peaks.

By setting a rough resolution in Part II : Chapter 2.D.II)(3), we could obtain

trapezoidal peaks which could have looked like flat top peaks if the modulations were not affecting the peaks shape (see further the Figure 2-58). However, it could be that the maxima of the modulated intensity are still close to the full intensity as it is shown for the study in Figure 2-58 and the mechanism proposed for these peak modulations in Part II : Chapter 2.E.IV)(3) will prove that it is the case. There is always a modulation of the intensity due to the rf-phase (see Figure 2-23), especially if we are close to the border of the stability area. The results of Figure 2-43, Figure 2-44 were obtained with a squared beam, the intensities of peaks have been summed over all phases. This presentation of the transmission in Figure 2-43, Figure 2-44 dependence on the initial conditions did not envisage the dependence with the aperture angle (?).

When the resolution becomes rough we can hope to be close to conditions of full transmission, if the ion optics was properly tuned to focus the ions at the entrance of the quadrupole, and if necessary in the proper direction. More tests should be made however in order to determine for different examples the exact transmission of the quadrupole.

II) Studies of the mass peaks modulation

This subsection is presenting some generic features of the modulations of the peaks; it precedes the discussion of their possible origin in the next subsection.

(1) Peak modulations are not discriminative effect

One feature to insist on is the fact that the modulations do not seem to arise from discriminative effects. It will be also confirmed in the next section (Part II : Chapter 2.E.IV)) in the study related on the influence of ions.

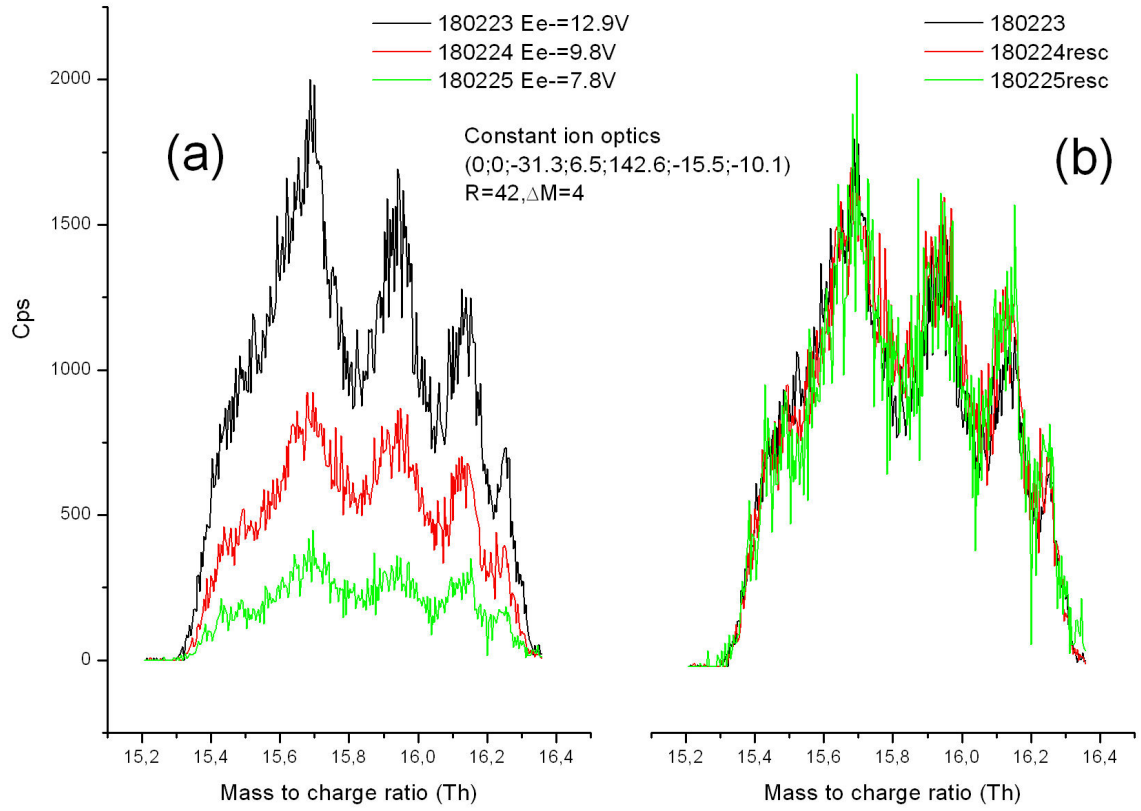

Figure 2-48 : (a) Mass peak of O^- from the three resonances: the green curve draws the mass peak of O^- ions arising from the 1st resonance at Ee-=7.8V, the red corresponds to the 2nd resonance at Ee-=9.8V and the black one to the 3rd resonance at Ee-=12.9. Once rescaled (b), the three curves superimposed. As a result, the modulation do not depends on the initial transverse kinetic energies of the ions at the entrance of the quadrupole. All O^- mass peaks are equally affected by the modulations.

From section (Part II : Chapter 2.C) we know that the average energy released at the formation of O^- ions varies much from one resonance to another.

Each Mass peak of Figure 2-48 (a) is associated with one of the three resonances of the DEA to water.

If the modulations would arise from some discriminative processes affecting more strongly some ions than others depending on their initial transverse kinetic energies, we would expect some variation in the amplitudes or positions of the waves between the mass peaks of Figure 2-48 , as it is observed for the relative intensities of the three resonances when the ion optics is changed. However it is not the case for these modulations; once rescaled the amplitudes and positions of the waves on the mass peaks are the same for ions from different resonance (Figure 2-48 (b)).

(2) Influence of diverse variations

When the dwelling time of the measurement is changed, the positions and magnitudes of the modulations remain the same: this phenomenum is stationary. An example of it is given in Figure 2-49, the black and the red curves were taken in the same conditions but with different dwelling time, and nevertheless they superimposed.

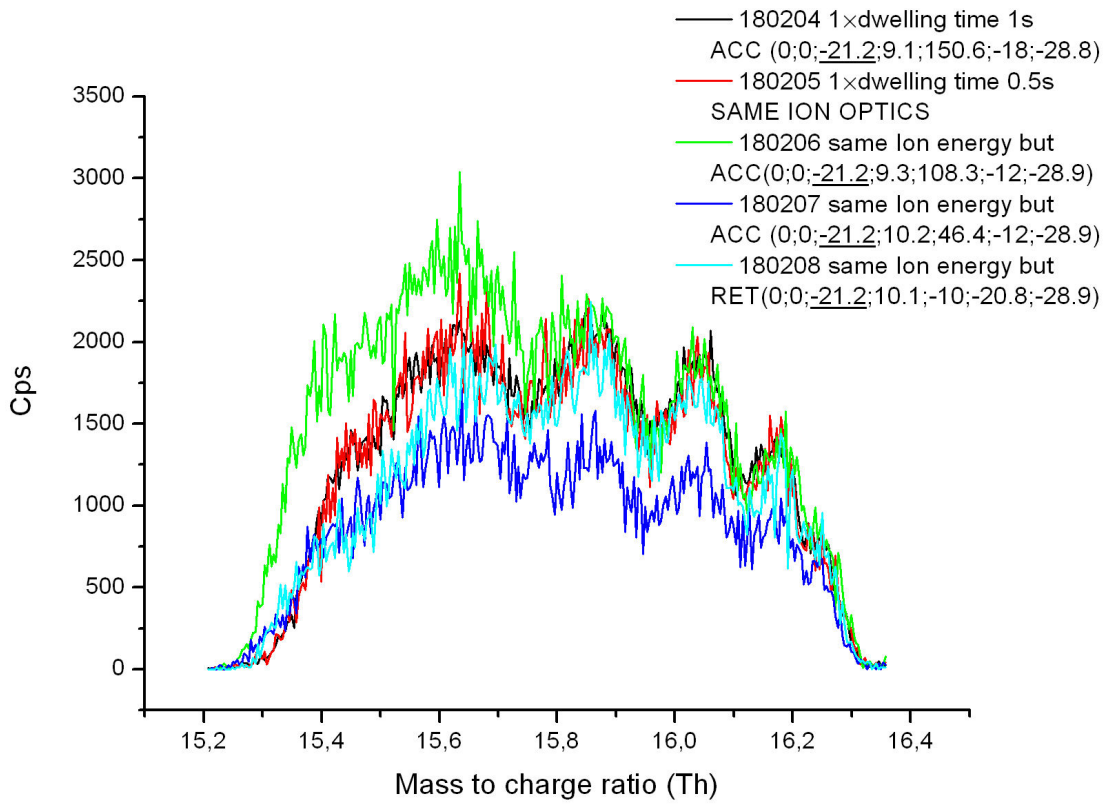

Figure 2-49 : Effect of ion optics and dwelling time on the mass peak modulations. The dwelling time is of no importance (red and black curves superimposed) showing that the modulations results from some stationary phenomenum. Influences of ion optics variations are shown by the other curves: the position of modulations and their relative magnitude are not modified apart from the discriminative effect due to the change of ion optics at the beginning of the peak.

Examples of variations of the ion optics only (ion energy excluded) give a hint that the modulations are not much influenced by the ion optics settings as well. The variation of ion optics has an influence on the low mass end of the peak corresponding to the highly discriminative zone of the stability area (see Part II : Chapter 2.E.V)), but the curves are otherwise nicely superimposing over the rest of the peak.

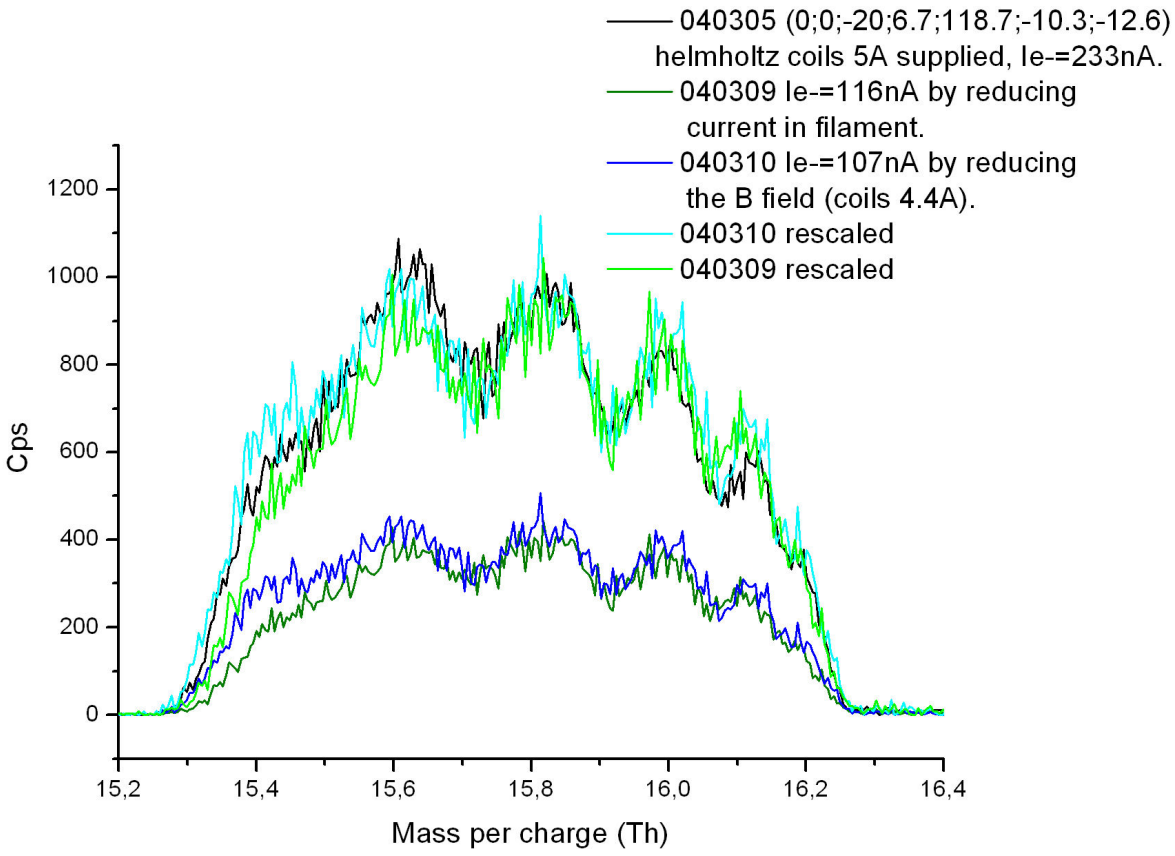

Figure 2-50 : Effect of lowering of e- current and magnetic field. The green curves show the effect of lowering the current by reducing the emission of the filament, the blue curves show the effect of diminishing the $\vec{B}$ field resulting in a comparable reduction of electron current Ie-. Once rescaled, the effects are negligible, the magnitude and position of the modulations have not been influenced.

The influences of variations of the e- current intensity and magnetic field are tested in the examples of Figure 2-50. The e- current was first reduced by lowering the emission of electrons from the filament, it results more or less in an overall decrease of the intensity of the mass peaks, no important changes in the positions and magnitudes of the modulations are observed. As well, a decrease of magnetic field intensity comparably lowering the electron current has no particular influence on the positions and relative magnitudes of the modulations. This gives a hint that the modulations do not arise from saturation effects of the detector or from some space-charge effects or some effects due to the presence of the magnetic field.

The special influence of the deflection plate at the exit of the quadrupole is considered in the Figure 2-51 . Here also the influence of variation of the deflection voltage is negligible, however a first example of the influence of ion energy (IE) is also shown in the Figure 2-51.

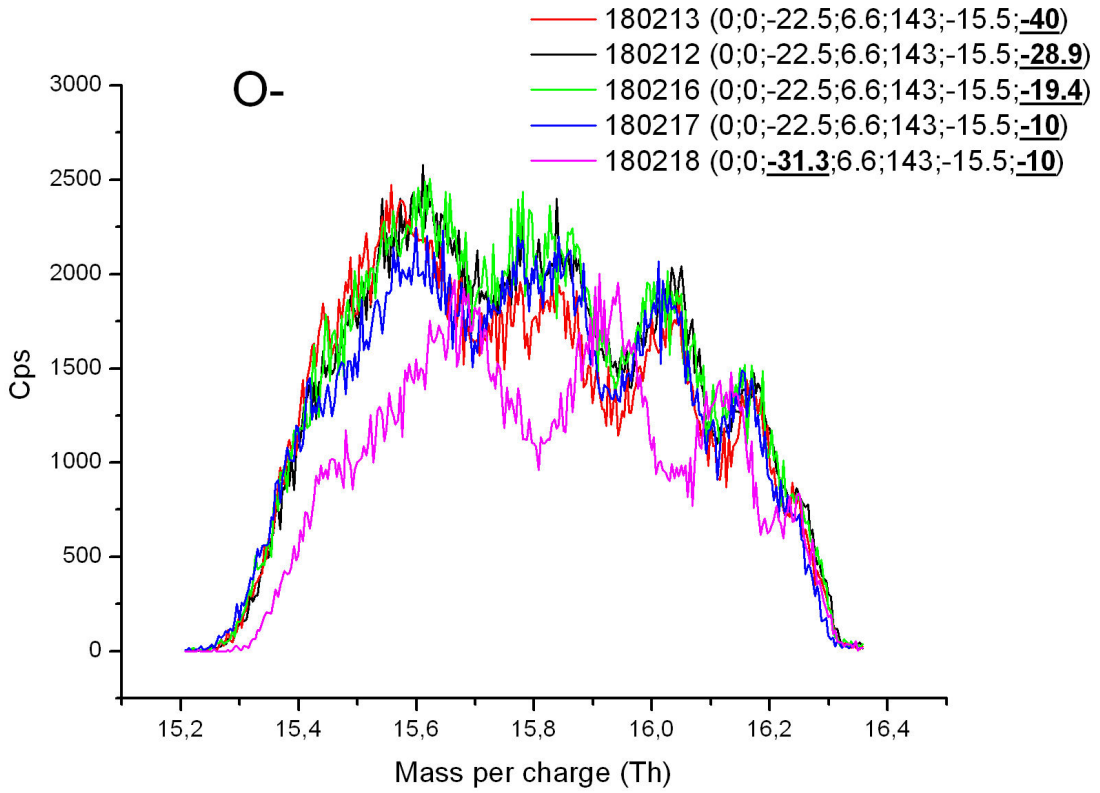

Figure 2-51 : Effect of the influence of the deflector before the channeltron. By varying the deflection voltage from -40V to -10V, no big change in the position and amplitude of the waves of modulation is observable. However, we have here a first evidence of the sensitivity of the waves to a modification of the ion Energy (speed of ions) which leads to important variations of the positions and amplitudes of waves (curve in majenta).

The calibration of the mass peaks presented in Figure 2-52 is missing, its importance is not crucial here; the curves show some mass peaks of O- as in the precedent figures. The effect of lowering of the channeltron high voltage is tested in Figure 2-52, without particular influence on the positions and magnitudes of the modulating waves. However, another example of the influence of a change in ion speed injection is given here. The displacement of the wave positions and the change in magnitudes are also evident, moreover the reduction of peak width is more pronounced in this energy range (variation from 10 to 20V) compared to the precedent example of Figure 2-51 (variation from 20 to 30V); it leads to an increase of the resolution when the ion injection is increased in agreement with the results of precedent studies (see section (Part II : Chapter 2.E.IV)), and in contradiction with a generally accepted idea that it is always better to inject the ions with low speed into the quadrupole to obtain a better resolution).

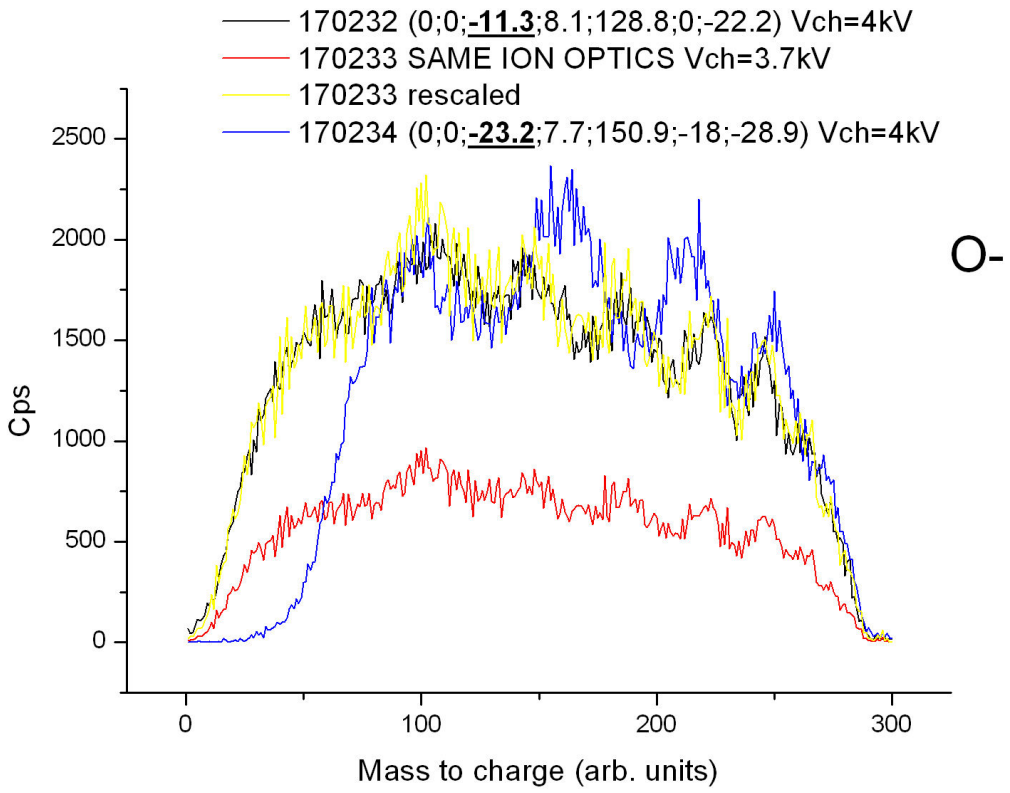

Figure 2-52 : Effect of changing the channeltron voltage. The overall intensity is changed but no difference in relative positions and magnitudes of the waves is observed. The blue curve gives a second example of the modification of the mass peak when the ion energy is increased: at comparable sensitivity the resolution is higher for injection speed of ions higher (in this domain of ion energy at least, [54]).

(3) Influence of the position in the stability area

The influence of the modification of the position of the operating line in the stability area is shown in Figure 2-53. The displacement of the maxima and minima of the modulations is evident, as well as the change in relative magnitudes of the modulations which increases when the quadrupole resolution increased (ΔM increased). The peak at higher resolution appears as the cut of the final part of the peak at lower resolution. This observation can lead to attribute the origin of the modulations to nonlinearities occurring along lines of resonances traversing the stability area as shown in Figure 2-56. But further inspection of this phenomenon shows that it could not explain the observed influence of the ion energy on the modulations. Another mechanism will be finally proposed which satisfyingly explains all features observed in this subsection.

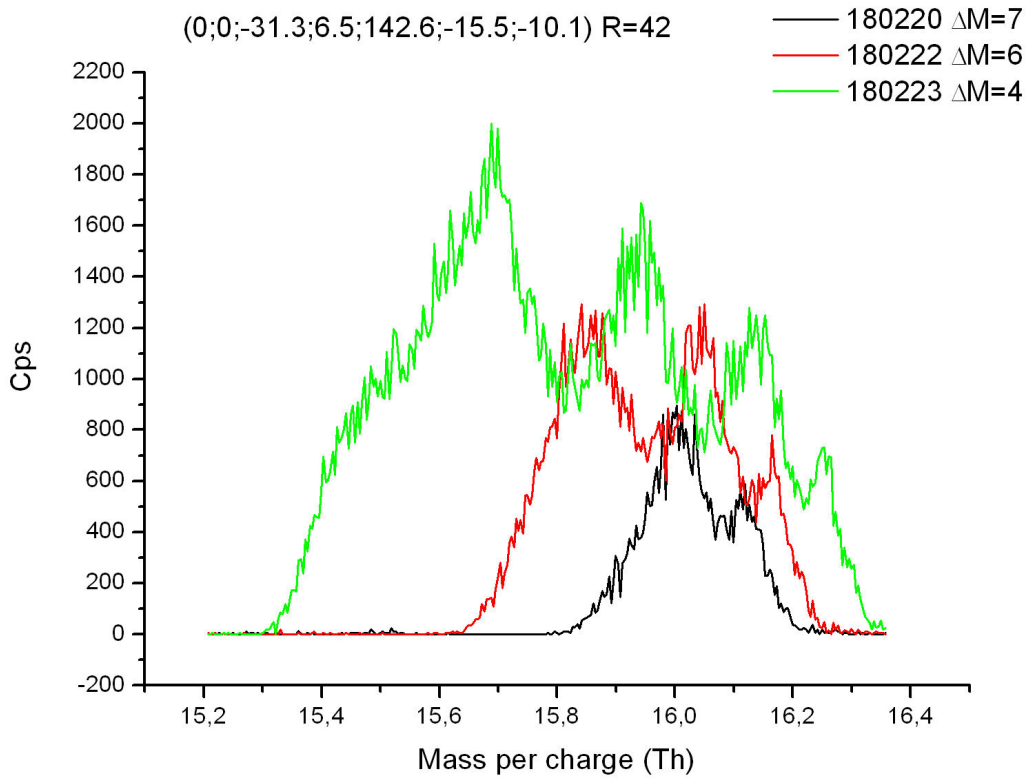

Figure 2-53 : Effect of the change of quadrupole resolution. We observe the modification of the position and magnitudes of the waves according to the vertical position in the stability area. This effect could be explained by nonlinearities of the field along some resonance lines inside the stability area, but we will see that the displacement of the waves with the ion energy requires another mechanism for the formation of the waves.

To conclude about these observations: the main dependences observed are the dependence with the ion energies and the dependence with the position of the operating line in the stability area. They both have an important influence on the positions and magnitudes of the modulating waves and on the resolution of the quadrupole.

III) Research on the origin of the mass peaks modulation

By searching for the origin of the modulations of the mass peaks, I found many possible causes mentioned in the literature which can produce such peak modulations. One good possibility was the existence of “resonance dips” due to nonlinear distortions in the quadrupole field. This possibility is examined in the following paragraph, even if it came to be rejected finally, because it teaches in general on the quadrupole’s sensitivity to small defaults in the construction and in particular about possible pitfalls of replacing hyperbolic

rods by circular ones.

(1) Nonlinear field effects due to circular rods

Since it is possible to approximate the ideal hyperbolic quadrupole field by properly adjusting the radii and positions of circular electrodes, the replacement of hyperbolic shaped electrodes by circular ones is common practice in the design of quadrupole mass filters, their fabrication and mounting being much simpler than hyperbolic electrodes. However, small errors in the shape or in the construction of the electrodes structure can dramatically increase the nonlinear components of the field and produce resonances by causing some ion trajectories to become unstable that otherwise, in a perfect field, would be stable and limited in amplitude.

Figure 2-45 shows a schematic cut of the four identical rods with the grounded case around: in [61] and [62], it is mentioned that the optimum position for approximating the hyperbolic field with circular electrodes depends little on the position of the grounded case. The arrangement of the rods is then defined by the two parameters (r, r0) only, defined in Figure 2-45 (or (r, R) in [62]).

In the section "theory of quadrupole", the quadrupole field was presented as being produced by hyperbolic electrodes giving rise to a field of the form:

$$\Phi(x,y,t)=\frac{(U-V\cos\omega t)(x^2-y^2)}{2r_0^2}= \quad (U-V\cos\omega t)\times \mathrm{Re}\{A_2 z^2\}, \qquad z=x+iy \quad (1)$$

The potential field in a quadrupole mass filter with circular rods can be written as:

$$\Phi(x,y,t)=(U-V\cos\omega t)\times \mathrm{Re}\{A_2 z^2+A_6 z^6+A_{10} z^{10}+...\}, \qquad z=x+iy, \qquad (2)$$

Due to the symmetry of the quadrupole, the nonlinear terms contributing to the field are of order z^{4n+2}. The coefficients $\{A_N\}_N$ are the harmonic amplitudes.

Linear behavior to oppose to nonlinear behavior:

A linear working field corresponds to harmonic N=2, for which the field components $E_x \propto x$ and $E_y \propto y$ and thereby the force exerted on ions is proportional to the displacement from axis. When harmonics of superior orders contribute to the field, the field components are nonlinear and coupled (see the terms of the development corresponding to the sixth-order distortion in Figure 2-54 and the corresponding deviation from the hyperbolic equipotential

contours).

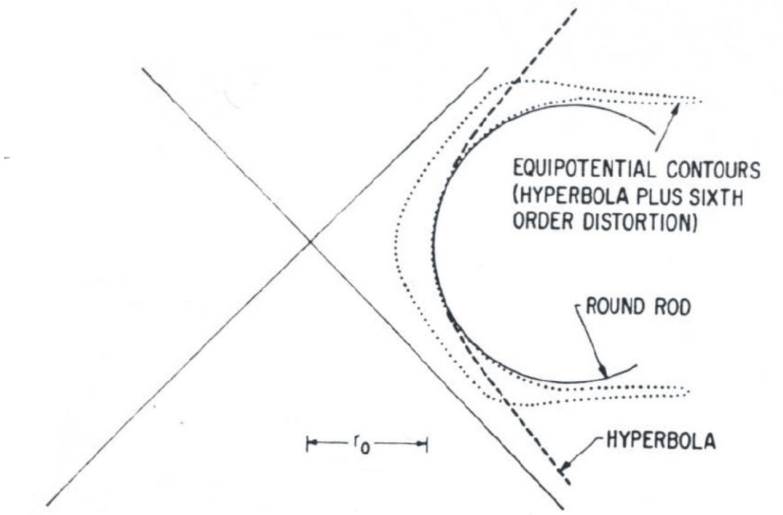

Figure 2-54: Equipotential contours (dotted lines) for simulated circular rods using the equation $\Phi(x,y,t) = (U - V\cos\omega t)\times\left(\frac{1}{2r_0^2}(x^2-y^2) + A_6(x^6 - 15x^4y^2 + 15x^2y^4 - y^6)\right)$**. To be compared with the hyperbolic contours lines (dashed line).** A_6 **is equal to** 10^2 **in this illustrative example of field distortion taken from [63].**

It has become common practice to choose the quadrupole design parameters (r, r0) such that the field term $A_6 z^6$ becomes zero, leaving only apparently weak nonlinear contributions of $A_{10} z^{10}$ and higher order terms. In this way, if we neglect the terms higher than $A_{10} z^{10}$ included, the field is a good approximation to the perfect hyperbolic field.

The dependence of the coefficients A_N on the geometrical size and disposition of the electrodes is presented for the lower order terms of the expansion in Figure 2-55.

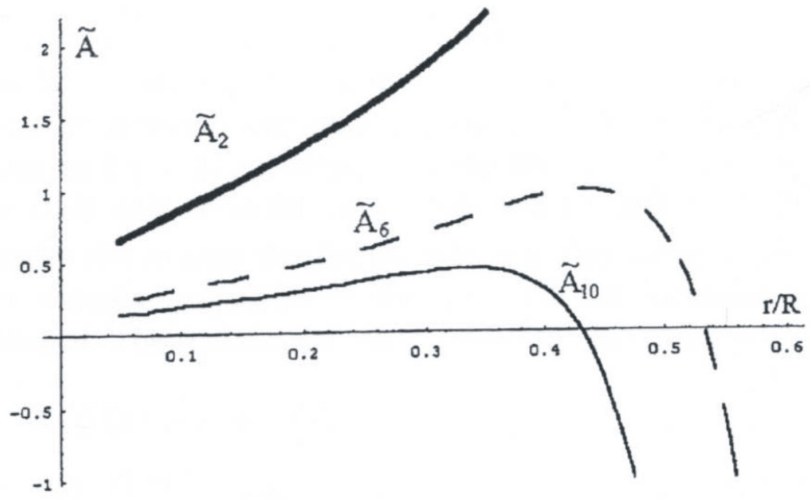

Figure 2-55: Taken from [62]. Harmonic coefficients $\tilde{A}_i(r/R)$ defined by the scaling law $A_i(r,R)\times R^i = \tilde{A}_i(r/R)$ as functions of r/R. In [62], the author choose R=(r+r$_0$) and r as reference length for determining the dimensions of the rods structure, it would have been more adapted in our case to rescale the harmonic coefficients using r$_0$ or r as scaling parameters.

The arrangement chosen in our quadrupole is characterized by the ratio $\eta = \frac{r}{r_0} = 1{,}1557$ where r is the radius of the electrodes (r equals to 4.75mm in our case) and r_0 is the radius of the circle inscribed between the rods (r_0 = 4.11mm). We obtain $r/R = 0.536$ close to the value for which the coefficient A_6 vanishes in Figure 2-55 ($\tilde{A}_i(0.534) = 0$ corresponding to $\eta = 1.1451$).

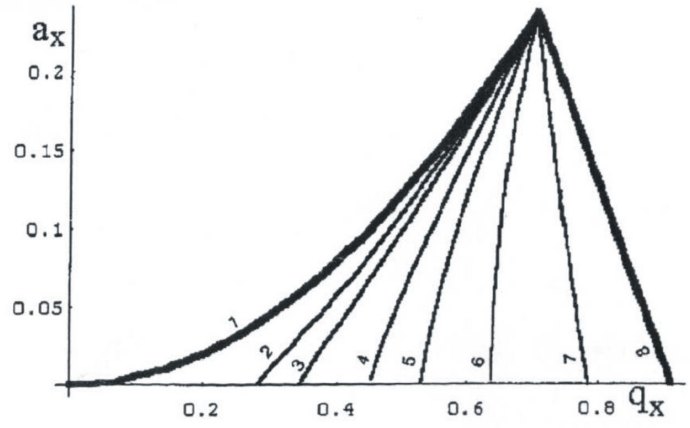

Figure 2-56: Stability diagram and resonance lines: inside the stability area are drawn the resonances lines corresponding to distortion order 10. Taken from [62].

In [62], they estimated that the contribution of the $A_{10}z^{10}$ term to the field is of the order of 10^{-3} in the case of A6=0 and that, with a deviation of the ratio η by 1%, the contribution by the A_6z^6 term becomes of the same order of magnitude as the one expected

by the $A_{10}z^{10}$ term i.e. 10^{-3}. These distortions of the field give rise to some resonance lines passing trough the stability area. The intensities and positions of these lines were calculated in [62] for the terms A_6z^6 and $A_{10}z^{10}$. Figure 2-56 shows the position of the resonance lines determined for the $A_{10}z^{10}$ term. The resonances cause ions to have unstable trajectories under some conditions where they would normaly have stable trajectories. The resonances can lead to peak splitting as we observed in our mass peaks.

The Author of [62] were interested in determining the resonances intensities in the tip of the stability area since they observed that the tip of the stability area becomes a broad spot due to cumulation of nonlinear resonances. Even small changes in the ratio η (i.e. r/R) can greatly modify the available cross section (ACS) [62]; they realized that there exists an alternative possibility for choosing the design of the rods structure (ratio η) which can improve considerably the ACS by balancing the nonlinear terms to decrease their resonance effects (ACS +40%). They found out that the right ratios for achieving this improvement is close to $\eta = 1.1$.

Small defaults in the installation are enough to "turn on" lines of resonant modulation of the transmission: The authors of [61] investigated different effects of imperfection of the rods placement. The simplest types of displacements of the circular rods structure were examined, and the corresponding multipole components in the expansion of the field were calculated. They found that displacements of 0-0.01 have little effect on the non removable harmonics (N=10, 14) but create strong multipole components in the lower orders (N=3, 4, 5, 6), which strongly distort the shape of a mass peak through a resonant enhancement in the amplitude of the oscillations of the ions in the multipole field. They also examined the effect on the multipole expansion of a small asymmetry in the supplied voltages, and observed that it "turns on" the harmonics N=4, 8, 12, 16 ... In [64], the effect of the addition of harmonics in the rf-voltages was also examined and it was observed that the sensitivity generally goes down as more harmonics are added compared to the sine wave.

The magnitude of the resonances are expected to be more important when the ions remain longer in the quadrupole i.e. when the ions are slow; this is observable in Figure 2-57. Indeed, simulations have been performed to estimate the magnitude of nonlinear resonances as a function of the time spent by the ions in the field and of the position in the stability area [54]. The decreasing q/a ratios indicated in graph (a) of Figure 2-57 are associated with operating lines of increasing resolution, hence we can estimate that the magnitude of distortions increases when we come closer to the tip of the stability area. The conditions become more stringent at high resolution due to the combination of the closer approach to the tip of the stability diagram and the necessity for more rf-cycles in the field (see Part II :

Chapter 2.E.IV)(2), Figure 2-64). Some order of magnitude of the number of rf-cycles experienced by ions in our quadrupole are given in Part II : Chapter 2.E.IV)(2).

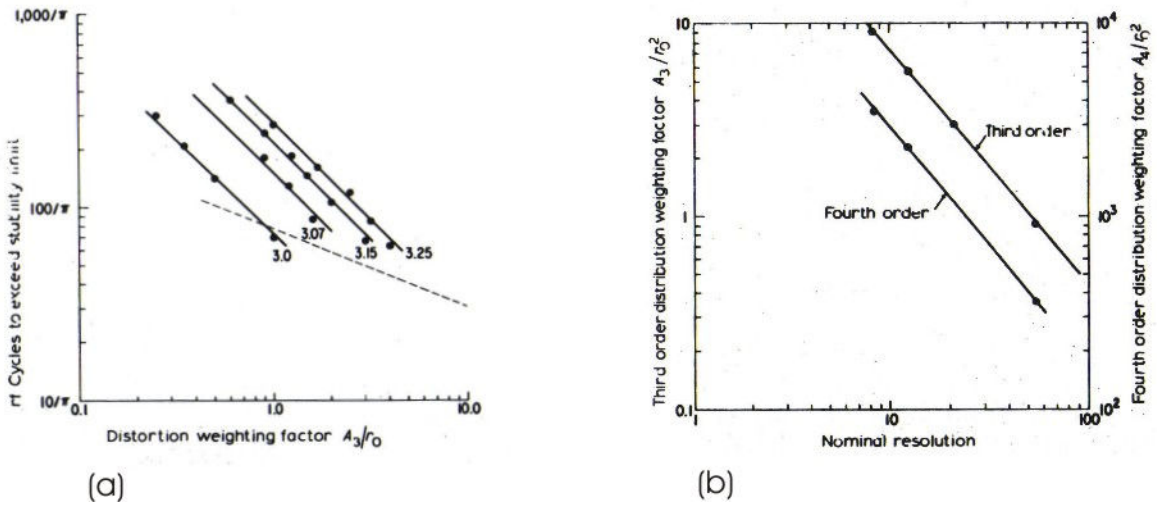

Figure 2-57 : Estimations (from simulations at one phase of rf-voltage only [54]) of the magnitude of nonlinear resonances as a function of the time spent by ions in the field and of the position in the stability area (log-log plots). (a) maximal third order distortion weighting factor and maximal number of rf cycles before an ion at the (a,q) position of the main resonance dip will exceed ten times its initial displacement; q/a ratios are given on each curve and correspond to nominal resolution 54, 20, 12, 8. (b) Using von Zahn's criterion for maximal resolution attainable $R = n^2/12.25$ [59], maximum fourth order and third order distortion weighting factors tolerable as a function of the nominal resolution.

Dawson estimated according to these results that the sixth order resonance lines caused by round rods might become significant at resolutions of a few hundreds.

The hypothesis that the modulations could find their origin in such non linear resonances was rejected since no particular increase of the magnitude of the modulations was observed when the resolution was increased (Figure 2-53) and especially the dependence on the ion injection speed is inverse than expected if the modulations would be due to nonlinear resonances. Indeed it will be clear in the next paragraph that the modulations arise when ion energies become greater than 10eV and that their amplitudes increase with increasing ion speed. Moreover according to the results in Figure 2-57, since our experimental resolution was about 20 and the number of rf-cycles spent by ions in the quadrupole around 30, the appearance of distortions effects could only arise from important defaults in the construction of the apparatus.

(2) Other possible causes for peak splitting:

Apart from the fields imperfections due to geometrical errors in the rods structure or time-varying errors in the rf-voltages applied or simply to local contaminations of the rods

which were examined in the precedent paragraph, many causes for peak splitting are mentioned in the literature [54]. Another one holds our attention as possible candidate for explaining the peaks structure on our mass peaks.

Leck et al [60] simulated the effect of varying the exit aperture of a finite length quadrupole. Ions were uniformly and randomly arising from a circular disk centered on the quadrupole axis at its entrance at uniformly distributed random instants (random rf-phase). Fringing fields and transverse initial velocities spread were not included. Ions were detected if they passed a circular disk at the exit of quadrupole.

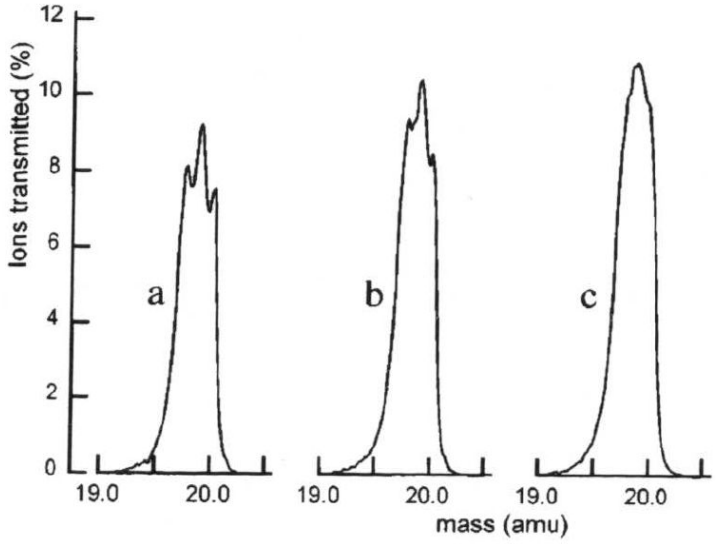

Figure 2-58 : [60]Appearance of peak splitting due to the reduction of exit aperture (area of detection in the simulation). (a) $0.5r_0$, (b) $0.67r_0$, (c) unlimited.

Figure 2-58 shows the results. Structures appear on the mass peak when the exit aperture is reduced. The exact characteristics of the quadrupole are not specified in [60], but the modulations on the mass peak arise with an exit aperture of $0.5r_0$, which corresponds to the size of our exit aperture ($0.5r_0$) all proportions kept. Unfortunately, the authors [60] were not able to investigate these structures in more details and to predict which parameters must be altered to produce a particular experimentally observed structure. However, some features tell us that it could correspond to the mechanism of formation of the structure on our mass peaks: the author [60] noted that there is a dependence of position of dips and shoulders of modulations with the resolution, as we observed in Part II : Chapter 2.E.II)(3). The next paragraph will examine particularly the importance of the injection speed of ions concerning the appearance of structure on our mass peaks. These subsequent observations will lead us to the proposal of a mechanism for the appearance of modulations on our mass peak, which is related to the observations of peak splitting in [60] due to the reduction of the exit aperture.

IV) Influence of ion energy on the ion transmission

It is generally accepted that it is better to inject the ions slowly into the quadrupole, actually we will make some observations in this part that make us reconsider this point of view, indeed it seems more advantageous for our experiments to choose a faster injection.

(1) Experimental observations

This paragraph relates about a three days experiment concerning the influence of the speed of ions traversing the quadrupole on the filtering. Over three days the flow of water and electron current were maintained constant, but the conditions evolved slightly. So, care had to be taken for comparative studies interrupted by long time periods between measurements done on different days.

For every measurement of figure 2-59 and figure 2-60, ion optics settings were retuned to obtain the maximal signal for Ee-=12.6V (O- ions from the third resonance), so that the ion injection was optimized for every change of ion energy. Unless there was a mistake of tuning, the maximal intensity achievable at a given ion energy was obtained. Hence the evolution of the intensity of the peaks is significant.

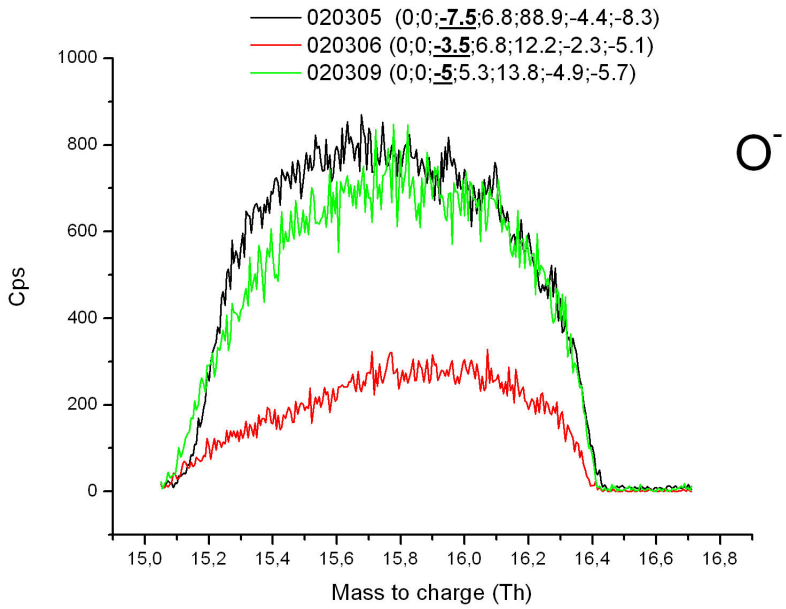

figure 2-59: The mass peaks become smooth again when the entrance speed of the ions is decreased. We also observe a change of shape of the mass peak when the speed becomes very low (from IE=-5V to IE=-3.5V).

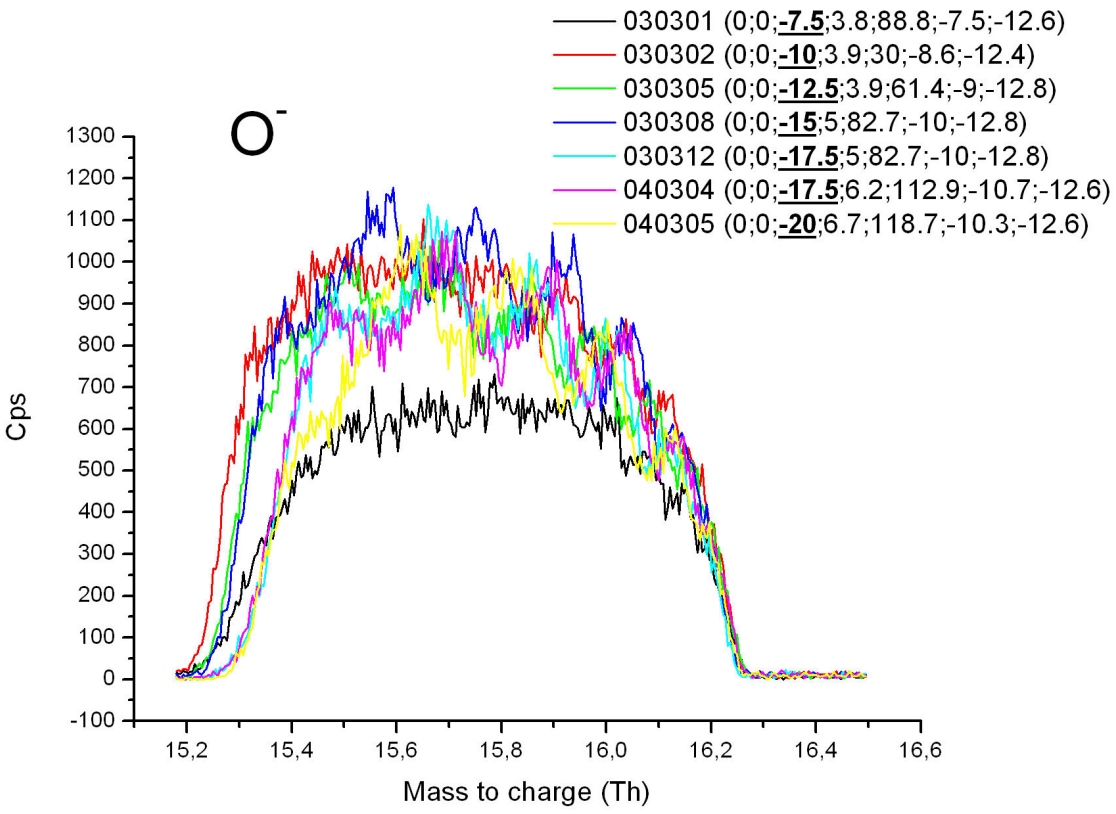

figure 2-60: Evolution of the mass peak of O^- as a function of the acceleration of ions going through the quadrupole. The apparition of the modulations on the mass peaks begin for the value IE=-10V approximately.

The last measurement of the preceding day was repeated as first measurement of the following day in order to ensure the continuity between the different set of measurement and make the comparison over the days possible. The figure 2-61 compares the last measurement of one day with the first measurement of the next day to tell about the quality of the transition.

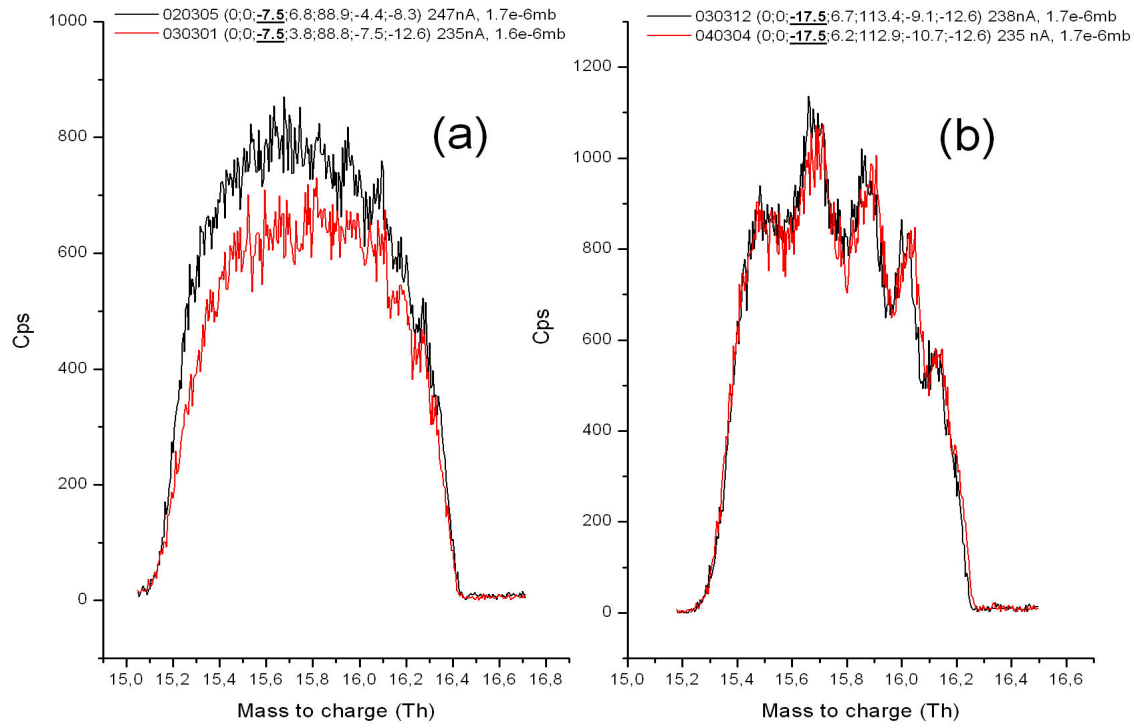

figure 2-61 : Continuity between the days for the pursuit of the comparison. Measurements were repeated at the same ion energy (IE) as the last measurement of the preceding day to give the possibility to compare. (a) the continuity between 0203 and 0303 is relatively good, however slight changes in the conditions of pressure and e- current induced a change of intensity and the modification of other factors have also modify slightly the peak shape which looks more to be in transitory shape for 030301 at IE=-7.5V as it was the case for IE=-5V in the preceding day; (b) the continuity between 0303 and 0403 is very well achieved.

From figure 2-59 and figure 2-60, we observe that the modulations of the mass peaks are vanishing when the ions are traversing the quadrupole slowly enough. As shown in figure 2-59 an inversion of the peaks shape occurs also for very slow ion injection (~5eV on this example) and the peak shape resembles then the “normal” peak shape expected for a mass peak shown in Figure 2-43 and Figure 2-44. This inversion is not insignificant, [60].

We observe in figure 2-60 that the modulation start to appear at IE=10V. When the injection energy is increasing over 10V, the waves become more pronounced and their positions are changing as was already emphasized in (Part II : Chapter 2.E.II)(2)). The width of the mass peak also reaches a maximum for about IE=10V and the maximal peak intensity is also achieved nearby this value of IE. The relation between resolution and ion speed will be discussed in Part II : Chapter 2.E.IV)(2).

When the ions are traversing too slowly the quadrupole field, we notice the appearance of strong discriminating effects in the measured cross sections (figure 2-63 (b)). When the ions go slowly, all ions which should be rejected by the quadrupole field are rejected, only the ions which have the correct mass and which entered the quadrupole under some limiting conditions, can reach the end of the quadrupole. As a consequence, the slower

the ions are injected, the more efficient is the selection, but the discrimination becomes also more effective.

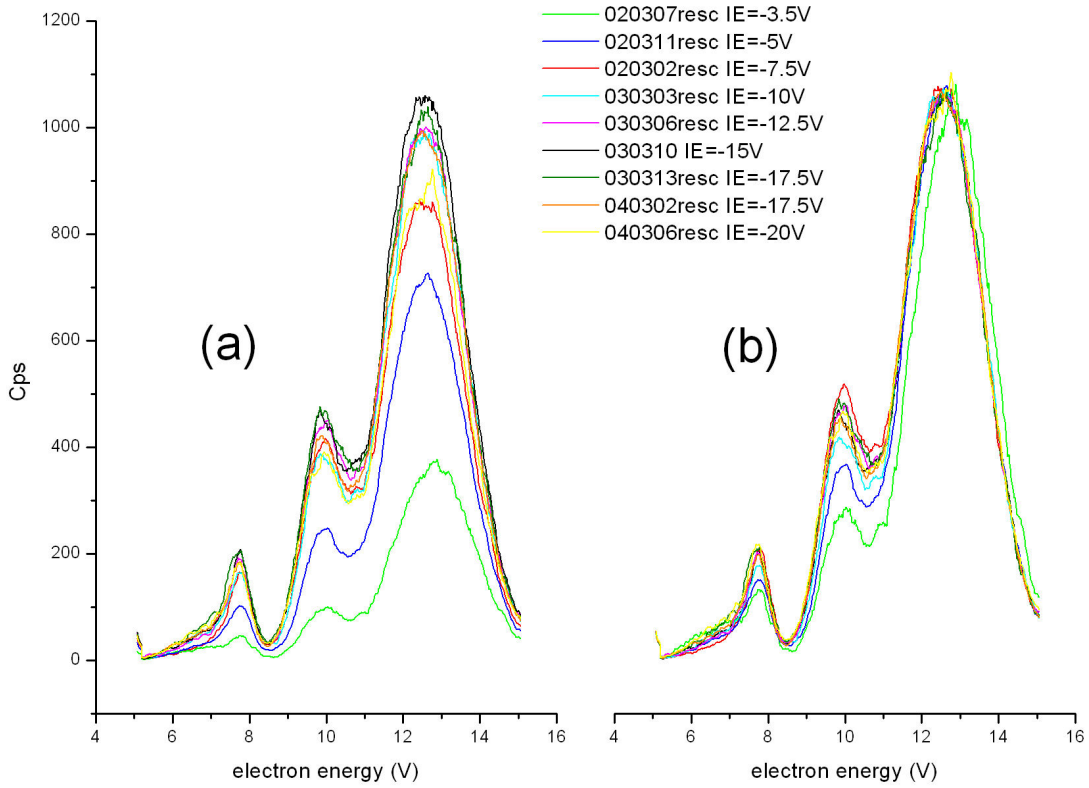

figure 2-62: Discriminative effect appearing at low ion speed. (a) CS taken at maxima of the mass peak. (b) The curves are rescaled to match the third peak of measurement 030310 (IE=-15V). The CS taken at IE=-15V,-17.5V,-20V have been taken on the maxima of the modulation, figure 2-63 shows anyway that the CS taken on maxima or minima agree perfectly in relative intensities.

Moreover, a shift in the energy scale is observable (IE=-3.5V, green curve in figure 2-62) when ions are sent with too low kinetic energy, the resonant peaks return to their previous positions as the ion energy (IE) is increased back from -3,5V to 5V. Actually it is just the effect of discrimination since we observe the same thing when we go to too high resolution.

The intensity of the peaks start to decrease from IE=20V down to the level of IE=-7.5V. However, once rescaled, a nice agreement is obtained between the cross sections measured for ion energy from IE= -7.5V to IE=20V. Discriminative effects appear under IE=-7.5V.

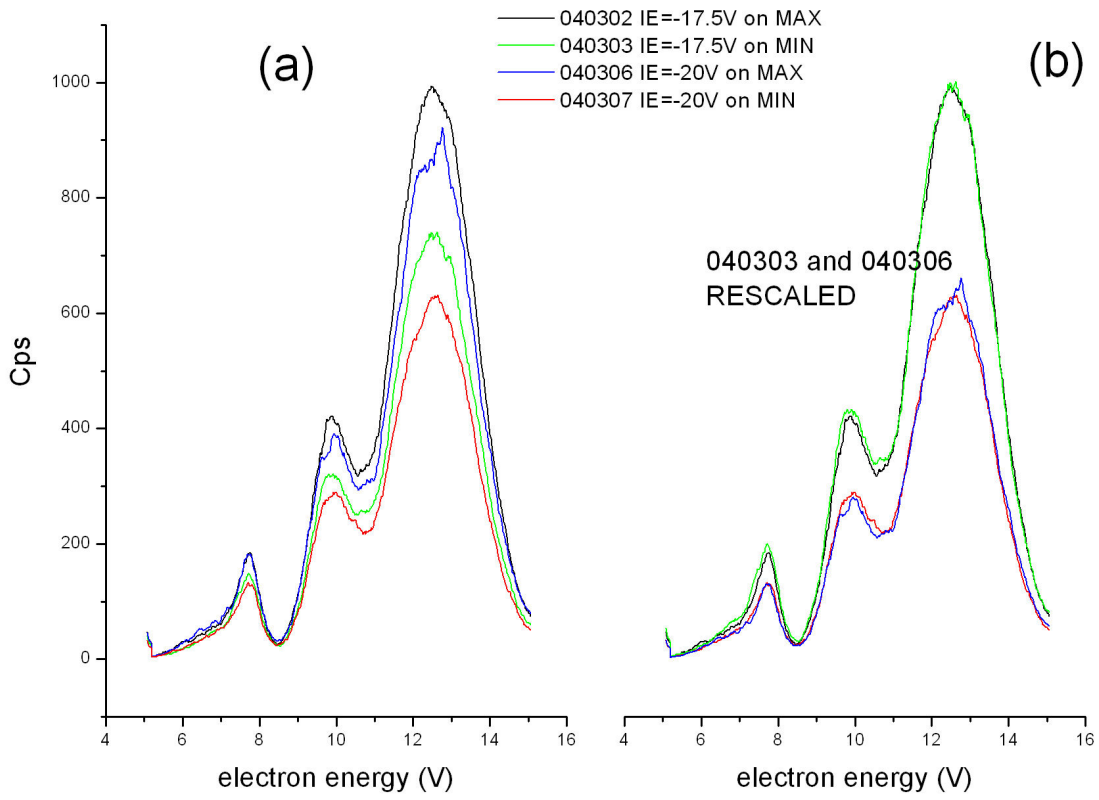

figure 2-63: Comparison of the CS taken at the Min and the Max of the mass peak modulation of O^- For IE=-17.5V and IE=-20V.

With the results shown in figure 2-63, we have the confirmation that the modulations of mass peaks are not discriminative effects (see Part II : Chapter 2.E.II)(1)), since cross sections measured at a minimum or at a maximum of the modulations perfectly superimpose once they are uniformely rescaled. The curves taken on min and max for IE=-15V show a similar agreement once rescaled.

(2) Injection speed and transmission

The relation between the sensitivity and the resolution of the quadrupole is illustrated by Figure 2-64. According to Dawson [54] these results are typical; we can expect similar behavior for our quadrupole. It was already mentioned in (Part II : Chapter 2.E.II)(2)) that we observe a significant increase of resolution when the ion energy is increased from 10V to 20V at comparable sensitivity. Such a behavior is understandable when considering the results of Figure 2-64: at comparable sensitivity, the resolution is increased when the ion energy is increased (the concept of sensitivity was introduced in (Part II : Chapter 2.E.III)(1), it measures the exit flux of ions from the quadrupole as a function of the amount of gas target in the source).

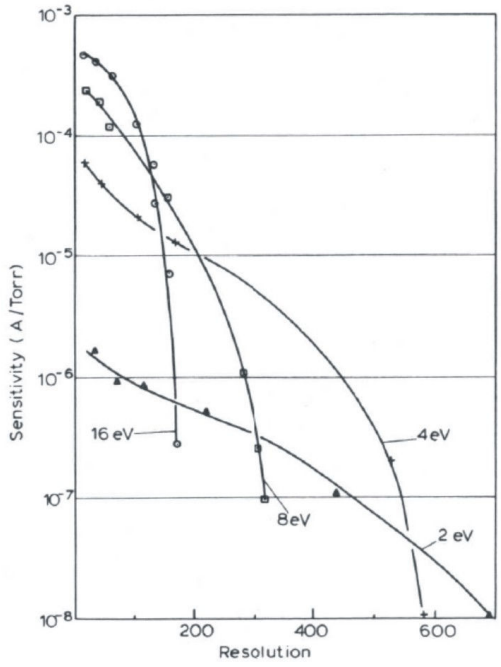

Figure 2-64 : Taken from [54]. Relationship between sensitivity and resolution at various ion injection energies obtained for Ar^+ formed by a electron beam of 1mA.

In our example, the width of the mass peak becomes maximal for injection energies close to 10V and decrease afterwards again as can be seen in figure 2-60.

The results of Figure 2-64 tell us that a compromise should be made between the maximal attainable resolution and the ion speed injection. If ions are sent slowly into the quadrupole, the maximal resolution is attainable, but the transmission is low. When only a low resolution is needed, as is the case for the present experiment (R=20 is enough to separate two adjacent mass peaks in the spectra of water), we can send the ions faster and reach the maximal sensitivity.

However in our case, we reach a maximum intensity of the peak for ion energy of about IE=10V and the peak intensity start to decrease from IE=20V as already observed, hence there is a broad maximum of the sensitivity after which it decreases again.

What is the effective speed of the ions through the quadrupole?

In section (Part II : Chapter 2.C.I)) the potential applied to the extraction lens L2 was called “ion energy” and it is the value we refer to when we speak about ion energy (IE) since it corresponds to the accelerating potential experienced by the ions from the exit of the collision chamber to the entrance of the quadrupole. Actually we can expect that this value (IE) underestimates the true energy of the ions at the entrance of quadrupole, due to the presence of fringing fields at the entrance of the quadrupole, which give a kick to the ion speed. It was reported by Story mentioned in [54] that the gain in ion energy between the entrance and the exit of the quadrupole can be attributed to fringing fields. These results are

shown in Figure 2-65: there is roughly a factor of two between the ion energy of injection, which is comparable to the ion energy determined by L2 (IE), and the ion energy after the quadrupole. In the ideal quadrupole no acceleration should take place, only transverse field are applied.

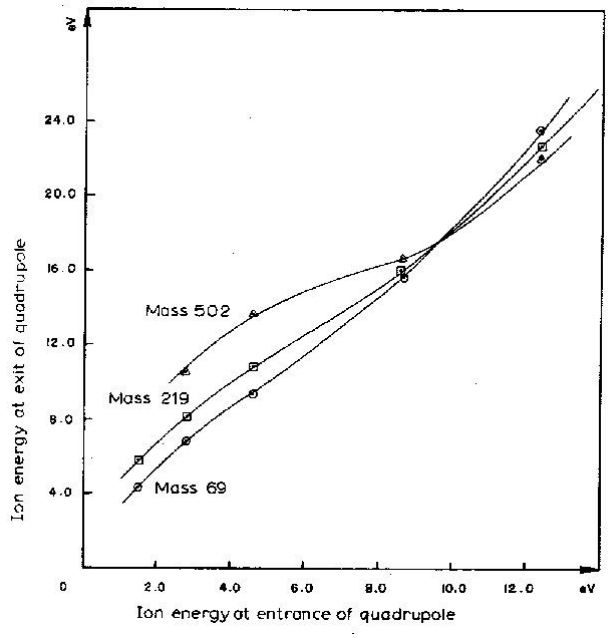

Figure 2-65 : Taken from [54]. Experimental results from Story showing the increase of ion energy due to transmission through the quadrupole.

Fringing fields at the entrance do not only accelerate the ions into the quadrupole; they also can have a defocusing effect and thereby increase the initial displacement of the ions at the entrance of the quadrupole, and their transverse velocities as well. Indeed, as the ions are approaching the entrance of the quadrupole, they experience the fringing field as a weakened quadrupole fields as if the operating point was sent towards lower (a;q) in the stability diagram representing the region of instabilities for these ions.

From a theoretical point of view in (Part II : Chapter 2.D.I)(1)), the quadrupole was supposed infinitely long (at least sufficiently long) and only transmission independent of the transit time of the ions in the quadrupole was assessed. However, ions are not all equally unstable; some ions which should be rejected in a long enough quadrupole can pass through the quadrupole only due to its finite length. Figure 2-66 illustrates this point: it shows the results of some simulation [64] testing the dependence of the transmission on the length of quadrupole only, without taking into account fringing fields.

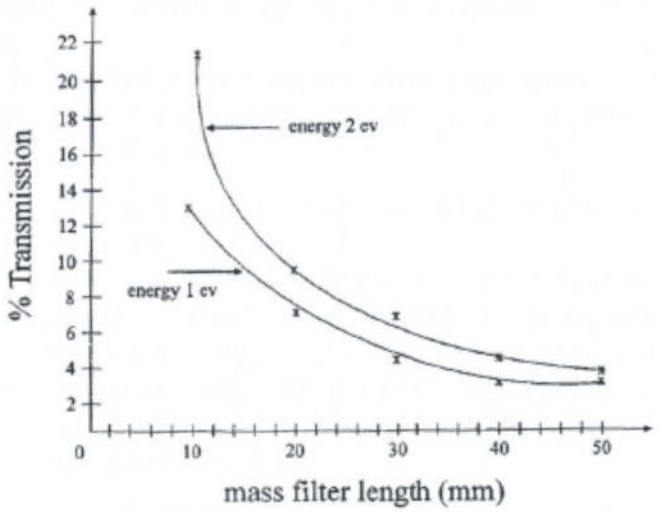

Figure 2-66 : Taken from [64]. Simulated transmission of ions trough the quadrupole as a function of the rods length. Injection point was chosen at 0.3mm in the x-direction and 0.3mm in the y-direction i.e. roughly 10% of aperture of the total entrance aperture of radius r_0=2.75mm.

Number of rf-cycle, is it normal what we observe? The speed of ions v_z , the length of the quadrupole L and the frequency of the rf-field f are related by $N = \frac{fL}{v_z}$, where N is the number of rf-cycles experienced by the ions when they travel through the quadrupole, it can be defined as the "effective length" of the quadrupole. In more practical units we can rewrite $N = \frac{\bar{f} \times \bar{L}}{\bar{v}_z}$ where $\bar{f}$ is in MHz, $\bar{L}$ is in mm and $\bar{v}_z$ is in mm.μs^{-1} given by $\bar{v}_z = \sqrt{\frac{2\bar{K}}{\bar{m}}} \times 9.8226967$, $\bar{K}$ in eV and $\bar{m}$ in amu. The number of rf-cycle experienced by an ion inside the quadrupole appears to be the parameter determining the effects of the limitation of quadrupole's length [60].

Some order of magnitudes for our experiments $\bar{L} = 200$, $\bar{f} = 2.5$ are tabulated in Table 7. Taking into account the influence of fringing fields at the entrance, the ion energy (IE) is underestimating the actual energy of the ions traversing the quadrupole.

$\bar{K}$ (eV)	8	10	20	30	40	60
N	50	45.5	32.2	26.3	22.8	18.6

Table 7 : Number of rf-cycles in our experiment for a given kinetic energy of ions $\bar{K}$.

The effect of fringing field becomes detrimental when ions take more than 3 or 4 rf-cycles to pass through; it is the case for low-energy ions or the heaviest ones [54]. In our case,

it would start to take more than 1 rf-cycles for ions of less than 8eV to pass fringing fields spreading over r_0=0.411cm long (r_0 is a usual order of magnitude for fringing field extension [54]). Too slow ions are highly defocussed by fringing field, but on the other hand, small fringing field can be beneficial as the study of Dawson [54] proves it in Figure 2-67.

We can expect these results to be generic. A gradual entry into the quadrupole field seems to produce a near equivalence for of all phases and thereby an enhancement of sensitivity [54]. If the order of magnitude r_0 is a good estimation of the extension of the fringing fields in our case, their effects on the sensitivity are not so significant and the acceptance ellipses should be close to those obtained without fringing field (first graph of Figure 2-67 and Figure 2-24).

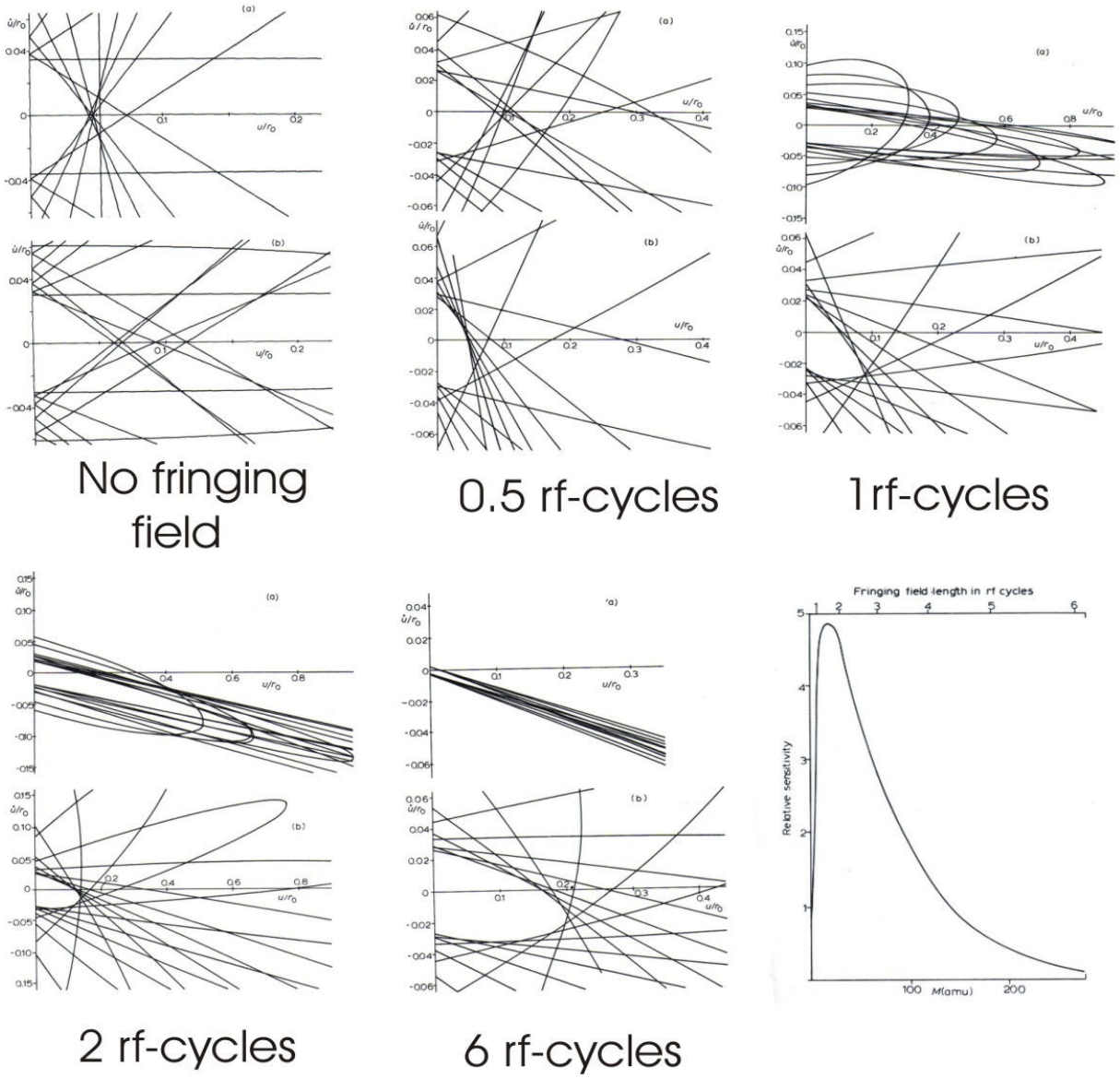

Figure 2-67 : Taken from [54]. Relative sensitivity of the mass filter as a function of the fringing field length (or ionic mass if the axial energy is $Ez=15.5r_0^2$, r_0 is given in cm). The acceptance ellipses are given in the y-direction (upper graph) and in the x-direction (lower graph) for various fringing field length in rf-cycles at (a,q)=(0.2334,0.706).

Very often people are more interested in having a better resolution than a greater transmission. For our study of water we are interested to estimate the lost of transmission through the quadrupole since we don't need high resolution to perform our measurement. So it is better for us to inject the ions rather fast in order to enhance the transmission.

By referring to figure 2-59 and figure 2-60, we can roughly say that the increase of speed from the IE=-3.5V to IE=-10V leads to a gain of sensitivity of 5. When the ion energy continues to increase the sensivity starts to decrease slowly from IE=-12.5V.

These results encourage us to believe that a higher injection speed can be chosen as it can be beneficial to reduce the effect of fringing field and to enhance the transmission if a high resolution is not needed.

At the exit the fringing field have a strong defocusing effect mentioned in [54] and in [65]. Ions tend to be accelerated by the exit fringing fields but slow moving ions emerging with large y values may be trapped within the fringing fields or at certain phases even reflected back into the device [54]. This is an important remark which leads to another proposal for the origin of peaks modulations.

(3) Determination of the modulations mechanism

In this paragraph we need to describe in more details the oscillatory motion of the ions in the quadrupole field: it can be seen as the superposition of motion with a definite frequency of oscillation.

In the x-direction, equation 2-8 can be rewritten:

$$x(t) = k_+ \sum_{n=-\infty}^{+\infty} C_{2n} \sin\left[(n + \frac{\beta_x}{2})\omega t \right] + k_- \sum_{n=-\infty}^{+\infty} C_{2n} \cos\left[(n + \frac{\beta_x}{2})\omega t \right]$$

k_+ and k_- are constants depending on the initial conditions only, C_{2n} are terms of the expansion which depend on the (a, q) position in the stability area. β_x was defined in equation 2-8.

The relation giving the frequencies of the ions oscillation in the x-direction follows:

$$\Omega_{x,n} = (n + \frac{\beta_x}{2})\omega, \qquad n = 0, \pm 1, \pm 2... \qquad \text{2-29}$$

The frequencies of ion motion are independent of the rf-phase when the ions enter the quadrupole. But they depend on the position of the operating point in the stability area

through the parameter β.

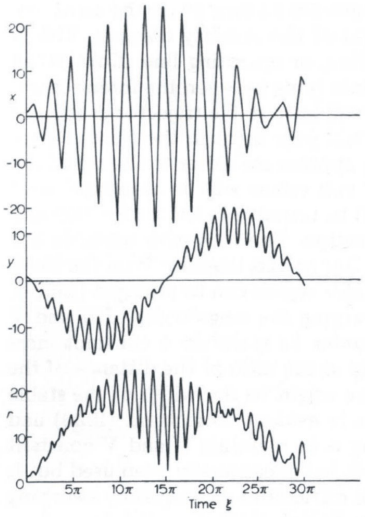

Figure 2-68 : Taken from [54]. Typical ion trajectories for a point near the tip of the stability area.

The mechanism proposed to explain the modulations is based on the fact that collection effects of ions occur in the quadrupole. The ion oscillations have the appearance of beats with the fundamental frequencies Ω_x, Ω_y. Indeed ions have wavelike motion, whose frequencies, given by the formula 2-29, are only depending on the position in the (a, q) plane at which the quadrupole is running. Stationary waves of ion motion are formed in the quadrupole, if the ions tend to reach the exit aperture on the center line of the quadrupole and the ion transmission will be a maximum. On the contrary, if the ions reach the exit near the rods, the fringing fields can defocus the ions and decrease the transmission to the detector, leading to a minimum of the peak modulations. The condition for the ions to exit the quadrupole at the center is given by the relation:

$$(\lambda_x/2)k_x = L, \qquad k_x = 1,2,3...$$

Where L is the quadrupole length and λ_x is the wavelength of the ion motion $\lambda_x = v_z T_{\Omega_x}$, T_{Ω_x} being the period of the ion fundamental oscillation with frequencies Ω_x.

The mechanism proposed explains well the observations made in Figure 2-51, Figure 2-52 and Figure 2-53 concerning the dependence of the modulations on ion energy (i.e. the injection speed of the ion), as well as their dependence on the position of the operating line in the stability area. But why then do the modulations disappear when the ion speed is decreased? In [65] the authors suggested that it can come from the energy spread of the sources which tends to wash out the structure. When the ion beam becomes more monocinetic the structure becomes more pronounced. More effort should be made to collect the ions when

they are highly defocused. The influence of deviation plate's voltage does not affect much the modulations as we observed in Figure 2-51.

V) Across the stability area

The observed discrepancies between measured cross sections motivated a deeper analysis of the ions filtering by the quadrupole. The aim is the characterization of discriminative effects due to filtering and the search for a possibility to avoid them.

The use of the two precedently-defined different types of focusing settings (RET and ACC) offer the possibility to vary systematically the conditions of focusing into the entrance of the quadrupole.

In the precedent subsections, we could characterized the modulations observed on mass peaks and find their origin. They revealed to be no discriminative effects of the filtering. We are now concerned with estimating the discriminative effects occurring by moving the operating point across the stability area. A series of experiments were performed to determine the evolution of the cross section related to changes of the operating point in the stability area.

(1) At constant ion optics:

In Figure 2-69 displays the variation of measured cross section when the operating point is varied across the stability area at constant ion optics. The ion optics was tuned for maximizing the signal at the position MB=16.05amu identified as the position of maximum intensity in the tip of stability area (on the line R=42, ΔM=7.5). The alternance of the magnitude of successive cross section curves is due to the modulations of the mass peaks observed in the precedent subsection. Due to the peaks modulations even small changes of the mass button position leads to important changes in the signal intensity: for instance the magnitude of cross section is decreased by a factor 1.7 between the position MB=16.05amu and MB=16.1amu!

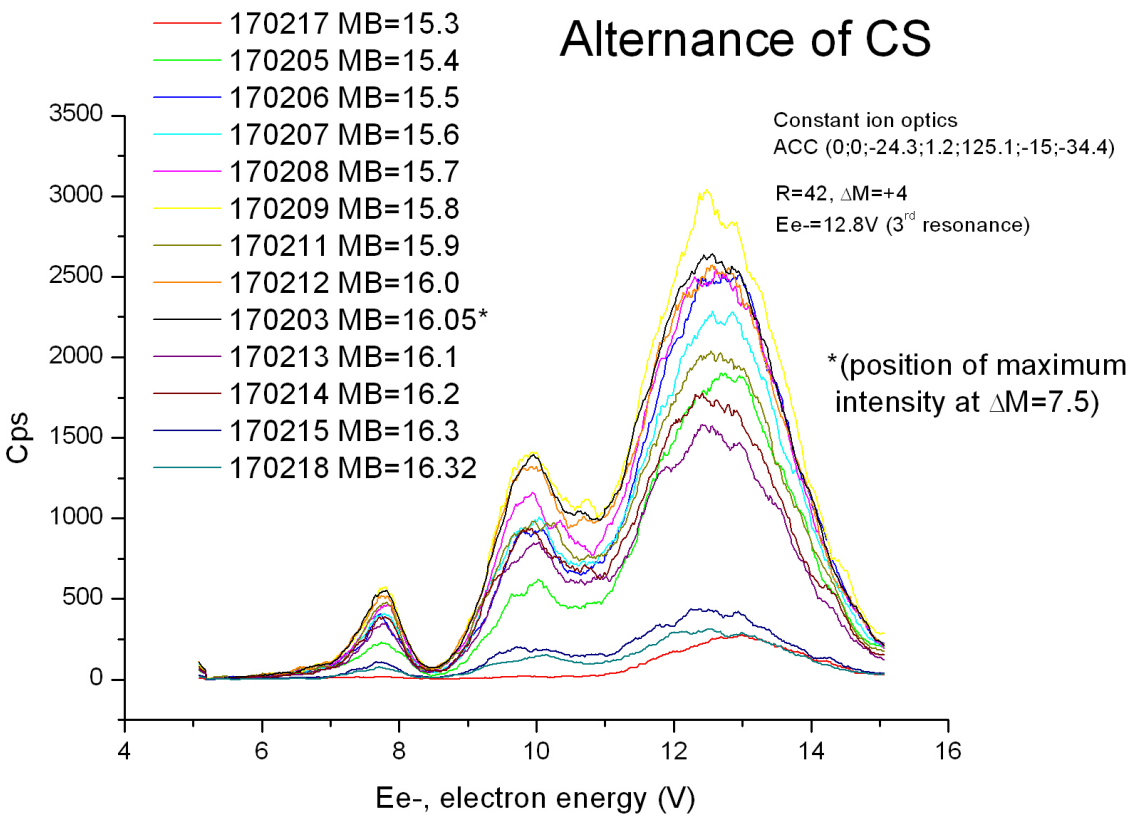

Figure 2-69 : Alternance of cross sections. At constant ion optics, the intensity of cross section varies by a factor of 10 across the stability area. The overall intensity of the curves alternates at the maxima and minima of the modulations described in the precedent section.

Compared to the results of the next paragraph it examplified the obtainable measurements when the ion optics is not readapted to the changes of position in the (a,q) plane. In Figure 2-70, the cross sections of Figure 2-69 were rescaled to match the third peak of the curve 170203 at MB=16.05amu, in order to compare the change of relative peak intensities as a function of the mass button position. We note a good agreement of the relative intensities within 20% of the second peak maximum intensity for mass button positions upper than MB=15.7amu. Discriminative effects are particularly observable for lower MB values. Relative intensities of cross sections agree inside the heart of stability area corresponding to the interval MB=15.9 to MB=16.2.

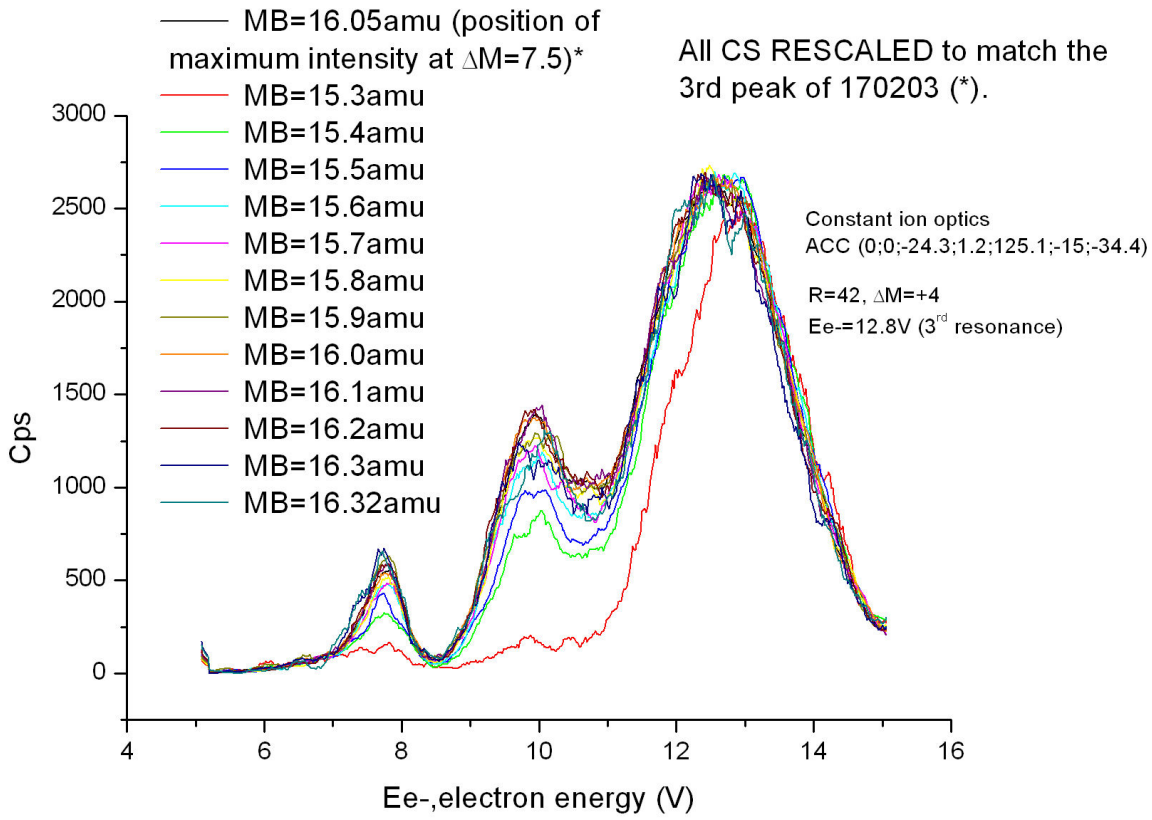

Figure 2-70 : Comparison of the relative cross section. The curves of Figure 2-69 have been rescaled to match the third peak of 170203. The discriminative effects are evident at the lowest values of mass button (MB). From MB=15.6amu, the curves come closer to each other. We are in the heart of the stability area where the discriminative effects are minimized.

(2) Optimized signal

Compared to the precedent paragraph, in this paragraph we look at the effect of systematically retuning the ion optics after every changes of the position in the stability area. The use of both types of focusing settings precedently defined (RET and ACC), which focuses the ions at the entrance of the quadrupole into different kinematic conditions (displacement and transverse speed), gives a systematic way to reveal the occurrence of discriminative effects. Due to the non homogeneity of mean kinetic energy released of O^- ions associated with the different resonant peaks, tuning for maximizing the signal of the third resonant peaks is expected to be different than tuning for maximizing the signal of the second peak and reveals as well the occurrence of discrimination. All along this paragraph, energy scales are uncorrected (peaks maxima at 12.8V correspond to actual value close to 12eV, and peaks maxima at 9.8V correspond to peaks at nearly 9eV).

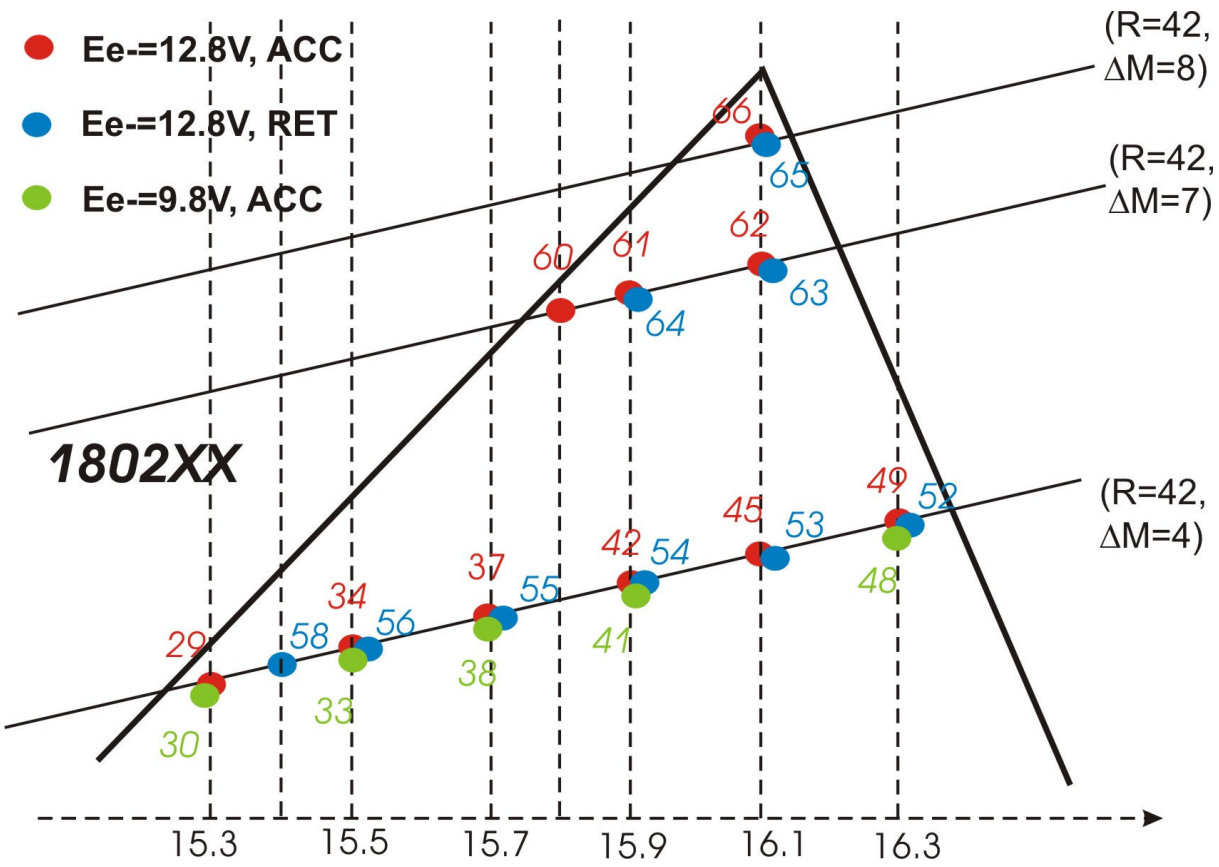

Figure 2-71 : Map of exploration of the stability area.

The Figure 2-71 shows a map of the exploration of the stability area which was performed on the 18/02/2005, the measurements have been numbered in chronological order and these numbers permit their identification all along this paragraph, each measurement is located in the stability area by this number in the Figure 2-71. By increasing ΔM, three operating lines have been explored. In order to reveal the discriminative effects, measurements were made systematically with both type (ACC and RET) of ion optics focusing settings defined in (Part II : Chapter 2.B.II))and the tuning was optimized for obtaining the maximal ion signal at the energies 9.8V or 12.8V corresponding to the second peak and third peak respectively. For these peaks we know from (Part II : Chapter 2.C) that the average kinetic energy released differs much, resulting in different optimal ion optic focusings for maximizing the signal.

Figure 2-72 shows the evolution of the mass peaks of O^- along with the change of ΔM. At ΔM=8, the ion signal of the third resonant peak (12.8V) was maximized for ion optics of ACC type at the mass button position MB=16.1amu. The peak is considerably reduced with the increase of resolution and we can expect to observe the appearance of discriminative effects along this vertical evolution in the stability area.

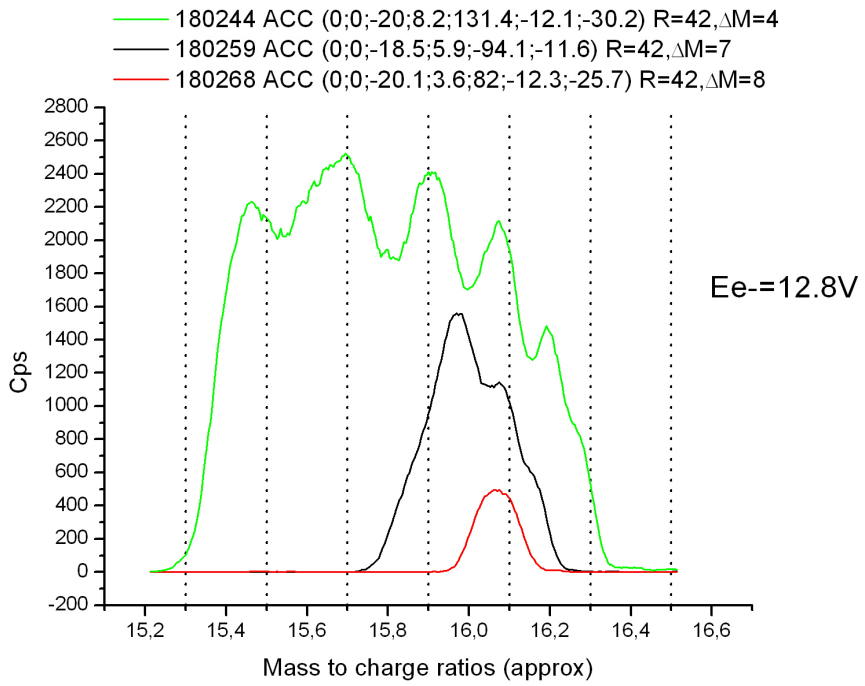

Figure 2-72 : Evolution of O- mass peaks along a vertical displacement in the stability area (change of ΔM).

Figure 2-73 shows all O- mass peaks recorded along the operating line at R=42, ΔM=4. After every changes of mass button position (MB) or of electron energy (Ee-) the ion optics was retuned. Indeed after every slight changes of mass button (MB), corresponding to a manual displacement along the operating line, the conditions of stability are expected to vary, and a reoptimization of the signal can be necessary to readapt the focalization to the changes and try to find always the maximal signal achievable. This readaption is also expected to be different for ions from the second (Ee-=9.8V) or third resonant peak (Ee-=12.8V) resonant. Hence, the ion optics was retuned after every changes of electron energy (Ee-) as well.

From the last subsection (Part II : Chapter 2.E.IV)), we knows that changes of ion energy induce displacements of the peaks modulations. It is observable also in the Figure 2-73. Hence the ion energy must also be included in the constant retuning of ion optics settings.

Ion optics settings associated with the measurements of Figure 2-73 are given in the Figure 2-75 and **Figure 2-76**. The measured cross sections associated with the mass peaks of Figure 2-73 are specified in parenthesis in the legend. Mass peaks were measured with the ACC type of focusing with the exception of 180251 which gives an example of the mass peaks obtained with the RET type of focalization. It reveals important differences existing between both types of focusing. A much higher ion energy (IE~-40V) needed to be chosen for measurements with RET ion optics type in order to maximize the signal (at ΔM=4).

The quadrupole acts as a low-mass filter in one direction and as a high mass

filter in the x-direction as defined in Figure 2-46. The existing gap on the low mass side of the peak 180251 is due to the particular focussing conditions achieved by the RET type which leads to a higher discrimination of ions along the y-direction.

We have here evidence that the different focalization types RET and ACC really achieve different conditions of focalization.

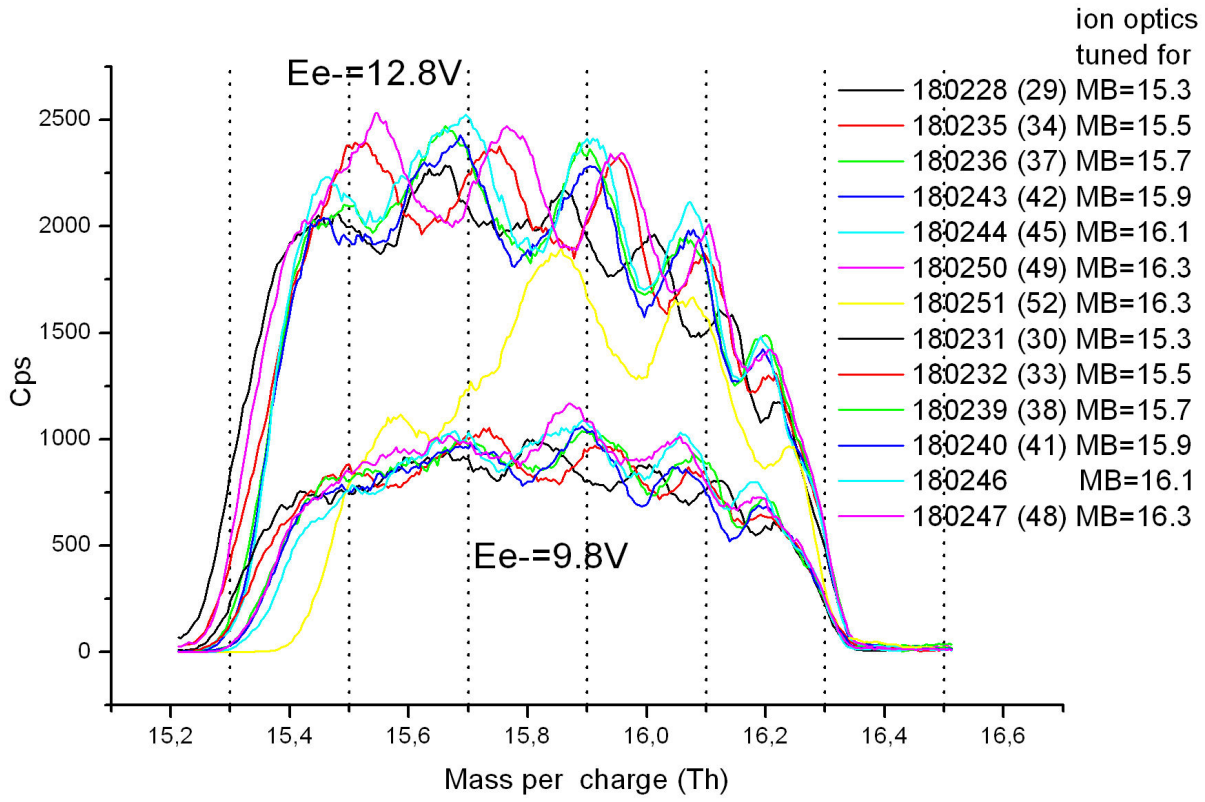

Figure 2-73 : Every time the ion optics was retuned for obtaining the maximum signal at a given MB position , CS were taken at different Ee- to see the discriminative effect appear.

There is now to speak about the limitation of the procedure for finding the optimum signal: it can be spoilt by mistakes since we were limited in time to determine every time the optimization of the ion optics, even if the effort was constantly done to achieve the maximum signal. However, looking at Figure 2-73, we notice that the average intensities of the peaks remain roughly constant when MB was varied proving that the optimization was succeeded somehow.

The associated cross sections are shown in Figure 2-74. Considering that these measurements all result from an optimization process (research for maximal signal) and that the differences in ion yields observed are only due to changes in the position of mass button along an operating line (even small difference lead to big variation), or (and), to a change of the type of focusing (conditions of pressure and electron current were constant during all the experiment), we are compelled to think that it is impossible to perform reliable quantitative

measurements with this apparatus unless special care is taken. Again, unless before each measurement an effort was made to reoptimize the ion signal, these measurements can be considered as a simulation of the dispersion of results obtained by an experimentalist who would not care enough or be aware of the influence of some parameters of the set-up.

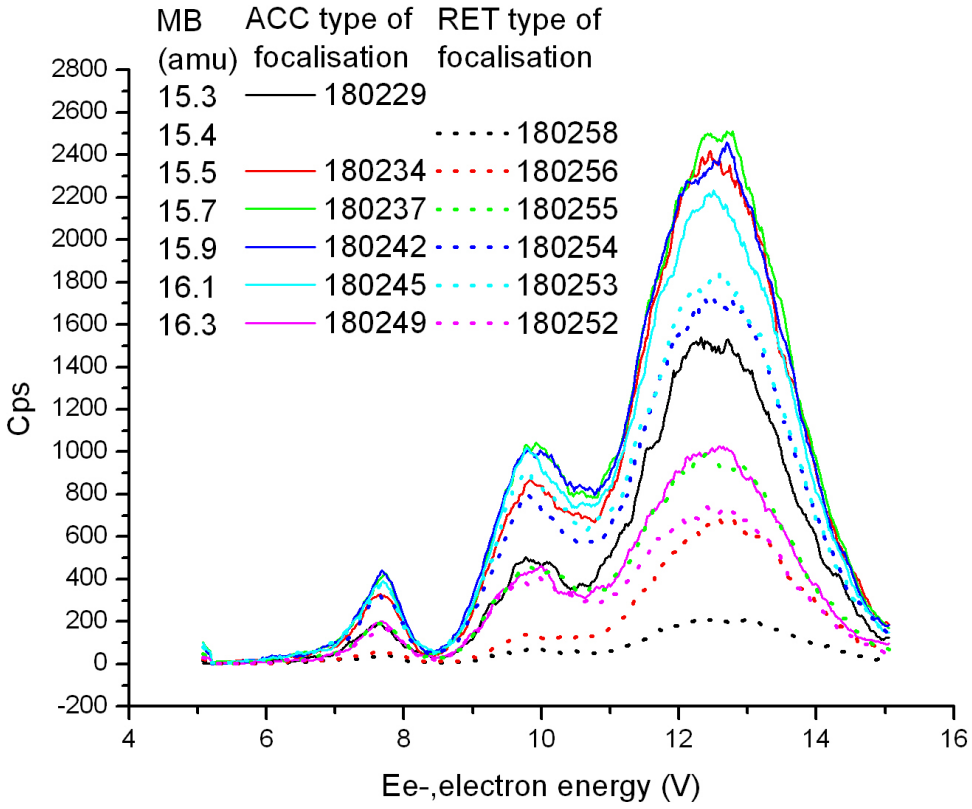

Figure 2-74 Cross section measured along the operating line R=42, ΔM=4 (roughest resolution).

We see clearly on this example (Figure 2-74) that the difference of yield intensity obtained with ACC and RET type diminish when we are closer to the end of the mass peak. This is another indication that discrimination of ions occur along a particular direction with the RET type of focusing. The O^- ions are very much discriminated for the lowest values of MB, as we could expect from the shape of the mass peak obtained with the RET type tuned for maximal signal of the third peak of 180252 in Figure 2-73. We observe also here that small changes of position of the mass button (MB) can have important consequences on the intensity: a change from MB=15.7 to MB=15.9amu leads to doubling of the intensity from 180255 to 180254. We already saw in the last subsection (Part II : Chapter 2.E.IV)) that even the slightest changes may have big influences on the overall intensity due to the modulations on mass peaks. The modulations of peaks were huge for the RET type because of the high Ion Energy of injection (IE>40V) and it explains the difference of intensity between 180255 and 180254; reminding that these modulations are no discriminative effects, they affect the overall intensity only. Indeed, the relative intensities are not much changed between 180255 and

180254 as we can see in Figure 2-75. It is observable that the variation of relative intensities of peaks, which results from some discriminative effects, is constant in the heart of the stability area where the dependence of the initial conditions of entrance of ions is reduced. The Figure 2-75 is studying the effect of the change of ion optic type on the cross sections (RET or ACC).

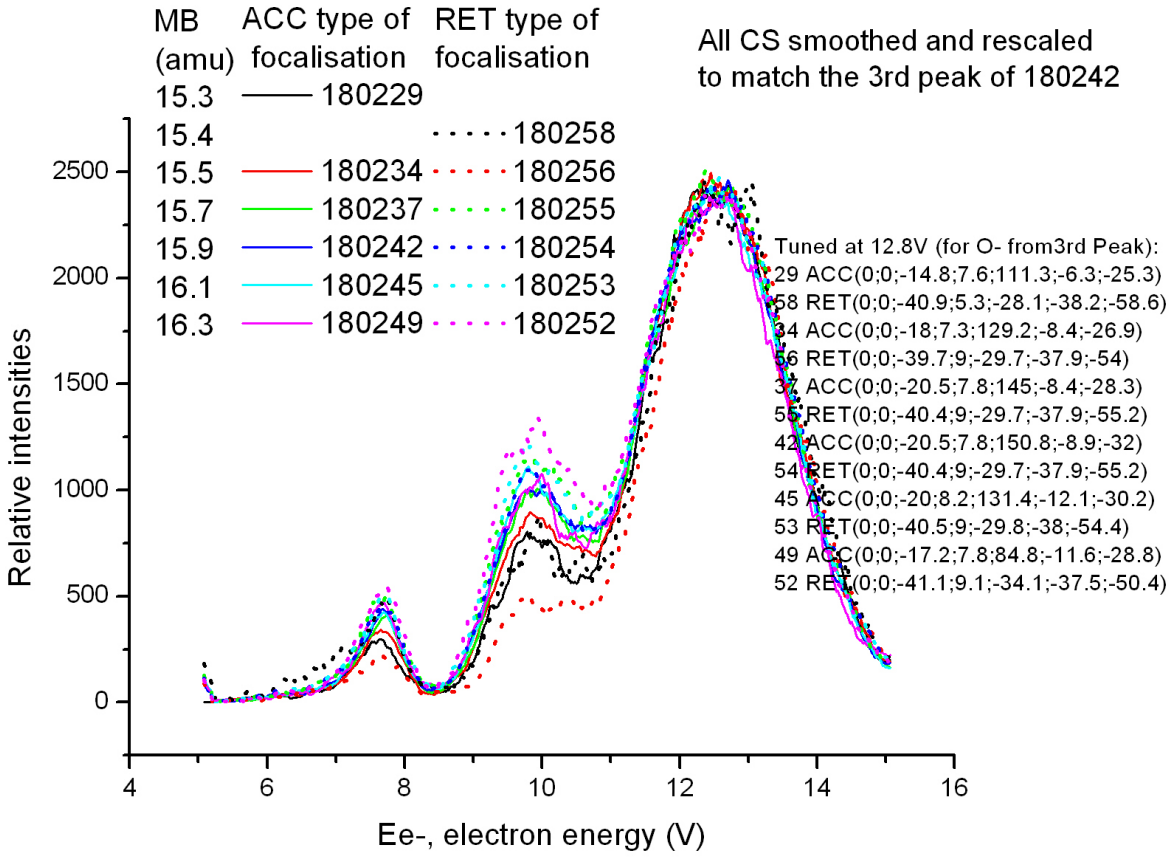

Figure 2-75 : Sensitivity to the change of ion optics type as defined in section. For every time optimized. The ion optics settings associated with each measurement are given in the legend.

There is a large dispersion of the first and second peak. The aim of this study was to observe the appearance of discriminative effects in dependence on the position in the stability area: it was expected that the dependence on ion optics settings would decrease inside of the heart of the stability area, discriminative effects being important only at the border of the stability area. In the Figure 2-75, it reveals to be true. The cross sections obtained with different ion optics settings RET or ACC from MB=15.7amu to MB=16.1amu all agree within a small band of less than 20% of the 2nd peak height of 180242. And the measurements performed at the border of the stability area are more sensitive to changes of the ion optics. However, it is not completely evident for the extreme at MB=15.4amu for the RET type in which case the changes of ion optics (compared to MB=15.3amu for the ACC type) seems not to be felt whereas an important discrepancy between 180234 and 180256 appears for MB=15.5amu, which lies more inside of the stability area. And especially the second peak of

180256 is under the second peak of 180258, whereas we would expect the opposite since the discriminative effects are expected to be even much stronger at the extreme border before the signal vanish. It is probably so because the optimization of ion optics settings for having the maximal signal at 12.8V was not well achieved for 180256. Sometimes it is difficult to know if we have achieved this maximal value, and mistakes can be made.

However, the results obtained in the heart of the stability area from MB=15.7 to MB=16.1amu for this operating line (R=42, ΔM=4) are in satisfying agreement and we noticed a lower influence of the ion optics in this region. It can be seen also that the results obtained with different ion optics settings become again divergent for the extreme position MB=16.3amu, but we observed generally that strong discriminative effects occur only in a very narrowed region at the highest positions of mass button (MB), and generally we have to be more careful about discriminative effects occurring for the lowest positions of MB. We have seen that the filtering of the lower side of the mass peaks is associated with the y-direction and that the filtering of the upper side of the mass peak is associated with the x-direction (directions defined by the rods in Figure 2-45). We can conclude that the effects observed are depending on the particular spatial configuration of our installation and the fact that the ionization is produced along the direction defined by the axis of the monochromator.

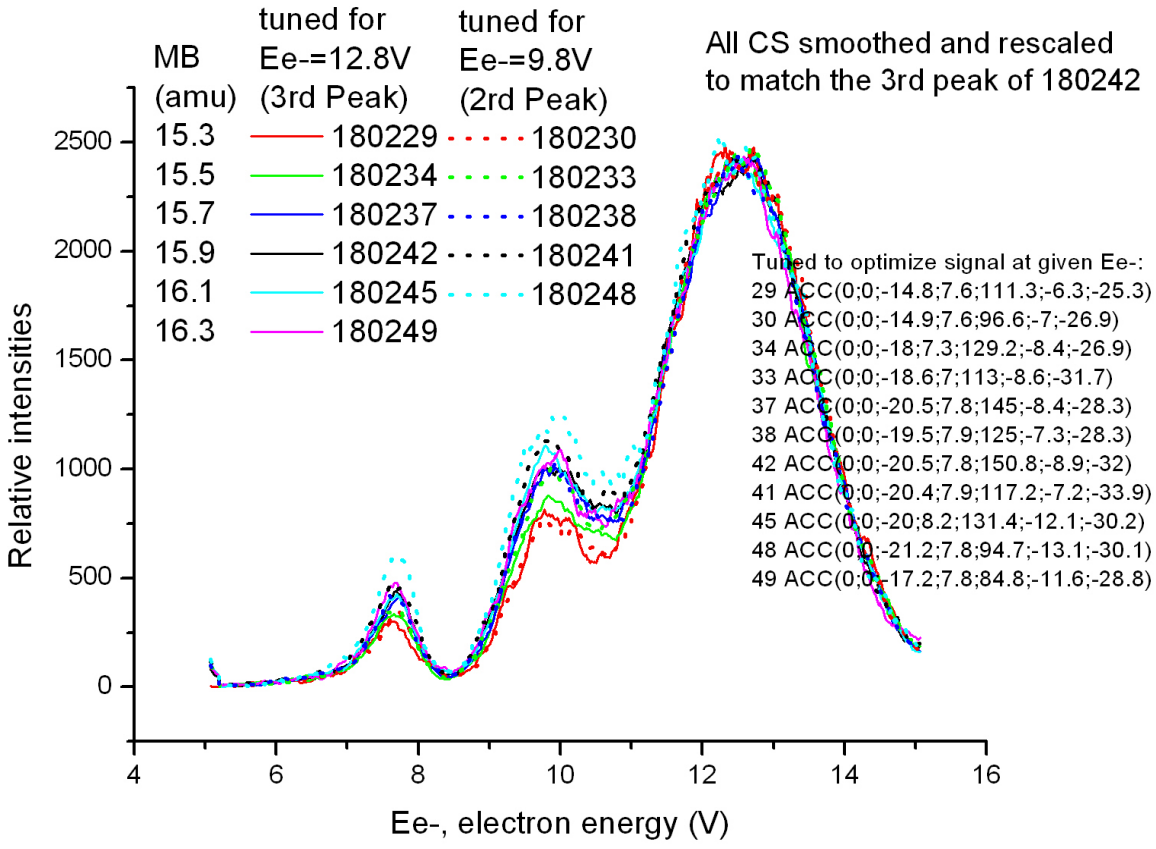

Figure 2-76 : Ion optics tuned for optimizing the ion signal of O- arising from different

resonances.

Again, the effect of optimizing the ion signal at different electron energies corresponding to different resonances of electron attachment to water were also performed in order to reveal discriminative effects. Since we know that the average kinetic energy distribution differs much between the second and third resonances, and that, there should be a tendency, as a consequence, that the optimal tuning of ion optics for finding maximal signal at one energy corresponding to one resonance do not necessary coincide with the optimal tuning determined for electron energies corresponding to the other resonance.

The results of **Figure 2-76** show again that the cross section measured in the heart of the stability area are in rather good agreement with each other after modification of ion optics for optimization at Ee-=12.8V or at Ee-=9.8V. The results also show a decrease of the second peak for MB=15.5amu at Ee-=12.8V which can be catch up by retuning the ion optics at Ee-=9.8V. But it is not so manifest and in **Figure 2-76** , this effect is not observable for the results at MB=15.3amu between 180229 and 180230.

These effects are however really existant in some conditions …

Figure 2-77 and Figure 2-78 show examples of "peak catch up" which can be realized after retuning the ion optics to find settings better suited for the transmission of ions of one resonant peak than for the other.

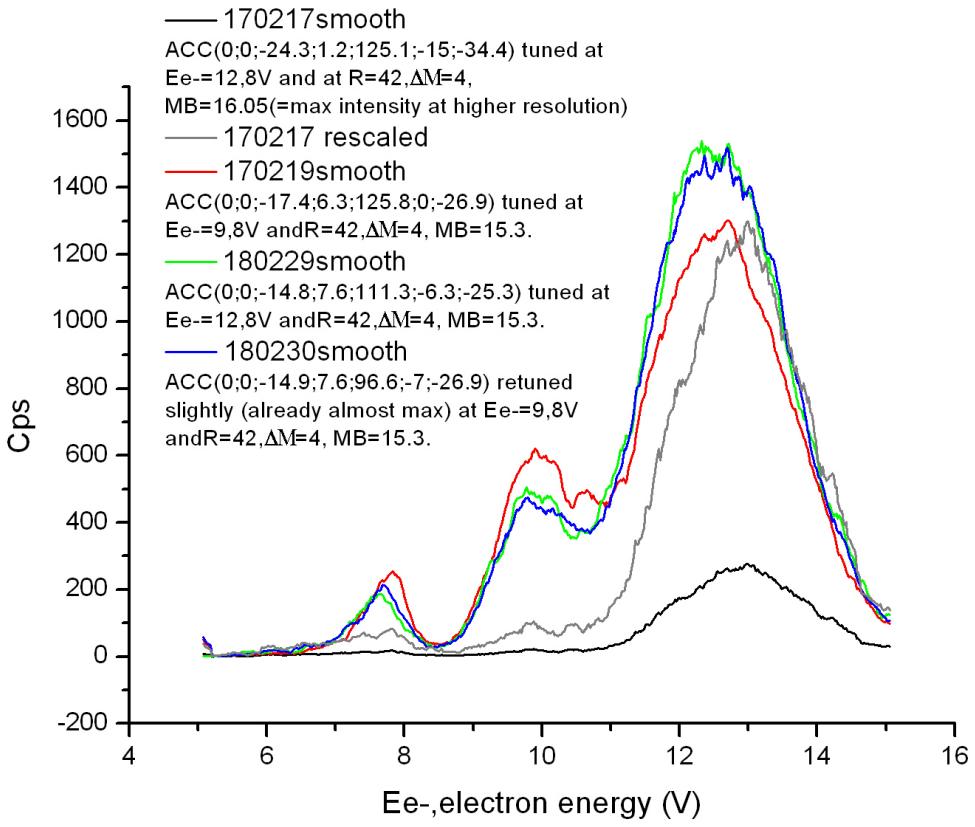

Figure 2-77 : Minor Effects of "peak catch up" with ACC type of focalization. We saw in Figure 2-76 that the alternative tuning at Ee-=12.8V or Ee-=9.8V did not influence much the relative cross section in the case of 180229 and 180230. Another example of "peak catch up" obtained with the ACC type of focalization is shown with the comparison of 170217 and 170219.

170217 was measured at MB=15.3amu with ion optics settings which were adapted for achieving a maximal transmission at MB=16.05amu for Ee-=12.8V, the cross section obtained at MB=15.3amu shows the second peak strongly discriminated. A readaption of the ion optics by retuning at Ee-=9.8V realized a true "peak catch up" of the second resonant peak of 170219, the discrimination then taking place for ions of the third resonance. The curves 180229 and 180230 are redrawn in Figure 2-77. In comparison with 180229 and 180230, 170217 was firstly tuned at MB=16.05amu which explained that the ion optics was not adapted to MB=15.3amu, therefore the difference is greater. There might also have been an error of tuning for 180230 since the ion optics was almost unchanged with respect to 180229 and 170219 shows that the second peak could have been more enhanced with regards to the third one. Especially because of the mass peaks modulation of intensity (depending on IE), it is difficult to be sure that a maximum was found during the tuning procedure.

However the effect of catching up the second peak was again very important when using the RET type of focusing at MB=15.5amu as shown in Figure 2-78. The effect is apparent between 180257 and 180256 rescaled.

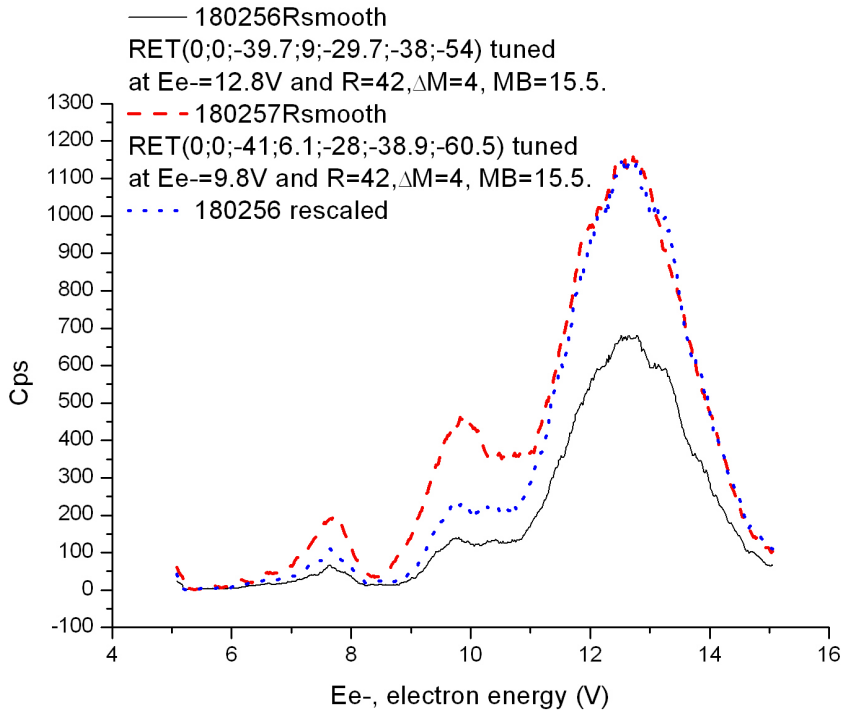

Figure 2-78: Peak catch up with RET type of focusing.

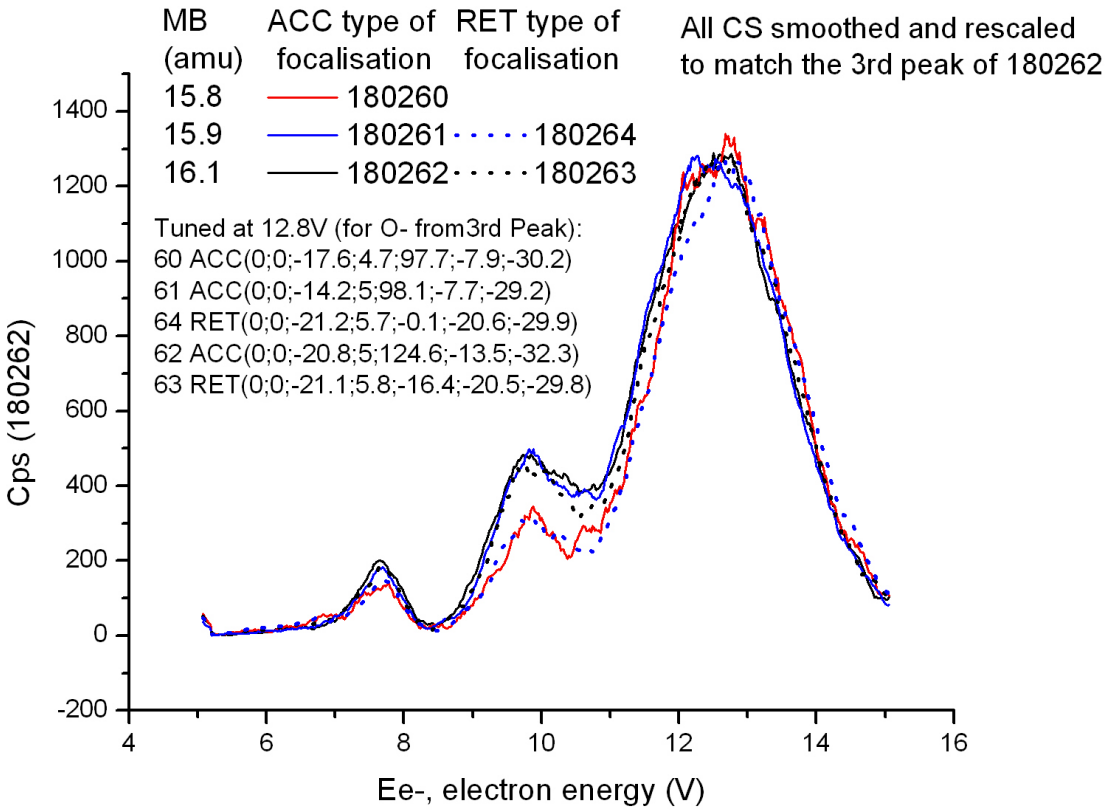

Figure 2-79 : Evolution of CS along the operating line at ΔM=7.

The Figure 2-79 shows the evolution of the cross section measured along the operating line

(R=42, ΔM=7) with both types of ion optics focusing settings ACC and RET. As represented in Figure 2-71, the intersection defined with the stability area is in this case much shorter, giving rise to a better resolved mass peak (Figure 2-72), but less transmission (diminished roughly by a factor of 2). The heart of the stability area is represented by the position MB=16.1amu, the results obtained with the focusing type ACC and RET agree well for this position. It must be emphasized that the same systematic optimization was performed before every measurement on this operating line (ΔM=7) and of the next one also, as it was performed for the measurements at ΔM=4. As already observed, the RET type of focusing is giving rise to stronger discrimination effects than the ACC type: in Figure 2-79, the second peak is already strongly discriminated at the position MB=15.9amu and is vanishing for the position MB=15.8amu. The cross section curve obtained with the ACC type is comparably discriminated at MB=15.8amu only. It was also observable for the operating line at ΔM=4.

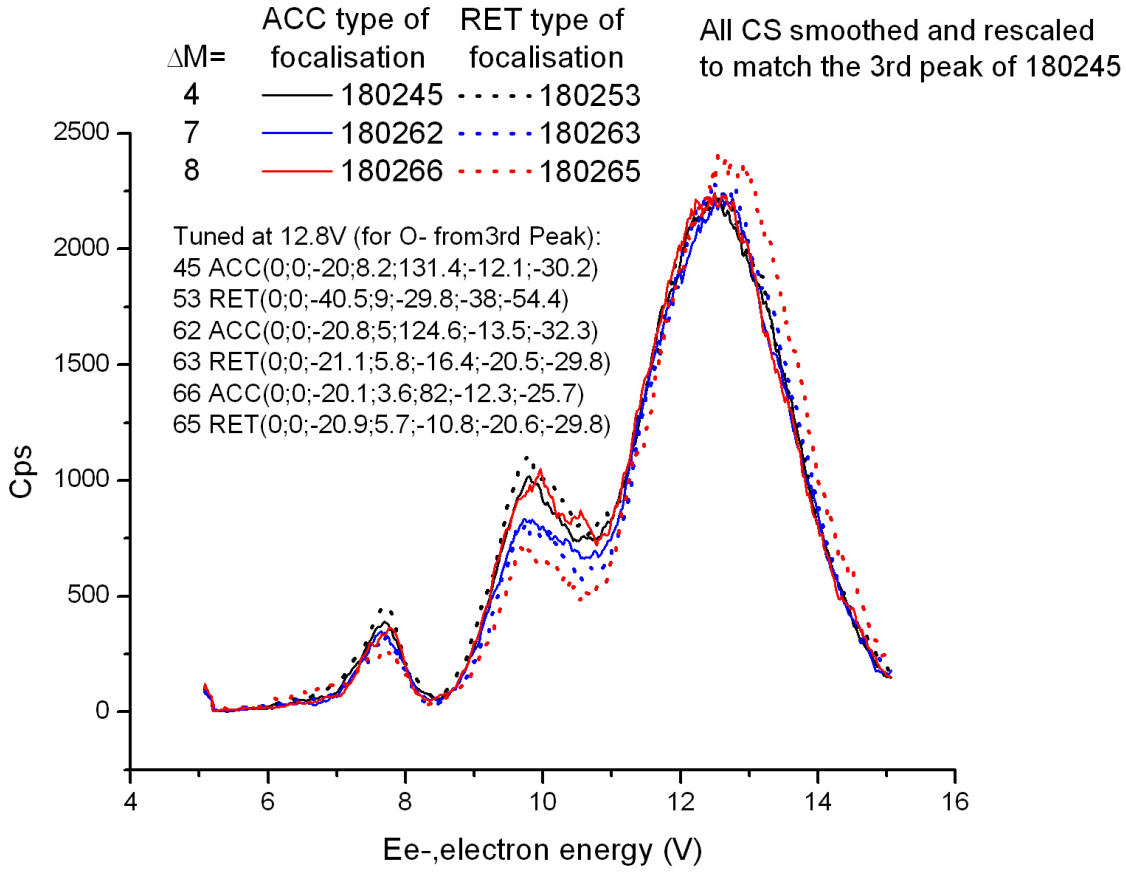

Figure 2-80 : Vertical evolution of the cross section in the stability area. At strong resolution close to the apex of the stability area we observe strong discriminative effects (red curve) outlined by the difference between the cross section determined with RET and ACC type of focalization and a shift in the case of apparent shift of the position of the 3rd peak which reveals that the beginning of the peak (constituted by faster ions) is more discriminated than the end of the peak. Difference between RET and ACC, ACC is less discriminated (66 like 45), their difference increases when resolution increases?

The last results of this study are presented in the Figure 2-80 showing the vertical evolution of the measured cross section taken at fixed position MB=16.1amu for increasing value

of ΔM until ΔM=8 after which the ion signal vanished. We observe an increase of the sensitivity to the change of ion optics (RET or ACC) with the increase of the resolution (increase of ΔM): by looking at Figure 2-71, we can consider to have entered the triangular region of peak shape already at ΔM=8, for which the transmission is much reduced and the sensitivity to the change of ion optics is clearly observable in Figure 2-80 revealing the presence of discriminative effects. It defines the heart of the stability area in the vertical direction, when the resolution becomes too high the cross sections might be discriminated.

F. Conclusions of this study

This study brings us to consider many important questions concerning the quadrupole spectrometry. Can we have 100% transmission of the ions through the quadrupole? What is the importance of discriminative effects to expect in the quadrupole? In what conditions?

The field of research on quadrupole mass spectrometry is still active as it is proven by the existence of recent studies whose purpose is precisely to answer the influence of various factors on the transmission and discrimination of ions in quadrupoles.

As discussed in Part II : Chapter 2.E.I), we might be close to full transmission on the top of the mass peaks modulation when the resolution is low enough as indicated by the nearly trapezoidal form found for the mass peak in Part II : Chapter 2.D.II)(3). But a study of the transmission should be performed with various systems of known absolute cross sections and the performance of the apparatus should be further determined. In particular, the importance of the direction of injection of the ions into the quadrupole revealed to be of great importance and should be taken into account for such studies. The determination of absolute cross sections for the dissociation channels of the DEA to water presented in the next chapter have been performed before these investigations on the transmission and discrimination in the quadrupole. The important discrepancies between our results and the previous investigations of Compton and Christophorou, and Melton can be explained by the neglect of the fine tuning of the apparatus when the measurements were done (see Part II : Chapter 2.E.V)(2)).

Do we have the possibility to obtain true relative cross sections? The results of the last section indicate that it might be possible if:

- The extraction from the collision is switched off (conclusion of Part II : Chapter 2.C).
- The ion optic focusing lenses are tuned for maximal signal (ACC type preferably) and the quadrupole settings are located inside the heart of the stability area.

The ion injection speed should not be too low since the ions are remaining a long time in the quadrupole and are subjected to stronger discriminative effects (see Part II : Chapter 2.E.IV)(1)). However the injection speed should not be too high, since the modulation of the mass peak intensity becomes important and render the tuning more difficult. The sensitivity of the quadrupole as defined in Part II : Chapter 2.E.I) decreases also slowly from a certain ion speed injection (Part II : Chapter 2.E.IV)(2)). The modulation of the mass peaks, identified as being due to periodic ion-collection at the exit of the quadrupole in Part II : Chapter 2.E.IV)(3), are no discriminative effects (see Part II : Chapter 2.E.II)(1)). Therefore, they only affect the overall intensity of the cross sections and have only to be taken into account for the eventual determination of absolute cross sections.

Chapter 3. Dissociative Electron Attachment to Water and Heavy Water

A. Basic experimental observations

When water vapour is bombarded by electrons in the energy range 5 to 15 eV, three anion products are detected with common characteristics features of the cross sections: in decreasing order of magnitude come the yields of H^-, O^- and OH^-. The formation of H^- and O^- are attributed to the direct dissociation of monomer of water:

$$e^- + H_2O \rightarrow H^- + OH \qquad 3\text{-}1$$

$$e^- + H_2O \rightarrow O^- + H_2 \qquad 3\text{-}2$$

The mechanism of formation of OH^- is still the subject of discussion and its origin will be further discussed in Part II : Chapter 3.D.III).

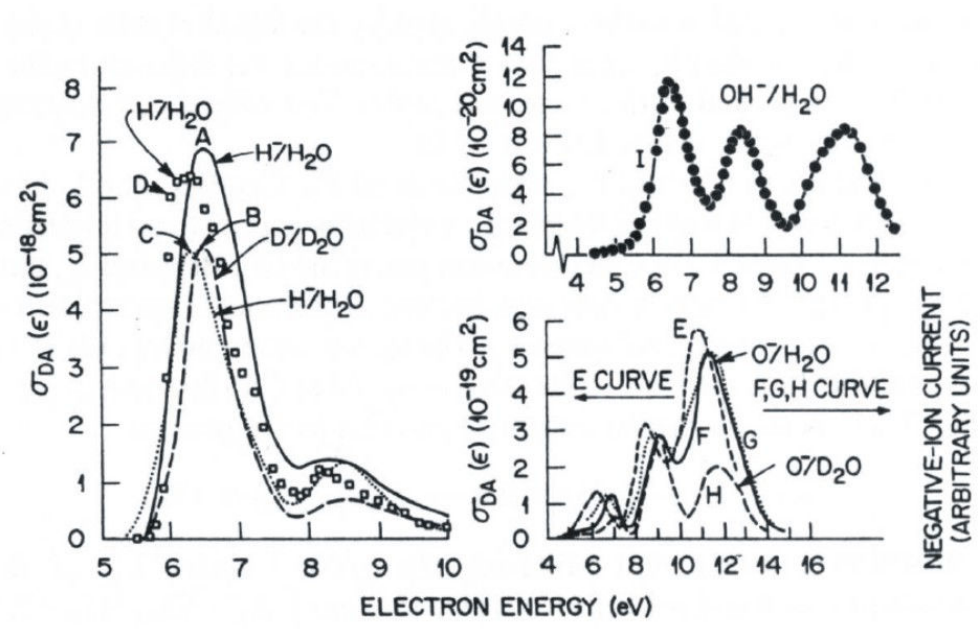

Figure 3-1 : Comparison of previous studies reproduced from the book of Christophorou et al [70]. Absolute cross section for the different dissociation channels are shown. Results A, B, F, H are from Compton et al [83] ; results C from Buchel'nikova [66] ; G from Dorman [67] ; D, E, I from Melton [68].

Every cross sections is characterized by three resonant peaks located at incident electron energy near 7eV, 9eV and 12eV as it is shown in Figure 3-1. The third peak of H^- is missing in Figure 3-1 but it was clearly observed in the experiment of Belic et al [69].

In Figure 3-1, reproduced from [70], are shown the estimated absolute cross sections from previous experiments among which the results of Melton [68] are believed to give the best estimations for the different channels. Figure 3-2 gives the estimated absolute cross section from our first results. For these results, the sensitivity to the fine tuning of the quadrupole and ion optics revealed in chapter 2 was not taken into account.

Our estimated cross section for the dissociation channel into H^- is much higher than previous estimations (our first peak height of H^- close to 3×10-17 cm^2 is higher than the result of Melton by a factor 5). These previous estimations are in better agreement with recent theoretical investigations of Haxton et al [78], who predicted a peak height of 5.99×10^{-18} cm^2.

Approximate ratios of magnitudes can be determined from the highest peak intensity of every yield as tabulated in Table 8.

	$\frac{\sigma(H^-)}{\sigma(O^-)}$	$\frac{\sigma(O^-)}{\sigma(OH^-)}$	$\frac{\sigma(H^-)}{\sigma(OH^-)}$
Melton [68]	$\simeq \frac{6.5\times10^{-18}}{5.5\times10^{-19}} \simeq 12$	$\simeq \frac{5.5\times10^{-19}}{12\times10^{-20}} \simeq 4.6$	$\simeq \frac{6.5\times10^{-18}}{12\times10^{-20}} \simeq 55$
Our results	$\simeq \frac{3\times10^{-17}}{3\times10^{-18}} \simeq 10$	$\simeq \frac{3\times10^{-18}}{1.5\times10^{-19}} \simeq 20$	$\simeq \frac{3\times10^{-17}}{1.5\times10^{-19}} \simeq 200$

Table 8: Comparison of relative magnitude of absolute cross sections.

The relative magnitude of the processes 3-1 and 3-2 which we determined are comparable with the results of Melton. However the comparison of the ratios $\sigma(O^-)/\sigma(OH^-)$ and $\sigma(H^-)/\sigma(OH^-)$ indicates that the relative abundance of OH^- compared to H^- and O^- was much lower in our experiments than the one reported by the other authors. This fact can be another indication that OH^- is not a direct product of dissociative electron attachment to the water molecule and that its formation is dependent on the particular conditions in the apparatus used for the measurement (see Part II : Chapter 3.D.III)).

Despite the many efforts to improve the method of determination of the absolute cross sections, important discrepancies in the results were persistent which make doubtful the reliability of the results of Figure 3-1. Apart from the possible failure to achieve reproducible conditions of experiments (see Part II : Chapter 3.C), these discrepancies could be

attributed to the lack of careful tuning of the quadrupole and ion optics settings only, as it was shown in the chapter 2. For this reason, the approximate agreement between our relative magnitude and the one determined by Melton for the ratio $\sigma(H^-)/\sigma(O^-)$ can be fortuit only. And no certain conclusion can be drawn from these results.

In Figure 3-2 is also shown in the right graph the corresponding magnitudes of dissociative attachment to heavy water. As observed by other authors [83], we note that the magnitudes of the different dissociative attachement processes to D_2O are of the same order than the corresponding processes of dissociative attachment to H_2O.

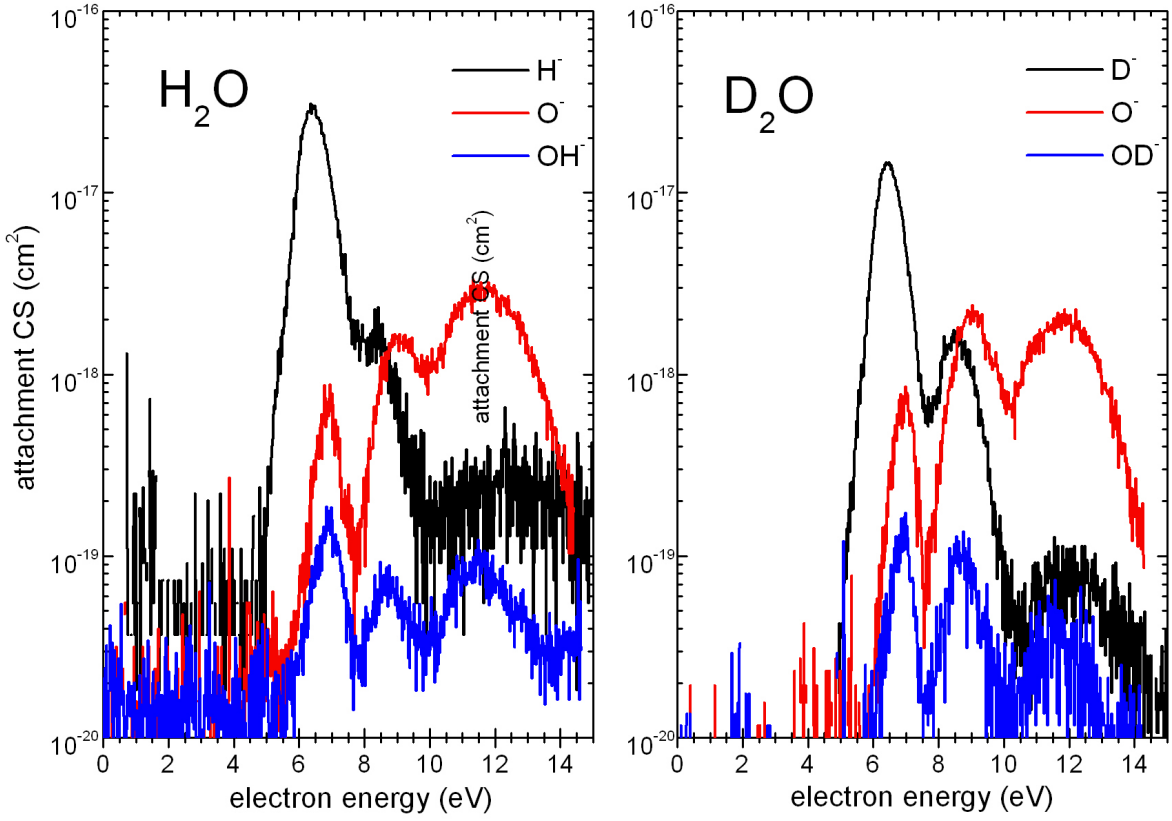

Figure 3-2 : Estimated cross section of the different channels from our first results.

From these observations, we conclude that a determination of absolute cross sections would require further investigations which were not performed for this study. However, the study of the sensitivity of the quadrupole let envisage the possibility to determine undiscriminated relative cross sections. A complete analysis of the discriminative effect on the cross section was only performed for the yield of O^- from H_2O. But, on the other hand, the shapes of the cross sections for the formation of H^- or OH^- showed less dependence on the quadrupole filtering.

After an introduction on our theoretical understanding of the dissociative electron attachment, the method of determination of the absolute cross sections is briefly presented in

Part II : Chapter 3.C as well as a description of the gas inlet system. Then, our relative cross sections will be compared with the results of precedent works and the question of formation of OH^- will be addressed.

B. Theory of DEA

I) General theory

Different resonant processes can lead to the formation of a temporary negative ion by interaction of an e^- with an atom or molecule [70]. This can happen by shape resonance i.e. the atom or molecule (in ground or excited state) is polarized by the approach of the e- which is trapped by the conjugate action of the repulsive centrifugal force and the attractive force arising from the polarization. Or, this can happen via so called Feshbach resonances which are of two types: the nuclear excited Feshbach resonance which involves the coupling of the kinetic energy of the captured electron to molecular vibration (slow incoming electron), it is the mechanism type describing the attachment to CCl_4; and the electron-excited Feshbach resonances which occurs when an incoming electron excites electronically the target molecule (fast incoming electron) and is concomitantly captured in the field of the excited electronic state of the target, it is the mechanism describing the attachment to water molecules. For both Feshbach resonances the electron affinities (EA) of the molecules are positive and the negative ion state lies energetically below the parent state (CCl_4 in the first case and H_2O^* in the second case) leading to longer life time of the transient anions than in the case of shape resonances.

A schematic electronic transition is represented in the Figure 3-3 in a Born-Oppenheimer potential energy diagram. Such a diagram represents the potential energy of a diatomic molecule as a function of the internuclear distance, for a polyatomic molecules it can be seen as a two dimensional cuts through hyper dimensional surfaces along a reaction coordinate Q. In this work we are concerned with the electron attachment to H_2O molecules and to CCl_4 molecules. The two mechanisms of electron attachment we are concerned with in this work are represented in Figure 3-3: a molecular potential curve is associated with the electronic states of the neutral molecule AX (for a polyatomic molecule Q=A-X) either the molecular state of the H_2O molecule or the molecular state of the CCl_4 molecule. The molecular potential lying above the neutral state corresponds to a purely repulsive electronic state AX^-

can corresponds in our case to one of the H_2O^{*-} state or to the formation of a CCl_4^{*-}.

The Franck-Condon principle states that an electronic transition occurs within a stationary nuclear framework because the electronic motion is much faster than the nuclear motion. The nuclear locations remain unchanged during a transition but then readjust once the electrons have adopted their final distribution. The Franck Condon principle tells that the transition from the electronic state of the neutral water molecule to the negative occurs via a vertical transition. Moreover, the transition occurs from the vibrational state of the lower electronic state to the vibrational state that it most resembles in the upper electronic state. For the transition to a continuum repulsive electronic state from the vibrational ground state of the molecule as in Figure 3-3, the continuum state wave function can be approximated by a delta function at the point of vertical transition if the repulsive potential is steep enough or equivalently if the dissociation width Γ_d is large enough (see [72,71]). This approximation is known as the "reflection principle"; the shape of the X^- ion yield is thus a Gaussian profile of the ground vibrational wave function of AX reflected at the repulsive potential in Figure 3-3.

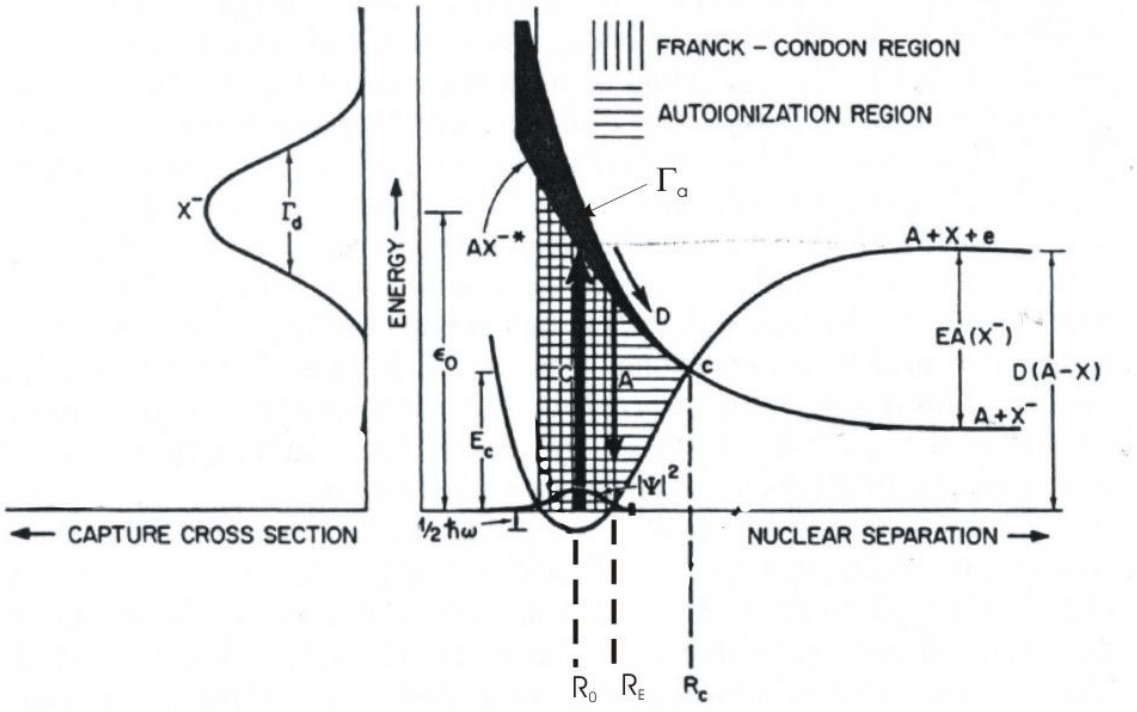

Figure 3-3 : Diagram taken from [70]. Schematic representation of the mechanism of electron dissociative attachement to a diatomic molecule AX.

The physical process of dissociative electron attachment can be decomposed in two steps: the capture of the free electron by the molecule is followed by the dissociation of the anion

formed. So that the cross section of the dissociative electon attachment can be written:

$$\sigma_{DEA} = \sigma_C \sigma_D \qquad 3\text{-}3$$

The cross section of capture σ_C from the ground state is given by the formula determined by O'Malley et al [72] for diatomic molecules or "diatomiclike" molecule (comparable to diatomic molecule, like OH-H for our case):

$$\sigma_C = \frac{4\pi^{\frac{3}{2}}\hbar^2}{2m_e E}\,\bar{g}\,\frac{\Gamma_{\bar{a}}}{\Gamma_d}\exp\left[\frac{(\frac{1}{2}\Gamma_a)^2 - (\bar{E}_0 - E)^2}{(\frac{1}{2}\Gamma_d)^2}\right] \qquad 3\text{-}4$$

Where E is the incident electron energy; $\bar{g}$ is a statistical factor including the weight factors for rotational and electronic angular momemtum as well as the relative spin multiplicity ; Γ_a is the total autodetachment width, $\Gamma_{\bar{a}}$ is the partial autodetachment width which is equal to the Γ_a when there is only one electronic channel open (the exact definition of the quantities in the formula 3-4 are given in [72]); Γ_d is the dissociative attachement resonance width; $\bar{E}_0 = \varepsilon_0 + \frac{1}{2}\hbar\omega$ where E_0 is the electron energy at the peak of the cross section. The different quantities entering the formula are represented in the Figure 3-3.

σ_D in equation 3-3 is the probability of dissociation once the electron has been captured. Indeed, the negative ion resonant state (NIRS) formed by one the capture of the electron is a non-stationary state of the electron-molecule system which can auto-ionize reverting back to the initial products AX + e^-. A bound electron in a molecule is characterized by a wave function which can be expressed as $\Psi_n \propto \exp\left[-iE_n t/\hbar\right]$ where E_n is the real energy eigenvalue of the Hamiltonian operator associated with the quantum number n. The probability density $|\Psi_n|^2$ is independent of time and the state is stationary. However the NIRS is characterized by a complex energy which can be written $E - \frac{1}{2}i\Gamma_a(R)$. Hence the probability density $|\Psi|^2 \propto \exp\left[-\Gamma_a t/\hbar\right]$ is time dependent and the state can decay with a characteristic autodetachment time $\tau_a = \hbar/\Gamma_a$.

For the dissociation to occur, the nuclei must fly apart sufficiently fast so that the dissociation can compete with the autoionization. The width of the resonant potential energy curve in Figure 3-3 to illustrate the variation of Γ_a with R, it is decreasing with increasing R to express the increase of autodetachment probability with decreasing R. Once reaching the

internuclear separation Rc represented in Figure 3-3 the state AX^- has no longer enough potential energy to revert back to AX + e^-, and the dissociation takes place. So that the probability σ_D is determined by:

$$\sigma_D = \exp\left[-\int_{R_E}^{R_C} \frac{\Gamma_a(R)dR}{\hbar v(R)} \right] \qquad 3\text{-}5$$

Where $v(R)$ is the relative velocity of separation. Finally an approximate expression of σ_D is given by :

$$\sigma_D \simeq \exp\left(-\frac{\tau_d}{\overline{\tau_a}} \right) \qquad 3\text{-}6$$

Where $\overline{\tau_a} = \frac{\hbar}{\overline{\Gamma_a}}$ is the mean autoionization lifetime and $\overline{\Gamma_a}$ is the average autoionization width.

$\tau_D = \int_{R_E}^{R_C} \frac{dR}{v(R)}$ is the time needed for the nuclei to reach the limit separation beyond which the dissociation is inevitable.

Hence the cross section of dissociative electron attachement to a diatomiclike molecule is given by the formula:

$$\sigma_{DEA} = \frac{4\pi^{\frac{3}{2}}\hbar^2}{2m_e E} \overline{g} \frac{\Gamma_{\overline{a}}}{\Gamma_d} \exp\left[\frac{(\frac{1}{2}\Gamma_a)^2 - (\overline{E}_0 - E)^2}{(\frac{1}{2}\Gamma_d)^2} \right] \exp\left[-\int_{R_E}^{R_C} \frac{\Gamma_a(R)dR}{\hbar v(R)} \right] \qquad 3\text{-}7$$

By conservation of energy, the kinetic energy of the fragment X^- is given as a function of the incident electron energy ε, the electron affinity EA(X), the dissociation energy of the neutral molecule D(AX), the internal energy of the neutral fragment E_n and β the ratio of the fragment X- to the molecule mass :

$$E_{X^-} = (1-\beta)(\varepsilon + EA(X) - D(AX) - E_n) \qquad 3\text{-}8$$

The internal vibrational energy level of the fragment OH in the dissociation channel H^-+OH were observed in the experience of Belic [69].

II) The case of CCl_4

The use of CCl_4 for the calibration of the energy scale has been explained in chapter 1. The mechanism of dissociative attachment to CCl_4 is illustrated in the Figure 3-4 reproduced from the thesis of D.Muigg [73].

The Cl^- ion yield observed experimentally (see chapter 1) is given as illustration of the reflection principle on the right of the Figure 3-4. We recognize the first resonant peak at 0eV whose position is used for the calibration of the energy scale and the second peak positionned 0.8eV farther.

Exclusively Cl^- ions have been detected as product-anion of the dissociation process of CCl_4^-. CCl_4^- has a very short lifetime prior to dissociation due to the antibonding character of the potential curves and the existence of a weak attractive well only, as shown in the Figure 3-4.

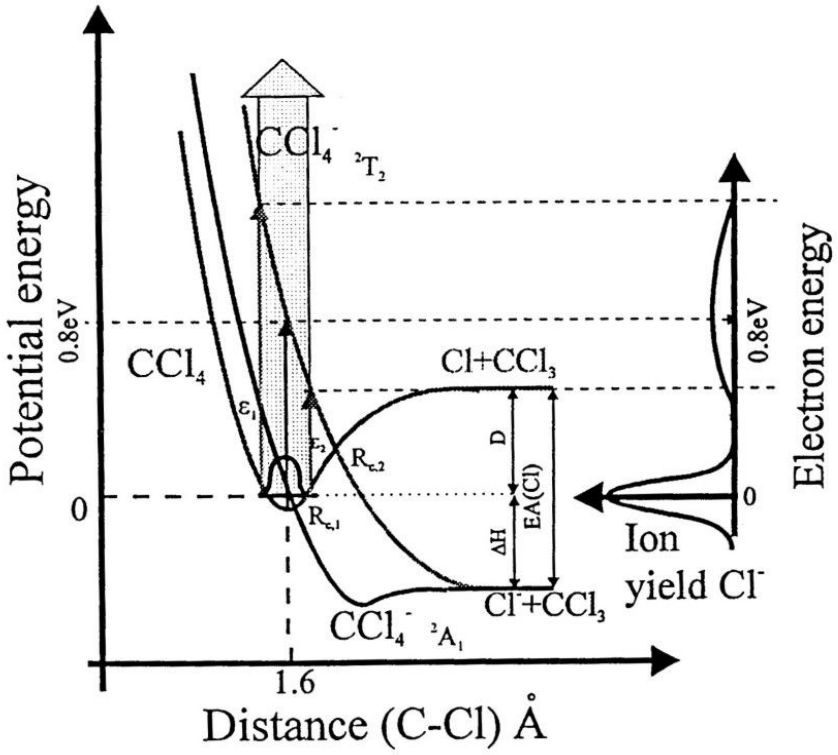

Figure 3-4 : Mechanism for the formation of Cl- from the disscociative attachment to CCl_4. Taken from the thesis of D.Muigg [73].

The height of the second peak used for the calibration of cross section is estimated at 5×10^{-16} cm^2 at T=300°C if the resolution is fine enough to avoid the overlapping of the second peaks at 0.8eV and the intense s-wave resonant peak at 0eV [74]. When the electron energy resolution becomes coarse the interval between the two peaks is shrinking below 0.8eV. For the calibration of cross sections to be valid, it is necessary to achieve a fine enough

resolution and ensure a good stability of the electron energy distribution over the energy range of the study.

III) The case of water:

A great deal of information on water can be found in the website of M.Chaplin [75].

The ground state of H_2O is well described by SCF wave functions: The SCF orbitals, in order of increasing energy, are labeled $1a_1$, $2a_1$, $1b_2$, $3a_1$, $1b_1$ (C_{2v} symmetry). They are represented in Figure 3-5. The $1b_2$ and $3a_1$ orbitals are the main bonding orbitals (they are largely responsible for the donation of hydrogen bonding), while the $1b_1$ orbital is nonbonding (it has pz^2 character predominantly with no contribution from the hydrogen 1s orbital and mainly contributes to the "lone pair"). $4a_1$ is the lowest unoccupied orbital which is the antibounding counterpart of $3a_1$ orbital.

The hypothesis that a shape resonance occurs has been rejected by Sanche and Schultz [76]: incoming electrons is attached at relatively high kinetic energies (>7eV) thus has a low probability to be captured in the LUMO $4a_1$ and creates a shape resonance.

The earlier theoretical work of Jungen et al [82] gave basis for the assignement of the three dissociative attachment peaks to three Feshbach resonances. There are six low lying dissociative electronic states of water $^{1,3}B_1$, $^{1,3}A_1$ and $^{1,3}B_2$ which correspond to the promotion of an occupied $1b_1$, $3a_1$ or $1b_2$ electron into the antibonding $4a_1$ orbital. These states are the parents of three doubly excited anion states with configurations $1b_1 4a_1^2$, $3a_1 4a_1^2$, and $1b_2 4a_1^2$, corresponding to the three main dissociative attachment peaks as illustrated in Figure 3-5.

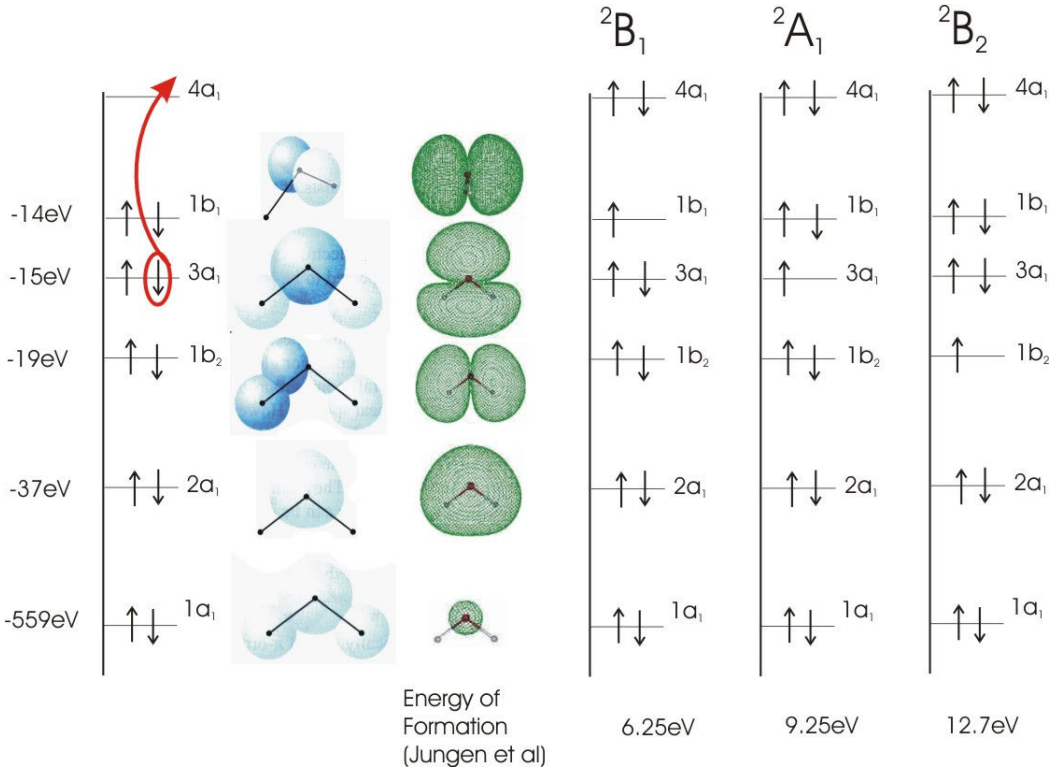

Figure 3-5 : Picture of the Feshbach resonances mechanism for the formation of a negative ion of water.

There were a lot of experimental investigations of the DEA to water but only a few theoretical studies, the first ab initio calculations of dissociative attachement are reported in recent papers of Haxton et al [77,78]. They calculated the potential surface for the $^2B_1$ resonance state in its full dimensionality. That surface $V = E_R - i\Gamma_a/2$ is complex in the region in which this state is metastable. Both, the real part and the width Γ were calculated by ab initio methods, the real part in large scale configuration interaction calculations and the width from complex Kohn variational scattering calculations (see details in [77,78]). In [77,78], they discuss the mechanism of dissociation of the $^2B_1$ state into the different channels. In their most recent paper [79], they discuss further the dissociation mechanism pictured by preliminary studies of the other resonances $^2A_1$ and $^2B_2$ and envisage also the existence of the dissociation channel O^- + H + H revealed by experiments of Curtis and Walker [80].

C. Experimental setup for measuring water

The gas inlet system is described in this paragraph; the rest of the apparatus was described in chapter 1 and 2. The Figure 3-6 shows the gas handling system.

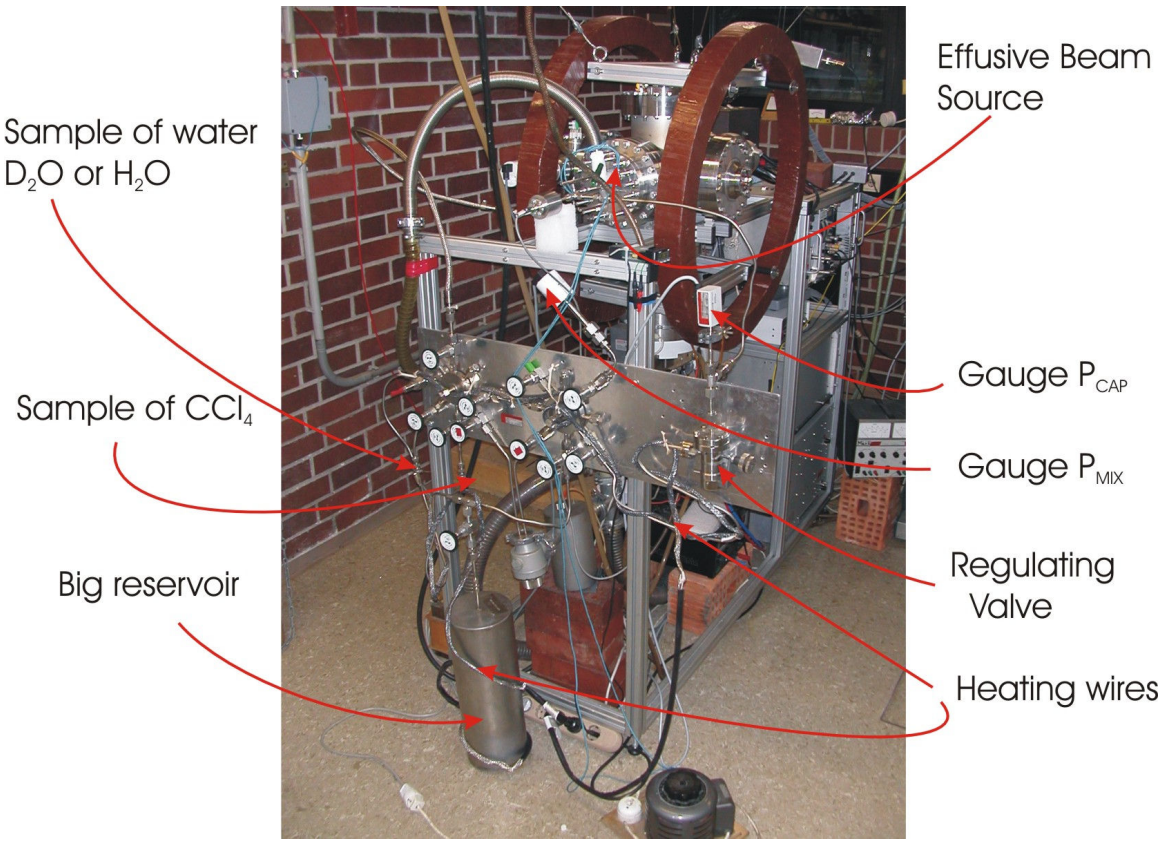

Figure 3-6 : Gas handling system.

In the following we briefly describe the method used for the determination of the absolute cross section. We used the known cross section of the second peak of dissociative attachment to CCl_4 (see Part II : Chapter 3.B.II)) to calibrate the cross sections. The gases could be introduced as a mixture in known ratio or separately one after the other. In the case of the introduction as a mixture, the ratio of densities was determined by the ratio of partial pressures in the volume of the gas handling system. In this case, the determination of the ratio could be erroneous: even if precaution were taken (heating of the gas handling system), condensation of water cannot be avoided easily. If we work at vapor pressure, the ratios will change with time since the pressure of water remains constant whereas the pressure of CCl_4 diminishes. So the partial pressure of water should be lower than the vapour pressure.

In the case of the separate introduction of the gases into the chamber, the ratio of gases can be determined more accurately but on the other hand the potential of the electrodes of the monochromator are expected to vary strongly from one gas to another and thereby the electron energy distributions and electron current in the monochromator. So that the conditions of measurement can not be maintained and have to be corrected. For this reason, the mixture of gases is usually preferred for the determination of absolute cross section.

A big reservoir was used firstly to ensure a constant flow and stabilize the conditions

of the measurement. Unfortunetly, this big reservoir was leaking, the first peak of O^- was enlarged due to the presence of O_2 from the air (comparable to the first peak of Melton in Figure 3-9). So, the only volume of the gas handling system was filled during the measurement of absolute cross section.

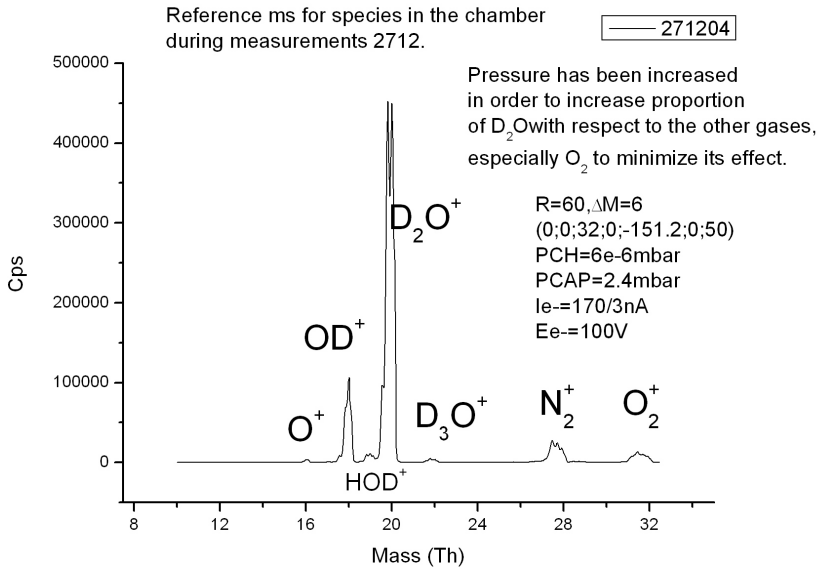

Figure 3-7 : Typical mass spectrum of gas composition in the collision cell during the experiment.

Several pump-freeze-thaw cycles were performed to degas the liquid water prior to measurement. Unfortunately an important leak rendered null the procedure of purification, and the presence of air is clearly observable in the mass spectrum of Figure 3-7. The pressure of water vapour was increased up to $6\text{-}7\times10^{-6}$ mbar in order to increase the proportion of water with respect to the other gases, especially O_2 to minimize its effect.

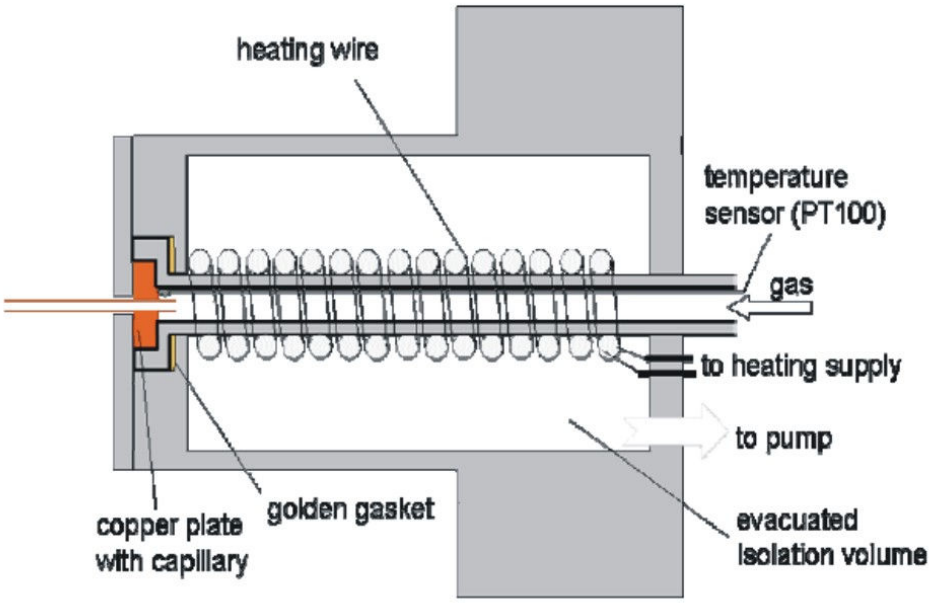

Figure 3-8 : Effusive molecular beam source of our apparatus. Taken from the thesis of P. Cicman [81].

The effusive beam source is described in the thesis of Peter Cicman [81], see Figure 3-8: "The effusive molecular beam source (EMBS) consists of a heated stainless steel gas tube (120mm long, 6mm diameter). The tube is terminated by a copper plate from which a narrow copper capillary (~150μm diameter) extends towards the collision chamber of the trochoïdal monochromator. A well defined molecular beam with a narrow angular distribution function is formed by effusion of the molecules through this capillary. The EMBS is resistively heated (temperature range 300-650K) using a heating cord wound around the gas tube. The temperature of the EMBS is measured using a PT100 sensor. The gas inlet system of MBS is working at higher pressure (typically P_{MIX}=10-1000mbar) and the gas is introduced to the MBS through a precise regulating valve, reducing the gas pressure to P_{CAP}~10^{-3}-10^{-1}mbar. At these pressures the mean free path of the molecules in the MBS is much longer than the typical dimension of the MBS and thus the collisions of the molecules with the walls are dominant. We assume that the molecules are in thermal equilibrium with the walls of the EMBS and thus the temperature of the molecules is equal to the temperature of the walls measured by the PT100 sensor. "

D. Experimental Results from the past and comparison

I) Formation of O^-

As explained in the introduction of the second chapter this study was initiated to review the results of the past which were possibly plagued by some discriminative effects and try to shed light on unresolved problems.

It was the purpose of the preceding chapter to try to determine if we can obtain some undiscriminated cross sections taking into account the discrimination occurring along the path towards the detector. We end up by concluding that the closest curve to an undiscriminated cross section was given by a measure taken in the heart of the stability area of the quadrupole.

For O^- from H_2O the extensive analysis of chapter 2 gives the resulting cross section in black presented in Figure 3-9. As well, in this Figure is shown the result of our first investigations obtained by performing measurements without careful tuning of the ion optics settings and of the position of the operating point in the stability area of the quadrupole. Rather important differences in the relative peaks intensities of the second peak can be noted between our results. Jungen et al [82] were aware of this important dependence on the focalization conditions chosen for the measure and stressed it out by giving cross sections obtained in two different focalization conditions. It is remarkable that their results show a similar discrepancy as the one existing between our first result and the one considered as less discriminated (421802) according to the analysis of the chapter 2.

These results are shown in Figure 3-9 and compared to other precedent measurements of Melton [68] and Compton et al [83]. For the comparison the curves were rescaled for matching the third resonant peak.

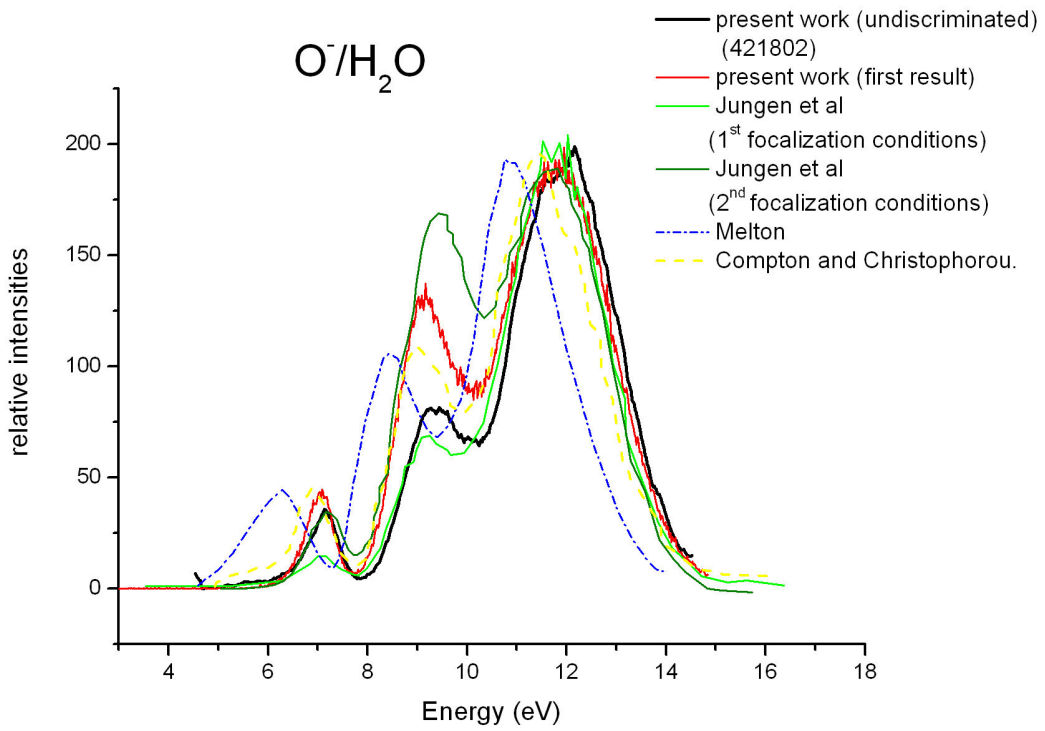

Figure 3-9 : Comparison of cross sections for the yield of O^-/H_2O by electron attachment obtained in this work with precedent studies from other author.

Jungen et al used a commercial mass spectrometer for their measurement. Our measured "undiscriminated" cross section lies between their results given for different focalization conditions. Melton used a high transmission source in order to determine faithful cross section and avoid discrimination. Compton and christophorou used a swarm technique to determine their cross sections.

Our energy scale was calibrated using the determination of the first momentum of the Cl- distribution as explained in the chapter 1. The energy scale of the first results was determined using our finest resolution (±0.1eV).

Jungen et al [82] determined peaks energy positions in good agreement with ours, they used the 0eV s-wave resonance of SF_6 to calibrate their energy scale. They assume accuracy within ±0.1eV of the energy scale, as well.

Compton and Christophorou also used the capture by SF_6 for their energy scale calibration and are in rather good agreement with other.

Melton used two gas test calibrations (vertical threshold (O^-/CO) at 9.5eV and O^-/O_2 at 4.4eV) resulting however in an energy calibration shifted about 1eV under the other determinations in Figure 3-9. The first peak of his cross section is much wider than the first peak of other measurements in Figure 3-9. It is probably due to the presence of O_2 used for

calibration in the gas background as we could observe in our experiment.

II) Formation of H^-

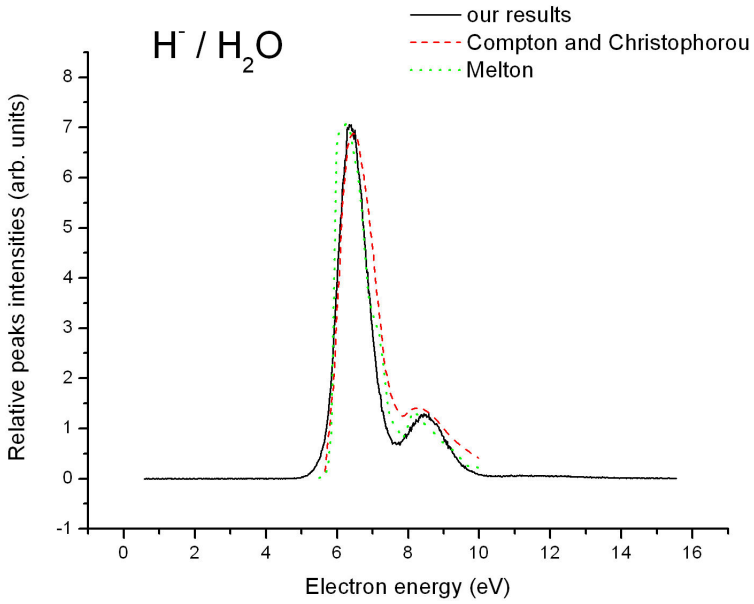

Figure 3-10 : Comparision of the relative intensities of the H^- yields from different author. The curves were rescaled to match the first peak.

The measurements of H^- were not subject to an analysis of discrimination occurring during our experiment. Due to the lightness of the H^- particules and the important kinetic energy which they carry it is expected that the discriminative effects are huge for this species. So only the position and width of the peaks are relevant in this study. However the relative intensities of our peaks are in good agreement with the precedent results of Melton [68] and Compton [83]: in Figure 3-10, the relative intensities of the H^- yields obtained by the different authors are compared.

We saw in Part II : Chapter 3.A that our determination of absolute cross sections is 5 times larger than the determinations of Melton and Compton which agree on the order of magnitude. But the O^- abundance was enhanced in the same proportion compared to the other authors which indicates that the huge difference can not be attributed only to discrimination difficulties since the light H^- ions would be much more influenced than O^-. In Figure 3-10 we notice however that the relative intensities given by the different author agree well.

Astonishingly, the positions of the peaks maxima are in rather good agreement as well: even the peaks positions determined by Melton are in agreement with ours and those of Compton, whereas they were shifted with respect to the other authors in the O^- yield. It must

be ascribed to the use of different calibration gases by Melton. All other authors found a shift between the position of the first peak of H^- and the first peak of O^-.

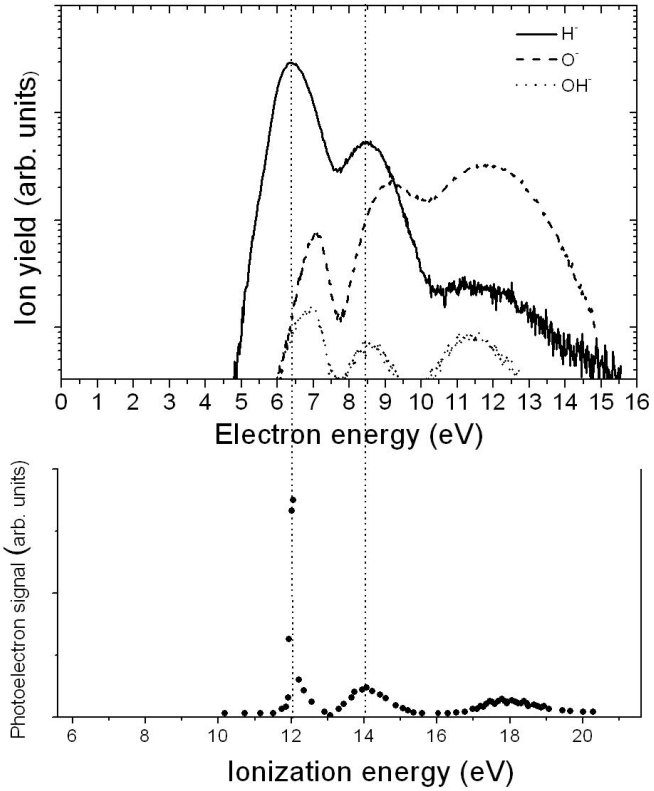

Figure 3-11 : Comparison of peaks position of our first results with the positions of photoelectron emission peaks.

In Figure 3-11 the shift between the peak maximum of O^- and H^- at 7 and 6.5 eV respectively is apparent. In our conditions of experiments there is coincidence between the OH^- and O^- peaks position. The H^- formation cannot be at the origin of the OH^- by ion-molecule reactions in these conditions (see Part II : Chapter 3.D.III)).

Haxton et al [77] do not explain this shift in energy position of the first peak of O^- with respect to H^- first peak by the presence of a potential barrier as was supposed by Jungen et al [82], but rather think the concept of a "dynamical barrier". The channel $O^- + H_2$ is still forbidden at the onset. The reason for that is dynamical: in order for the wavepacket to reach that channel, it must move essentially perpendicular to the gradient of the potential energy surface. Indeed, the surface is steeply downhill in the r1 and r2 directions (r1 and r2 correspond to the bond lengths) but mostly flat in the bending angle θ, as described in their paper [77]. In order to reach the O^-+H_2 well, of course it must move in the -θ direction. Speaking semi-classically, trajectories which access this well will have momentum in the negative θ direction when they start, and therefore will not contribute to the cross section at onset. The cross section at onset is due to trajectories which start with a minimum of

momemtum and potential energy. In other words, those trajectories which start at the edge of the initial vibrational wavepacket of H_2O with no momentum follow the gradient towards H^- + OH.

As the momentum of the incident electron is increased, components of the initial wavepacket which have significant momentum in the -θ direction will be sampled, which will yield O^- + H_2.

Haxton et al also intend to study the dissociation of the other resonances of water. It should shed some light on the reason of the weakness of the third resonant peak for the H^- channel.

III) Formation of OH^-

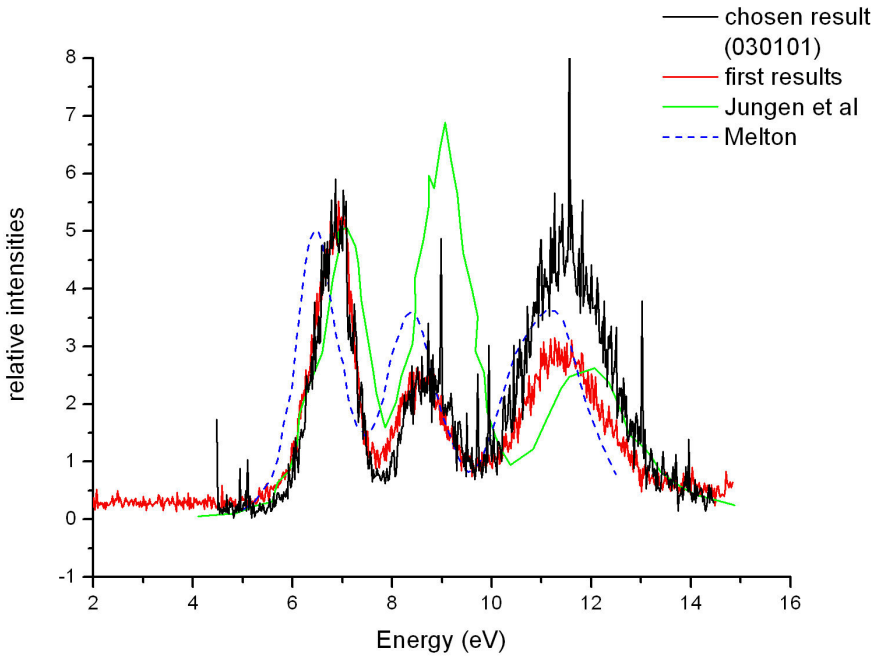

Figure 3-12 : Our measurements of the OH^- yield compared to previous results.

There are various opinions in the literature about the origin of the detected OH^- (or OD^- for D_2O).

The existence of three resonant peaks for the yield of OH^- whose maxima corresponds within experimental error to the maxima found for O^- let suppose a priori that the formation of OH^- is formed by dissociative attachment from the same electronic state of H_2O (see Figure 3-11).

$$e^- + H_2O \rightarrow H_2O^{-*} \rightarrow OH^- + H \qquad 3\text{-}9$$

However, Christophorou and Compton [83] didn't observe this product ion at low pressure under 10^{-6}mbar. They studied the pressure dependence of the OH^- yield with the pressure of H_2O in the range 10^{-5} to 10^{-3} Torr and determined the origin of OH^- to be due to ion-molecule reactions:

$$e^- + H_2O \rightarrow H_2O^{-*} \rightarrow H^- + OH \qquad 3\text{-}10$$

$$H^- + H_2O \rightarrow OH^- + H_2 \qquad 3\text{-}11$$

$$e^- + H_2O \rightarrow H_2O^{-*} \rightarrow O^- + H_2 \qquad 3\text{-}12$$

$$O^- + H_2O \rightarrow OH^- + OH \qquad 3\text{-}13$$

The highest cross sections are attributed to reaction 3-11 with respect to reaction 3-13 [84].

Melton [68] did a study with pressure as well, in the range 8×10^{-7} to 2×10^{-5} mbar. They didn't find any change of cross section for the OH^- yield in this range of pressure. According to these observations they concluded in favor of a dissociative attachment (reaction 3-9) process failing with finding another mechanism.

Jungen et al [82] also revealed the presence of OH^- at lower pressure which is not attributable to ion-molecules reactions only for two main reasons. First, as a rule, the previous studies [84] have revealed that ion-molecule reaction even with high quite large cross sections can be neglected at pressure lower than 10^{-5} Torr in a conventional mass spectrometer with relatively short residence time in the ion source. Second, they stressed out that if OH^- stems from reaction 3-11 mainly, the peaks maxima of the OH^- yield should coincide with those of the H^- yield (first peak at 6.5eV). And, if they might effectively coincide in the pressure range 10^{-5} to 10^{-3} Torr as observed by Compton and Cristophorou in [83], it is not the case in the

lower pressure range at pressure of 10^{-6} Torr for which Jungen et al performed their experiment. They observed rather an agreement with the peaks of the O^- yields (first peak at 7eV) at this pressure. Our results confirm the observation of Jungen et al.

We observed the presence of OH^- even at the lowest pressure (~10^{-7}mbar) and the variation with pressure always gives a coincidence of the OH^- peaks maxima with the corresponding peaks maxima of O- up to pressure 4×10^{-5} mbar. It excludes the possibility of formation through the ion-molecule reaction 3-11.

We can observe in Figure 3-13 however that the relative peaks intensity of the OH^- signal is slightly modified by the change of pressure, whereas the O- yields remain invariable.

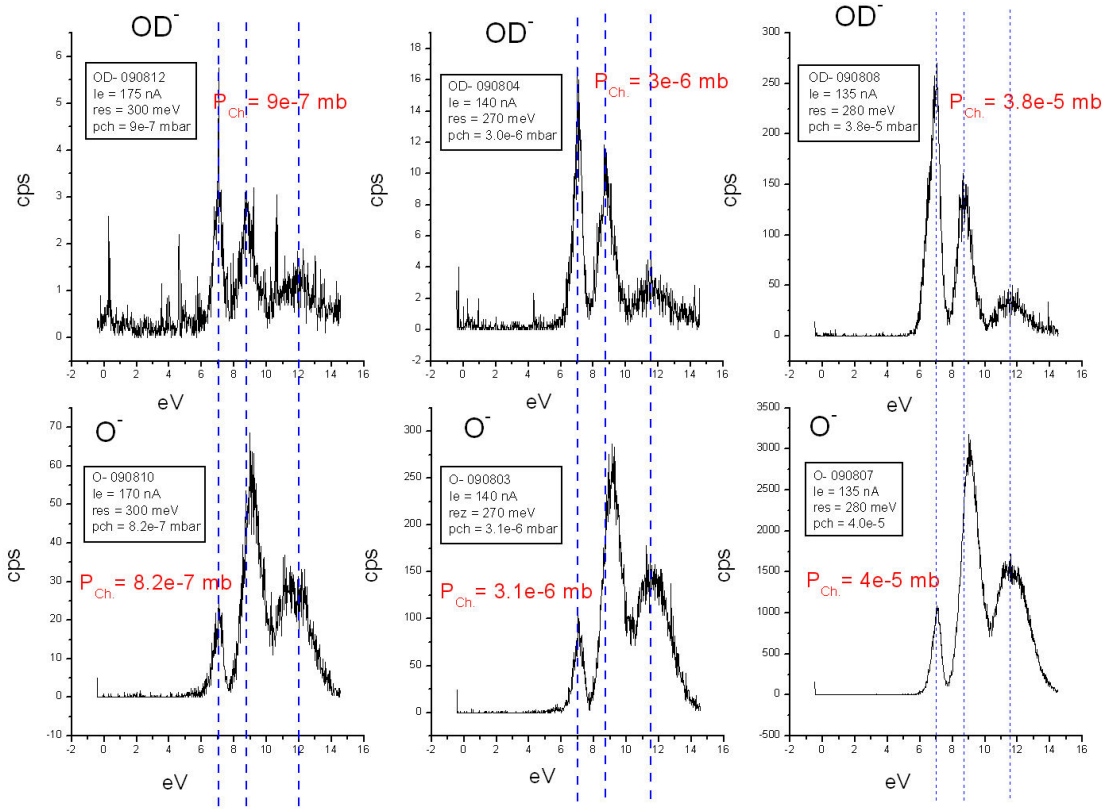

Figure 3-13 : Study of O- and OH- yields coincidence with the pressure. Extraction was used to enhance the signal (L1 ;L2)=(-0.5V;0.5V), so that the cross sections are deformed but the position of the peaks are unaltered by extraction.

Haxton [77,78] excludes the possibility of formation of OH- from theoretical considerations. Their study of the dissociation of the lowest anion state $^2B_1$ (first peak) revealed that it either correlates asymptotically with the $OH(^2\Pi)+H^-(^1S)$ or $H_2(^1\Sigma)+O^-(^2P)$. The third arrangement channel $H(^2S)+OH^-(^1\Sigma)$ observed at each resonant peaks is excluded by

symmetry as long as coupling to other potential energy surfaces is omitted.

Klots and Compton [85] studied the electron attachment to van der Waals cluster of water, expanded through a sonic nozzle. They excluded the direct formation by electron attachment and the possibility of intermolecular ion-molecule reaction as well. They proposed another mechanism which takes place in two steps:

$$e^- + (H_2O)_2 \rightarrow H^-(H_2O) + OH \qquad 3\text{-}14$$

$$H^-(H_2O) \rightarrow OH^- + H_2$$

So, the origin of the OH^- must be related to the dimeric content in the effusive beam. Klots et al [85] studied the abundance of OH^- as a function of the stagnation pressure: the signal of OH^- effectively follows the H_3O^+ and the $(H_2O)_2^+$ ion signals, each of which can be taken as monitoring the dimeric content of the nozzle beam.

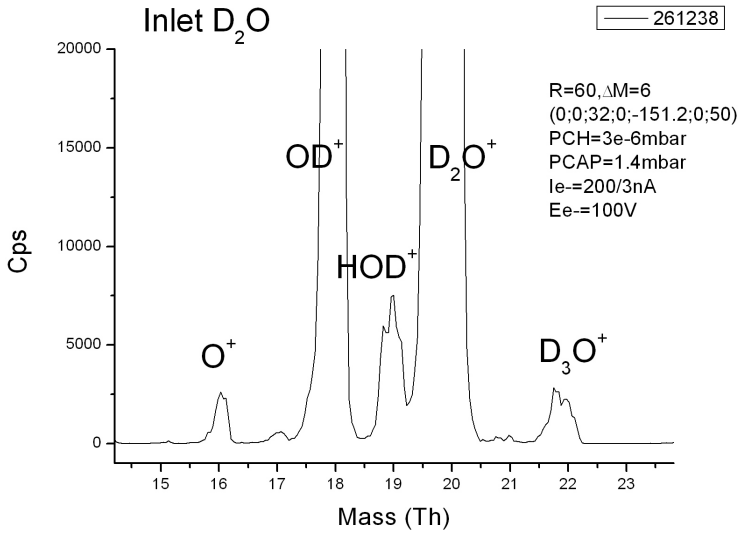

Figure 3-14 : Abundance of D_3O^+ in the mass spectra indicates the presence of dimer in the effusive beam of water vapor.

A typical mass spectrum taken at 100eV in our experiments is shown in Figure 3-14. We found 22 amu mass peak which can only be attributed to the ionization of dimer $(D_2O)_2$ into $D_3O^+ + OD^-$ if the natural deuterium exchange reaction $D_2O + D_2O \rightarrow D_3O^+ + OD^-$ can be neglected. Usually mass spectra were taken at 70eV or 100eV so that the dimers could not be softly ionized and they were not observed in the mass spectrum: At 15eV, close to ionization threshold, Klots et al already found the $(H_2O)_2^+$ signal to be less than 10% of the H_3O^+ signal. Hence, the important abundance of D_3O^+ indicates the presence of dimer in the effusive beam

of our experiment which could be at the origin of the OH^- detected according to the mechanism of Klots.

Mechanism 3-14 associated with the dissociative attachment of a water molecule of the dimer according to the dissociation channel H^- + OH is supplemented by the mechanism associated with the other dissociative channel O^-+ H_2:

$$e^- + (H_2O)_2 \rightarrow O^-(H_2O) + H_2 \qquad 3\text{-}15$$

$$O^-(H_2O) \rightarrow OH^- + OH$$

In their study Klots et al remarked that the reaction 3-15 only occurs for dimer.

Indeed reactions 3-14 and 3-15 are particular cases of more general reactions. For water clusters of size n, Klots et al proposed in analogy with well known mechanism for nitous oxide cluster $(N2O)_n$:

$$e^- + (H_2O)_n \rightarrow H^-(H_2O)_{n-1} + OH \qquad 3\text{-}16$$

$$H^-(H_2O)_{n-1} \rightarrow OH^-(H_2O)_{n-2} + H_2$$

And, via the supplemented channel:

$$e^- + (H_2O)_n \rightarrow O^-(H_2O)_{n-1} + H_2 \qquad 3\text{-}17$$

$$O^-(H_2O)_{n-1} \rightarrow OH^-(H_2O)_{n-2} + OH$$

Reaction 3-15 is the only one retained to give rise to the third resonant peak of OH- (at 11.8eV), since the third resonant peak of the H^- channel from monomer is practically inexistent.

A study by Knapp et al [86] shows the stability of long cluster of heavy water to electron attachment at 0eV (Figure 3-15). And they confirmed that the most abundant anion water cluster products from electron attachment between 5 and 10eV are the $OD^-(D_2O)_n$ ($n \geq 1$). Figure 3-15 shows the yields summed over the series of ions $(D2O)_{n-1}OD^-$ ($2 \leq n \leq 9$), the shape of the H- yields of Figure 3-10 is clearly recognizable. According to Klots et al [85], this shape is characteristics of the $OH^-(H_2O)_n$ ($n>2$) yields, only the yield of OH- formed from the dimer (n=2) has a non negligible resonant peak at 11.8V. So that they concluded that the

reaction 3-17 does occur only for dimers.

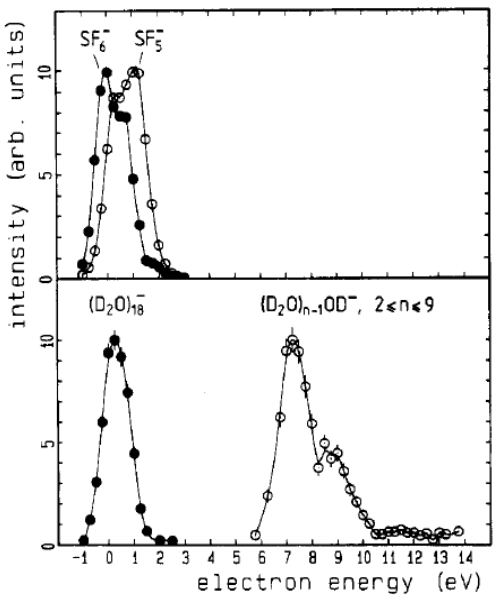

Figure 3-15 : Reproduced from [86]. Results on electron attachment to deuterated water clusters.

If the origin of OH^- can be assigned to the mechanism 3-14 and 3-15, we can expect a dependence with the temperature since the cluster contents of the effusive beam must be very dependent with temperature. We performed such a study of the change of OH^- with temperature; our apparatus allows a study with temperature increase up to 350°C about (see Part II : Chapter 3.C), the results are shown in Figure 3-16. The overall intensity of the O^- signal at 307°C is increased by roughly a factor 1.4 with respect to the initial signal intensity at 20°C. But, the relative peaks intensities of the O^- signal remain unchanged with the increase of temperature, whereas we can clearly notice the increase of the first peak of the OH^- signal with regards to the other peaks. Indeed from 20°C to 307°C, the first peak of OH^- signal is increased by a factor 1.5 roughly whereas the second peak intensity decreases by about a factor 0.6, and the third peak remains roughly constant with the change of temperature.

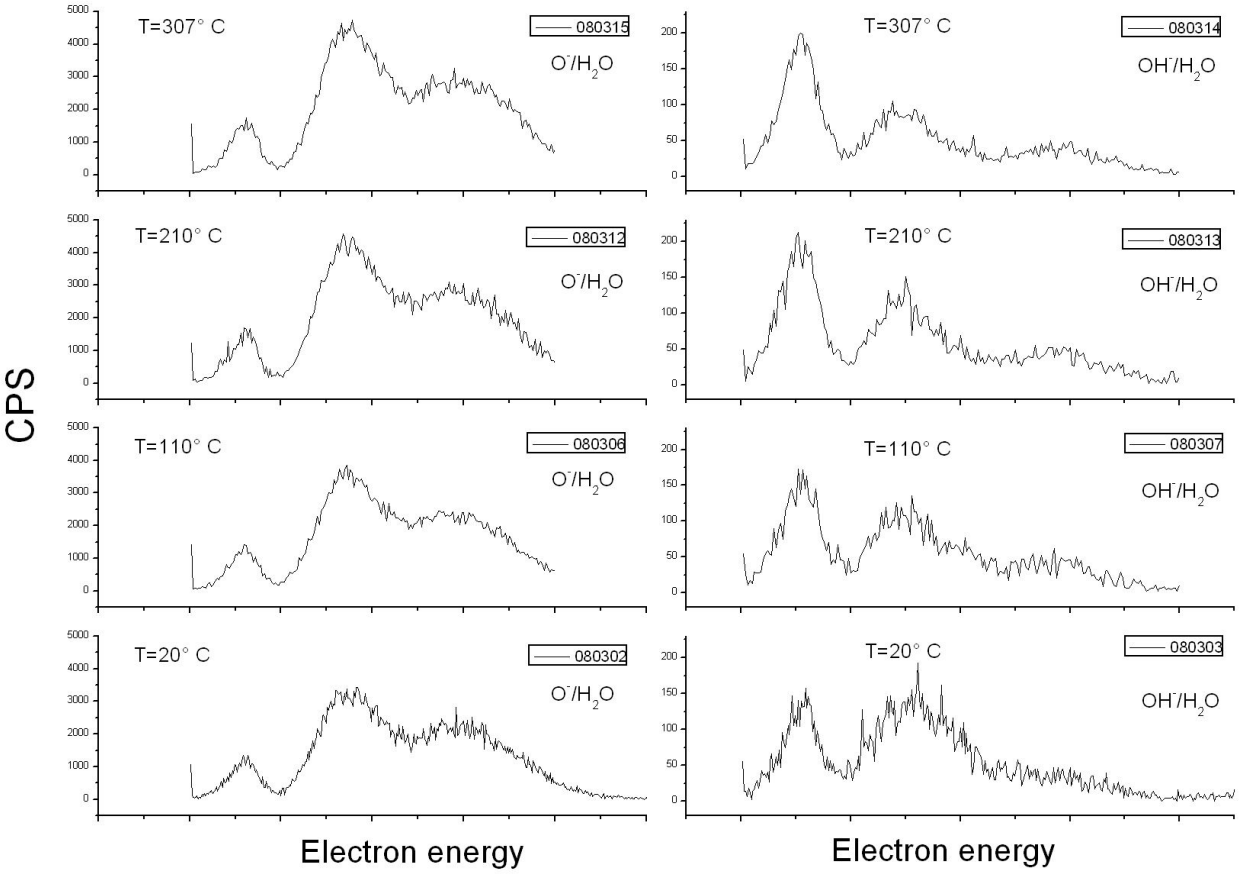

Figure 3-16 : Influence on the OH^- signal with the temperature. Cross sections taken with extraction (L1 ;L2)=(-2 ;2), in identical conditions of focalization. The effect of increase of the temperature is similar to the increase of pressure. The relative intensity of the first peak of OH- increases significantly with the increase of temperature, whereas no effect concerning the relative intensity can be noted for the O^- yield.

If we supposed that the conditions of experiments were constants, the changes observed can be attributed to the increase of temperature only. The influence of temperature on the water vapor is to populate higher rotational and vibrational energy levels than the ground state. The effect of rotational excitation on the cross section is expected to be negligible [79]. However the vibrational excitation can affect dramatically the cross section in the OH + H^- channel [79]. The abundance of clusters is also dependent dramatically with temperature.

If the mechanism of Klots is effectively describing the formation of OH^-, the reaction 3-14 and 3-15 must be influenced differently by the increase of temperature and lead to the variation of cross section observed in Figure 3-16. Dependence with the pressure was also observed in Figure 3-13, which leads to a similar change of the shape of the OH- signal. Further examination should be made to determine the mechanism(s) responsible for the formation of OH^-.

IV) Isotopic effect

The isotopic effect was studied for the yields H^- and D^- as well as O^- from H_2O or from D_2O by Compton and christophorou. Jungen et al gave a study for OH^-/OD^- also.

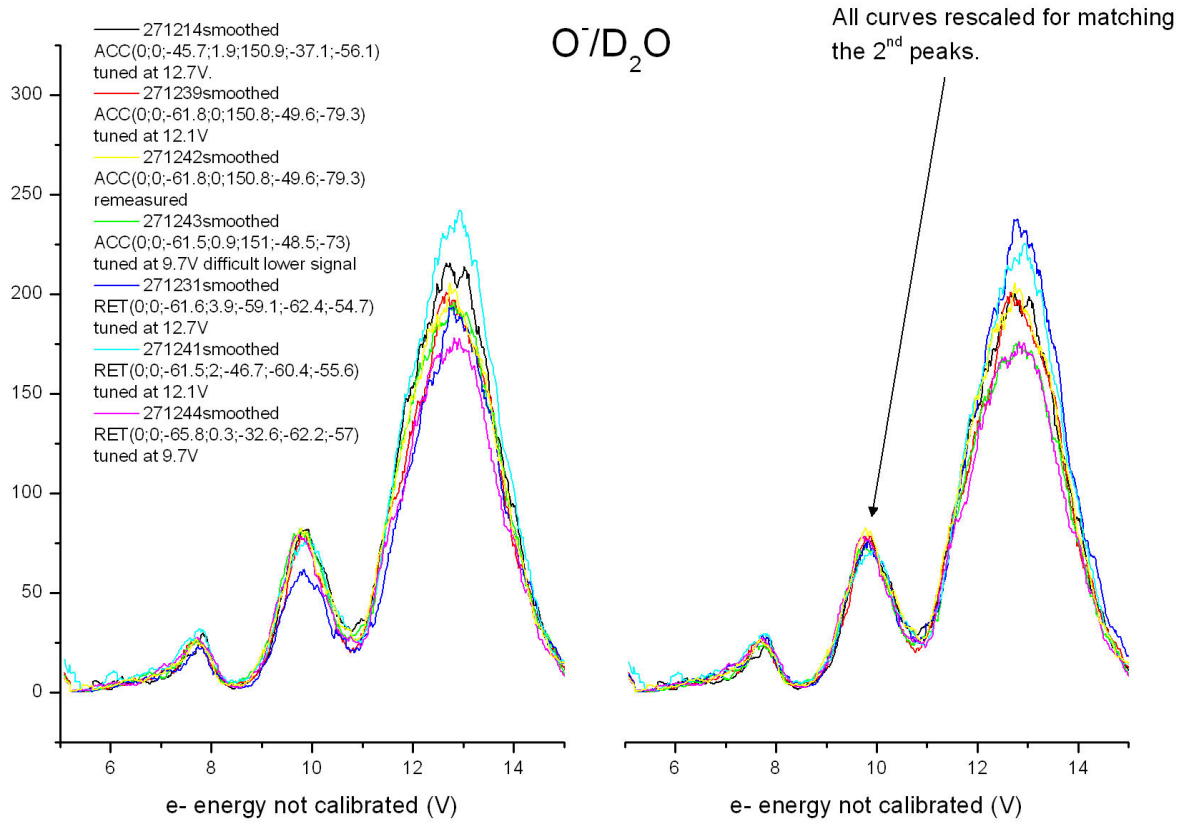

Figure 3-17 : Measurement of O-/D_2O in various conditions. 271239 was retained as final result. Cross sections are rescaled to the second peak for comparison in the right graph.

Figure 3-17 shows a collection of results obtained for the dissociation channel into O^- from D_2O: 271239 was retained for the comparison with O^-/H_2O.

Figure 3-18 displays the comparison to precedent works as well as to our first results. Our results agree on the fact that the third peak's intensity is higher than the second peak, whereas Compton and Christophorou [83] determined a smaller third peak for the yield of O- from D_2O and ascribed this change to the isotopic effect (see further). In chapter 2, we obtained similar results as Compton et al (or Jungen et al, 2nd foc.) when a small extraction field was applied. Without extraction the resulting cross section gave invariably a higher third peak as is shown in Figure 3-17.

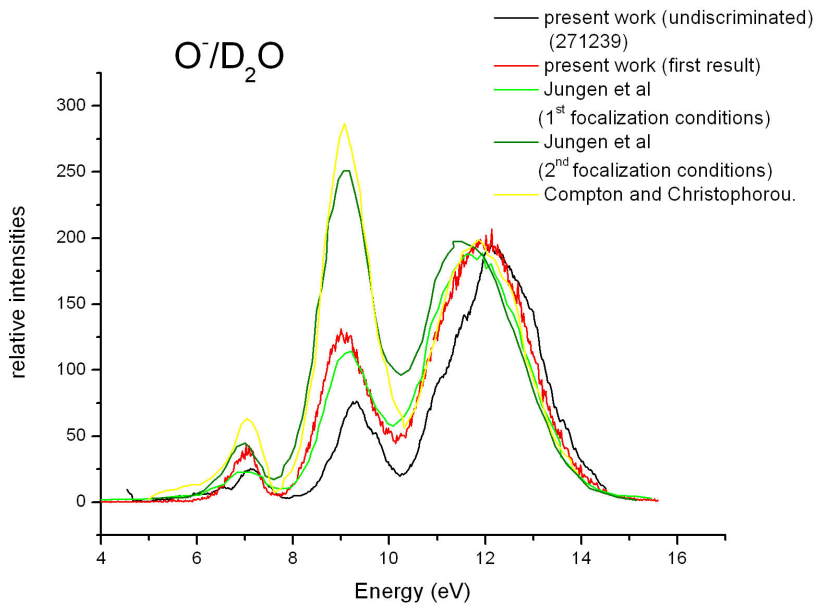

Figure 3-18 : Comparison of our results with other authors.

What do we expect for isotopic effect from the theoretical point of view?

It is described in [70] and [72]. The mass dependence of the cross section given by the formula 3-7 for a diatomiclike molecule can be decomposed as follows. There is a contribution from the survival probability σ_D : since isotopic species experience the same forces, the relative velocities of separation $v(R)$ are proportional to $\mu^{-\frac{1}{2}}$, where μ is the reduced mass. Hence, the survival probability depends on μ as $\exp[-const \times \mu^{\frac{1}{2}}]$. The other mass dependent quantity is the dissociation width Γ_d (see [72]):

$$\Gamma_d \propto \mu^{-\frac{1}{4}} \qquad 3\text{-}18$$

As a consequence, for $E \simeq E_0$ in formula 3-7, the mass dependence of the maximal cross section can be written:

$$\sigma_{DEA} \propto \mu^{\frac{1}{4}} \times \exp[-const \times \mu^{\frac{1}{2}}] \qquad 3\text{-}19$$

Depending on the case it can be that the heavier isotope has a larger cross section or inversely. If the autoionization probability Γ_a is large, then the second term of 3-19 is the most important and σ_{DEA} is smaller for the heavier isotope. It is called direct isotopic effect. If, on the other hand, Γ_a is small, then the first term of 3-19 is the most important and σ_{DEA} is larger for heavier isotopic effect. This is the inverse isotopic effect. Small direct isotopic

effects are are found for most of the molecules (see [70]) in which case the heavier isotope has a smaller cross section but of the same order of magnitude.

The formula 3-18 is predicting a smaller width for the heavier species.

The case of water was studied by Compton and Christophorou [83].

The comparison of their H- and D- yields is given in Figure 3-1; they found the ratio

$\frac{\sigma(H^- / H_2O)}{\sigma(D^- / D_2O)} = 0.74$ close to $\left[\frac{\mu(H^- - OH)}{\mu(D^- - OD)}\right]^{\frac{1}{2}} = 0.72$ as it should.

What about the width of the resonances?

$\frac{\Gamma_d(D^- / D_2O)}{\Gamma_d(H^- / H_2O)}$ is determined to be equal to $\left[\frac{\mu(H^- - OH)}{\mu(D^- - OD)}\right]^{\frac{1}{4}} = 0.85$ from the theory (equation 3-18). If, on the one hand, our determinations of absolute cross sections are not reliable, and as a consequence the ratio of the peaks intensities between isotopes is not relevant, on the other hand, the ratio of the widths of our isotopic peak is in perfect agreement with the prediction of the theory. Whereas the ratio determined from the results of Compton et al is slightly lower than the expected value, as shown in Figure 3-19.

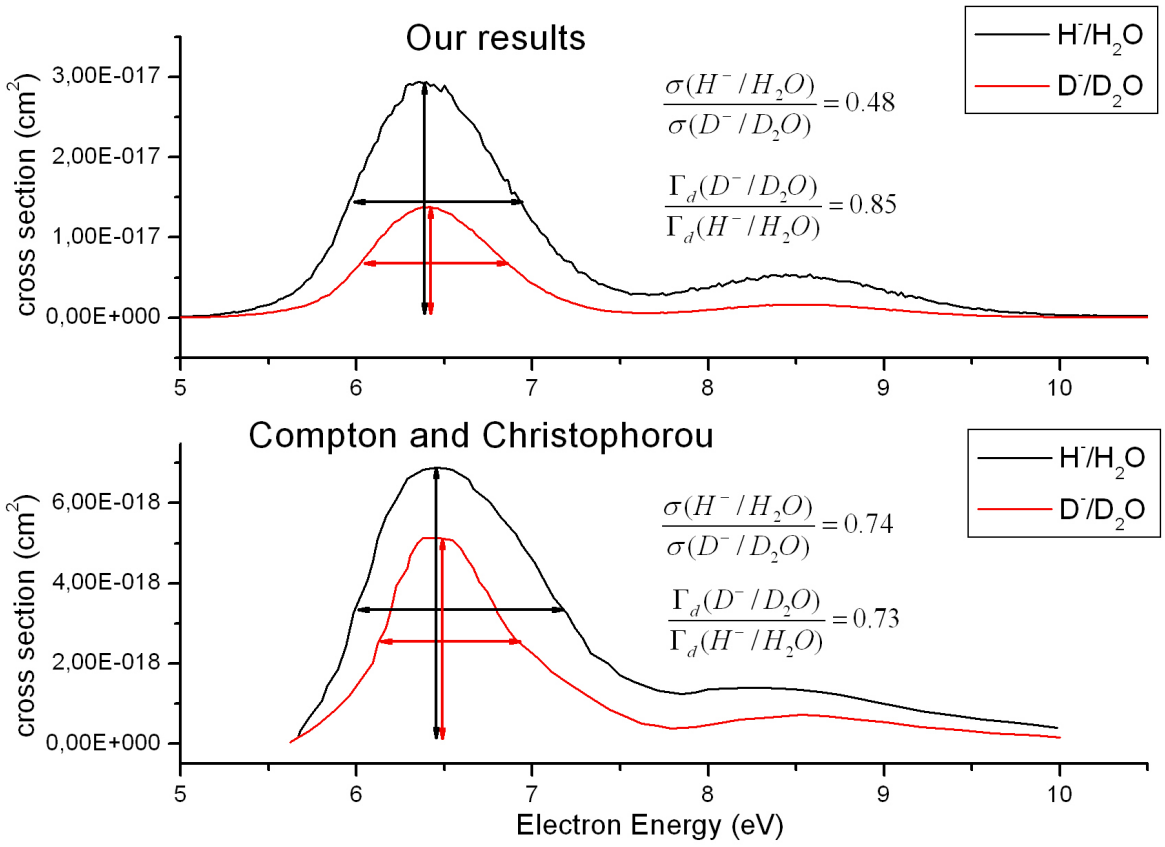

Figure 3-19 : Comparison of isotopic effects found for our results with isotopic effects found by Compton and Christophorou.

Haxton et al [78] determined theoretically a small inverse isotopic effect which is in disaccord with the results of Compton and Christophorou, as well as ours if our estimation of the peaks magnitude can be taken as an indication. They found first peaks heights of 5.99×10^{-18} and 7.04×10^{-18} cm^2 for H^- from H_2O and D^- from D_2O.

Our results for the O- yield from H_2O and D_2O are compared in Figure 3-20. A reduction of the width of the peaks is observed for the heavy water in both cases (first results and undiscriminated), as it should.

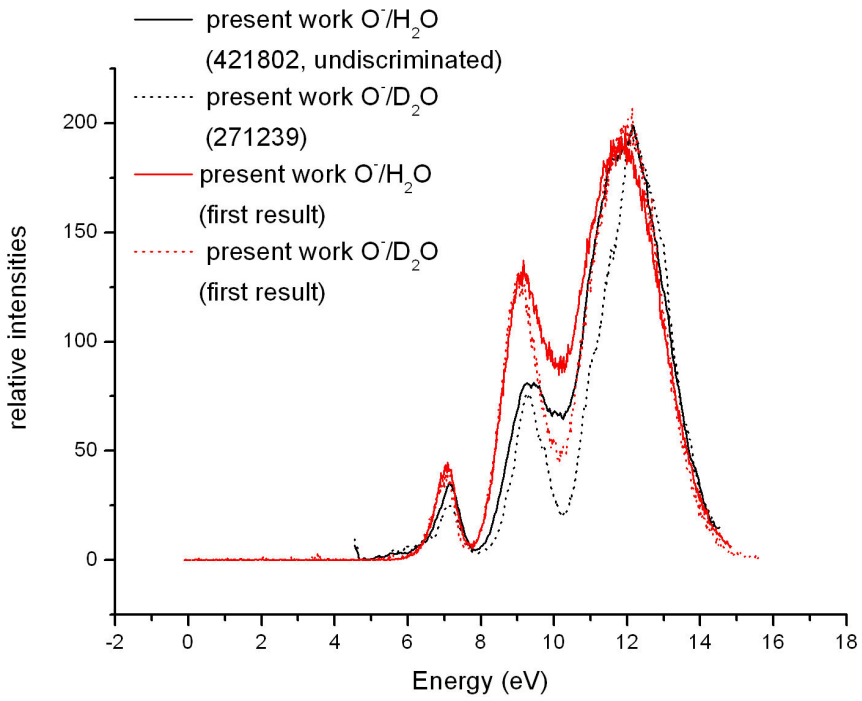

Figure 3-20 : The yields from H2O and D2O are compared. Both pair of curves show the same effect. This is the expected isotopic effect.

Since the determination of absolute cross section revealed to be not reliable, we can only look further at the relative cross sections. Figure 3-21 shows the relative peaks intensities determined by other authors for the O- yield.

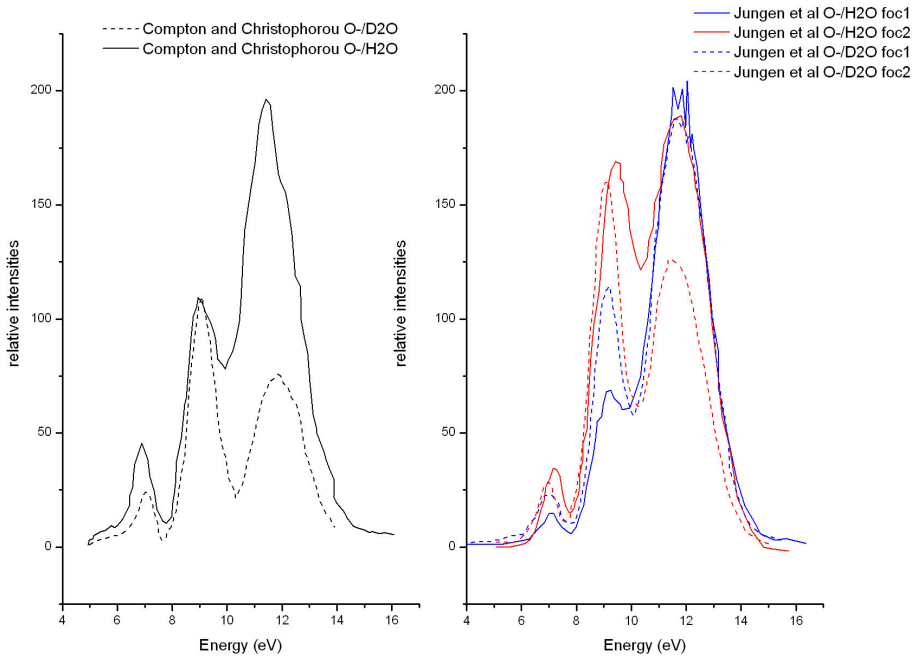

Figure 3-21 : Results from other author on the isotopic effect.

As remarked by Jungen et al [82], the smaller third peak found by Compton and Christophorou for the deuterated species and interpreted by them in terms of gound state isotopic effects [83], should rather be ascribed to some extent to discriminative effects of high energy ions of the third peak. If we compare the yields of Compton and Christophorou for the deuterated species with the typical discriminated yields we found in our study of the effect of extraction from the chamber (chapter 2, Figure 13), we are compelled to think that the results of Christophorou were effectively plagued by high kinetic energy ions discrimination.

Compared to both authors, our results give quasi-identical relative peaks intensities for water or heavy water. The discrepancies observed can be ascribed to dependence on the kinetic energy discrimination of the different apparatus.

Compton and Christophorou determined the origin OH- to be due to ion-molecule reactions. Hence it was no purpose to study the isotopic effect for this fragment. However, by their observations, Melton [68], then Jungen et al [82] throw back into question the formation of OH- as explained in Part II : Chapter 3.D.III).

The Figure 3-23 shows the comparison of our determined cross section for the yield of OD^- with the results of Jungen et al [82]. Again, we compare our first results with chosen results obtained after further investigations of the influence of ion optics settings on the cross sections. However, as already explained, the analysis of discrimination for the case of OD^- was only partial; the position of the operating point in the stability area of the quadrupole relatively to the heart of the stability area is undetermined for these measurements. Nevertheless, the variation of ion optics didn't induce any changes of the relative peaks

intensitites under different conditions as shown in Figure 3-22.

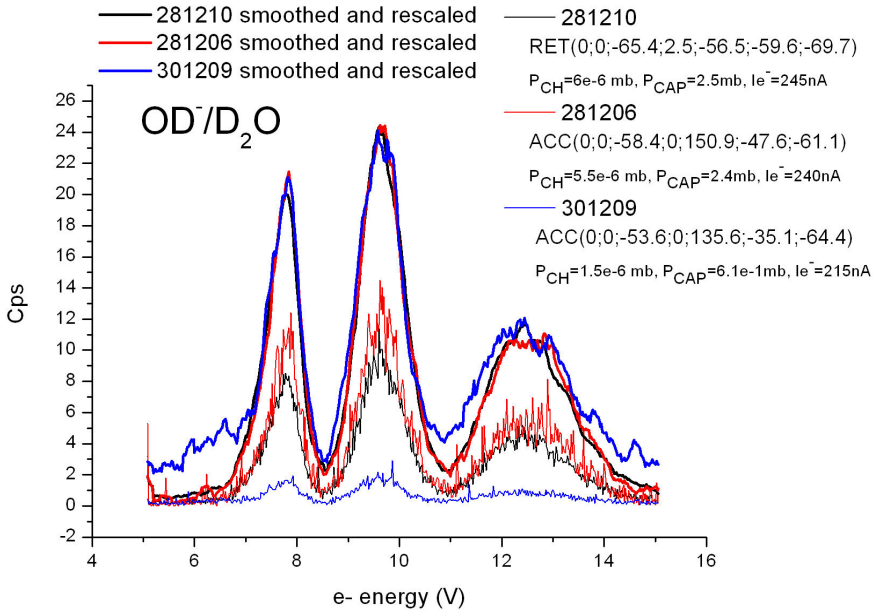

Figure 3-22 : Measurement of OD^- under different conditions gives invariably the same relative peaks intensities.

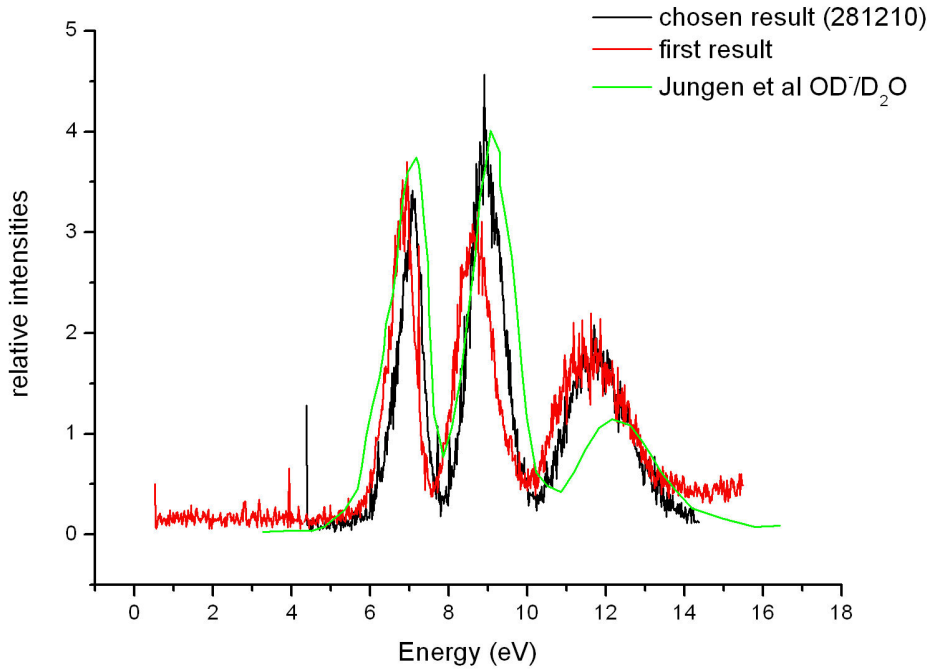

Figure 3-23 : Our results (first results and chosen results from Figure 3-22), compared to the results of Jungen et al [82].

Finally, the Figure 3-24 shows the difference of relative peaks intensities found for the formation of OH^- and OD^- in the studies of the electron attachment to H_2O and D_2O respectively.

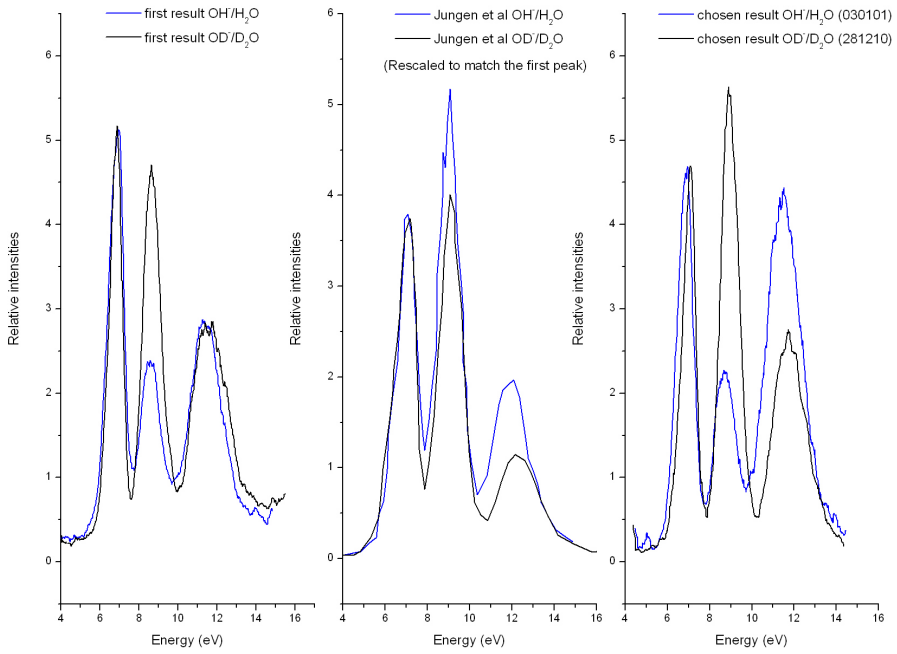

Figure 3-24 : Comparison of our results for isotopic effects for the yield of OH- OD- compared to the results of Jungen et al. All OD^- yields were rescaled to match the first peak of the OH^- yield.

Again discrepancies between results arise. The invariance of cross section found in Figure 3-22 under different focalization conditions give to the chosen results some more reliability, but more work should be made to fully analyse the variation of cross section under different conditions of measurements. In Figure 3-12, we note that the OH^- yield of Jungen differs much from the results of the other authors which determined a smaller second peak in agreement with our results. This larger second peak for the yield is therefore suspicious. The other discrepancies can be ascribed to discriminative effects. Our results agree on an increase of the second peak as isotopic effect for the formation of OD^- compared to the formation of OH^-.

E. Conclusion:

Apart for the O^-/H_2O yield, a detailed analysis of discrimination for the other yields was not performed. Hence we remain on an indetermination for the yields of O^-/D_2O, H^-/H_2O, D^-/D_2O, OH^-/H_2O, OD^-/H_2O. However, the relative cross sections of H^-/H_2O and D^-/D_2O determined by different authors are in rather good agreement. And by analysis, we could gain some information on the validity of the different results for OH^-/H_2O and OD^-/D_2O. The analysis performed in the second chapter constitutes a first step towards a better

understanding of discrimination in our apparatus. The variety of the results demonstrates the necessity of a more complete examination of the discrimination problem when fragment with high kinetic energies are produced. Also it shows that real calibration with various known cross sections should be undertaken in order to be able to determine faithfully absolute cross section with this apparatus.

We found good agreement with other authors concerning the determination of the position of resonant peaks. Besides, the determined isotopic effect on the width of the $^2B_1$ resonant peak is in very good agreement with the expected result from theory, indicating as well that the electron energy resolution was accurate enough.

Conclusions

The interest of this work was to present some initial steps of a larger program towards the understanding of the effect of radiation at the molecular scale.

The basic collision sytem H+/H on helium was investigated in the first part and presented as an archetypal system of interest for the understanding of fondamental aspects of the charge change phenomena. These studies were also performed as a general test of the functioning of the apparatus before going to more complex systems. The satisfying agreement obtained with previous studies of Shah et al and Dubois et al for the impact respectively of H^+ and H on helium is favorable for a pursuit of the studies.

The review of the dissociative electron attachment to water in the second part of this thesis was the occasion to make a full study of the discrimination problem in the trochoïdal electron monochromator of the Institut für Ionenphysik of Innsbruck. This study draw attention to the many difficulties for the determination of cross section with this apparatus and should be of interest for further studies employing the same apparatus.

The experimental program to which the present studies belong is progressing through the investigation of other basic biological systems at the university of Lyon and at the Institut fur Ionenphysik, Innsbruck. In particular, proton impact experiments have been carried out upon water, uracil, thymine, adenine, and cytosine targets using the same apparatus tested and developed over the course of the present helium impact work [3,87]. The experiments carried out at Innsbruck include electron attachment, including dissociative electron attachment upon gas phase biomolecules such as uracil, DNA bases, and deoxyribose ([88,89,90,91,92,93,94,95,96,97,98]). Both groups are extending their radiation damage research program into the cluster phase.

References

[1] L.H.Toburen (1998). Radiat. Environ. Biophys., **37**, 221-233.

[2] H. G. Paretzke (1987). *? And kinetics of Nonhomogeneous Processes – Radiation track structure theory*. John Wiley & Sons, Inc.

[3] B. Coupier et al (2002). Eur. Phys. J. D. **20**, 459-468.

[4] J.T. Park, (1983). Interactions of Simple Ion-Atom Systems. Adv. At. Mol. Phys., **19**, 67.

[5] L. H. Andersen, L. B Nielsen and J. Sorensen (1988). J. Phys. B: At. Mol. Opt. Phys., **21**, 1587-1602.

[6] R.D. Dubois, A. Köver (1989). Phys. Rev. A, Vol **40**, No 7, 3605.

[7] L. J. Puckett, G. O. Taylor, D. W. Martin (1969). Phys. Rev. **178**, 271.

[8] E. Pederson Horsdal and L. Larsen (1979). J. Phys. B: At. Mol. Phys., **12**,4099.

[9] P. Hvelplund, A. Andersen (1982). Phys. Scr. **26**, 370.

[10] M.Schulz (1995). Int. J. of Mod. Phys. B, Vol. 9, No. **25**, 3269-3301.

[11] Rudd et al (Oct. 1985). Rev. of Mod. Phys. Vol. **57**, No.4., 965.

[12] B.H. Bransden and M.R.C. McDowell (1992). *Charge Exchange and the Theory of Ion-Atom Collisions*. Oxford University Press.

[13] Earl W. McDaniel, J.B.A. Mitchell, M.Eugene Rudd (1993). *Atomic particle projectiles – Heavy particle projectiles*. John Wiley & Sons, inc.

[14] Earl Mc.Daniel (1989). *Atomic collisions – Electron and Photon projectiles*. John Wiley & Sons, inc.

[15] N.F. Mott, H.S.W. Massey (1952). *The Theory of Atomic Collisions*, 2nd edition. Oxford University Press, Oxford.

[16] H.A. Slim, E.L Heck, B.H. Bransden and D.R. Flower (1991a). J. Phys. B: At. Mol. Opt. Phys., **24**, 1683-1694.

[17] H.A. Slim, E.L Heck, B.H. Bransden and D.R. Flower (1991b). J. Phys. B: At. Mol. Opt. Phys., **24**, L421-L424.

[18] H.A. Slim, B.H. Bransden and D.R. Flower (1995). J. Phys. B: At. Mol. Opt. Phys., **28**, 1623-1642.

[19] M.Kimura, C.D. Lin (1986). Phys. Rev. A, **34**, 176.

[20] T.A. Green, H. I. Stanley, Y.C. Chiang (1965). Helv. Phys. Act., **38**, 109.

[21] K.L Bell, V. Dose, and A. E. Kingston (1969). J. Phys. B **2**, 831.

[22] O. Heil, R.D. Dubois, R.Maier, M. Kuzel, and K-O.Groeneveld (1992). Phys. Rev. A, Vol. **45**, No.5, 2850.

[23] M. E. Rudd, J. S. Risley, J. Fryar, and R. G. Rolfes (1980). Phys. Rev. A, Vol. **21**, No.2, 506.

[24] M. E. Rudd and R. D. Dubois (1977). Phys. Rev. A **16**, 26.

[25] M.A. Bolorizadeh and M.E. Rudd (1986). Physical review A, Vol. **33**, No.2, 893.

[26] PhD Thesis of Franck Gobet.

[27] B.Farizon, M.Farizon, M.J. Gaillard, E. Gerlic, S.Ouaskit, Nucl. Instr. and Meth. in Phys. Res. B 00 (1995) NIB00638 T.

[28] R.J.Cotter (1997). *Time-of-Flight Mass Spectrometry – Instrumentation and Applications in biological research*. ACS Professional Reference books. American chemical society, Washington, DC.

[29] D. Jaeks, B. Van Zyl, R.Geballe (1965). Phys. Rev., Vol.**137**, Num. 2A, A340.

[30] M.B. Shah, J.Geddes, H.B.Gilbody (1980). J. Phys. B: At. Mol. Phys. **13**, 4049-4058.

[31] M.B.Shah and H.B.Gilbody (1982). J.Phys. B: At. Mol. Phys. **15**, 3441-3453.

[32] M.B.Shah and H.B.Gilbody (1985). J.Phys. B: At. Mol. Phys. **18**, 899-913.

[33] P. M. Stier and C. F. Barnett (1956). Phys Rev.,**103**, 896.

[34] M.C. Bacchus-Montabonel (2002). Int. J. Mol. Sci., **3**, 114.

[35] Fogel et al (1959). Sov. Phys. JETP, **8**, 390.

[36] J.F. Williams (1966). Phys. Rev., **150**, 7.

[37] D.Belkic and I.Mancev (1991). Phys. Script. Vol. **45**, 35-42.

[38] V. I. Gerasimenko (1962), Sov. Phys. JETP, **14**, 789.

[39] C.D. Lin (1979). Phys. Rev. A, **19**,1510.

[40] M.B. Shah, P. McCallion and H.B. Gilbody (1989). J. Phys. B: At. Mol. Opt. Phys. **22** 3037-3045.

[41] H. Tawara, A. Russek, (1973). Charge Changing Processes in Hydrogen Beams. Rev. of Mod. Phys., Vol. **45**, Number 2, p.178.

[42] G.Bernardi, P. Focke, S.Suarez, and W. Meckbach (1994). Phys. Rev. A, Vol.**50**, No 6, 5338.

[43] L. Sanche (1995). Scanning Microscopy, Vol. **9**, No. 3, 619-656.

[44] PhD Thesis of Wolfgang Sailer.

[45] W.E. Barr, W.A. Perkins (1966). Rev. Sci. Instrum., **37**, 1354.

[46] A. Stamatovic, G.J. Schulz (1968). Rev. Sci. Instrum., **39**, 1752.

[47] D. Klar, M.-W. Ruf, H. Hotop (2001). Int. J. Mass. Spec., **205**, 93-110.

[48] V. Grill, H. Drexel, W. Sailer, M. Sailer, M. Lezius, T.D. Märk (2001). Int. J. Mass. Spec., **205**, 209-226.

[49] J.W. Bond and M.P. Gough (1981). J. Phys. D: Appl. Phys., **14**, 1153-65.

[50] N. Mason, Y. Itikawa (2005). *"Cross sections for electron collisions with water molecules"*. Journal of Physical and Chemical reference data. Vol **34**, issue 1, p1-22.

[51] H.Wollnik (1999). Ion Optics in Mass Spectrometers. J. Mass spectrum. **34**, 991-1006.

[52] P.Cicman, M.Francis, J.D. Skalny, T.D. Märk (2003). Int. J. Mass. Spec., **223-224**, 271-278.

[53] E.De Hoffmann, J.Charette, V.Stroobant (1996). Mass spectrometry: Principles and Applications. Wiley Edition.

[54] Peter H. Dawson (1995). Quadrupole Mass Spectrometry and its applications. AIP Press.

[55] D.Lefaivre and P.Marmet (1974). Rev.Sci. Instrum, **45**, No. 9, p 1134.

[56] R.Nagarajan and P.K. Ghosh (1974). Int. J. Mass Spectrom. Ion Phys., **12**, 79.

[57] W.M. Brubaker, 9th Colloq. Spectrosc. Intern., Lyon, France, June, 1961.

[58] V.W. Hughes and H.L. Schultz (1967). Volume 4, Atomic and electron physics, Part A: Atomic Sources and Detectors. Academic Press.

[59] W.Paul, H.P.Reinhard and U. von Zahn (1958). Z.Phys. **152**, 143.

[60] J.R. Gibson, S. Taylor, and J.H. Leck (2000). J.Vac. Sci. Technol. A, **18**, 1.*"Detailed Simulation of mass spectra for quadrupole mass spectrometer systems"*.

[61] D.J. Douglas, T.A Glebova, N.V. Konenkov, and M. Yu. Sudakov (1999). Technical Physics, Volume **44**, number 10. *"Spatial Harmonics of the field in a quadrupole mass filter with circular electrodes"*.

[62] J. Schulte, P. V. Shevchenko, and A.V. Radchik (1999). Rev. Sci. Instrum., Volume **70**, number 9. *"Nonlinear field effects in quadrupole mass filters"*.

[63] P.H. Dawson and N.R.Whetten (1969). J. Vac. Sci. and tech., Volume **7**, number 3. "*Quadrupole Mass Filter: Circular Rods and Peak Shapes"*.

[64] A.C.C. Voo, R. Ng, J.J. Tunstall, and S.Taylor (1997). J.Vac. Sci. Technol. A, **15**, 4. "Transmission through the quadrupole mass spectrometer mass filter: The effect of aperture and harmonics".

[65] Zhaohui Du, D.J. Douglas, Tatyana Glebova, N.V. Konenkov (2000). Int. J. Mass. Spec., **197**, 113-121. "Peak structure with a quadrupole mass filter operated in the third stability region".

[66] I. S. Buchel'nikova (1959). Sov. Phys. JETP Engl. Trans, **8**, 783-791.

[67] F.H. Dorman(1966). J.Chem. Phys. **44**, 3856-3863.

[68] C.E. Melton (1972). J. Chem. Phys. **57**, No 10, 4218.

[69] D.S. Belic, M. Landau and R.I. Hall (1980). J. Phys. B : At. Mol. Phys., **14**, 175-190.

[70] L.G.Christophorou et al. *Electron-Molecule Interactions and their Applications*. Volume I. (1984). Academic Press. Inc. (Chapter 6 : « Electron attachment processes »)

[71] P.W. Atkins and R.S. Friedman. Molecular Quantum Mechanics - Third edition. (1997). Oxford University Press.

[72] T. F. O'Malley (1966). Phys. Rev., vol. **150**, No. 1, 14-29.

[73] PhD Thesis of D. Muigg.

[74] S.Matejcik, A. Kiendler, A.Stamatovic, T.D. Märk (1995). Int. J. of Mass Spectrom. and Ion Proc. **149-150**, 311-319.

[75] http://www.lsbu.ac.uk/water

[76] L. Sanche and G. J. Schulz (1972). J.of Chem. Phys., Vol. **58**, No.2, 479.

[77] D. J. Haxton, Z. Zhang, C.W. Mc Curdy, and T.N. Rescigno (2004). Phys. Rev. A, **69**, 062713.

[78] D. J. Haxton, Z. Zhang, H-D. Meyer, T.N. Rescigno and C.W. Mc Curdy (2004). Phys. Rev. A, **69**, 062714.

[79] D. J. Haxton, T. N. Rescigno and C.W. McCurdy (2005). Phys. Rev. A, **72**, 022705.

[80] M. G. Curtis and I. C. Walker (1992). J.Chem. Soc. Faraday. Trans. **88**, 2805.

[81] P. Cicman (2004). PhD thesis « Cross electrons molecular beam studies of molecules of atmospheric relevance ».

[82] M.Jungen, J. Vogt and V. Staemmler (1979). Chem. Phys.**37**, 49-55.

[83] R.N. Compton and L.G. Christophorou (1967). Phys. Rev. Vol. **154**, No. 1, 110.

[84] J. A. D. Stockdale, R.N. Compton, and P.W. Reinhardt (1969). Phys. Rev., **184**, No 1, 81.

[85] C.E Klots and R.N. Compton (1978). J. Chem. Phys., **69**(4), 1644.

[86] M. Knapp, O. Echt, D. Kreisle, and E. Recknagel (1987). J. Phys. Chem., **91**, 2601-2607.

[87] F. Gobet, S.Eden, B.Coupier, J.Tabet, B.Farizon, M.Farizon, M.J.Gaillard, M.Carré, S.Ouaskit, T.D. Märk, and P.Scheier (2004). Phys. Rev. A, **70**, 062716.

[88] S. Ptasinska, P. Limao-Vieira, S. Denifl, P. Scheier and T.D. Märk, Electron attachment to monomeric and dimeric forms of glycolaldehyde. *Chem. Phys. Lett.* **401** (2005) 227-231

[89] S. Denifl, S.Ptasinska, M. Probst, J. Hrusak, P. Scheier and T.D. Märk, Electron attachment to the gas-phase DNA bases cytosine and thymine. *J. Phys. Chem. A* **108** (2004) 6562-6569

[90] S. Denifl, S.Ptasinska, M. Probst, J. Hrusak, P. Scheier and T.D. Märk, Electron attachment to the gas-phase DNA bases cytosine and thymine. *J. Phys. Chem. A* **108** (2004) 6562-6569

[91] S. Ptasinska, S. Denifl, P. Scheier and T.D. Märk, Inelastic electron interaction (attachment/ionization) with deoxyribose. *J. Chem. Phys.* **120** (2004) 8505-8511

[92] S. Denifl, S. Ptasinska, G. Hanel, B. Gstir, M. Probst, P. Scheier and T.D. Märk. Electron attachment to gas-phase uracil. *J. Chem. Phys.* **120** (2004) 6557-6565

[93] S. Denifl, S. Ptasinska, P. Scheier and T.D. Märk, Electron impact ionization of 5- and 6-chlorouracil: appearance energies. *Int. J. Mass Spectrom.* **232** (2004) 99-105

[94] S. Denifl, S. Matejcik, S. Ptasinska, B. Gstir, M. Probst, P. Scheier, E. Illenberger and T.D. Märk, Electron attachment to chlorouracil: a comparison between 6-ClU and 5-ClU. *J. Chem. Phys.* **120** (2004) 704-709

[95] S. Ptasinska, S. Denifl, A. Abedi, P. Scheier and T.D. Märk, Dissociative electron attachment to gas-phase glycine. *Anal. Bioanal. Chem.* **377** (2003) 1115-1119

[96] S. Denifl, S. Ptasinska, M. Cingel, S. Matejcik, P. Scheier and T.D. Märk, Electron attachment to the DNA bases thymine and cytosine. *Chem. Phys. Lett.* **377** (2003) 74

[97] G. Hanel, B. Gstir, S. Denifl, P. Scheier, M. Probst, B. Farizon, M. Farizon, E. Illenberger, and T. D. Märk, Electron Attachment to Uracil: Effective Destruction at Subexcitation Energies. *Phys. Rev. Lett.* **90** (2003) 188104 1-4

[98] S. Denifl, S. Matejcik, B. Gstir, G. Hanel, M. Probst, P. Scheier and T.D. Märk, Electron attachment to 5-chloro uracil. *J. Chem. Phys.* **118** (2003) 4107-4114

NOM : COUPIER (avec précision du nom de jeune fille, le cas échéant) Prénoms : Bruno	DATE de SOUTENANCE 17 novembre 2005

TITRE : Studies towards the understanding of the effects of ionizing radiations at the molecular scales (20 to 150keV H^+/H + He Collisions; Dissociative Electron Attachment to Water).

Numéro d'ordre : 206-2005

DIPLOME DE DOCT.	DOCTEUR-INGENIEUR	DOCTORAT D'ETAT	DOCTORAT DE 3e CYCLE	Spécialité :
X	☐	☐	☐	Physique-Interaction particule matière.

Cote B.I.U. – Lyon : T 50/210/19 / et bis	CLASSE :

RESUME :
Ce travail s'inscrit dans le cadre d'études récentes pour la compréhension à l'échelle moléculaire des effets des rayonnements ionisants sur les systèmes biologiques, mises en oeuvre par le groupe IPM de l'IPNL en collaboration avec l'Institut für Ionenphysik de l'Université d'Innsbruck. Il est composé de deux parties. La première présente un nouvel ensemble de mesures des sections efficaces d'ionisation de l'hélium par impact de protons ou d'atomes d'hydrogène dans la gamme d'énergie d'intérêt pour la radiobiologie (20 à 150keV). Il s'agit de systèmes modèles d'intérêt pour la compréhension des phénomènes de base, et les collisions H + He ont fait l'objet, jusqu'à présent, de peu d'études utilisant les techniques de coïncidences. En outre, cette étude avec l'hélium a été faite dans l'intention de réaliser un test général de fonctionnement de l'appareillage avant d'aller vers des systèmes plus complexes. Des études similaires ont été ensuite réalisées en remplaçant la cible d'hélium par l'eau ou par des molécules d'intérêt biologique (Uracil, Thymine …). La seconde partie de la thèse traite d'un autre type de radiations ionisantes que l'on peut voir comme une des conséquences secondaires des radiations étudiées dans la première partie. Des électrons de faible énergie (1 à 16eV) sont émis lors du bombardement de la matière par des protons ou des atomes d'hydrogène rapides; ces électrons ayant à leur tour des effets ionisants sur l'environnement. Une étude de l'attachement dissociatif des électrons sur l'eau a été entreprise à l'université d'Innsbruck, motivée par l'existence d'importants désaccords entre les précédentes études sur le même sujet. Le problème de la discrimination des ions à grande énergie cinétique dans le monochromateur trochoïdal utilisé pour cette étude a fait l'objet d'une attention particulière.

MOTS-CLES : collisions ion - atome, biomolécules, effets des rayonnements ionisants, ionisation, capture électronique, techniques de coïncidence, spectrométrie de masse à quadrupôle, monochromateur électronique trochoïdal, attachement d'électron libre, radiolyse de l'eau, hélium, DNA.

Laboratoire de recherche : Institut de Physique Nucléaire de Lyon et Institut für ionenphysik (Leopold Franzens Universität - Innsbruck)

Directeurs de recherches : M. Farizon et T.D Märk

Président du jury : Mme S. Schindler Composition du jury : N. Moncoffre – M. Farizon – T.D Märk	277 pages